Design and development of tapered geometry semiconductor optical sources

Brooks, N. S.

Award date:
1998

Awarding institution:
University of Bath

Design and Development of Tapered Geometry Semiconductor Optical Sources

Submitted by

N.S. Brooks

for the degree of Doctor of Philosophy

of the University of Bath

1998

N.S.Brooks

ProQuest LLC
789 East Eisenhower Parkway
P.O. Box 1346
Ann Arbor, MI 48106-1346

Summary

This thesis describes the design and characterisation of high power, tapered waveguide semiconductor lasers. The propagation characteristics of passive tapered waveguides of different shapes and sizes are analysed and their usefulness in high power lasers is discussed. A computationally efficient model for parabolically tapered lasers is described and used to predict the performance of such devices. Results from the experimental characterisation of parabolically tapered bow-tie lasers are shown to agree with the simulation results.

Simulation and experiment results are used to discuss the possible advantages of current segmentation and facet coatings in improving device efficiency.

An experimental comparison of differently shaped bow-tie lasers is described demonstrating the superior efficiency of the parabolic shape. Experimental results from large flare angle linearly tapered bow-tie lasers show that high power output in a high quality diverging beam is possible using cavity spoiling elements.

Output powers of 200mW CW from a parabolically tapered bow-tie laser and 600mW from a bow-tie laser array are shown. Far field intensity profiles of parabolically tapered bow-tie lasers are shown to have FWHM of 3°.

Acknowledgements

My thanks are due to my supervisor Dr. J. Sarma, for his ideas, encouragement, wisdom and endless discussions. I am also indebted to Dr. Ian Middlemast for teaching me everything that I know, and to Mr. Trevor Ryan for his amazing ability to interpret my requirements and fabricate the devices that I needed.

My gratitude goes to Prof. P. Bhattacharya and Dr. K. Kamath of the University of Michigan for the InGaAs material, and to Dr. J. Tomm and Dr. A. Jaeger of the Max Born Institüt, Berlin for the CW measurements.

My thanks also go to my other colleagues and friends for their help, advice and their sanity restoring powers in my times of need.

"How far that little candle throws his beams!"

William Shakespeare

Contents

List of Figures

Glossary

α	Absorption loss of material (Chapter 4)
α_0	Gain constant (Chapter 3)
$\alpha_{l,p,e}$	Tapered waveguide expansion coefficient (Chapter 2)
β_m	Propagation constant of mode 'm'
$\Delta\beta_m$	Correction to propagation constant
χ_R	Constant relating refractive index change to carrier density
ε	Dielectric constant of material (ε_0 is free space value)
$\Delta\varepsilon$	Perturbation to dielectric constant
γ_A	Auger recombination constant (Chapter 4)
η	Effective refractive index of (vertical) waveguide mode
η_D	External differential quantum efficiency (Chapter 4)
η_0	Internal quantum efficiency (Chapter 4)
λ	Wavelength of light in (λ_0 is free space value)
μ	Permittivity of material (μ_0 is free space value)
ν	Frequency of light
θ	Dimension in spherical polar coordinates
θ_i	Electrical length of dielectric layer 'i' in transmission line analogy
ρ	Charge density
σ	Conductivity of material
τ	Carrier lifetime
ω	Angular frequency of light
ψ	Eigenfunction in Schrödinger's equation (Appendix 4)
Γ	Confinement factor of waveguide mode (Γ_v = vertical confinement factor)
Λ	Spatial period of grating
b	Half-thickness of symmetric waveguide
c	Speed of light in free space
d	Thickness/length of dielectric layer
g	Gain of material

g_m	Gain of mode 'm'
h	Planck's constant
j	$\sqrt{-1}$
k	Wavenumber (k_0 is free space value)
m	Magnetic polarisation vector
n	Refractive index
n_0	Doping density of active layer (Chapter 3)
p	Electric polarisation vector
q	Electronic charge
t	Time
w	Width of waveguide (Chapters 2, 4)
x	Dimension in Cartesian Coordinate System
y	"
z	"

A_{pm}	Amplitude of mode 'm' in section 'p' of tapered device
A	Constant relating gain to current density (Chapter 4)
B	Magnetic displacement vector
B_R	Bimolecular recombination constant
C	Normalisation constant (Chapter 2)
D	Electric displacement vector
D	Diffusion coefficient
A,B,C,D	Matrix coefficients (Chapter 6)
E	Electric field vector
E_n	Eigenvalue in Schrödinger equation (Appendix 4)
F	General component of electromagnetic field
$F_m(x)$	Lateral mode field profile
G	Round trip gain in Fabry-Perot cavity
H	Magnetic field vector
$\hat{H}$	Hamiltonian operator in Schrödinger equation (Appendix 4)
I	Intensity
I	Current
J	Current density
L	Length of cavity

N	Carrier density
N_T	Transparency carrier density
P	Photon density
R	Power Reflectivity of facet
T	Transmission coefficient of facet
V	Voltage in transmission line
Y	Admittance
Z	Impedance

Chapter 1

Introduction

In the 30 years since the first semiconductor diode laser was demonstrated their use has become widespread to an extent that no-one could have imagined. Their small size and efficient nature has allowed the information revolution to take place. How many homes in the developed world today are without a CD player or a telephone? Without semiconductor lasers the domestic CD player would never have become a practical proposition and trans-oceanic telephone conversations would not be routed through optical fibres but via satellites with the associated long time delays between sending and receipt of data.

Various material types, including Indium Phosphide (InP) and Gallium Arsenide (GaAs), have allowed semiconductor lasers to be commercially produced with wavelengths between 1.55μm-0.67μm. More recently, advances with GaN and CdSe have made blue-green diode lasers a reality (λ<0.5μm).

There are numerous applications for high power semiconductor optical sources including intersatellite communications, pumping Erbium doped fibre amplifiers, various medical applications and second harmonic generation pump sources. The small size of semiconductor devices make them the only suitable source for some of these applications. Commercial, high power semiconductor sources are frequently arrays of low power devices. Monolithic, diode lasers emitting high powers in good output beams are still rare. The reasons for this lie in the design of the devices.

1.1 The Semiconductor Laser

The simplest form of semiconductor laser is probably the monomode rib waveguide device. Figure 1.1 shows a schematic of such a device fabricated from GaAs/AlGaAs double heterostructure material. Optical confinement to the active layer is provided by the vertical refractive index profile of the different material layers. Laterally, the etching of the rib produces an effective index variation (see appendix 1) and therefore a waveguide. Typical values for the active layer thickness and the rib width are 0.3μm and 3μm respectively. These values are chosen to ensure that only one guided mode

exists both vertically and laterally and hence the transverse field intensity distribution is well defined leading to a good output beam. Larger values would result in multiple waveguide modes being allowed which are likely to cause a deterioration in the beam quality of the device.

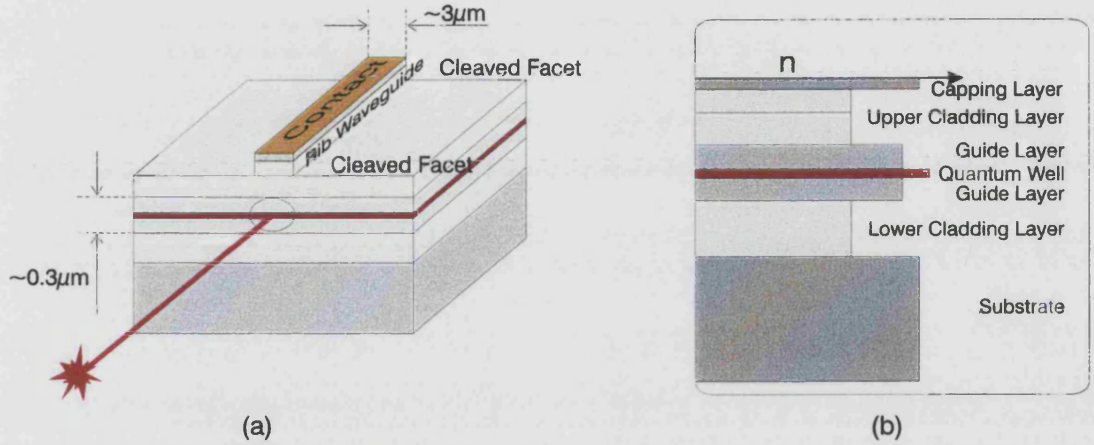

Figure 1.1. (a) Schematic diagram of a rib waveguide semiconductor laser. (b) Refractive index variation through a typical laser material.

However, the confinement of the optical power to such a small area is also the drawback of this device in terms of high power operation. The maximum power available from a particular device is limited by the optical power density that occurs within it, and more importantly, at the facet. If the power density at the facet exceeds a certain value then catastrophic optical damage (COD) occurs. Nonradiative recombination due to surface states causes the facet to heat up and if the power density is sufficiently high then the facet overheats (COD). The small spot-size of the single-mode waveguide laser limits the power available from this device to around 300mW.

1.2 High Power Semiconductor Lasers.

1.2.1 Facet Passivation

The optical power density at which COD occurs can be improved by facet passivation. Passivation techniques based on wet chemical solutions of inorganic sulphides can produce nearly ideal surfaces with a reduced density of surface states which are responsible for nonradiative recombination. Increases in output power of up to 2.5 times compared to untreated devices have been reported [1]. A COD threshold greater than 500mW has been claimed [2] for 980nm 4μm ridge waveguide lasers.

1.2.2 Broad Area Lasers

The obvious method of increasing the overall output power is simply to broaden the device. Larger widths allow higher powers to be produced for a given optical power density across the facet before the onset of COD. However, the output from broad area lasers tends to be spatially incoherent due to filamentation occuring in the device which is a result of self-focusing. As a consequence the far-field divergences are frequently more then 5 times the diffraction limit. Schemes involving external cavities have been tried in order to control the lateral field shape however such devices are then quite complex. Nonetheless broad area lasers have produced extremely high output powers (11W) even if the beam is of low quality [3].

1.2.3 Coupled Oscillators

In these devices an array of single-mode waveguide emitters are coupled and coherently locked in order to increase the output power. Several techniques have been proposed in order to achieve the coupling. One example is the 'Y-junction' laser array (figure 1.2). At a y-junction the light in the two waveguides is coupled. If the interfering waves are in phase then constructive interference occurs. If the waves are out of phase then destructive interference occurs. Therefore, in a device such as that shown in figure 1.2 the mode with the lowest threshold is that where all the emitters are in phase. However, as the current increases variations in carriers, and therefore refractive index, between different emitters changes the individual optical path lengths and increases the losses of this mode until finally the device begins to operate in multiple spatial modes. Single spatial mode powers of around 300mW have been reported [4] for these devices.

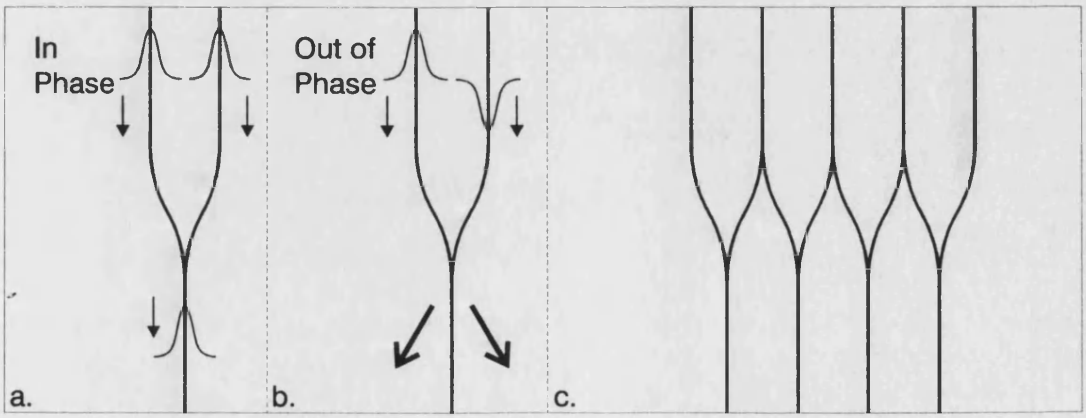

Figure 1.2. Schematic diagram of a 'Y-junction' laser. (a) Showing field variation for in-phase case, (b) out-of-phase case, and (c) a 'Y-junction' laser array.

1.2.4 Uncoupled Arrays

Many commercial high power diode sources are comprised of an array of uncoupled lasers. The individual laser elements can be narrow single-mode devices or even broad area devices. These devices produce very high powers (>10W) simply by having large numbers of elements but do not have the spatial beam quality or narrow wavelength range available from other devices.

1.2.5 Antiguide Arrays

These devices consist of an array of guided and antiguided regions with a relatively large index step between them. Carriers are injected into the low index (antiguided) regions and the light is generated into leaky modes which resonantly couple between the high gain regions. In-phase coupling occurs when the element spacing is equal to an odd integral number of half wavelengths. Antiguided arrays emitting 1W of power have been demonstrated [5] although only 0.6W was in the central lobe of the far-field. The disadvantages of antiguiding arrays are the complex fabrication procedure, which usually requires regrowth, and the extremely tight fabrication tolerances [6] necessary to meet the lateral resonance condition, particularly for large numbers of elements.

A similar device that also employs an antiguided structure is the three-core antiresonant-reflective-optical waveguide (ARROW). This device has a three element resonant antiguided array with pairs of quarter-wave reflectors at the sides (figure 1.3). These reflectors reduce the edge radiation losses of particular array modes composed of coupled fundamental (element) modes compared with array modes composed of coupled first-order (element) modes. 550mW at 0.98μm has been reported for this device [7].

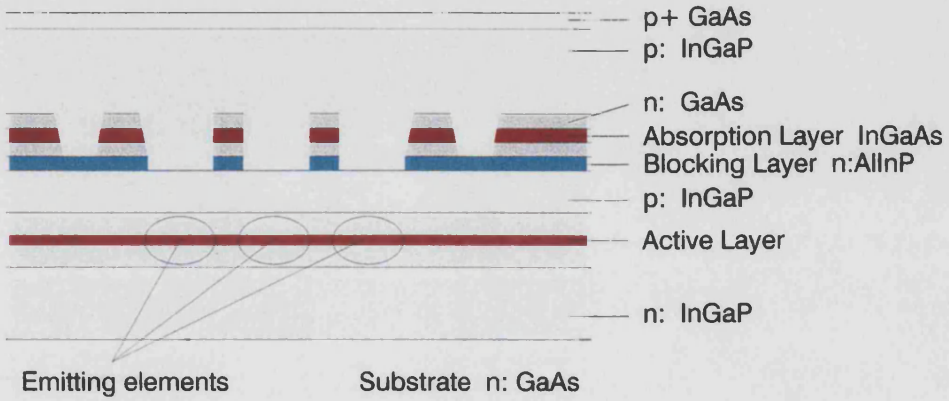

Figure 1.3.a. Schematic diagram of the end view of an ARROW device.

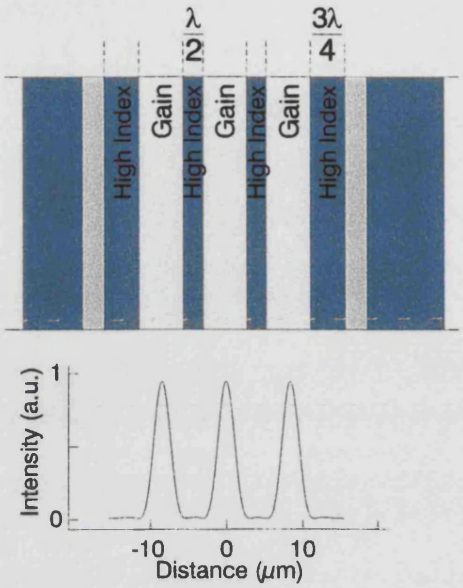

Figure 1.3.b. Schematic diagram of an ARROW device. Top view with plot showing approximate lateral intensity variation.

1.2.6 Unstable Resonators

Unstable resonators employ a diverging lateral field within a broad area device to reduce the tendency to self-focus and hence reduce the likelihood of filamentation. Perhaps the simplest and most successful method of producing a diverging beam has been the use of an etched curved facet at one end of the device (see figure 1.4). 1.5W CW from a single facet in a nearly diffraction-limited beam has been reported [8]. However, the focussed ion beam process used to create the curved facet is not readily suitable for batch production. Diffraction-limited output has also been reported by Biellak et al. [9] from devices fabricated by reactive ion etching. Single facet peak powers of around 500mW were obtained with 300ns pulses. The high quality mirrors were realised by using electron beam lithography to accurately define the curved shape.

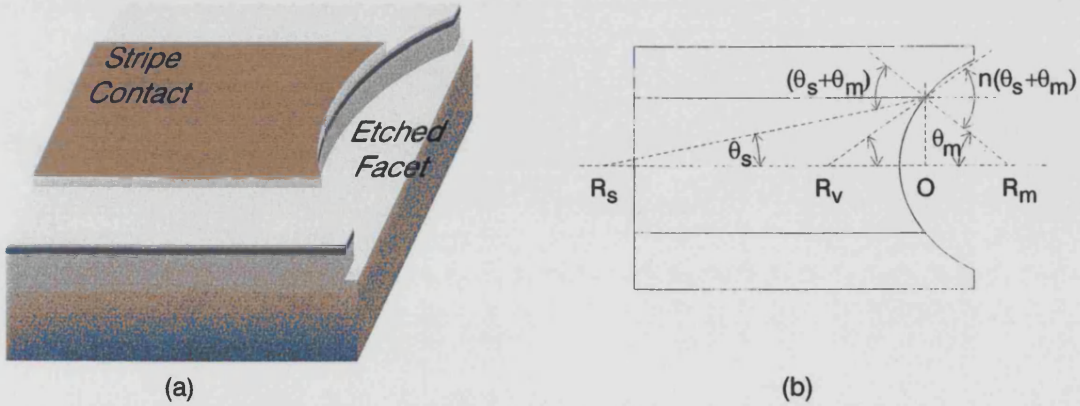

Figure 1.4. Schematic diagram of an unstable resonator semiconductor laser.

A disadvantage of unstable resonator devices is that the diverging beam within the device produces an astigmatic and laterally diverging output. Figure 1.4.b. shows the location, RV, of the virtual source of the diverging output which is given by:

$$R_V = \frac{1}{n \cdot \left(\frac{1}{R_S} + \frac{1}{R_M} \right) - \frac{1}{R_M}} \qquad \{1.1\}$$

where 'n' is the refractive index of the material, 'R_M' is the radius of curvature of the facet and 'R_S' is the Siegman centre [10].

1.3 Tapered Structures

Tapered devices are, quite simply, devices that have a region where the width changes along the length of the device (see figure 1.5). Such devices have several key advantages over other high power sources. Firstly, they can be very easily fabricated. Conventional double heterostructure or quantum well material can be used. Fabrication of the etched rib structure is a simple and well established process that does not require any regrowth or other complex steps. In addition, the narrow section should provide some control over the field shape. The wide facet of a tapered device increases the saturation output power compared to a narrow device simply by increasing the active volume at the facet. Also, for a given power output, the increase in the area will result in a corresponding decrease in the optical power density at the facet. This will reduce catastrophic optical damage (COD) at higher output powers. The devices fall into two categories. The first are devices without any explicit lateral wave guiding to confine the optical power in that direction. Within these devices the field is simply allowed to diffract from the narrow end to the wide end of the device. The second type of device has explicit lateral guiding which provides some control over the expansion of the field. Most of the work reported in the literature has employed little or no lateral index guiding.

Tapers have demonstrated high-powers, both CW and as Q-switched pulses when incorporated into a wide variety of device configurations such as tapered amplifiers, master oscillator power amplifiers (MOPA), tapered (unstable resonator) lasers and 'Bow-tie' lasers.

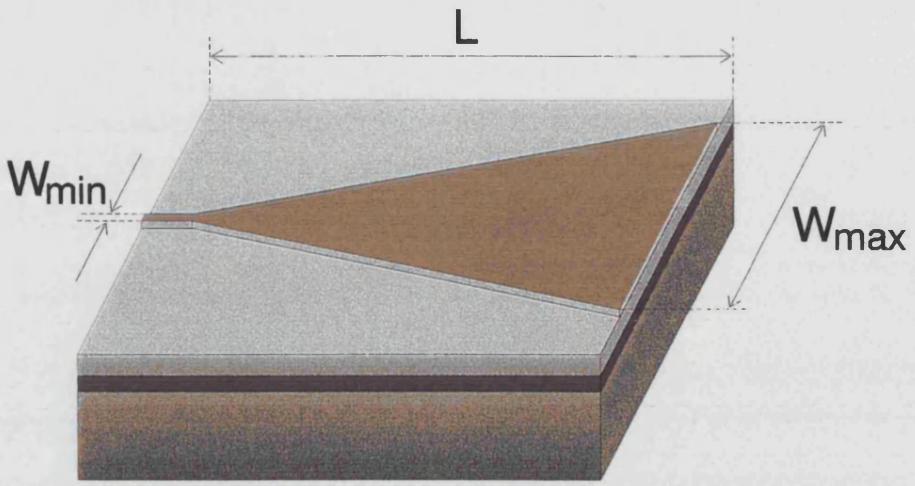

Figure 1.5. Schematic diagram of a tapered device.

1.3.1 Tapered Amplifiers

Tapered amplifiers have been demonstrated by a number of groups [11, 12, 13]. Powers as high as 4.5 W CW have been achieved. The devices essentially consist of a tapered gain region, which may or may not be index guided, between two anti-reflection (AR) coated facets. The disadvantage of these devices is that very high quality AR coatings (R=0.1%) are needed at the facets in order to prevent the device reaching lasing threshold. A further problem is that device operation is very easily affected by feedback due to external reflections which can cause the device to reach threshold.

A tapered amplifier with an integrated focussing lens has also been reported [14]. This device delivered greater then 1W CW. At powers up to 0.5W the output was focussed to a spot of size 8μm × 3μm. The disadvantage with this device is that it required a complex fabrication procedure including two epitaxial growth stages in order to integrate a passive output waveguide in which the beam is focussed.

1.3.2 Master Oscillator Power Amplifiers (MOPA)

Tapered amplifiers have been integrated with Master Oscillator lasers in order to achieve high powers. Of particular interest are monolithically integrated MOPA's where a distributed Bragg reflector (DBR) laser and tapered amplifier are integrated on a single chip (figure 1.6). These devices have demonstrated 2.2W CW at 854nm [15] and 3W CW at 980nm. However, these devices retain the disadvantages of the tapered amplifiers that high quality AR coatings are still needed. Perhaps the key advantage

with the MOPA configuration is that the single longitudinal mode spectrum of the DBR laser can be retained at the output of the power amplifier.

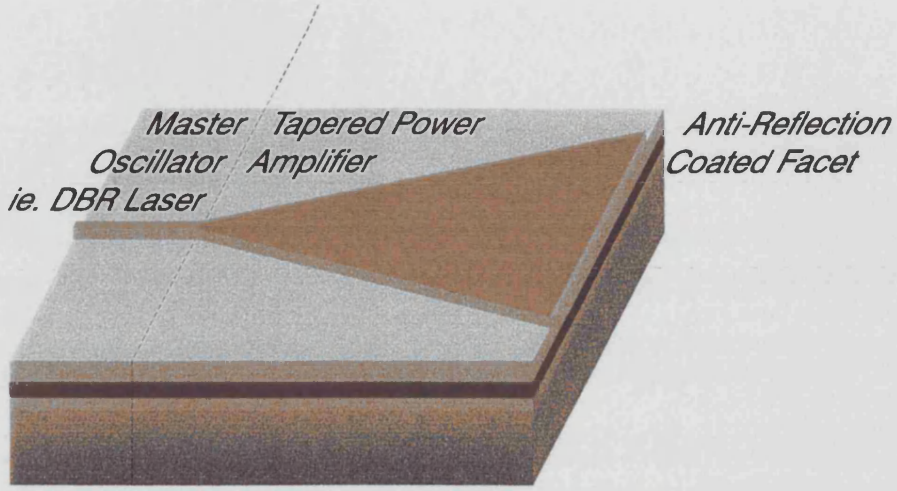

Figure 1.6. Schematic diagram of an integrated Master Oscillator Power Amplifier.

1.3.3 Tapered Lasers

Reported work on tapered lasers has concentrated on devices with no lateral index guiding and very heavily antisymmetric Fabry-Perot cavities where the narrow facet is high-reflection coated to greater than 99% reflectivity and the wide facet is AR coated to less than 1% reflectivity. A further common feature of these devices are cavity spoiling elements near the narrow end facet (see figure 1.7). These spoilers take the form of deeply etched pits which go through the active layer, forming an aperture for the optical field to propagate through and thereby restricting the width of the field. The narrow field then diffracts as it propagates from this aperture toward the wide end of the device. As a consequence, the field at the wide facet has a curved wavefront which remains curved on reflection from the facet. These lasers are therefore unstable resonators as there are not two counter propagating beams present.

Figure 1.7. Schematic diagram of a tapered laser with cavity spoiling elements.

Tapered lasers have demonstrated 4.2W CW at 980nm [16]. The disadvantage of these devices is again that high quality facet coatings are needed. In addition, the presence of a narrow region at a facet can still lead to high power densities occuring where non-radiative recombination is important causing COD. A further point to note is that the diverging beam reflected from the wide facet does not couple effectively back into the tapered gain region. A large amount of this reflected field is spilled out of the sides of the device and essentially 'lost' which reduces the overall efficiency of the device.

1.3.4 The Bow-tie Laser

The Bow-tie laser (figure 1.8) has a twin taper structure which gives it the advantage over single-tapered lasers that the device is wide at both facets. The narrow region does not occur near a facet therefore the high power densities that occur in this region will not lead to early failure from COD. Spoilers to the sides of the centre region can be used to limit the width of the optical field as in the case of single-tapered lasers.

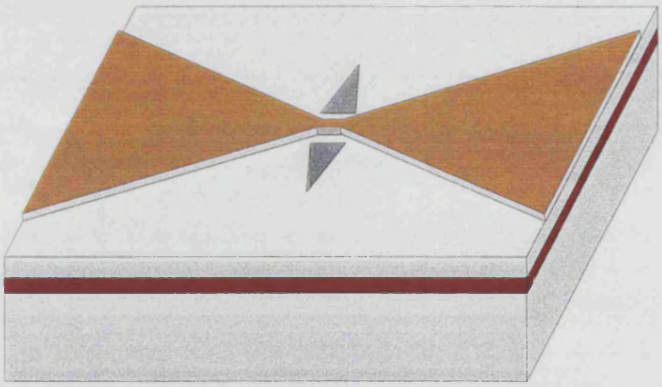

Figure 1.8. Schematic diagram of a rib waveguide bow-tie laser.

2mm long Bow-tie lasers have demonstrated 1W per facet CW at 860nm[17] with no AR coatings. Much smaller devices have been operated Q-switched to produce 5W peak power, 8ps pulses [18]. As with the single-taper lasers all of these devices still have planar facets which do not match the curved wavefronts that occur within them.

Alternatively, a twin-tapered stable resonator laser has also been demonstrated [19]. The device had a tapered gain region without lateral index guiding and two curved facets (figure 1.9). The positions and radii of curvature of the mirrors were chosen to form a near-concentric resonator. A further point to note is that cavity spoiling elements were not employed in this structure. The output power from this device is not mentioned. However, the work is of interest as it shows the different modes of

operation of the device. Stable resonator operation is only achieved at currents up to approximately three times threshold. Above five times threshold the device operates as an unstable resonator. Between these regions a transition regime is observed. The different operating regions occur because the nonlinear effects of carrier density on refractive index become more important at higher power levels. At the highest currents the device becomes strongly gain-guided.

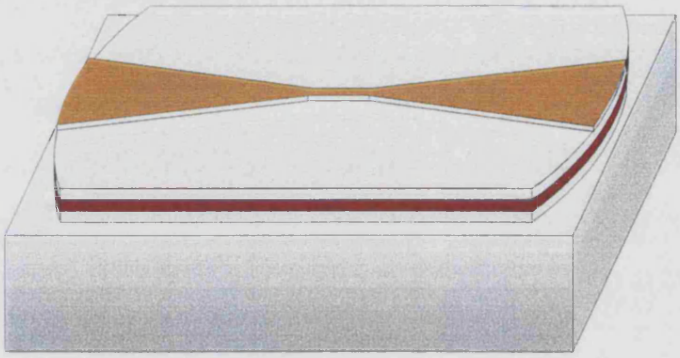

Figure 1.9. Schematic diagram of a twin-tapered stable resonator semiconductor laser.

1.4 Modelling of Tapered Structures

The primary aim of the work in this thesis was to optimise the design of the tapering guide to produce narrow far-field distributions with the optical power distributed across the whole waveguide. In order to meet this challenge tapered waveguides needed first to be analysed and therefore a model had to be developed.

Previous models for tapered devices have employed several techniques. Firstly, the Beam Propagation Method (BPM) has been used to model devices both with and without explicit lateral index guiding [20,21]. This is an entirely numerical technique that uses Fast Fourier Transforms. The advantage of the BPM is that it is quite general and can analyse almost all situations provided there are no large, sudden changes in refractive index. Perhaps the most important disadvantage is that it requires large amounts of computer memory and computation time. In addition, as an entirely numerical technique it does not give the same insight into device operation that quasi-analytical methods can.

Also, for devices with lateral index guiding, the Local Mode expansion method has been used by several authors/groups [22,23]. The local bound modes of the waveguide

are used to describe the optical field. Different procedures have been adopted for including the nonlinear effects of the carriers in active devices. These will be discussed in more detail later. The advantages of this method are that it can result in a computationally efficient model and that the expansion of the field in terms of the local bound modes can give a good insight into device operation. For these reasons the model used in this work [24] uses the Local Mode expansion method. The disadvantage is that the bound modes are not a complete mathematical set and therefore not all situations can be analysed. If large proportions of the field escape from the guide then this method alone is not applicable. This limitation will be discussed further later in the thesis.

Another model that has been reported is based on a Hermite-Gauss function expansion method [25]. The optical field within the device is expanded in terms of the set of Hermite-Gauss functions.

1.5 Thesis Layout

The work in this thesis is presented in approximately chronological order showing the design and development methodology employed. Thus, the next chapter contains a systematic theoretical study of the propagation properties of passive tapered waveguides. The model used for the analysis is described followed by simulation results for a range of tapered waveguides of different shapes and sizes that may be useful in moderately high power sources.

A description of the model used to analyse tapered lasers is presented in chapter 3. The problems encountered when analysing linearly tapered lasers using this model are discussed. Simulation results for several parabolically tapered lasers are then presented. The values of material parameters used and the sources of these values are found in appendix 6 rather than in the main text of the thesis. The first experimental results are also presented in this chapter. Comparisons will be made between simulation results and experimental results from the first parabolically tapered lasers measured. Descriptions of the experimental techniques used to characterise the devices are not found in this chapter but are instead detailed in appendix 5.

The possible advantages of facet coating to alter reflectivities and current segmentation are examined in chapter 4. Simulation results are presented showing the effects that

longitudinal current density variation and reflectivity variation have on the threshold current and slope efficiency of a parabolically tapered laser. Experimental results obtained from a number of anti-reflection coated single-taper lasers are also contained in this chapter.

The effect of taper shape on device operation is examined in chapter 5. Experimental results from a number of differently shaped bow-tie lasers are compared with measurements from a broad area laser. Some results from differently shaped bow-tie laser arrays with and without AR facet coatings are then presented. Details are also given in this chapter of measurements on devices fabricated from InGaAs QW material with wavelength-shifted regions. These devices included some large flare angle linearly tapered Bow-tie lasers.

Chapter 6 contains a theoretical study of the application of coarse gratings to Fabry-Perot cavity lasers in order to achieve discrimination between longitudinal modes. A model based on a transmission line analogy is described and simulation results presented.

Finally, some conclusions to be drawn from this work are presented in chapter 7 along with suggestions for future work.

References

[1] J.S.Yoo, H.H.Lee, P.Zory, 'Enhancement of Output Intensity Limit of Semiconductor Lasers by Chemical Passivation of Mirror Facets,' IEEE Photonics Technology Letters, Vol. 3, p.202-203, 1991.

[2] G.Beister, J.Maege, J.Sebastian, G.Erbert, L.Weixelbaum, M.Weyers, J.Würfl, O.P.Daga, 'Stability of Sulfur-Passivated Facets of InGaAs-AlGaAs Laser Diodes,' IEEE Photonics Technology Letters, Vol. 8, p.1124-1126, 1996.

[3] S.O'Brien, H.Zhao, A.Schoenfelder, R.Lang, 'High power AlGaAs-based 100μm aperture lasers at 870 and 970nm,' Proceedings of IEEE-LEOS annual meeting, postdeadline paper PDP1.3, Boston, USA, 1996.

[4] D.F.Welch, W.Streifer, P.S.Cross, D.R.Scifres, 'Y-Junction Semiconductor Laser Arrays: Part II - Experiments,' IEEE Journal of Quantum Electronics, Vol. 23, p.752-756, 1987.

[5] C.Zmudzinski, D.Botez, L.J.Mawst, C.Tu, L.Frantz, 'Coherent 1W continuous wave operation of large-aperture resonant arrays of antiguided diode lasers,' Applied Physics Letters, Vol. 62, p.2914-2916, 1993.

[6] D.Botez, A.Napartovich, C.Zmudzinski, 'Phase-locked arrays of antiguides: Analytical theory II,' IEEE Journal of Quantum Electronics, Vol. 31, p.244-253, 1995.

[7] C.Zmudzinski, D.Botez, L.J.Mawst, A.Bhattacharya, M.Nesnidal, R.F.Nabiev, 'Three-core ARROW-type diode laser: Novel high-power, single-mode device, and effective master oscillator for flared antiguided MOPA's,' IEEE Journal of Selected Topics in Quantum Electronics, Vol. 1, p.129-137, 1995.

[8] R.K.DeFreez, Z.Bao, P.D.Carleson, M.K.Felisky, C.Largent, 'High-brightness unstable resonator semiconductor lasers,' in Proc. SPIE, vol.1850, p. 74-83, 1993.

[9] S.A.Biellak, C.G.Fanning, Y.Sun, S.S.Wong, A.E.Siegman, 'Reactive-ion-etched diffraction-limited unstable resonator semiconductor lasers,' IEEE Journal of Quantum Electronics, Vol. 33, p.219-230, 1997.

[10] A.E.Siegman, Lasers, University Science Books, 1986.

[11] D.Mehuys, D.F.Welch, L.Goldberg, '4.5W CW near-diffraction-limited tapered-stripe semiconductor optical amplifier,' Electronics Letters, Vol. 29, p.219-221, 1993.

[12] J.N.Walpole, E.S.Kintzer, S.R.Chinn, C.A.Wang, 'High-power strained-layer InGaAs/AlGaAs tapered traveling wave amplifier,' Applied Physics Letters, Vol. 61, p.740-742, 1992.

[13] P.S.Yeh, L-F.Wu, S.Jiang, M.Dagenais, 'High-power high-gain monolithically integrated preamplifier/power amplifier,' Electronics Letters, Vol. 29, p.1981-1983, 1993.

[14] K-Y. Liou, M.G.Young, E.C.Burrows, R.M.Jopson, G.Raybon, C.A.Burrus, 'High-power broad area tapered amplifier with a monolithically integrated output focusing lens at 0.98μm wavelength,' IEEE Journal of Selected Topics in Quantum Electronics, Vol. 1, p.165-172, 1995.

[15] S.O'Brien, R.Lang, R.Parke, J.Major, D.F.Welch, D.Mehuys, '2.2W CW diffraction-limited monolithically integrated master oscillator power amplifier at 854nm,' IEEE Photonics Technology Letters, Vol. 9, p.440-442, 1997.

[16] E.S.Kintzer, J.N.Walpole, S.R.Chinn, C.A.Wang, L.J.Missagia, 'High-power strained-layer amplifiers and lasers with tapered gain regions,' IEEE Photonics Technology Letters, Vol. 5, p.605-608, 1993.

[17] I.Middlemast, J.Sarma, P.S.Spencer, 'Output Characteristics of High Power GaAs/GaAlAs Double Heterostructure Rib-Waveguide Bow-tie Lasers,' Integrated Photonics Research, Vol.6, 1996 OSA Technical Digest Series, p. 524, (1996).

[18] K.A.Williams, J.Sarma, I.H.White, R.V.Penty, I.Middlemast, T.Ryan, F.R.Laughton, and J.S.Roberts, 'Q-switched Bow-tie Lasers for High-energy Picosecond Pulse Generation,' Electronics Letters, Vol. 30, No. 4, p. 320, (1994).

[19] S.A.Biellak, Y.Sun, S.S.Wong, A.E.Siegman, 'Lateral mode behavior of reactive-ion-etched stable-resonator semiconductor lasers,' Journal of Applied Physics, Vol. 78, p.4294-4296, 1995.

[20] R.J.Lang, A.Hardy, R.Parke, D.Mehuys, S.O'Brien, J.Major, D.F.Welch,'Numerical analysis of flared semiconductor laser amplifiers,' IEEE Journal of Quantum Electronics, Vol. 29, p.2044-2051, 1993.

[21] K.A.Williams, I.H.White, R.V.Penty, F.R.Laughton, 'Gain-switched dynamics of tapered waveguide Bow-tie lasers: Experiment and theory,' IEEE Photonics Technology Letters, Vol.9, p. 167-169, 1997.

[22] G.Bendelli, K.Komori, S.Arai, 'Gain saturation and propagation characteristics of index-guided tapered-waveguide traveling-wave semiconductor laser amplifiers (TTW-SLA's),' IEEE Journal of Quantum Electronics Vol.28, p.447-457, 1992

[23] P.S.Spencer, I.Middlemast, R.Balasubramanyam, J.Sarma & K.A.Shore, presented at 'Semiconductor Lasers: Advanced Devices & Applications Conference', Colorado, USA, August 1995.

[24] N.S.Brooks J.Sarma & I.Middlemast, 'A Compact Model for Tapered Waveguide Semiconductor Optical Devices', SIOE conference, Cardiff, 1996.

[25] F.Causa, J.Sarma, M.Milani, 'Hermite-Gauss functions in the analysis of weakly non-uniform semiconductor optical devices,' proceedings of the International conference on Fibre Optics and Photonics, Madras, India, p.127-132, 1996.

Chapter 2

Passive Tapered Waveguides

The results of a theoretical study of the propagation characteristics of passive tapered waveguides are contained in this chapter. The chapter begins with a description of the mathematical model used to analyse such structures. A discussion of the desired properties of a tapered waveguide and the physical constraints on its design follows. Simulation results from the model for a number of tapered waveguides are then presented. The effects of various taper parameters such as flare angle and shape are shown and the significance of these results in terms of high power laser design is discussed.

2.1 The 'Stepped-Waveguide' Model

Approximations must be used in order to model the propagation of an optical field through a tapered dielectric rib waveguide (see figure 2.1.a). Firstly, in order to model three dimensional rib waveguides the Effective Index Method [1] was used to reduce the problem to two dimensions. To do this the vertical waveguiding properties of the device were found for the regions inside and outside of the rib using the transmission line analogy detailed in Appendix 3. For the single vertical mode of each of these regions an 'effective' refractive index, η_{eff}, was calculated corresponding to the ratio, c/v_{ph} of the speed of light in a vacuum and the phase velocity of the mode. These effective indices were then used to describe a 2-dimensional waveguide structure (figure 2.1.b).

A further difficulty was encountered with the continuously varying width of the taper. Although wave propagation through linearly tapering metal-walled horns can be described analytically in a polar coordinate system by radially propagating mode solutions [2] this approach was not applicable to dielectric waveguides. Therefore, a further approximation was adopted. The stepped-waveguide Local Mode Expansion method [3] approximated the taper to a series of parallel waveguides of different widths (see figure 2.1.c). Wave propagation through each section was considered separately and the fields matched at the interfaces. In this manner, the Cartesian coordinate system could be used which is generally to be preferred.

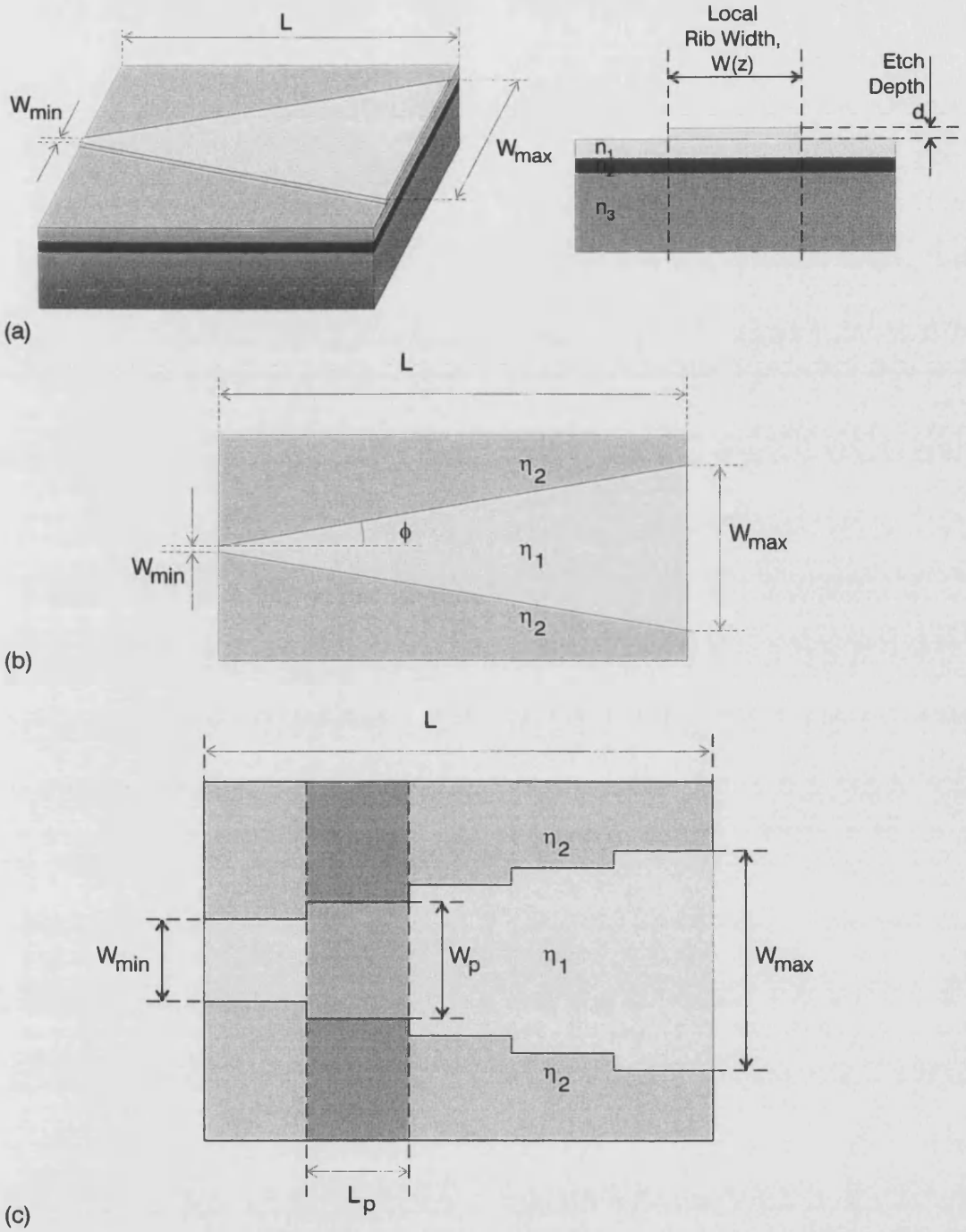

Figure 2.1. (a) Schematic diagram of a tapered dielectric rib waveguide. (b) 2-D tapered waveguide. (c) Stepped waveguide approximation.

For each waveguide segment the bound modes were found by solving the wave equation, {A1.9}, as shown in Appendix 1.

$$\nabla^2 F_m(x,y,z) + \omega^2 \mu \varepsilon' F_m(x,y,z) = 0 \qquad \{A1.9\}$$

where F_m is the field component, ω is the angular frequency of the light, μ is the permeability and ε' is the permittivity.

The discrete solutions found are the bound modes of the step, which for the TE_x case take the form:

$$F_m(x) = C_{m1}\cos(k_1 x) \quad \text{when } |x| \le b \quad \text{for symmetric modes} \qquad \{2.1.a\}$$

$$F_m(x) = C_{m1}\sin(k_1 x) \quad \text{when } |x| \le b \quad \text{for antisymmetric modes} \qquad \{2.1.b\}$$

$$F_m(x) = C_{m2}\exp(-k_2|x|) \quad \text{when } |x| \ge b \qquad \{2.1.c\}$$

where $k_1^2 = k_0^2\varepsilon_1 - \beta_m^2$, $k_2^2 = \beta_m^2 - k_0^2\varepsilon_2$ and $k_0^2\varepsilon_1 > \beta_m^2 > k_0^2\varepsilon_2$

and $b = \frac{w_p}{2}$ is the half-width of the guide.

C_{m1} and C_{m2} are normalisation constants whose values were chosen such that the field is continuous at $|x| = b$ and the field satisfied:

$$\int_{-\infty}^{\infty} F_m(x) \cdot F_m^*(x) \cdot dx = 1 \qquad \{2.2\}$$

Hence, the mode field profiles were normalised such that an amplitude of 1 corresponded to a power of 1 Watt being carried by that mode. These bound modes were used to describe the field within the step. Although the bound modes are not actually a complete set they are adequate to describe the field in many situations, especially for the propagation of a field from the narrow end to the wide end of a passive tapered device. For generality the continuum modes should also have been included. However, for reasons of simplicity they were ignored here. A discussion of the validity of this exclusion will be made later in this thesis.

The fields were matched at the interfaces between steps using the overlap integral:

$$A_{qn} = \sum_m \left[A_{pm} \int_{-\infty}^{\infty} F_{pm} \cdot F_{qn}^* \cdot dx \right] \qquad \{2.3\}$$

where A_{ij} is the amplitude of mode 'j' in step 'i'. F_{ij} is the modal field profile of mode 'j' in step 'i'. Reflections at the interfaces between the steps were ignored.

In general the amplitude of the fundamental mode was set to unity for the first step and all other modes had zero amplitude. At the end of the device the near field and far field

patterns were calculated. The near field is simply the total field intensity distribution across the guide, which to a good approximation for weak lateral guiding, is given by the following:

$$I(x) \propto E(x,L) \cdot E^{*}(x,L) \qquad \{2.4\}$$

where I is intensity and L represents the position of the end of the device on the longitudinal axis. The far-field intensity profile was calculated using the equation [4]:

$$I(\theta) = \cos^2(\theta) \cdot \left| \int_{-\infty}^{\infty} E(x,L) \cdot \exp[-k_0 \cdot x \cdot \sin(\theta)] dx \right|^2 \qquad \{2.5\}$$

This is simply the Fourier transform of the field at the facet multiplied by an obliquity factor, $\cos^2(\theta)$.

The stepped waveguide approach has previously been compared with experimental measurements on single taper passive guides and shown to be in good agreement by I.Middlemast et al. [5]. The sensitivity of the model to step length was tested by analysing otherwise identical structures using different step lengths. The differences in the output fields were then examined. Figure 2.2 shows a plot of local fundamental mode amplitude along the length of a device for step sizes of 2μm (dashed curve), 5μm (solid curve) and 10μm (dot-and-dashed curve). It can be seen that a step length of less than 5μm should be used to obtain accurate results from the model for a taper of this size. This corresponded to a maximum step in width of about 0.5μm in order to achieve accurate results. The shape of the near field appeared to be unaffected by step size.

This sensitivity to discretisation can also have implications in the design of devices. Since devices were fabricated using a photolithographic mask created by electron beam lithography the tapers within the devices will literally be approximated by very short straight guides. Therefore the resolution of the mask may have an effect on device performance. In fact the mask creation process had a resolution of 0.2μm which is less than half of the maximum step in width (0.5μm) quoted earlier. This was small enough not to affect device performance.

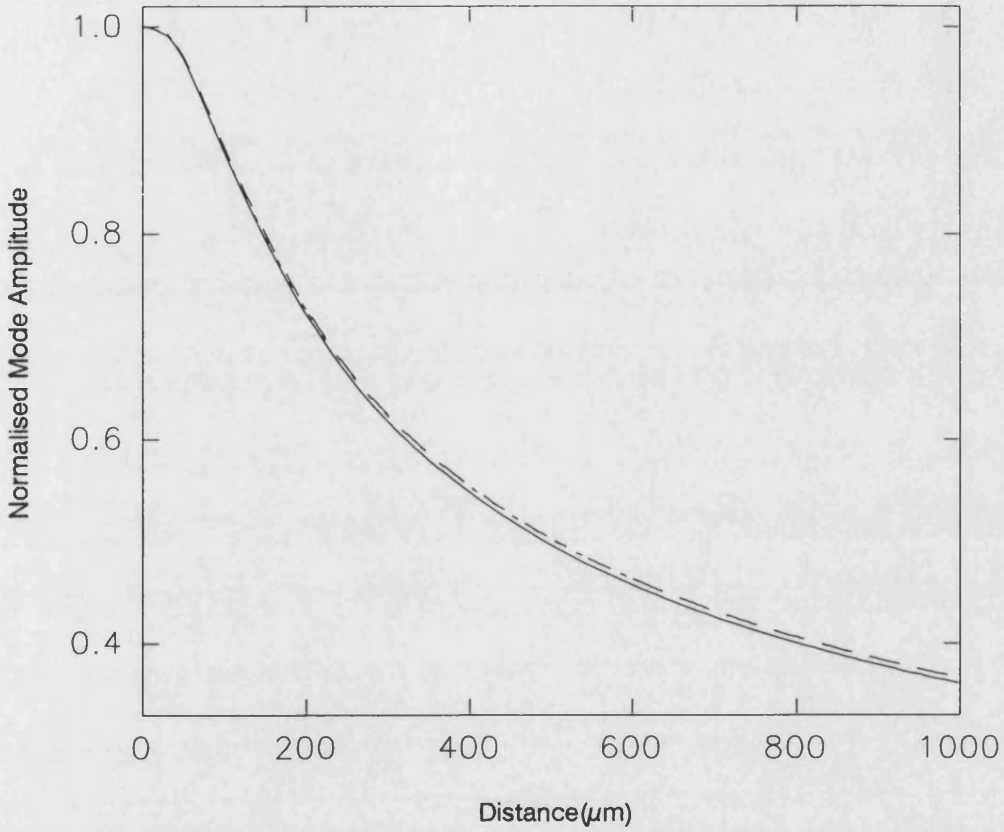

Figure 2.2. Fundamental mode amplitude variation in a 1mm long, 3-100μm wide, tapered waveguide calculated with different step lengths. Note that the '2μm' and '5μm' curves are coincident.

—— Step Length: 10μm
– – – Step Length: 5μm
····· Step Length: 2μm

2.2 Desired properties and physical constraints.

The guide at the output facet of a tapered device is multimoded laterally. It may be possible to use this quality to good effect in order to achieve high powered, and also high quality, output beams. However, one must first specify the 'desirable' qualities of the output field. The physical constraints limiting the design of devices are also considered here since they have an important bearing on device performance.

2.2.1 Beam Quality.

The quality of the light output can be measured in a number of ways. The most obvious measure is the full width at half maximum (FWHM) of the far-field intensity profile. Ideally, the far field profile should be diffraction-limited or at least similar to this limit. This means that the FWHM of the central peak should be similar to the narrowest achievable from an aperture of the same size. However, this measure is dependent on the width of the device and tells only a little about the overall profile of the field. It is also important to consider the shape of the far-field distribution and the fraction of the power within its central lobe. Ideally, all of the power should be in the central lobe of the far-field, i.e. the profile should have negligible side lobes.

The ideal near field profile to produce a diffraction limited far field is a rectangular shape with constant phase across the facet., i.e. 'wider' than the fundamental mode alone and 'flat' across the guide with a planar wavefront. This '*top hat*' shape has the added advantage that it should also reduce self-focussing effects and filamentation by depleting the carriers evenly. The modal amplitudes required at the output facet to approximate a rectangular near field profile can be easily calculated by performing the overlap integral between each mode profile and the rectangular pulse shape. Figure 2.3.a shows an approximate rectangular field intensity profile calculated for a 100μm wide guide supporting 17 symmetric bound modes at a wavelength of 860nm. It is found that the fundamental mode is dominant - it carries 9 times more power than the next symmetric mode. The antisymmetric modes all have zero amplitude as the desired rectangular profile is perfectly symmetrical. The intensity profile of the fundamental mode is shown for comparison. The far field intensity distribution that would result from the *top hat* profile is shown in figure 2.3.b The far-field resulting from the fundamental mode only is also shown.

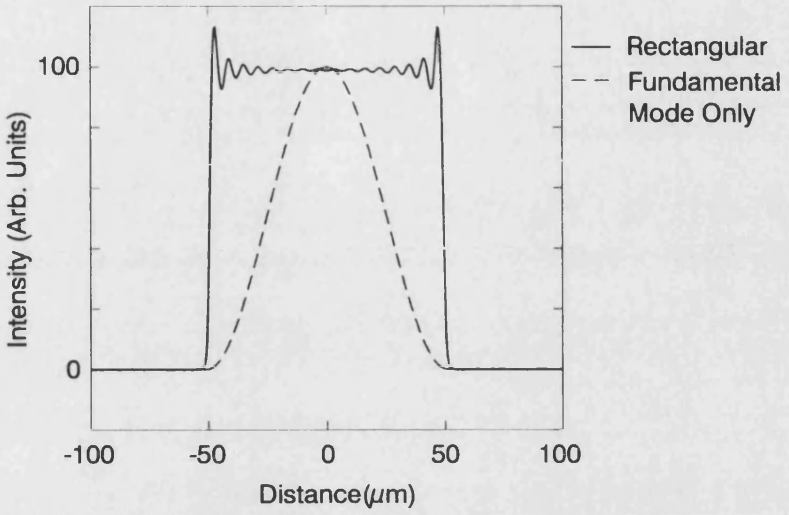

Figure 2.3.a. Approximately rectangular near field intensity compared with fundamental mode alone

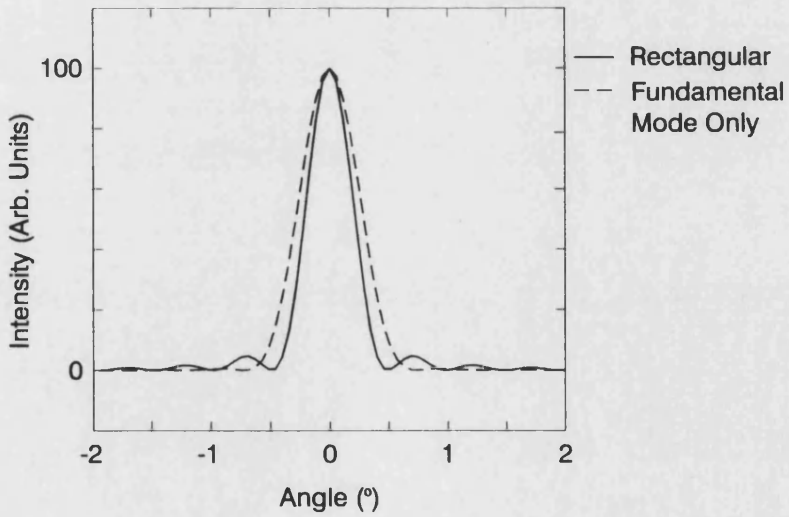

Figure 2.3.b. Far field intensity profiles from intensity distributions in figure 2.3.a.

At this point it must also be remembered that diverging fields can occur inside tapered devices and therefore the far-field can be much wider than the diffraction limit but without necessarily being of '*low quality*'. A perfectly cylindrical wavefront is easy to focus and can give a small lateral spot size, and hence, high-brightness output. The use of a cylindrical lens to correct the phase curvature is a frequently used procedure with tapered devices and unstable resonators reported in the literature [6]. A broad, *top hat* intensity distribution is still desirable.

To summarise then, in order to achieve a near diffraction limited far field the fundamental lateral mode must be dominant in the near field giving a broad intensity profile with a flat wavefront at the facet. In addition, since the diffraction limit is dependent on device width a further constraint will be made that the devices should have a far field with a central lobe full width at half maximum of 3° or less and preferably negligible side lobes. Diverging beams with a phase curvature could also be considered acceptable provided the near field intensity distribution is broad.

2.2.2 Lateral Effective Refractive Index Step

It was intended that devices be fabricated from standard double heterostructure or quantum well material with the lateral waveguide provided by a rib structure. Strong lateral guiding was desired in order to reduce the effect of carrier density on performance, therefore it was necessary to consider the maximum effective index step achievable from a rib waveguide fabricated from the materials available. Appendix 5 contains the details of the materials used in this work. Figures A5.1 and A5.2 show plots of effective index against etch depth from which it can be seen that index steps of around 0.006-0.01 were achievable by etching to within 0.1μm of the active layer.

2.2.3 Physical Dimensions

Alignment errors and the ultra-violet photolithography used to fabricate experimental devices set an absolute minimum size of 2μm for device features. However, to improve the probability of success it is more sensible to employ minimum widths of 3μm in devices.

A maximum dimension of 2mm was set since devices larger than this would be very susceptible to mechanical stresses and thermal variations.

2.3 Simulation Results from Linear Tapers

A number of passive tapered waveguides were analysed in order to study the effects of lateral guide strength and input field shape. The output fields obtained were compared with those that would result if the input field in each case had simply been allowed to diffract in a homogenous half-space. Figure 2.4 shows the fundamental mode field profiles for three waveguides that were used as the input fields in the analysis. Figure 2.5 shows the field intensity profiles that would be obtained if the input fields had diffracted over 1000μm in a homogenous half-space. It can be seen that, as one would expect, the narrowest input field diffracted to the widest output. It is also clear that in order to achieve a narrow input field in a dielectric waveguide a relatively large index step is needed. Figures 2.6 and 2.7 show the near field intensity profiles from different tapered waveguide cases. Again the widest profiles occurred with the narrowest input fields. Interestingly, the output width of the device had only a small effect on the profiles obtained. More significant tails were seen in the profiles from the diffraction cases than from the tapered waveguides but the results did not show any large differences.

Figure 2.8 shows the far-field profiles for the 100μm final width guided devices analysed. Note the large FWHM (up to 10°) of these profiles indicating that there was significant phase variation across the width of these devices. This was expected from devices where the field is essentially being allowed to diffract.

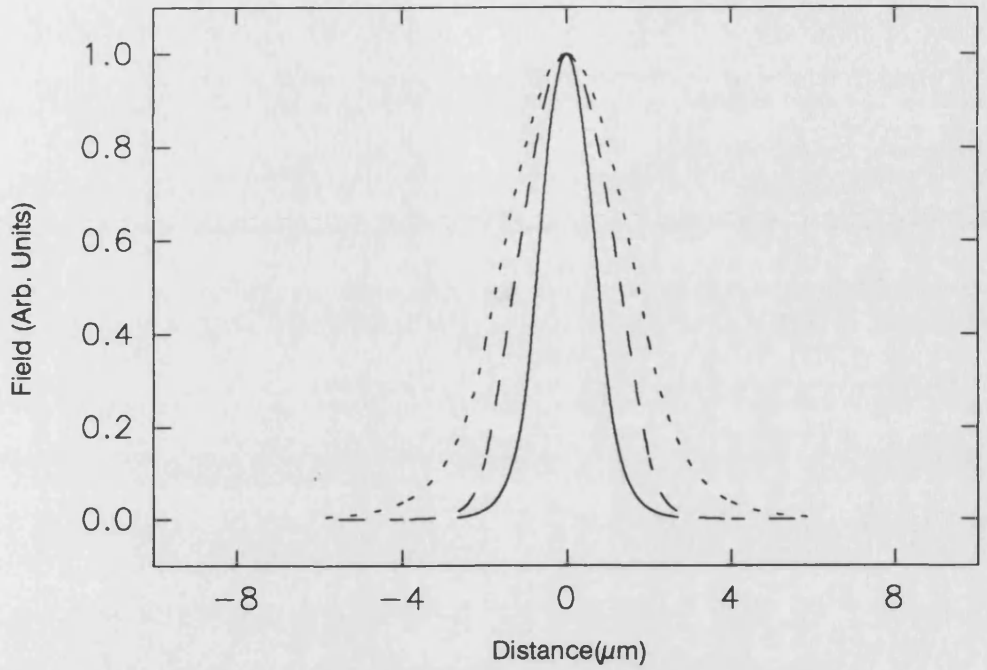

Figure 2.4. Fundamental mode field profiles of three different waveguides.
—— Width: 4.0μm, Eff. Index Step: 0.01
– – – Width: 1.8μm, Eff. Index Step: 0.01
····· Width: 4.0μm, Eff. Index Step: 0.002

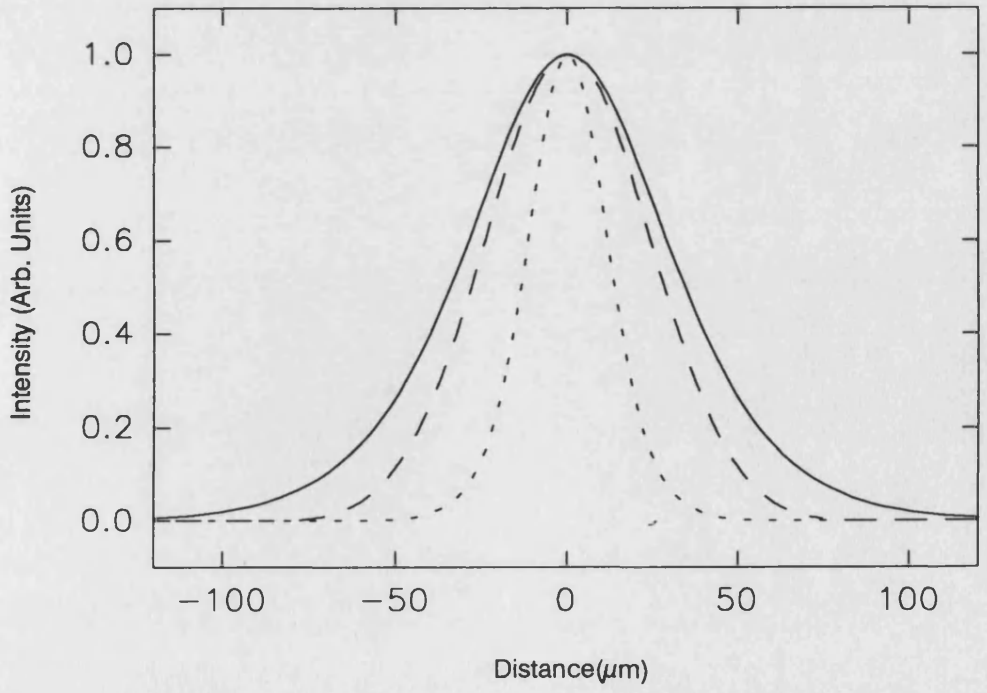

Figure 2.5. Resulting intensity profiles from diffraction of fields in figure 2.4 over distance of 1000μm through a homogenous medium.

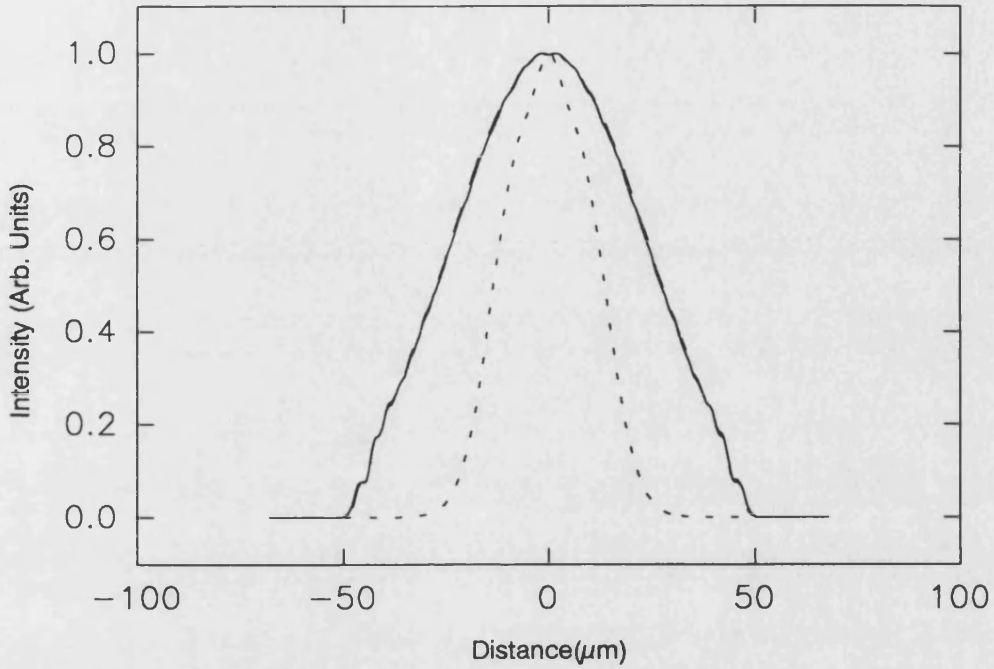

Figure 2.6. Near field intensity profiles of three 100μm wide tapered waveguides. The dotted profile is from the low index step device. The profiles from the high index devices are coincident.

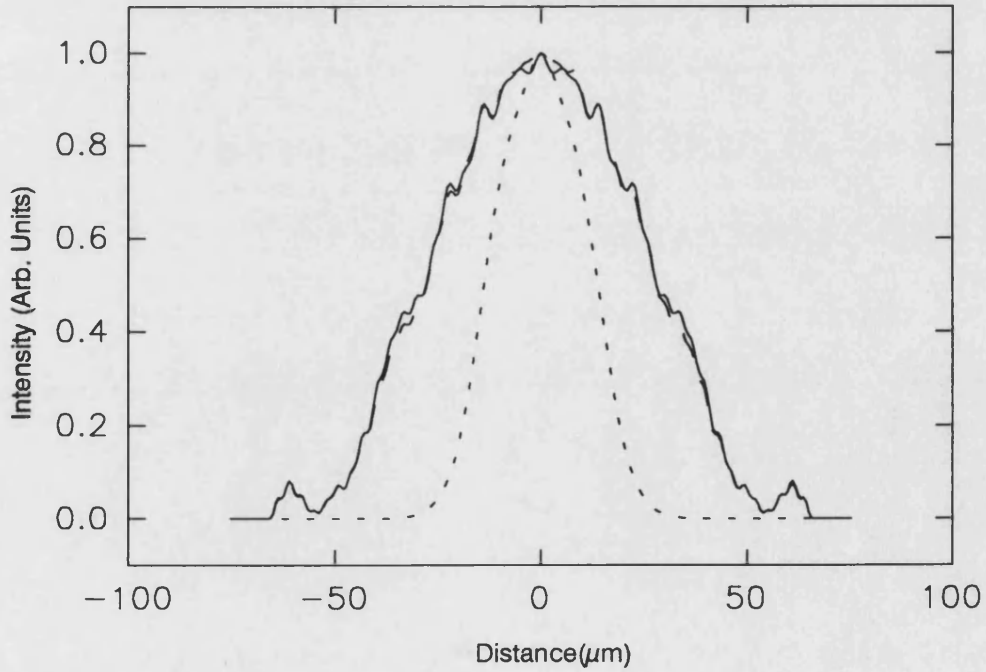

Figure 2.7. Near field intensity profiles from three 130μm wide tapered waveguides. The dotted profile is from the low index step device. The profiles from the high index devices are almost coincident.

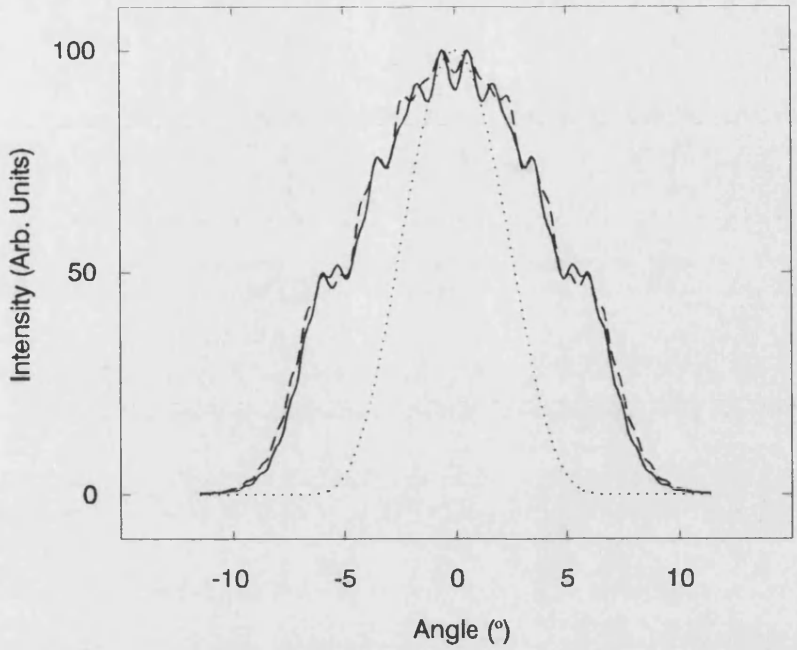

Figure 2.8. Far field intensity profiles from three 100μm wide tapered waveguides.
—— Input width: 4.0μm, Eff. Index Step: 0.01
– – – Input width: 1.8μm, Eff. Index Step: 0.01
····· Input width: 4.0μm, Eff. Index Step: 0.002

2.4 The Effect of Taper Shape

In the previous section only linearly tapered waveguides were considered. By changing the shape of laterally index guided tapers it is possible to achieve different field shapes from devices with the same initial and final dimensions. For this reason two alternatives to linearly tapered waveguides have also been analysed (figure 2.9). Some years ago it was shown [7] that parabolically shaped waveguide horns are a good shape for efficient coupling of the fundamental mode of a wide waveguide to a narrow waveguide. Exponentially tapered amplifiers have been proposed [8] in order to keep the power density approximately constant with length because the power grows exponentially along the length of such a device. The width variations are given by:

$$w_L(z) = \alpha_L \cdot z + w_0 \qquad \{2.6.a\} \text{ for the linear case,}$$

$$w_P(z) = \left(\alpha_P \cdot z + w_0^2\right)^{1/2} \qquad \{2.6.b\} \text{ for the parabolic case,}$$

and $$w_E(z) = w_0 \cdot \exp[\alpha_E \cdot z] \qquad \{2.6.c\} \text{ for the exponential case.}$$

where w_L, w_P, w_E are the widths of the linear, parabolic and exponential waveguides respectively, α_L, α_P, α_E are expansion coefficients and w_0 is the width at $z = 0$.

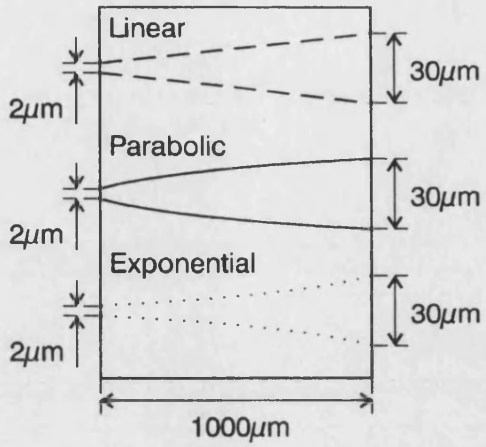

Figure 2.9. The three taper shapes analysed.

Figure 2.10.a shows the near field profiles that result from three differently shaped tapers of the same length (1mm) and with the same initial (2μm) and final widths (30μm). The dashed curve is the profile from a linear taper, the solid curve from a parabolic taper, and the dotted curve from an exponential taper. Figure 2.10.b shows the respective far-field profiles. It can be seen that the profiles for the linear and parabolic tapers are similar although the far-field for the parabolic device is slightly narrower. The exponential device has the narrowest near field and the widest far field profile making this device the least suitable for high power operation. Figure 2.10.c shows the lateral phase variation of the fields in the parabolic and linear structures and more clearly displays the difference between them. The field in the parabolic device has an almost constant phase across the region where the intensity is significant. However there is a significant variation in phase across the linearly tapered device and hence the output from this device has a considerable astigmatism. Figure 2.10.d shows the phase information in a different form. Points of equal phase (wavefronts) that occur in the devices are displayed. The cause of this difference in phase variation is shown in figure 2.10.e. This is a plot of (local) fundamental mode amplitude variation along the length of the devices. In the case of the parabolic device a higher proportion of the power is in the fundamental mode at the end of the device. In section 2.2 it was mentioned that this is a desirable characteristic of the field.

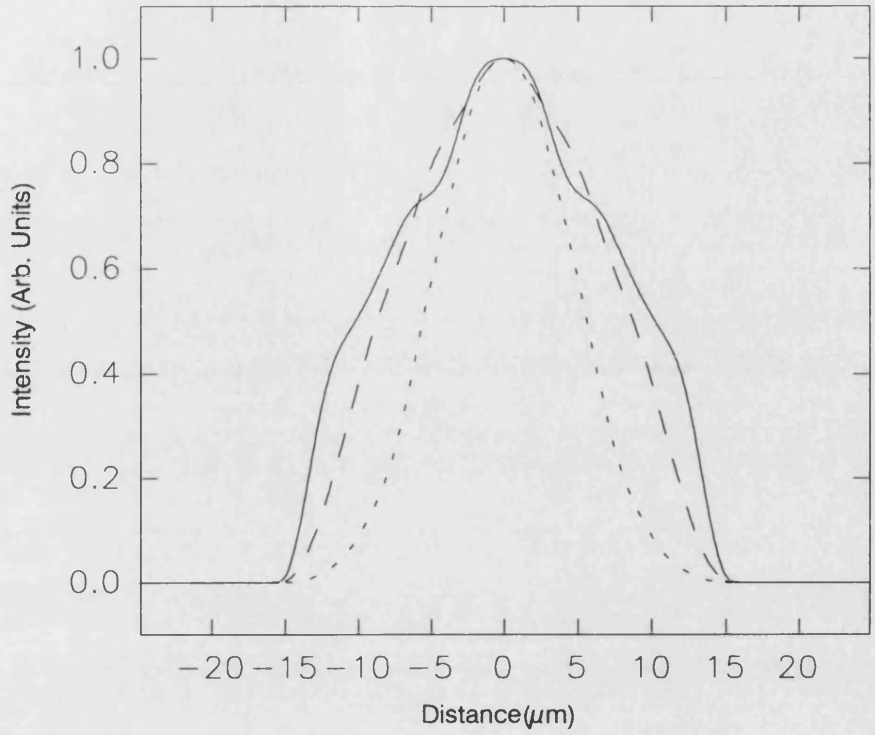

(a)

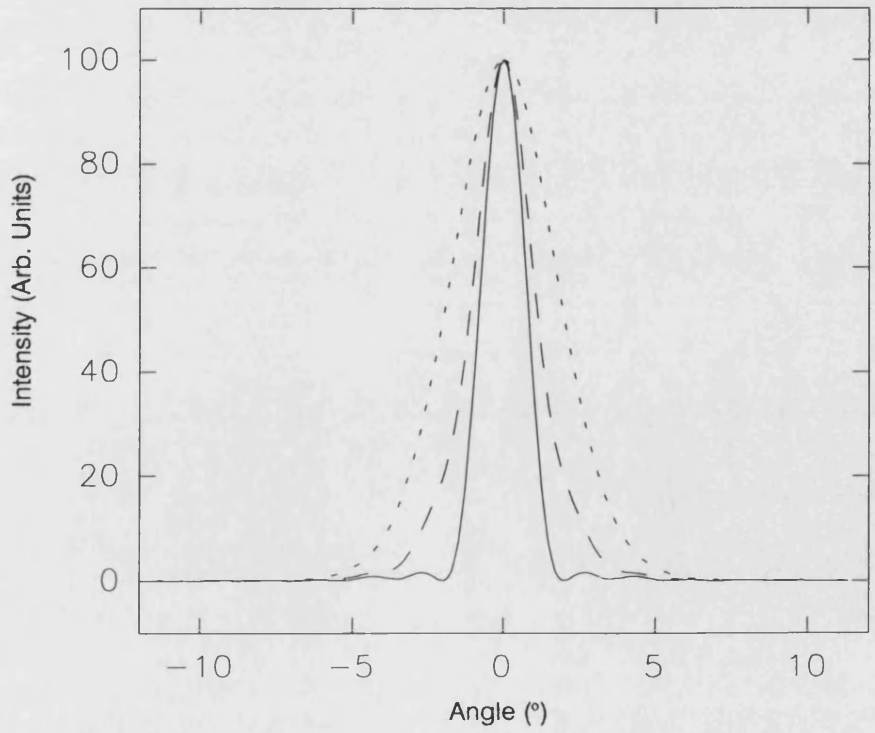

(b)

Figure 2.10. Comparison of parabolic, linearly and exponentially tapered waveguides. 1mm long, 2-30μm wide, effective index step = 0.01. Solid curves - parabolic devices. Dashed - linear devices. Dotted - exponential devices. (a). Near field intensity profiles. (b). Far field intensity profiles.

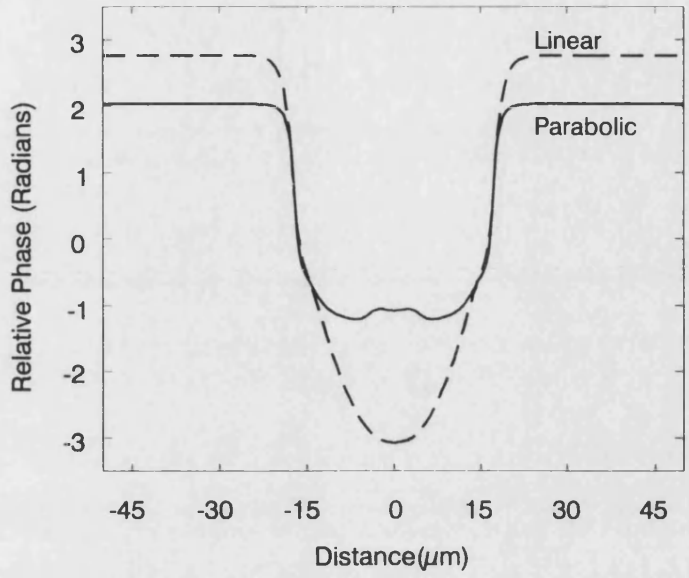

Figure 2.10.c Relative Phase Across Facet of Parabolic and Linear guides

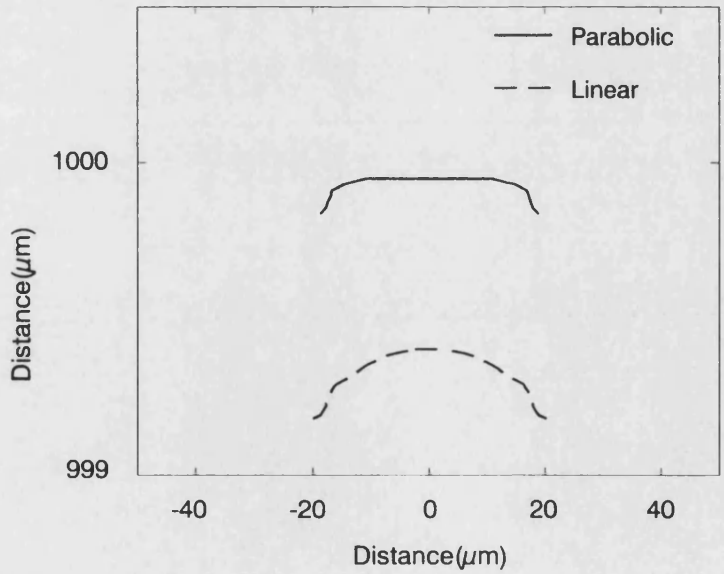

Figure 2.10.d Lines of equal phase (Wavefronts) near facet of parabolic and linear guides.

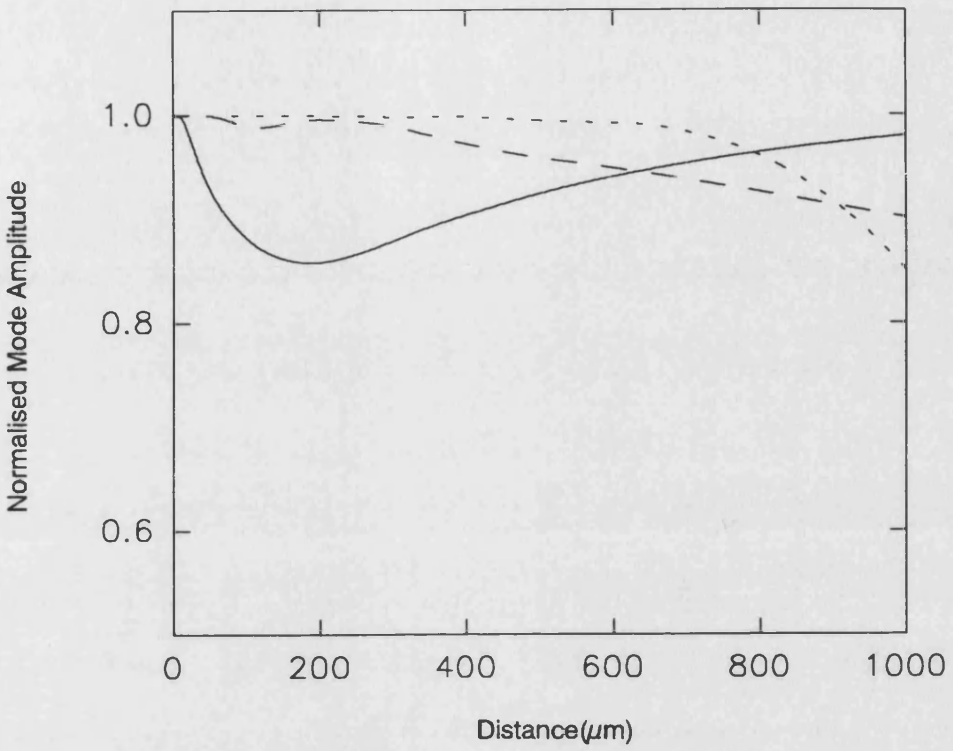

Figure 2.10.e. Comparison of parabolic, linearly and exponentially tapered waveguides. Calculated fundamental mode amplitude variation along the length of devices. 1mm long, 2-30μm wide, effective index step = 0.01. Solid curve - parabolically tapered device, dashed curve - linearly tapered device, dotted curve - exponentially tapered device.

Figures 2.11 and 2.12 show near and far field profiles for differently shaped devices of other sizes. The results for the 20μm wide parabolic device are particularly interesting because there is a dip in the near field profile and the far field has side lobes. In fact, by changing the length, or the index step, of this device it is possible to remove these features. Figure 2.13 shows the output that would be obtained from a number of similar parabolically tapered waveguides with a variety of effective index steps. Figure 2.14 shows how the output from parabolically tapered waveguides varies with taper length for the same initial (3μm) and final widths (20μm) and the same effective index step (0.005).

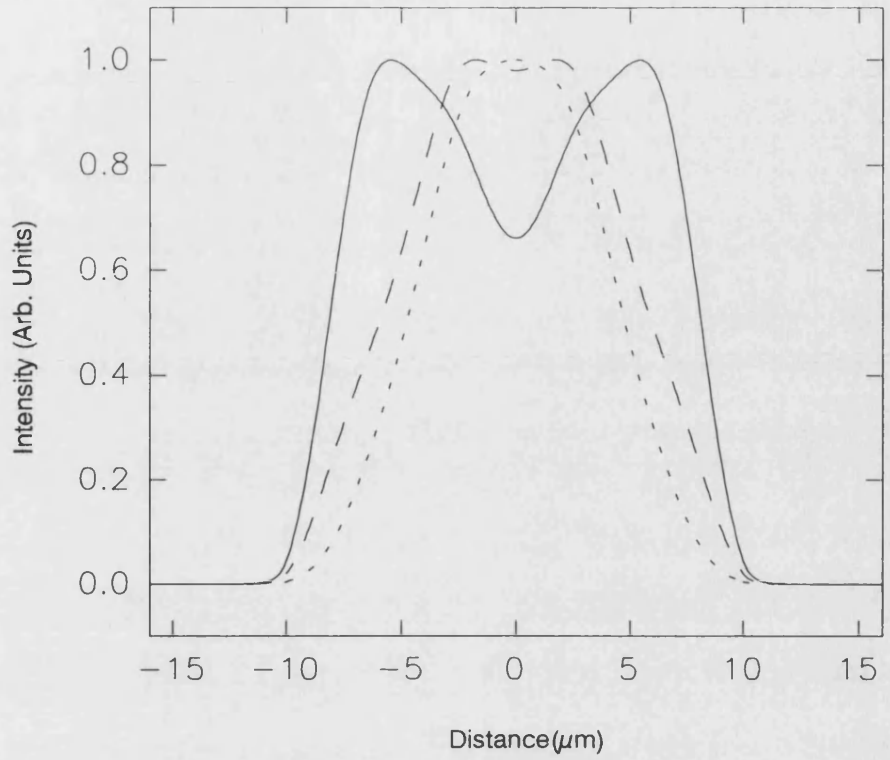

(a)

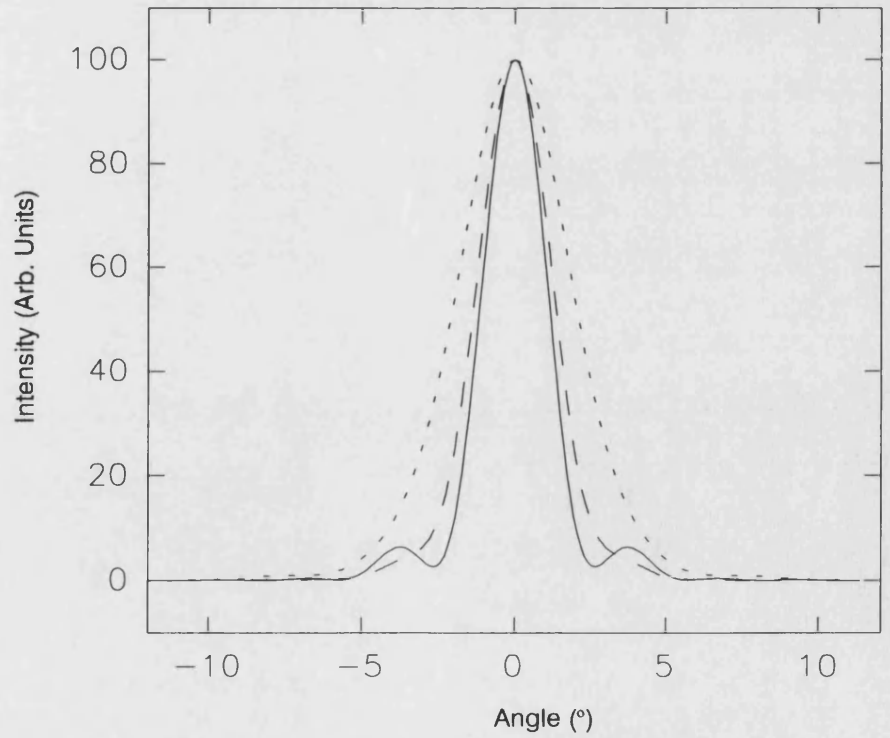

(b)

Figure 2.11. Comparison of parabolic, linearly and exponential tapered waveguides. 550μm long, 2-20μm wide, effective index step = 0.01. Solid curves - parabolic devices. Dashed - linear devices. Dotted - exponential devices. (a). Near field intensity profiles. (b). Far field intensity profiles.

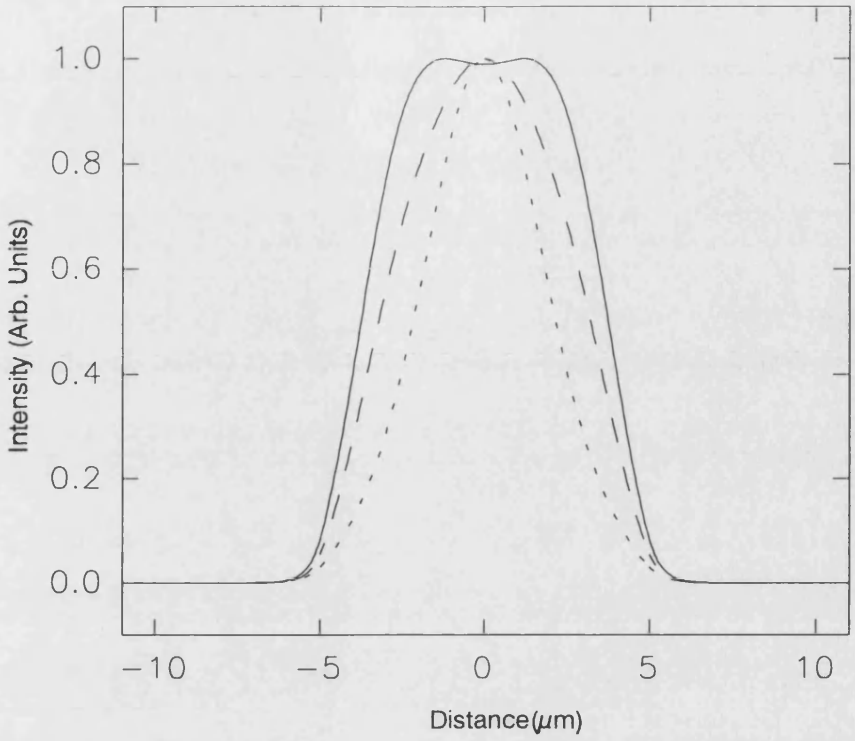

(a)

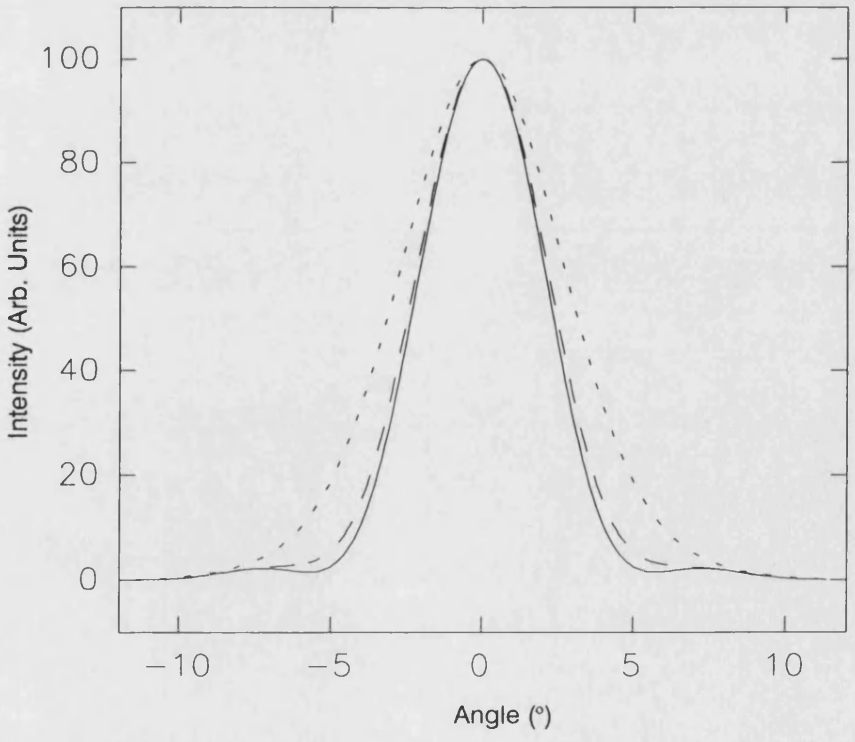

(b)

Figure 2.12. Comparison of parabolic, linearly and exponential tapered waveguides. 250μm long, 2-10μm wide, effective index step = 0.01. Solid curves - parabolic devices. Dashed - linear devices. Dotted - exponential devices. (a). Near field intensity profiles. (b). Far field intensity profiles.

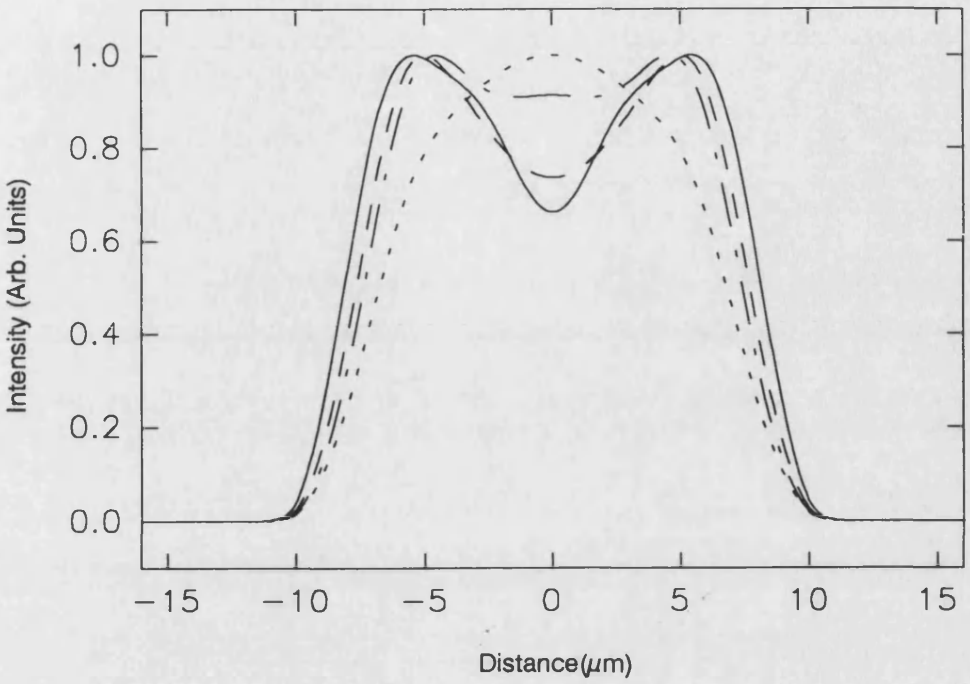

Figure 2.13. Near field intensity profiles from 20μm final width parabolically tapered waveguides of different lengths. Solid curve - 550μm long. Dashed - 600μm. Dash+dot - 650μm. Dotted - 700μm.

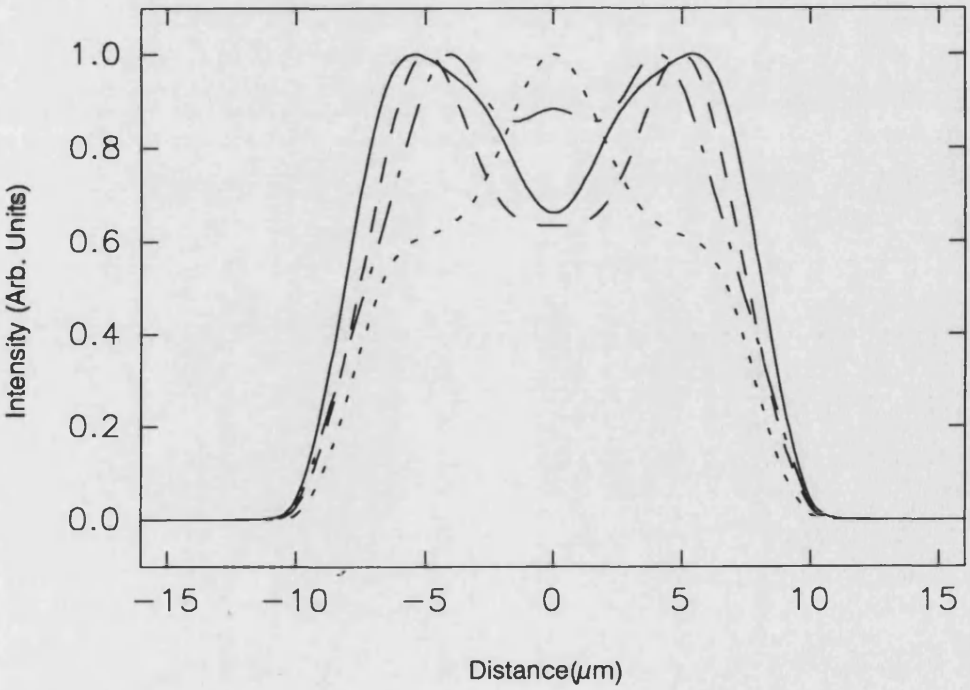

Figure 2.14. Near field intensity profiles from 550μm long, 20μm final width parabolically tapered waveguides with different index steps. Solid curve - $\Delta\eta = 0.005$. Dashed - $\Delta\eta = 0.006$. Dash+dot - $\Delta\eta = 0.008$. Dotted - $\Delta\eta = 0.01$.

One must note however that there is a limit to the width that one can reach with a parabolic shaped taper while still keeping the power in the fundamental local mode. Figures 2.15.a shows the near field profiles that result from two tapers of 2mm length and with 2μm initial width and 80μm final width. The dashed curve is the profile from a linear taper and the solid curve from a parabolic taper. Figure 2.15.b shows the respective far-field profiles. Although the far field FWHM from the parabolic device is still very narrow it does have significant side lobes and the reasons for this can be seen in the near field profile. This is no longer a broad, smooth distribution but has multiple sharp peaks which would be likely to cause filamentation at quite low power levels in a high power active device.

2.5 Conclusions

It has been shown that the widest fields, and therefore the highest powers, will be obtained from linearly tapered devices with well confined fields in the narrow region. However, the far fields from these devices have very large full widths at half maximum (FWHM) indicating highly divergent beams. Output from these devices will be astigmatic and will require cylindrical collimating lenses.

In section 2.2 it was found that most of the power should be kept in the fundamental mode in order to achieve narrow far field distributions. Using relatively strong index-guiding with a parabolic width expansion it has been shown that large proportions of the power can be kept in the fundamental mode. Therefore it should be possible to achieve moderate powers in narrow output beams that will not require external optics to correct any astigmatism. One must note however that there is a limit to the width that one can reach with a parabolic shaped taper while still keeping the power in the fundamental local mode.

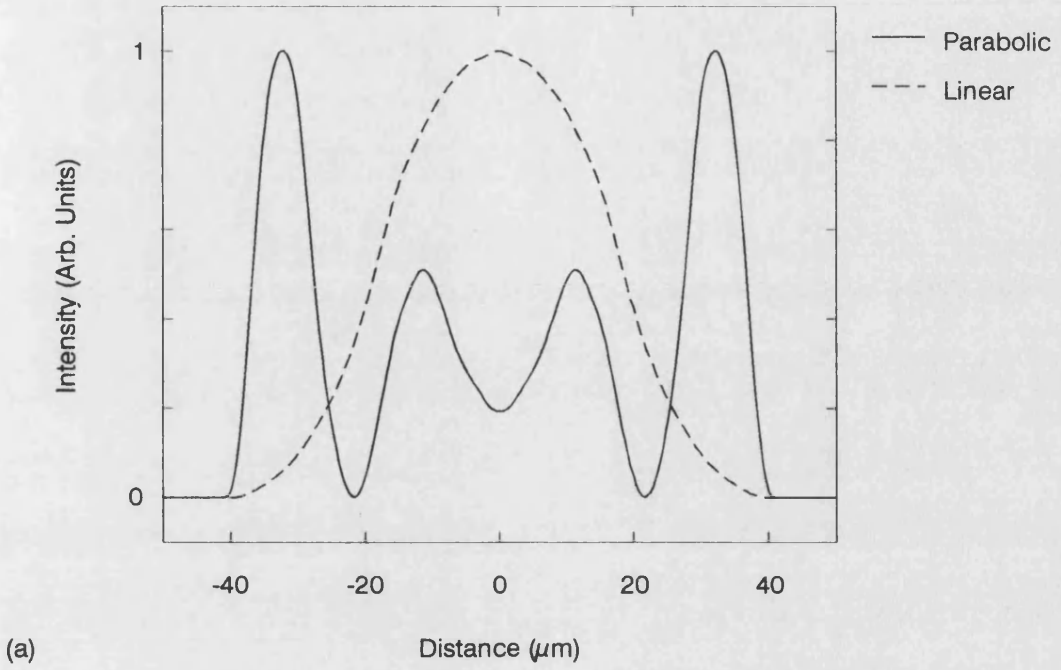

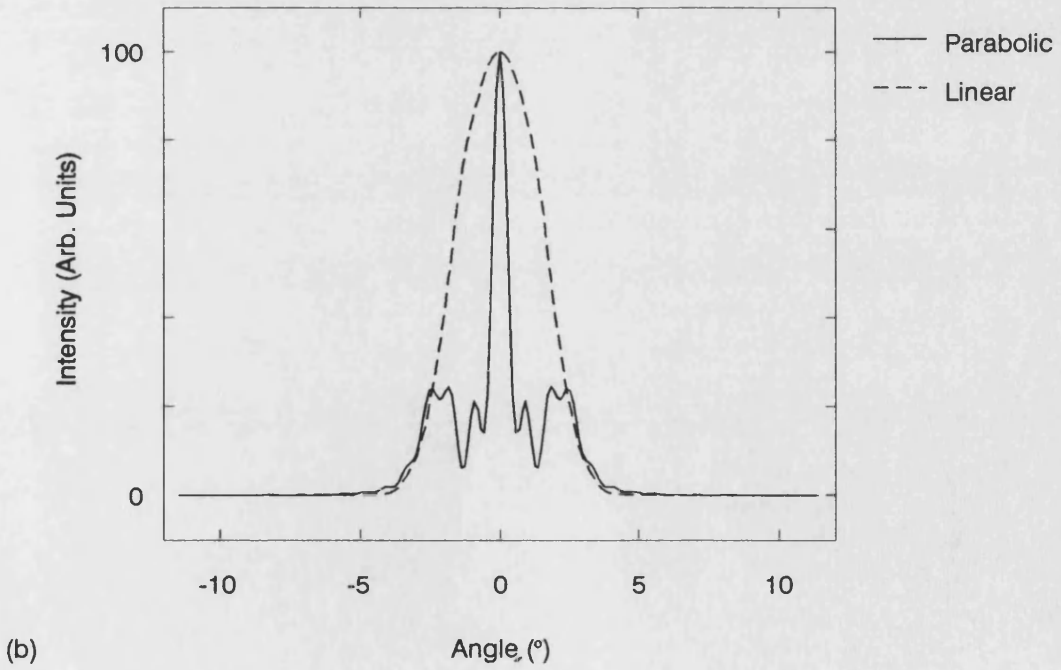

Figure 2.15. Comparison of parabolic and linearly tapered waveguides. 2mm long, 2-80μm wide, effective index step = 0.01. Solid curves - parabolic devices. Dashed - linear devices. (a). Near field intensity profiles. (b). Far field intensity profiles.

References

[1] G.P.Agrawal and N.K.Dutta, 'Long-wavelength semiconductor lasers,' Van Nostrand Reinhold (1986)

[2] F.Sporleder and H.-G. Unger, 'Waveguide tapers transitions and couplers,' Institution of Electrical Engineers, London, p. 97-98 (1979)

[3] D.Marcuse 'Light Transmission Optics (2^{nd} Ed.)' Van Nostrand Reinhold, New York, p. 388, (1982)

[4] Born and Wolf, 'Principles of Optics (6^{th} Ed.),' Pergamon, London, p. 52, (1986)

[5] I.Middlemast, J.Sarma, P.S.Spencer, 'Characteristics of tapered rib-waveguides for high power semiconductor optical sources,' IEE proceedings Part J, Vol. , p. , 1997

[6] R.J.Lang, A.Hardy, R.Parke, D.Mehuys, S.O'Brien, J.Major, D.F.Welch, 'Numerical analysis of flared semiconductor laser amplifiers,' IEEE Journal of Quantum Electronics, Vol. 29, p.2044-2051, 1993

[7] A.F.Milton, W.K.Burns, 'Mode coupling in optical waveguide horns,' IEEE Journal of Quantum Electronics, Vol. QE-13, p. 828-835, 1977

[8] G.Bendelli, K.Komori, S.Arai, Y.Suematsu, 'A new structure for high-power TW-SLA,' IEEE Photonics Technology Letters, Vol. 3, p. 42-44, 1991

Chapter 3

Lasers

A number of conclusions for the design of tapered waveguides in high power laser structures were reached in the previous chapter. However, it is important to remember that the results were solely for passive waveguides. Lasers are a more complex situation due to the presence of free carriers and the two counter propagating fields. These factors should be taken into account before fabricating laser designs that incorporate the earlier conclusions. In this chapter the extension of the stepped waveguide model to active devices is discussed. Some simulation results for travelling wave amplifiers and lasers are then given. Finally, some experimental results from fabricated parabolic bow-tie lasers are presented and comparisons made with simulation results.

3.1 Model

The stepped waveguide model was extended to analyse active devices. In order to do this a self-consistent solution for the optical field and the lateral carrier distribution must be found at every step along the length of the device. The non-linear effects of the carrier dependent refractive index must also be included. In Bendelli [1], the effect of carrier density on the refractive index was not included. Spencer [2] included the effects fully and repeatedly solved for the bound modes of the multilayer waveguide. Thermal effects on refractive index were ignored in both models. Whilst the Spencer model is the most general it is also computationally expensive.

If devices with large index steps are considered then it is possible to ignore the effects that the refractive index changes have on the shapes of the bound modes and simply include a complex correction to the modal propagation constants calculated from first order perturbation theory. This approach is known to be satisfactory for narrow ridge waveguide devices [3] and was adopted for this work. It should be noted that the total field distribution may still be altered by carrier re-distribution via the changes to the modal propagation constants. The method provides a large saving in computation time over a method that includes changes to the mode shapes. Thermal effects were still ignored although it will be shown in later chapters that such effects are important. The procedure followed for each waveguide segment is shown in figure 3.1.

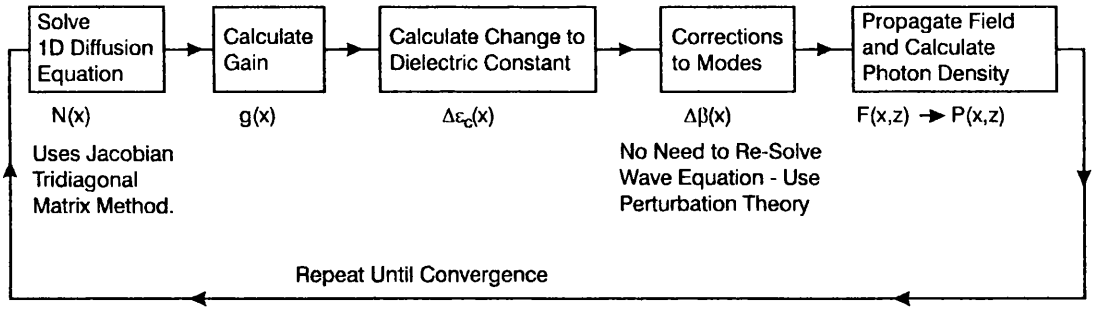

Figure 3.1. Flow diagram of iterative procedure to find self-consistent solutions for the field profile and the carrier density distribution within each waveguide step.

First, the 1D diffusion equation {3.1} is solved using a Jacobian tridiagonal matrix method [4].

$$D \cdot \frac{d^2N(x)}{dx^2} - B_R\left[N(x) + n_0\right] \cdot N(x) - \gamma_A \cdot N^3(x) - g(x) \cdot P(x) + \frac{J(x)}{q \cdot d} = 0 \qquad \{3.1\}$$

where 'D' is the diffusion coefficient, 'N(x)' is the carrier density, 'B_R' is the bimolecular recombination constant, 'n_0' is the active layer doping density, 'γ_A' is the Auger recombination constant, 'P(x)' is the photon density, 'J(x)' is the current density, 'q' is the electronic charge, 'd' is the active layer thickness and 'g(x)' is the local gain which is given by:

$$g(x) = \alpha_0\left(N(x) - N_T\right) \qquad \{3.2\}$$

where 'N_T' is the transparency current density, and α_0 is the gain constant. The photon density is assumed to be zero for this first iteration. The lateral carrier density distribution obtained is then used to calculate the change to the dielectric constant profile, $\Delta\varepsilon_c(x)$, given by:

$$\Delta\varepsilon_C(x) = 2 \cdot \Delta\eta(x) \cdot \overline{\eta}(x) + \Delta\eta^2(x) \qquad \{3.3\}$$

where '$\overline{\eta}(x)$' is the unperturbed effective refractive index profile and '$\Delta\eta(x)$' is the change to the effective refractive index due to the carriers and is given by:

$$\Delta\eta(x) = \Gamma_V \cdot \left(\chi_R \cdot \left[N_{REF} - N(x)\right] + j \cdot \frac{g(x)}{2 \cdot k_0}\right) \quad \text{for } N(x) > N_{REF}$$

and $$\Delta\eta(x) = \Gamma_V \cdot \left(j \cdot \frac{g(x)}{2 \cdot k_0}\right) \quad \text{for } N(x) < N_{REF} \qquad \{3.4\}$$

where 'Γ_V' is the confinement factor of the vertical mode, 'χ_R' is a constant and 'N_{REF}' is a constant.

Complex corrections to the propagation constants are then evaluated from perturbation theory (see appendix 4.) using:

$$\Delta\beta_m = \frac{k_0^2 \cdot \int_{-\infty}^{\infty} [F_m(x) \cdot \Delta\varepsilon_c(x) \cdot F_m(x)]dx}{2 \cdot \beta_m} \qquad \{3.5\}$$

where '$\Delta\beta_m$' is the correction to 'β_m', the propagation constant of mode 'm'. These correction terms are then added to the unperturbed propagation constants of the modes and the modes are propagated along half of the step. A new value for the photon density variation is calculated from the field at this point and used in the diffusion equation once more. The whole procedure is repeated until the field converges. At that point the modes are then propagated over the second half of the step and the process is started again for the next step.

In a laser there are two counter-propagating fields. Both of these fields, forward and backward, must be evaluated self-consistently in order to properly analyse the performance of a laser design. The model treats the laser as an initial value problem and introduces an initial field into the narrow end of the device. This field is propagated along the device to the wide end using the procedure above while initially assuming that the backward propagating field is zero. For every step the value of the calculated forward propagating field is stored for later use. At the wide facet a fraction of the field is reflected and becomes the backward propagating field. This field is then propagated back along the device while including the stored values of the forward propagating field in the optical field/carrier density self-consistency calculations of each step. At the narrow facet the field is again reflected. The procedure is then repeated until the field at the wide facet converges.

The calculations are time independent and only one wavelength value is used. Hence, when adding the counter propagating fields to evaluate the photon density within a step the intensities are used. The model cannot therefore predict the longitudinal mode spectrum of the laser.

Since a symmetrical bow-tie laser has two identical tapered regions a single-taper laser with a reflectivity of 1 at its narrow facet is analysed in order to save computation time.

3.2 Validity of Model

In order to test the validity of the model in ignoring mode shape changes a comparison was made between this model and the '*full*' model of Spencer [2] which incorporates changes to the mode shapes due to the presence of carriers. Figure 3.2 shows a comparison of near-field intensity distributions calculated for a linearly tapered amplifier by the two models. It can be seen that there is very little difference between the two profiles and the perturbation model can be considered accurate at such current density levels. However, the perturbation model took only 2 minutes of computation time to simulate the device whereas the full model took 25 minutes. The saving in computation time becomes even more significant when modelling lasers rather than single pass devices.

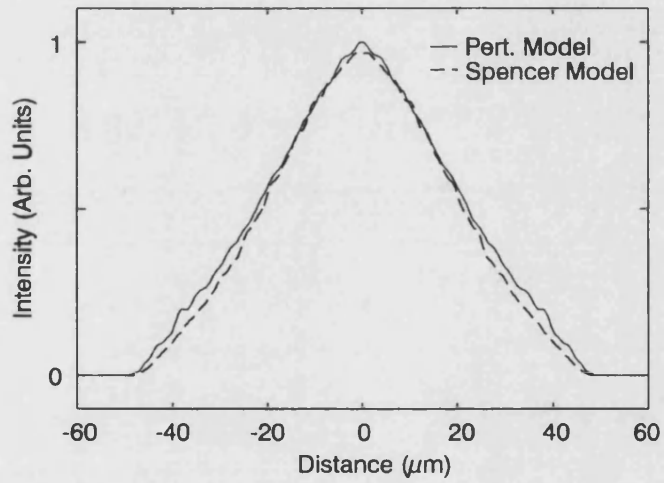

Figure 3.2. Comparison of Near field intensity profiles of a linearly tapered amplifier calculated by the perturbation model and by the Spencer model (incorporating mode shape changes). The amplifier was 1 mm long with width varying from 2μm to 100μm. An effective index step of 0.01 and a current density of 1.0 kA/cm^2 was used in each calculation.

3.3 Simulation results - Amplifiers

A comparison was made between parabolic and linearly tapered amplifiers. Figure 3.3 shows the calculated near and far field distributions for 30μm wide amplifiers. The results are similar to those for passive waveguide devices. There is only a small difference between the different shapes of device. The parabolic amplifier still has a slightly narrower far field profile.

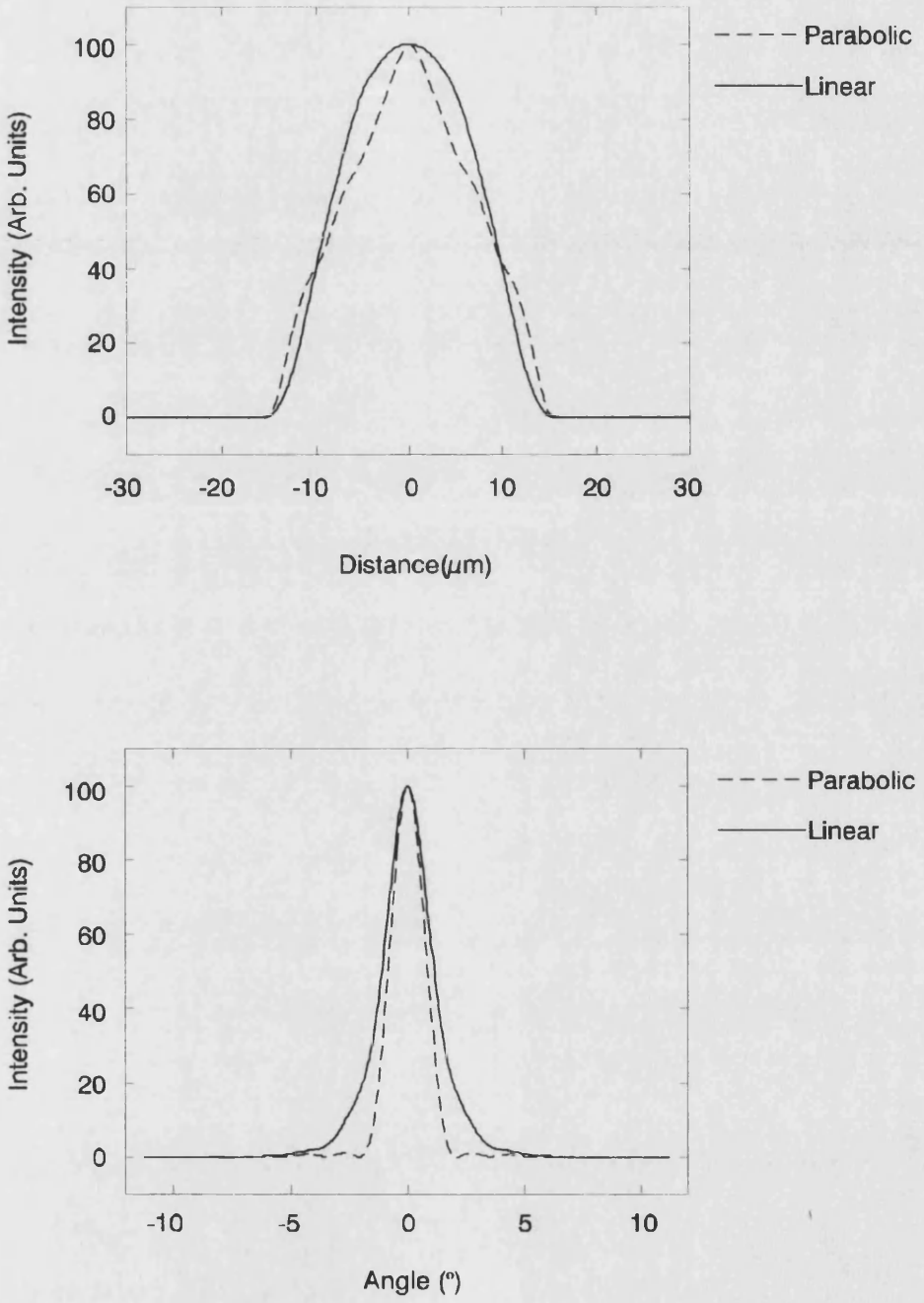

Figure 3.3. Comparison of characteristics of Parabolic and Linear Tapered Amplifiers. Each waveguide was 1 mm long with width varying from 2μm to 30μm. An effective index step of 0.01 and a current density of 1.7 kA/cm2 was used in each case (a) Near field intensity distributions. (b) Far field intensity profiles.

3.4 Simulation results - Lasers

In chapter 1 it was mentioned that the bound modes alone do not form a complete mathematical set and are therefore not always adequate to describe the total field. When a field is propagating through a tapered waveguide or travelling wave amplifier from the narrow to the wide region only then negligible amounts of power are coupled out of the bound modes and this limitation is unimportant. However, in order to model lasers, propagation in the reverse direction must also be simulated. In linearly tapered devices a significant amount of power is coupled into higher order lateral modes which is radiated from the sides of the device as these modes become cut-off approaching the narrow region. It was therefore found that analysing linearly tapered lasers is not possible with the current model.

However, parabolic tapered lasers have still been simulated since negligible power is coupled out of the fundamental lateral mode in these devices. Figure 3.4 shows the calculated variation of the optical power along the length of a 1 mm long, 30μm wide single taper laser.

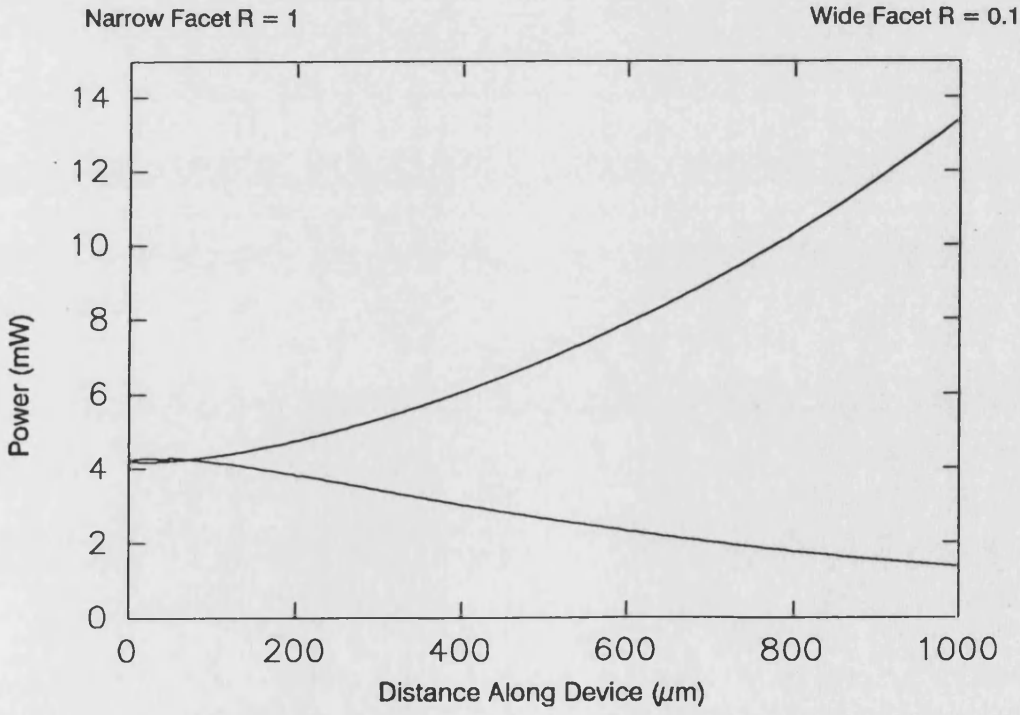

Figure 3.4. Plot of (Forward and Backward propagating) Power variation along length of Parabolic Tapered Laser. Total Optical Power within device is the sum of the two curves. Laser dimensions used were: Length: 1 mm; width: 2-30μm; effective index step: 0.01; current density: 1.05 kA/cm2; Narrow facet reflectivity: 1; and Wide facet reflectivity: 0.1.

Reflectivities of 100% (at the narrow facet) and 10% (at the wide facet) were used rather than standard values of 30% which result from uncoated cleaved facets. These values will reduce the total power in the narrow region of the device for a given output power from the wide facet. However, it can be seen that there is still a relatively large amount of power in the narrow region and therefore a very high power density at the narrow facet compared to the wide facet. This feature can be avoided by using the bow-tie laser structure. The narrow region in a bow-tie laser still has a similarly high power density but is no longer near the facet where surface states lead to high absorption and catastrophic optical damage. It should also be noted that due to the combined effects of the high power density and carrier diffusion the narrow region has a net absorption, not gain. It is not known what effect this may have on device operation.

Figure 3.5 shows the output characteristics of a parabolic bow-tie laser. It can be seen that the important characteristics of the passive tapered waveguide have been retained. The device has a near diffraction limited calculated far field FWHM of less than 2°.

Another laser has been analysed by the model. This is a small device with a width of 10μm at its widest point. Since the final width is only 5 times the narrow width it should be possible to avoid much higher power densities at the narrow facet than the wide facet simply by altering the reflectivities with facet coatings. Hence, a single taper laser was considered. The small width of this device was chosen because it is similar to the spot size of a single mode fibre and may be useful in improving the alignment tolerance in one dimension between a laser and fibre. Figure 3.6 shows the calculated output characteristics for this parabolic tapered laser.

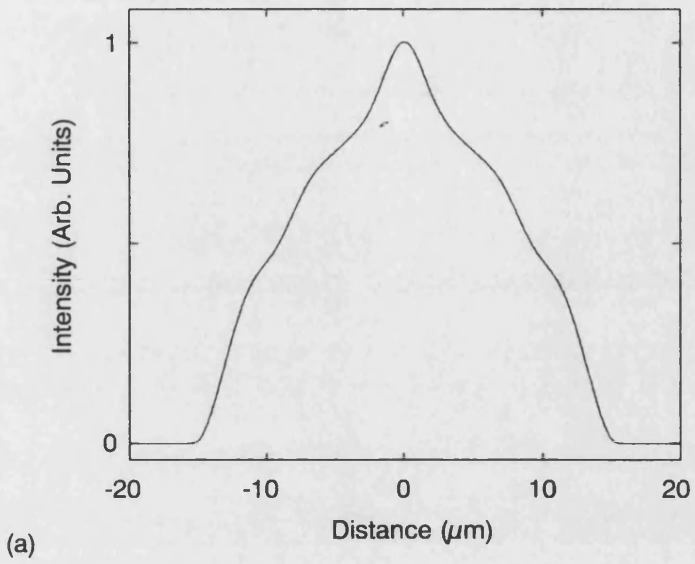

(a)

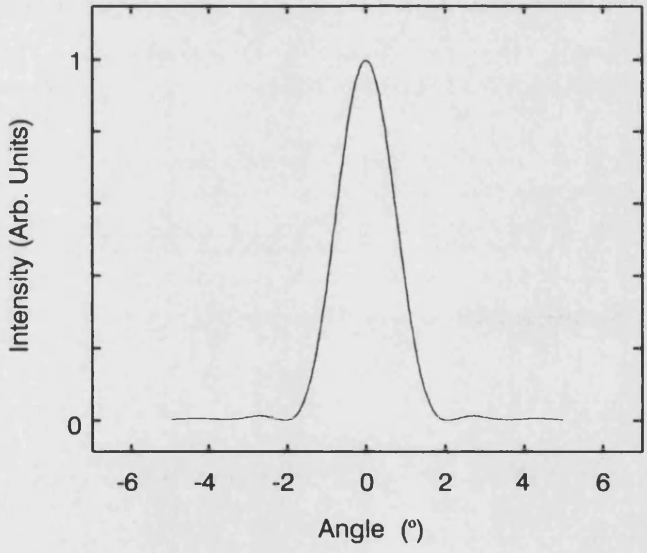

(b)

Figure 3.5. Calculated output characteristics of Parabolic Bow-tie laser.
The laser was 2mm long with width varying from 2μm at the centre to 30μm at each facet. An effective index step of 0.01 and a current density of 1.0kA/cm^2 was used.
(a) Near field intensity distribution. (b) Far field intensity profile.

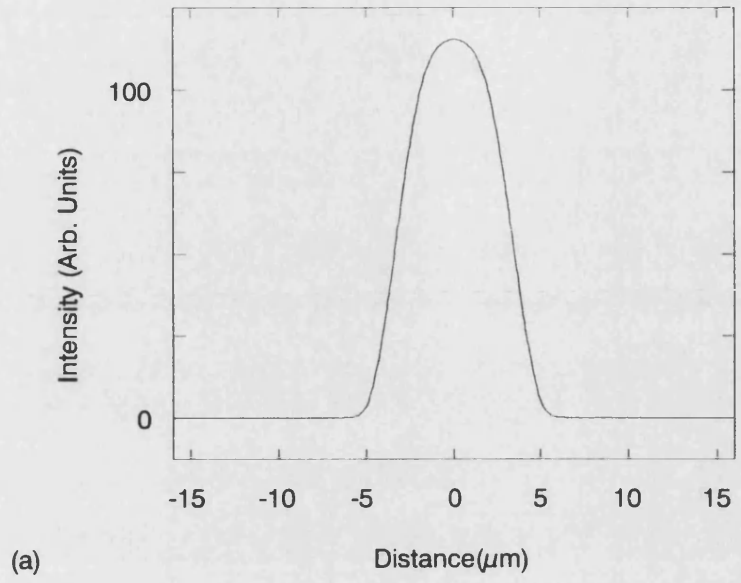

(a)

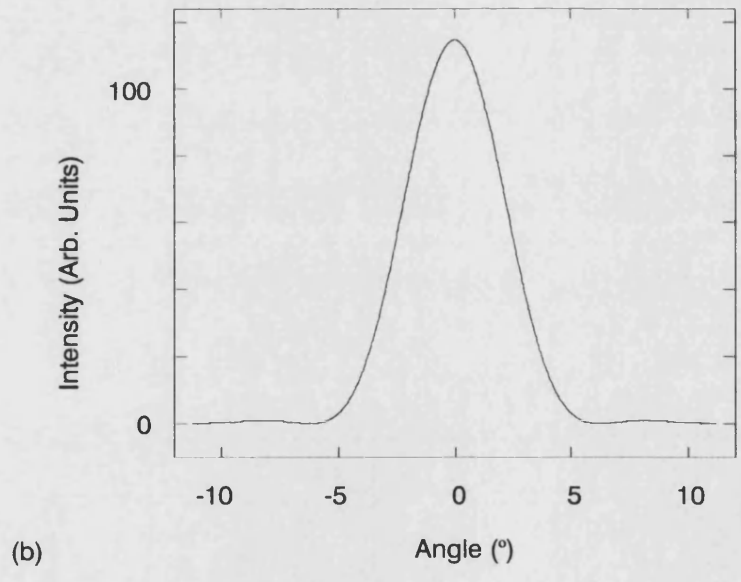

(b)

Figure 3.6. Calculated output characteristics of a Parabolic Tapered Laser. The laser was 300μm long with width varying from 2μm to 10μm. An effective index step of 0.005 and a current density of 1.4kA/cm^2 was used in the calculation.
(a) Near field intensity distribution. (b) Far field intensity profile.

3.5 Experimental results

A number of parabolic bow-tie lasers of different sizes were fabricated from material QT829B. The specification of this material can be found in appendix 5. The rib waveguides were ion beam etched to a depth of approximately 1.0μm giving an effective index step of ~0.006. However, the effective index step is very sensitive to etch depth in this region and therefore the actual index step could have differed from this. Deflector pits were wet etched through the active layer either side of the narrow centre regions at a distance of ~3μm from the side of the rib. Figure 3.7 shows a photograph of one of these devices. The two lines across the device show the edges of the rib waveguide and the triangles at the centre are the deflectors. The devices were mounted on copper heatsinks with Indium solder and tested with 1μs pulses and a duty cycle of 10:1. The experimental techniques used for the following measurements are detailed in appendix 6.

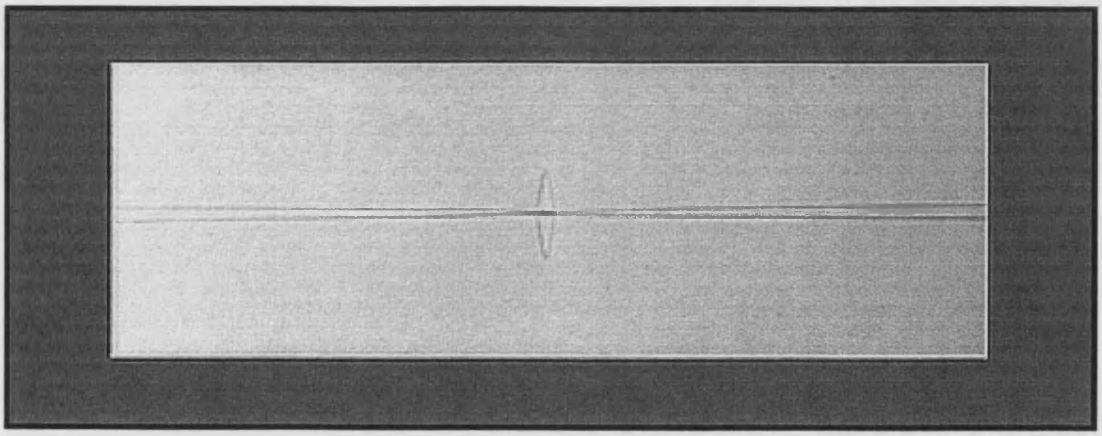

Figure 3.7. Photograph of a parabolic bow-tie laser similar to those measured. Note the deflectors to the sides of the centre region.

UB793

Device UB793 was 2 mm long. It had a 3μm wide and 50μm long straight central region and two 975μm long parabolically tapered regions to a final width of 30μm at the facets.

UB789 and UB794

Devices UB789 and UB794 were 1 mm long. Each had a 3μm wide and 50μm long straight central region and two 475μm long parabolically tapered regions to a final width of 20μm at the facets.

Figure 3.8 shows plots of light output (from a single facet) against current for devices UB793 and UB794. Kinks can be seen in the curves for both devices. Device UB793 emitted a peak power of more than 100mW without failure at 600mA. It was then tested at a lower duty cycle of 100:1 up to currents of more than 2A and emitted a peak power of more than 300mW from a single facet. A similar device was mounted on a diamond heatsink and tested CW at the Max Born Institüt, Berlin. This device emitted 200mW before failure at about 800mA.

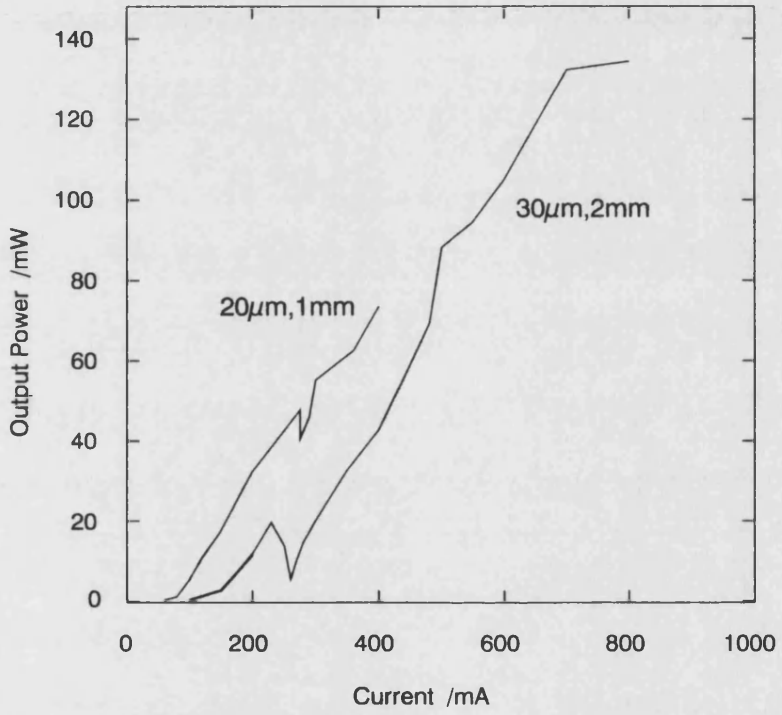

Figure 3.8. Light Output vs. Current characteristics of Parabolic Bow-tie Lasers UB793 and UB794. Measurements were taken using 1μs pulses with a duty cycle of 10:1

Figure 3.9 shows measured near and far field profiles for device UB793 along with curves calculated by the model. Figures 3.10 and 3.11 show similar results for devices UB789 and UB794 respectively. Excellent agreement can be seen between the experimentally measured output fields and those predicted by the model. All devices had far field FWHM of ~3°. Additional peaks outside of the rib waveguide were observed in the experimentally measured near-field distributions. Corresponding side lobes occurred in the far-field profiles. It was initially thought that these peaks were due to a misalignment of either the electrical contact to the rib or possibly of the etched deflectors. Subsequent measurements on straight broad area lasers fabricated at the same time also showed side peaks demonstrating that they are not caused by the taper and therefore cannot also be attributed to a misalignment of the deflectors.

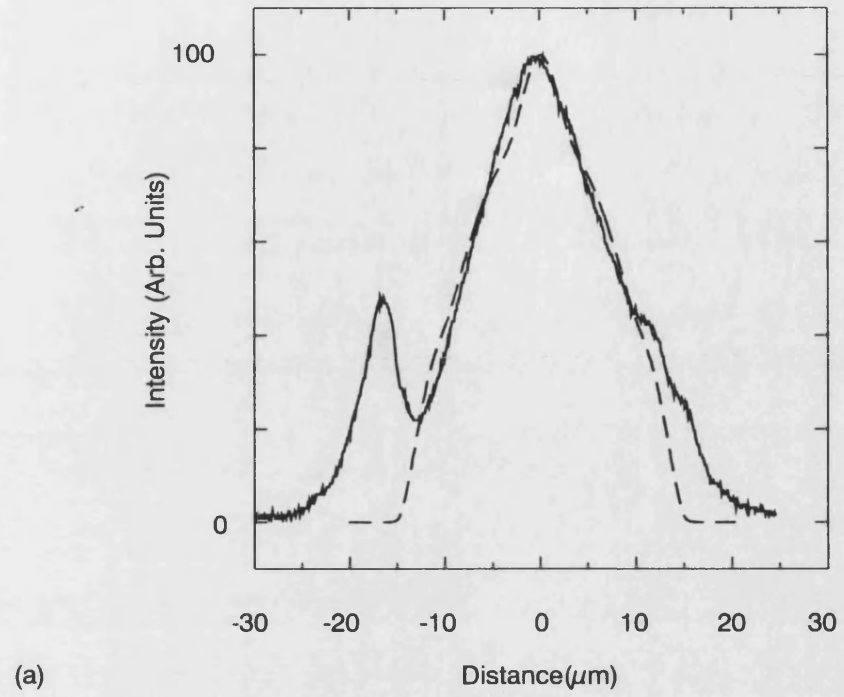

(a)

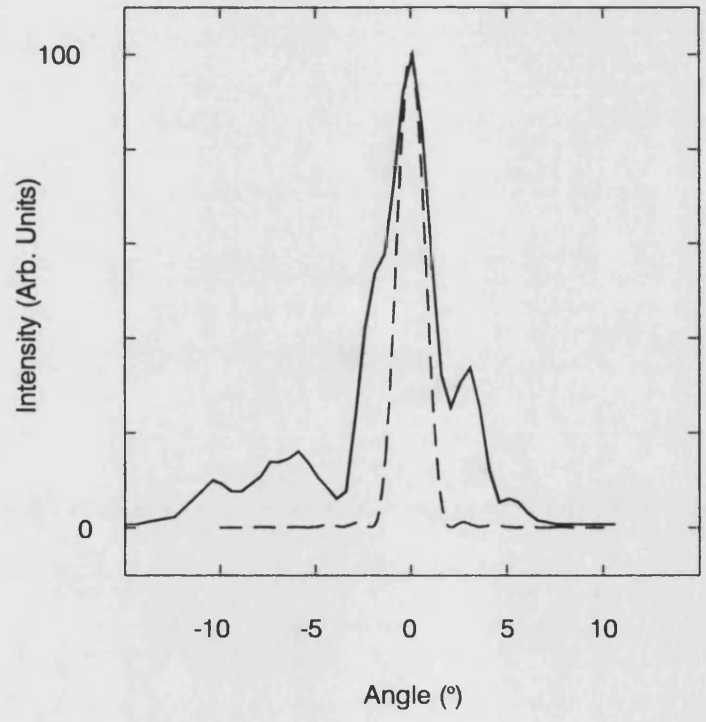

(b)

Figure 3.9. Output characteristics of UB793 Parabolic Bow-tie Laser. The laser was 2mm long with width varying from 3μm to 30μm. An effective index step of 0.009 was used in the calculation. Solid curve - experimental. Dashed - model. (a) Near field profile at 300mA, (b)Far field profile at 600mA.

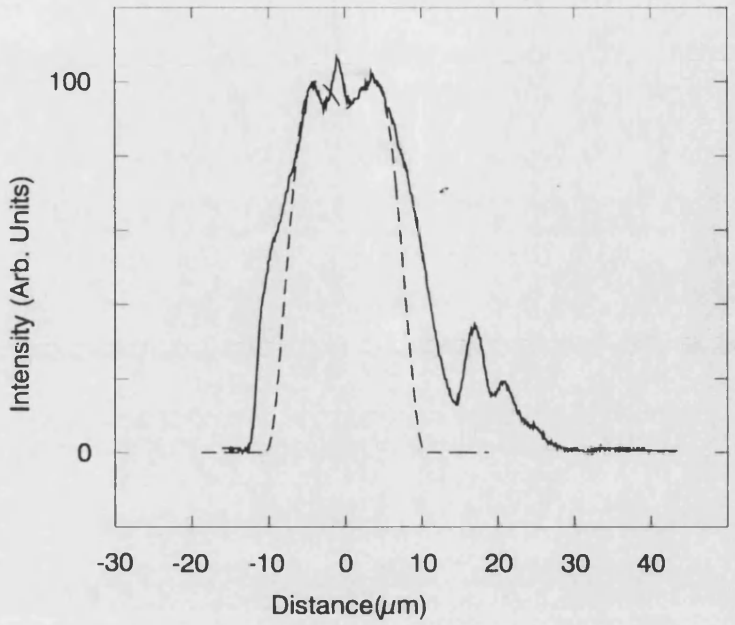

(a)

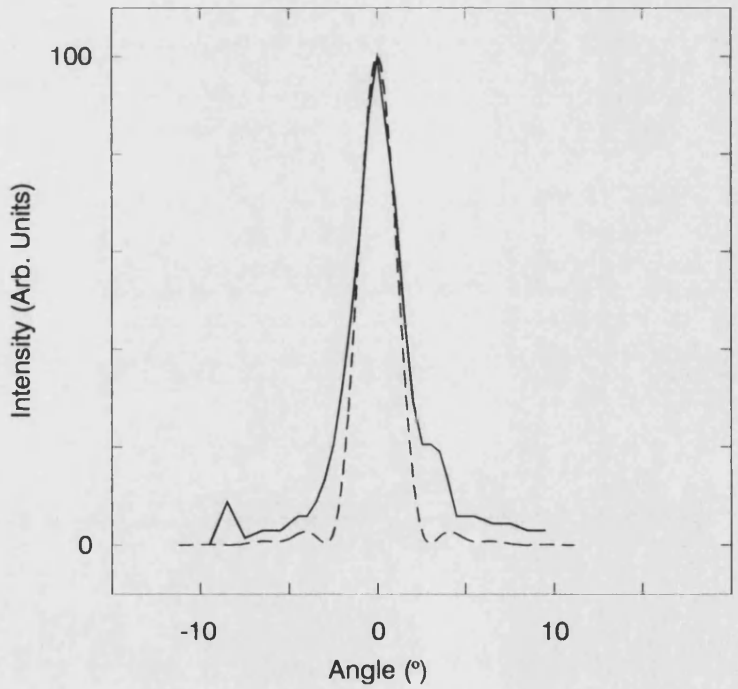

(b)

Figure 3.10. Output characteristics of UB789 Parabolic Bow-tie Laser. The laser was 1mm long with width varying from 3μm to 20μm. An effective index step of 0.009 was used in the calculation. Solid curve - experimental. Dashed - model. (a) Near field profile at 100mA, (b)Far field profile at 400mA.

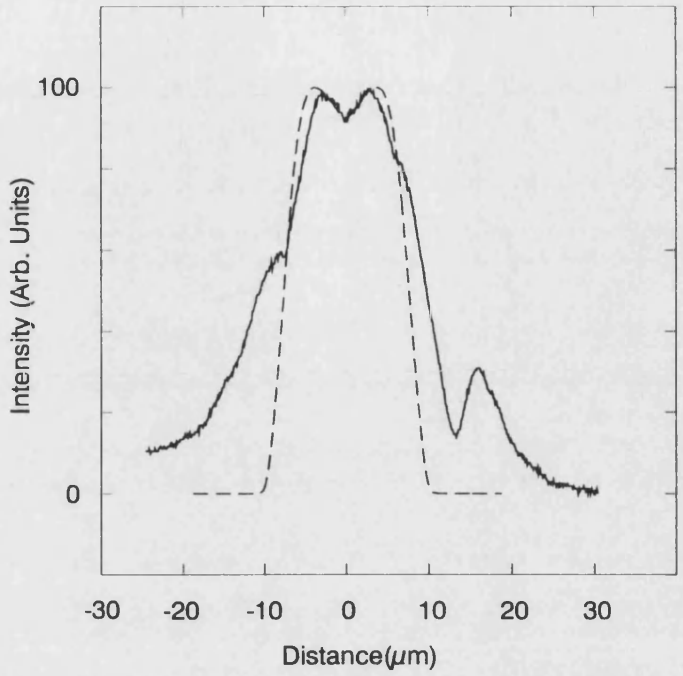

(a)

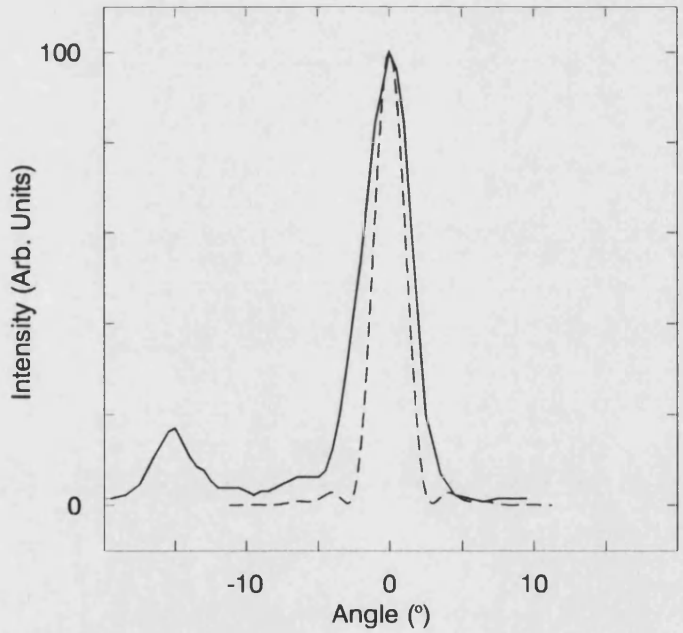

(b)

Figure 3.11. Output characteristics of UB794 Parabolic Bow-tie Laser. The laser was 1mm long with width varying from 3μm to 20μm. An effective index step of 0.009 was used in the calculation. Solid curve - experimental. Dashed - model. (a) Near field profile, (b)Far field profile.

Figure 3.12 shows experimentally measured near field profiles of device UB789 at several currents around the threshold current of the device. Well below threshold the near field profile follows the distribution of carriers in the device (the dotted curve in figure 3.12). Above threshold the near field shows the lasing mode that occurred within the rib waveguide (the solid curve). Therefore, from the figure it can be seen that there was a significant concentration of carriers outside of the rib on one side. These results concur with the hypothesis that the electrical contact is misaligned with the rib. The kinks that were observed in the output power vs. current curves for both devices may also have been a result of the same misalignment.

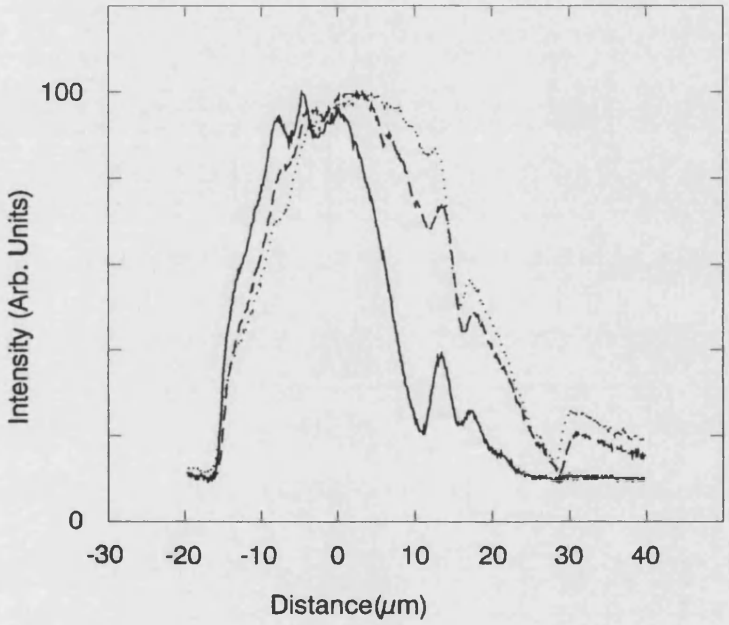

Figure 3.12. Near field profiles of UB789 Parabolic Bow-tie Laser at different currents. Solid curve - 100mA (Above Threshold), Dashed curve - 80mA (Near Threshold), Dotted curve - 60mA (Below Threshold).

Figure 3.13 shows the spectral variation of the light output from laser UB794 at various currents. The longitudinal modes with a spacing of ~0.2nm can clearly be seen. These results are interesting because they show that the device was operating quasi-single longitudinal mode, with side mode suppression of more than 6dB, up to a current of 230mA, more than three times the threshold current.

In figure 3.13.c a fine structure can be seen to each longitudinal mode profile indicating that multiple lateral modes are excited in the device. This is not visible in the strongest modes at the lower currents and may be the reason for the pronounced kink in the light output vs. current curve for this device.

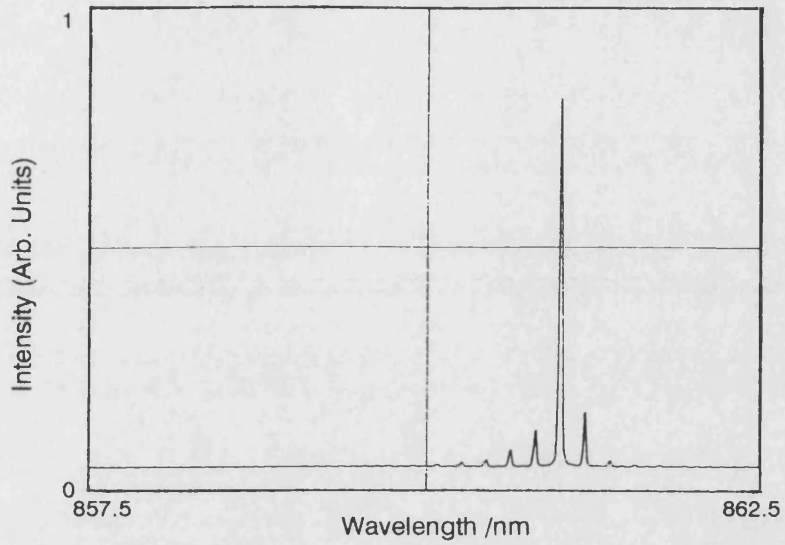

Figure 3.13.a. Emission spectrum at 110mA from UB794 parabolic Bow-tie laser.

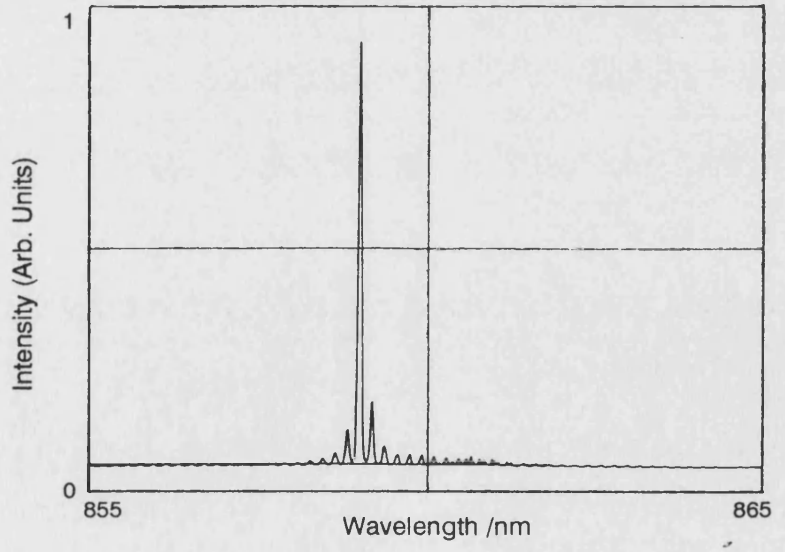

Figure 3.13.b. Emission spectrum at 230mA from UB794 parabolic Bow-tie laser.

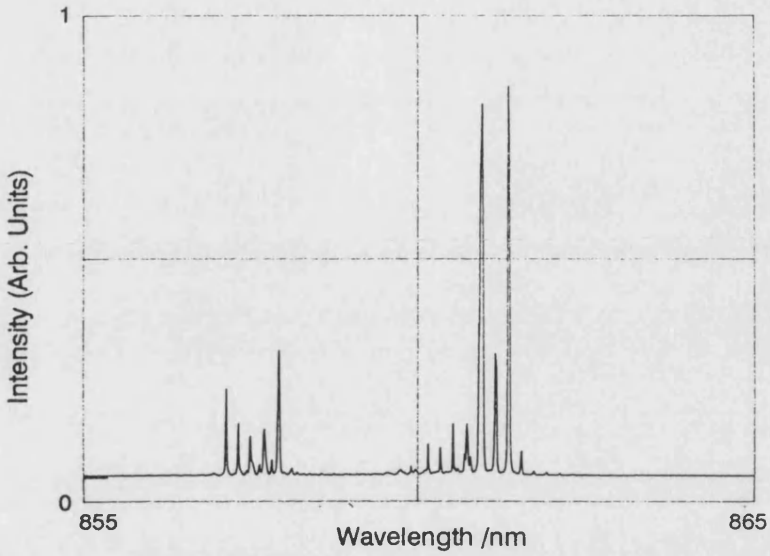

Figure 3.13.c. Emission spectrum at 300mA from UB794 parabolic Bow-tie laser.

3.6 Conclusions

A model for active tapered waveguide devices has been developed and shown to be computationally efficient. The model has been used in the design of parabolic tapered lasers including bow-tie lasers. Good agreement has been demonstrated between the model and experimental results from bow-tie lasers fabricated from conventional GaAs quantum well material. Additional features were seen in the experimental field profiles of the lasers and these were attributed to misaligned current contacts to the rib waveguides. A kink in the output power variation with current of device UB794 is accompanied by changes in the longitudinal mode spectra. The fine structure of these spectra indicate the presence of higher order lateral modes at high currents.

References

[1] G.Bendelli, K.Komori, S.Arai, IEEE Journal of Quantum Electronics Vol.28, No.2, p447, 1992.

[2] P.S.Spencer, I.Middlemast, R.Balasubramanyam, J.Sarma & K.A.Shore, presented at 'Semiconductor Lasers: Advanced Devices & Applications Conference', Colorado, USA, August 1995.

[3] G.P.Agrawal, 'Lateral analysis of quasi-index guided injection lasers: Transition from gain to index guiding,' IEEE Journal of Lightwave Technology, Vol. 2, p. 537, (1984).

[4] P.S.Spencer, R.Balasubramanyam, J.Sarma, K.A.Shore, Self-consistent solution of the diffusion equation for an active optical semiconductor device, Semiconductor Science and Technology, Vol.10, p.942-947, 1995.

Chapter 4

Anti-reflection coating and current segmentation

In the previous chapter a model was presented for parabolically tapered lasers. Simulation and experimental results were presented and compared for a small number of devices. Parabolic bow-tie lasers were shown to emit high powers with narrow lateral far field profiles. In this chapter some of the parameters of tapered laser design are further investigated. In particular, the effects of altering the wide facet reflectivity of a single-taper laser and longitudinally varying the current density are investigated. Simulation results are presented first. Some experimental results from a series of small single-taper lasers before and after facet coating are then detailed. These results are also used to investigate any effects from different lengths of straight region at the narrow end of a device.

4.1 Introduction

Facet coatings are widely used with high power semiconductor lasers to alter the reflectivities. Anti-reflection (AR) coatings are used on the output facets and high-reflectivity (HR) coatings on the back facets of single taper lasers to reduce the power density occurring in the narrow region. It was seen in the previous chapter that the high power density in the narrow region of a parabolically tapered laser can cause this region to have an overall loss rather than gain. The model has been used to see if this can be removed by altering the facet reflectivities or by applying different current densities to different regions along the length of a device. Altering the reflectivities also changes the threshold current and slope efficiency of the device. The effects on these quantities are also examined.

Consider the threshold gain condition [1] for a longitudinally homogenous laser:

$$g_{TH} = \alpha + \frac{1}{2L} \cdot \ln\left(\frac{1}{R_1 R_2}\right) \qquad \{4.1\}$$

where g_{TH} represents the threshold gain per unit length, α is the loss coefficient, R_1 and R_2 are the reflectivities of the narrow and wide facets respectively and L is the cavity

length. Assuming an offset-linear relationship between gain and current density (equation {4.2}) one can find an expression for the threshold current density per unit volume [2], J_{TH}, (equation {4.3}).

$$g = A(J - J_0) \qquad \{4.2\}$$

$$J_{TH} = J_0 + \left(\frac{1}{\Gamma A}\right)\cdot \alpha + \frac{(1/R_1R_2)}{2L} \qquad \{4.3\}$$

where J_0 represents the transparency current density, Γ is the confinement factor of the lasing mode, and A is a constant relating the gain to the current density. One can clearly see that the threshold current is dependent on the facet reflectivities and the device length. Longer devices with high reflectivities have lower threshold current densities. Reducing the device length or facet reflectivities increases the threshold current density.

The differential quantum efficiency of a device, η_D, relates the output power in photons per second to the current in electrons per second and is approximately given by [3]:

$$\eta_D = \frac{\eta_{ST}}{1 + 2\alpha L/\ln(1/R_1R_2)} \qquad \{4.4\}$$

where η_{ST} is the internal quantum efficiency for the generation of stimulated emission. α and η_{ST} are properties of the material and can therefore be considered constant for the purposes of this work. Although reducing the product of the facet reflectivities increases the threshold current density it also increases the differential efficiency of a device. Similarly, reducing the length has the same effect.

Therefore, there is a compromise to be made between high reflectivities for low threshold current density and low reflectivities for high slope efficiency. The optimum facet reflectivities for a device then depend on the desired output power. For low power operation, a low threshold current, and therefore high reflectivities will give higher overall efficiency. For high power operation, a high slope efficiency, and hence low facet reflectivities will result in higher overall efficiency.

4.2 Simulation Results

A number of devices have been simulated. A diagram to explain the notation used in this section is shown in Figure 4.1. In this and later sections the slope efficiency - measured in W/A - will be quoted rather than the differential quantum efficiency of the previous section. Slope efficiency is simply a more convenient measure especially when comparing with experiment results. A standard, 5-segment, single-taper device of 1mm length has been used for the simulations. In all cases, w_{min} = 3μm, w_{max} = 30μm, $L_1 = L_2 = L_3 = L_4 = L_5$ = 200μm and R_1 = 1. The value of R_2 was varied between 0.3 and 0.01.

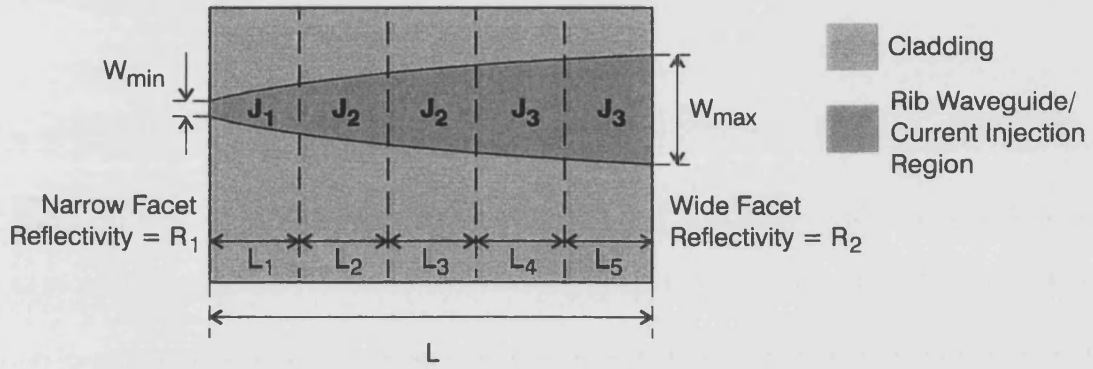

Figure 4.1. Schematic diagram of a tapered laser showing the notation used in this section.

Figure 4.2 shows output power against current plots for different values of R_2 when $J_1 = J_2 = J_3$. Table 4.1 contains the slope efficiencies and threshold current densities for the same cases.

R_2	J_{TH} (mA.μm^{-2})	I_{TH} (A)	Slope Efficiency (mW/A)
0.3	0.69	0.14	230
0.1	0.89	0.18	380
0.03	1.13	0.228	490
0.01	1.38	0.279	590

Table 4.1. Calculated threshold current, I_{TH}, and slope efficiency values for a 1mm long, 3-30μm wide, parabolically tapered laser for different wide facet reflectivity, R_2, values. The narrow facet reflectivity value was fixed at 1.

Figure 4.3 shows output power against (total) current plots when R_2 = 0.3, 0.1 and 0.03 and the current is longitudinally segmented. The curves show that there is little to be gained by varying the current density even by as much as 50%. Only minor changes in the threshold current occur.

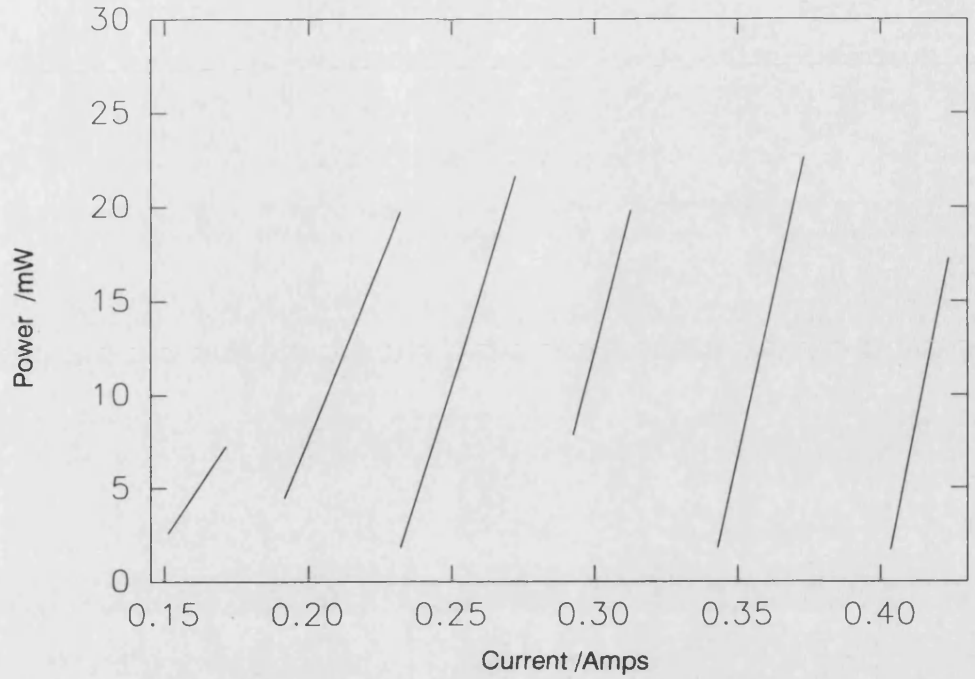

Figure 4.2. Light output vs current curves from 30μm final width, 1mm long parabolically tapered lasers with different wide facet reflectivities, R_2. From left to right R_2 = 0.3, 0.1, 0.03, 0.01, 0.003, 0.001.

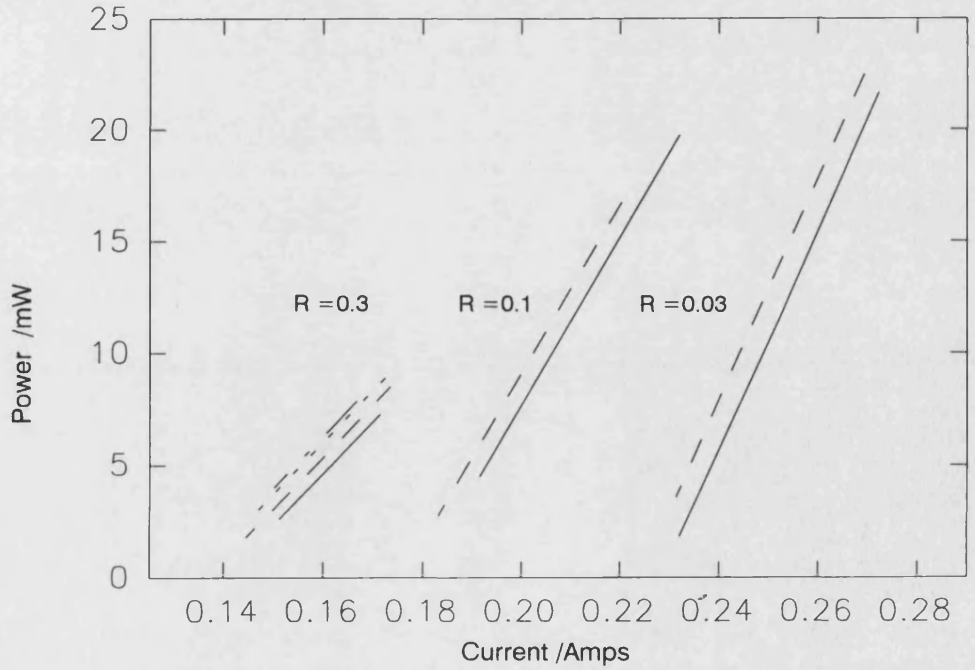

Figure 4.3. Simulated light output vs current curves from 30μm final width, 1mm long parabolically tapered lasers with longitudinal current density variation and different wide facet reflectivities, R_2 = 0.3, 0.1, 0.03. Solid curves - J(1)=J(2)=J(3).
Dashed - J(1)=1.1*J(2), J(3)=0.9*J(2). Dotted - J(1)=1.2*J(2), J(3)=0.8*J(2).
Dot+Dashed - J(1)=1.5*J(2) ,J(3)=0.8 *J(2)

Figure 4.4 shows a plot of the power variation along lasers with different wide facet reflectivities where the power density at the narrow end is the same in each case. The solid curves are for a device with $R_2 = 0.3$ at a current of 151 mA and the dashed curves are for a device with $R_2 = 0.03$ at a current of 252 mA. The output powers were 2.6 mW and 11.5 mW for the $R_2 = 0.3$ and $R_2 = 0.03$ cases respectively. Note that the forward and reverse propagating powers are plotted separately. In each case the upper curve is the forward propagating power (from the narrow facet towards the wide facet). Hence, the total power in the device with $R_2 = 0.3$ would be the sum of the two solid curves.

Figure 4.5 shows a plot of the power variation along a device for two current segmentation schemes. In each case the output power is 7.3mW. The total current needed in the segmented case was 166mA against 171mA in the homogeneously pumped case. It can be seen that the power density in the narrow region is essentially unchanged although the length of the lossy region can be seen to be slightly reduced in the segmented case due to the increased current density. This will not provide any advantage in a practical device. In fact, the increase in current density combined with the same optical power density as the homogeneously pumped case will cause this region of the device to heat up more and may make the device fail earlier.

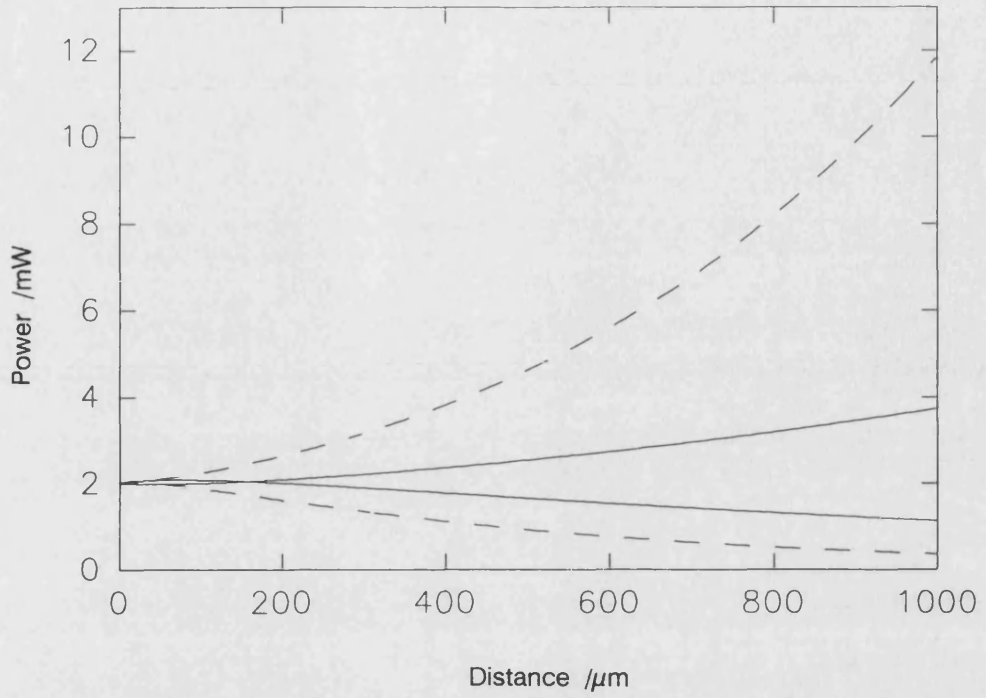

Figure 4.4. Longitudinal power variation in 30μm final width, 1mm long parabolically tapered lasers with different wide facet reflectivities. Solid curve - R(2)=0.3. Dashed curve - R(2)=0.03.

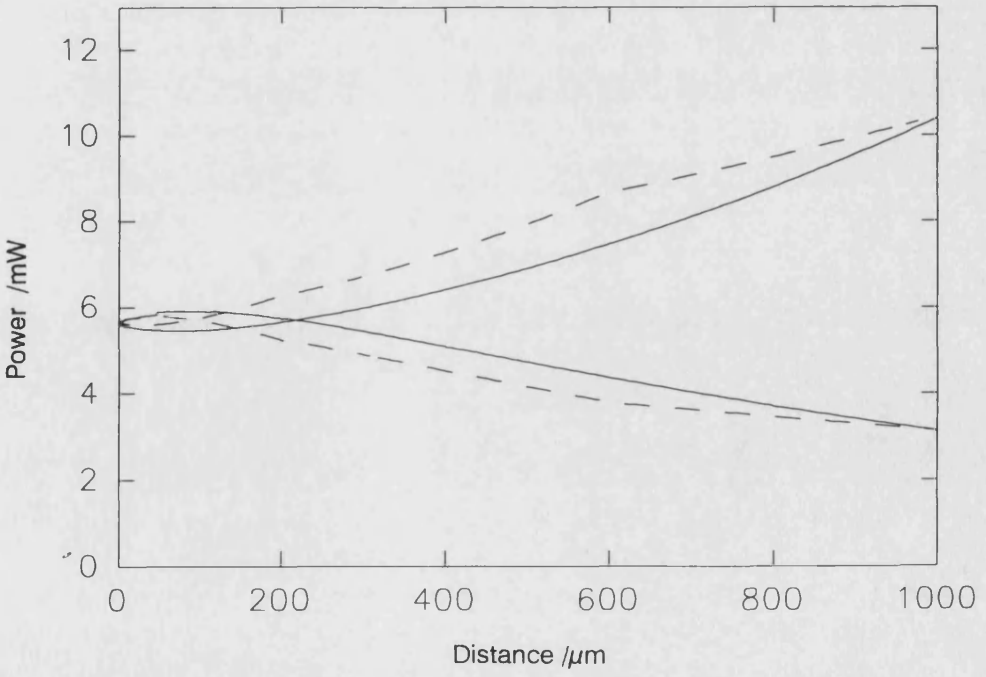

Figure 4.5. Longitudinal power variation in 30μm final width, 1mm long parabolically tapered laser with different longitudinal current density variations. R(2) = 0.3. Solid curve - J(1)=J(2)=J(3). Dashed curve - J(1)=1.2*J(2), J(3)=0.8*J(2).

4.3 Experimental Results

A number of small single parabolic taper lasers were measured before and after the wide facets were AR coated with a single layer of Zirconium Oxide/Titanium Oxide. The devices all had 300μm long tapered regions with width varying from 3μm to 10μm. 3μm wide straight regions of different lengths extended from the narrow end of the tapered region (see figure 4.6) to the facet in order to investigate the ability of such regions to filter out higher order lateral modes. Table 4.2 contains descriptions of the devices measured. None of these devices had cavity spoilers beside the narrow region.

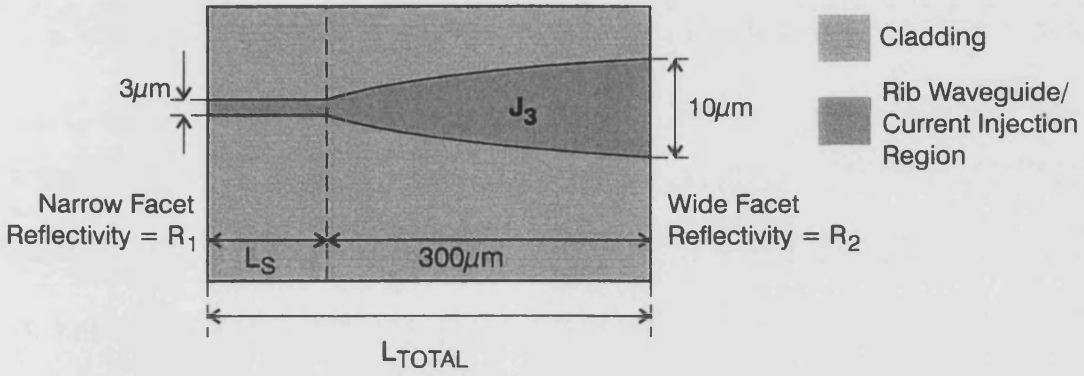

Figure 4.6. Schematic diagram of a tapered laser with a straight section.

Device No. :	UB856	UB854	UB853	UB855
Total Length, L_{TOTAL} (μm)	350	450	550	650
Taper Length (μm)	300	300	300	300
Straight Length, L_S (μm)	50	150	250	350
Wide facet width (μm)	10	10	10	10
Narrow facet width (μm)	3	3	3	3

Table 4.2. Dimensions of parabolically tapered lasers used in section 4.3.

Figure 4.7 shows the various light output against current curves from each facet before AR coating. The dashed curves are the narrow facet measurements. One can see that similar powers were obtained from wide and narrow facets in each case. This is to be expected in a device with equal facet reflectivities. Device UB853 was the exception but this was attributed to dirt on the rear facet reducing the measured power. The shapes of the curves are of particular interest. Devices UB856, UB854 and UB853 all show 3 clear operating regimes above threshold which is typical of gain guided devices. In the first regime the devices were operating approximately as they were designed to with the fundamental lateral mode dominant along the length (25-40mA for device UB854).

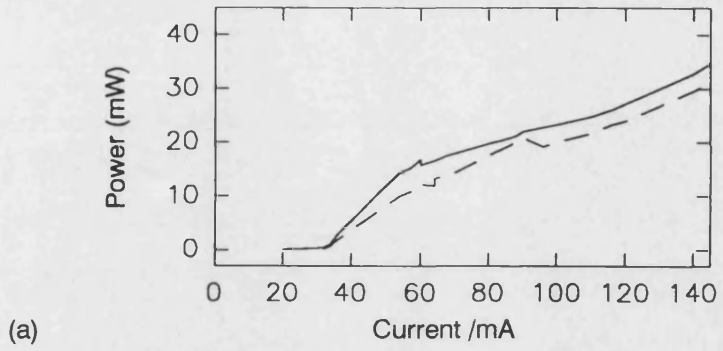

(a)

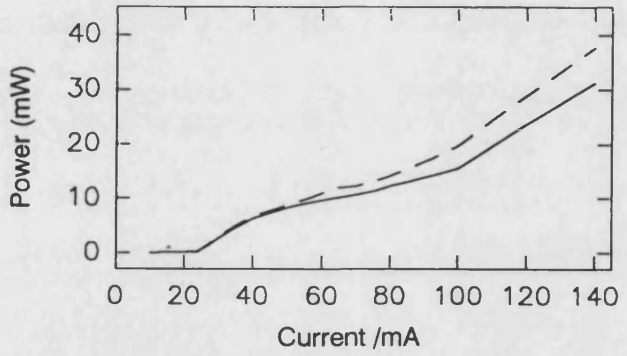

(b)

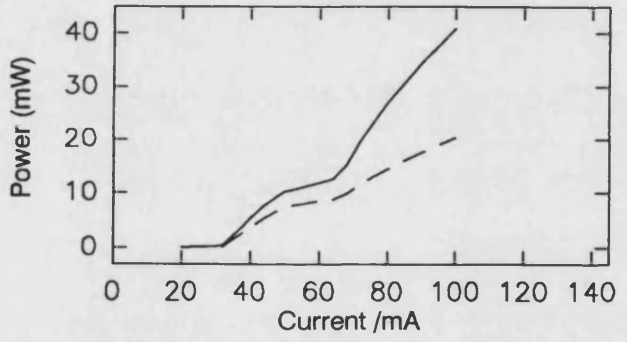

(c)

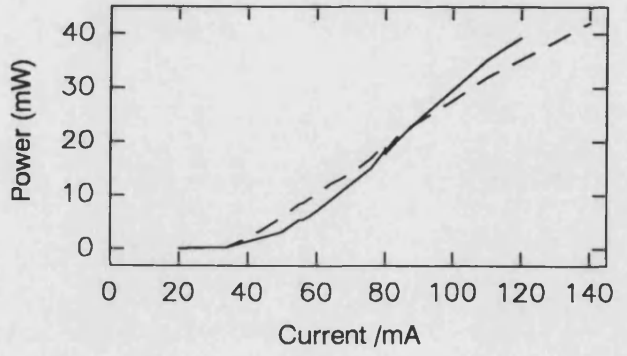

(d)

Figure 4.7. Light output vs current curves before AR coating for four tapered lasers of widths 3-10μm and different total lengths. (a) UB856 - 350μm long, (b) UB854 - 450μm long, (c) UB853 - 550μm, (d) UB855 - 650μm. Solid curves are wide facet measurements. Dashed curves are narrow facet measurements.

As the power density increases nonlinear effects become more important and the devices enter a transition regime (40 - 100mA for device UB854). Above this the devices are operating in a gain guided regime where the field shape is determined by the gain and carrier distribution rather than the lateral effective index variation that is provided by the rib waveguide (>100mA for device UB854).

Figure 4.8 shows the various light output against current curves from each facet after AR coating. Again the dashed curves are the narrow facet measurements. As expected, significantly different powers were measured from the front and back facets of all of the lasers. Also, the threshold current values all increased compared to the values before coating confirming the reduced wide facet reflectivity expected from the coating. These current increases have been used in the model to estimate the change in reflectivity for each device. Table 4.3 contains the threshold current values and the estimated wide facet reflectivity after AR coating. Since the devices were separately coated then these reflectivities were each different.

	Before		After		
Device No.	J_{TH} (mA.μm^{-2})	I_{TH} (mA)	J_{TH} (mA.μm^{-2})	I_{TH} (mA)	Estimated Wide Facet Reflectivity, R_2
UB856	1.41	32.5	2.91	67.0	5%
UB854	0.90	23.5	1.44	37.5	10%
UB853	1.09	31.5	1.66	48.0	6%
UB855	1.03	33.0	1.38	44.0	11%

Table 4.3. Measured threshold current, I_{TH}, and slope efficiency values for devices UB856, UB854, UB853 and UB855, 3-10μm wide, parabolically tapered lasers.

Table 4.4 shows the wide facet and total slope efficiency values for the different devices before and after coating. The wide facet slope efficiencies of the devices increased significantly which showed the usefulness of the coatings at increasing the usable power from the wide facets. The narrow facet efficiencies after coating were much lower showing that the powers in the narrow region of the devices were much lower.

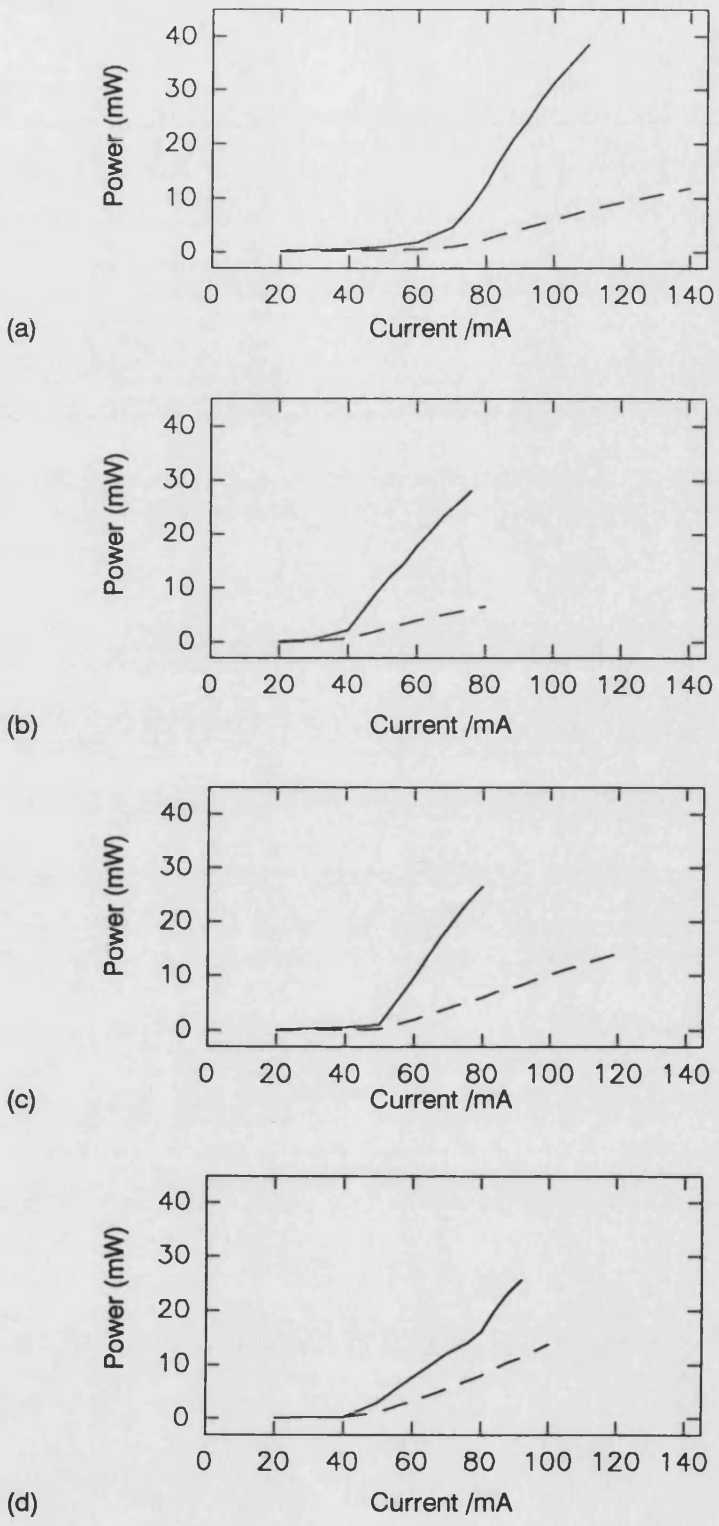

Figure 4.8. Light output vs current curves after AR coating for four tapered lasers of widths 3-10μm and different total lengths. (a) UB856 - 350μm long, (b) UB854 - 450μm long, (c) UB853 - 550μm, (d) UB855 - 650μm. Solid curves are wide facet measurements. Dashed curves are narrow facet measurements.

	Before		After		
	Wide Facet Slope Efficiency (mW/A)	Total Slope Efficiency (mW/A)	Narrow Facet Slope Efficiency (mW/A)	Wide Facet Slope Efficiency (mW/A)	Total Slope Efficiency (mW/A)
UB856	0.65 : 0.31	1.2 : 0.7	0.17	0.91	1.1
UB854	0.40 : 0.40	0.8	0.16	0.74	0.9
UB853	0.64 : 0.55	1.0	0.20	0.83	1.1
UB855	0.42	0.9	0.24	0.50	0.8

Table 4.4. Measured slope efficiency values for devices UB856, UB854, UB853 and UB855, 3-10μm wide, parabolically tapered lasers.

However, the total slope efficiencies of the devices have not all increased sharply. Figure 4.9 shows the combined wide and narrow facet output power against current curves for the devices both before and after coating. The dashed curves are after coating. It can clearly be seen that only devices UB856 and UB854 were more efficient after coating. This leads to the conclusion that the coatings are absorbing and possibly scattering some of the light.

Clear differences were seen in the near field intensity profiles of the devices measured before facet coatings were applied. Figures 4.10, 4.11, 4.12 and 4.13 show the near field intensity profiles from the facets of devices UB856, UB854, UB853 and UB855 respectively at different currents. Most of the lasers showed significant changes in the near field intensity profiles as the current increased. At high currents the two shorter devices (UB856 and UB854) showed multiple peaks in the profiles measured from the wide facets and side peaks away from the rib waveguides in the profiles from the narrow facets. These side peaks became prominent at the same currents that the kinks occurred in the light output against current curves. Device UB855 showed little change in field shape with current demonstrating that the increased length resulted in less sensitivity to the nonlinear effects on the waveguide.

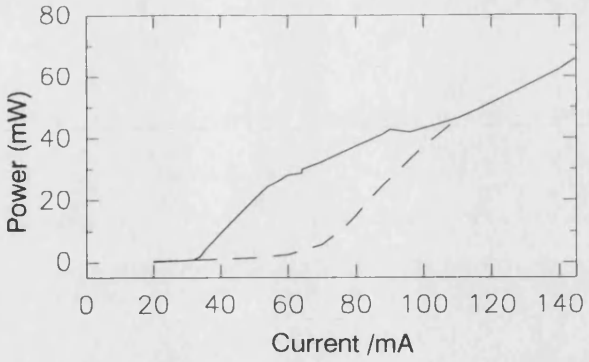

(a)

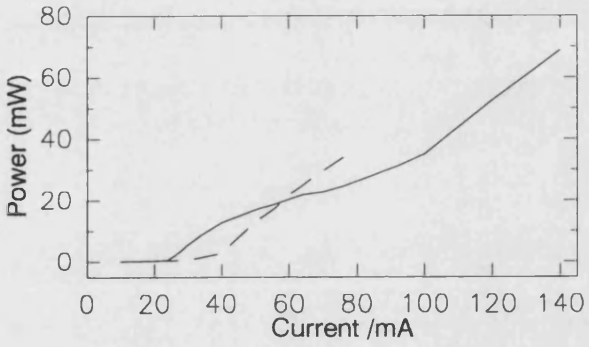

(b)

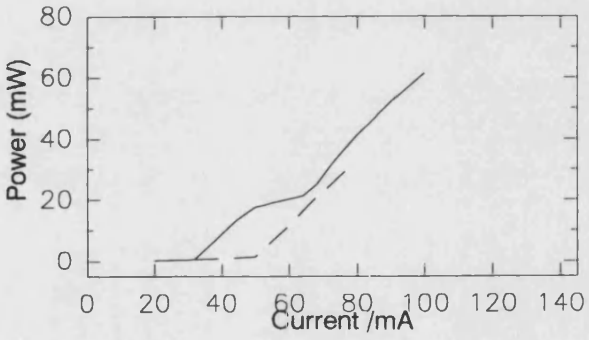

(c)

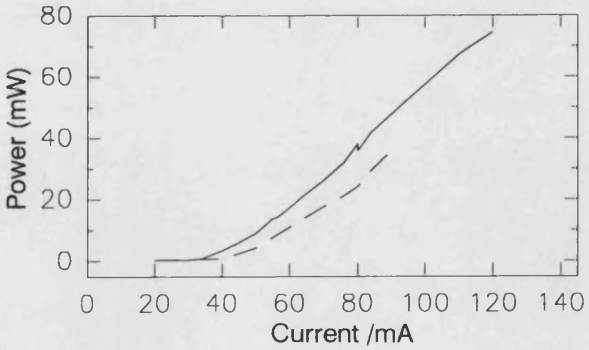

(d)

Figure 4.9. Total Light output (Both facets) vs current curves before and after AR coating for four tapered lasers of widths 3-10μm and different total lengths. (a) UB856 - 350μm long, (b) UB854 - 450μm long, (c) UB853 - 550μm, (d) UB855 - 650μm. Solid curves are uncoated results. Dashed curves are results after AR coating of 10μm wide facet with single layer of Zirconium Oxide/Titanium Oxide.

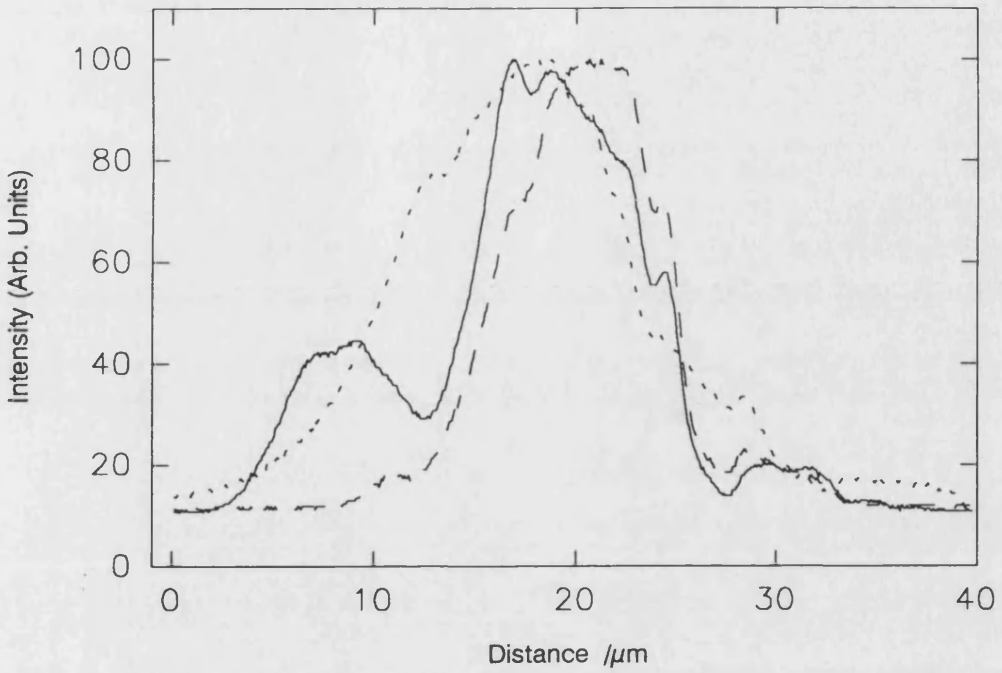

Figure 4.10.a. Near field intensity profiles at different currents from 10μm facet of UB856 before AR coating. 3-10μm width, 350μm total length parabolically tapered laser. Solid curve - Current = 140mA, Dashed curve - 40mA, Dotted curve - 20mA.

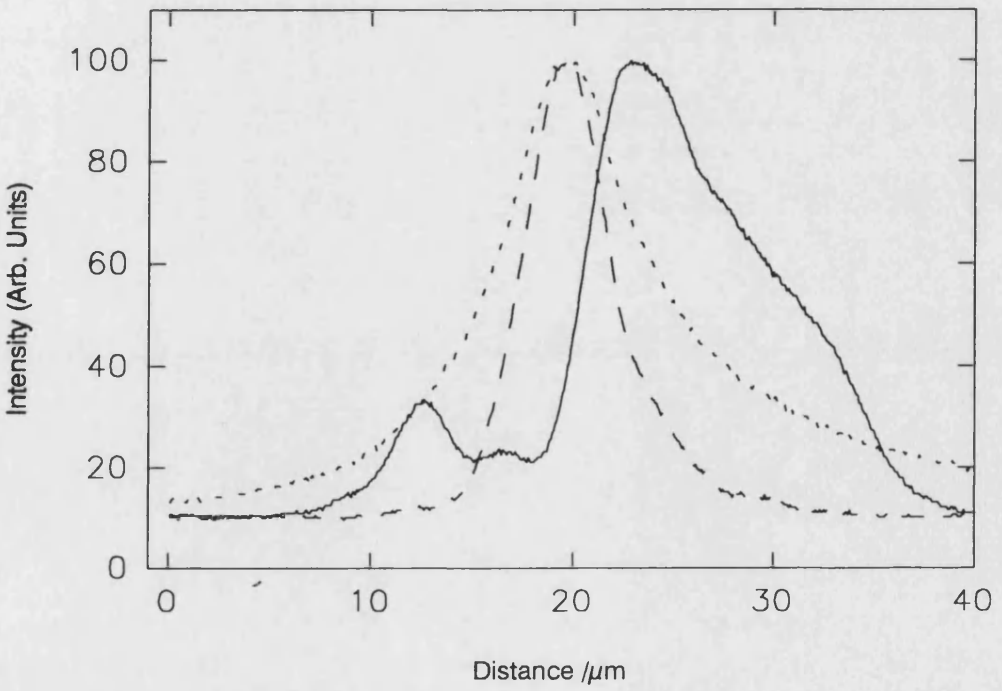

Figure 4.10.b. Near field intensity profiles at different currents from 3μm facet of UB856 before AR coating. 3-10μm width, 350μm total length parabolically tapered laser. Solid curve - Current = 140mA, Dashed curve - 40mA, Dotted curve - 20mA.

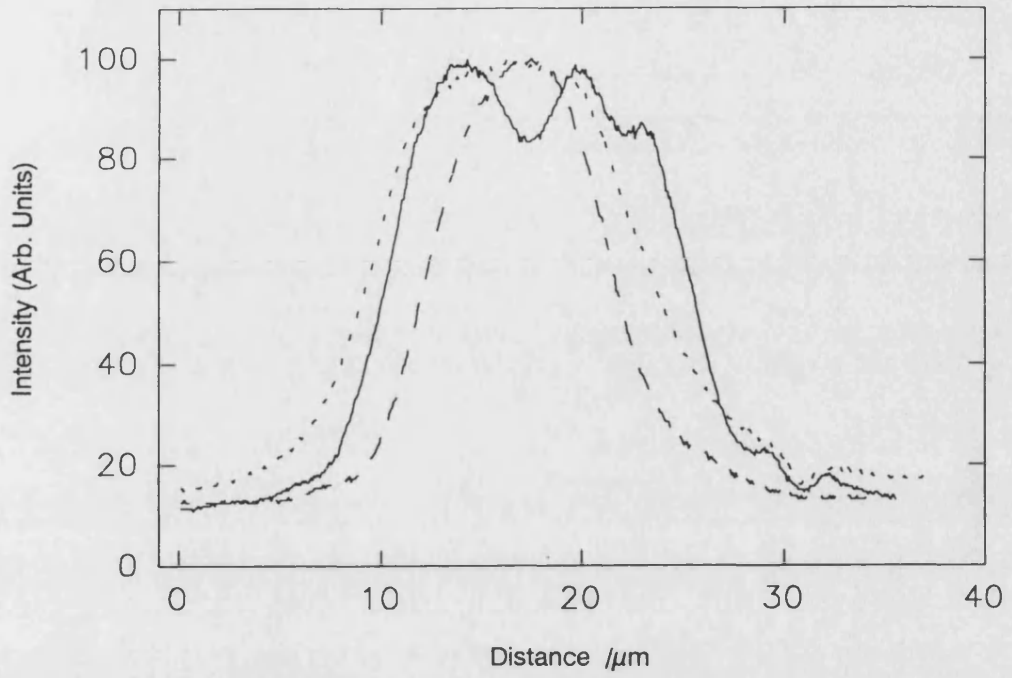

Figure 4.11.a. Near field intensity profiles at different currents from 10μm facet of UB854 before AR coating. 3-10μm width, 450μm total length parabolically tapered laser. Solid curve - Current = 138mA, Dashed curve - 51mA, Dotted curve - 10mA.

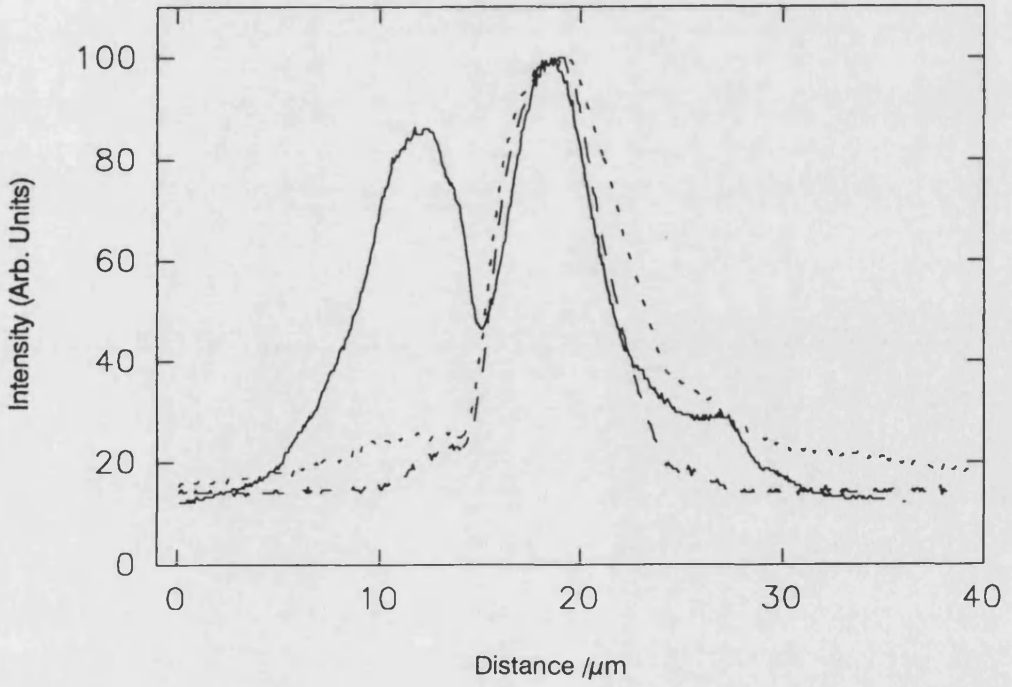

Figure 4.11.b. Near field intensity profiles at different currents from 3μm facet of UB854 before AR coating. 3-10μm width, 450μm total length, parabolically tapered laser. Solid curve - Current = 138mA, Dashed curve - 51mA, Dotted curve - 10mA.

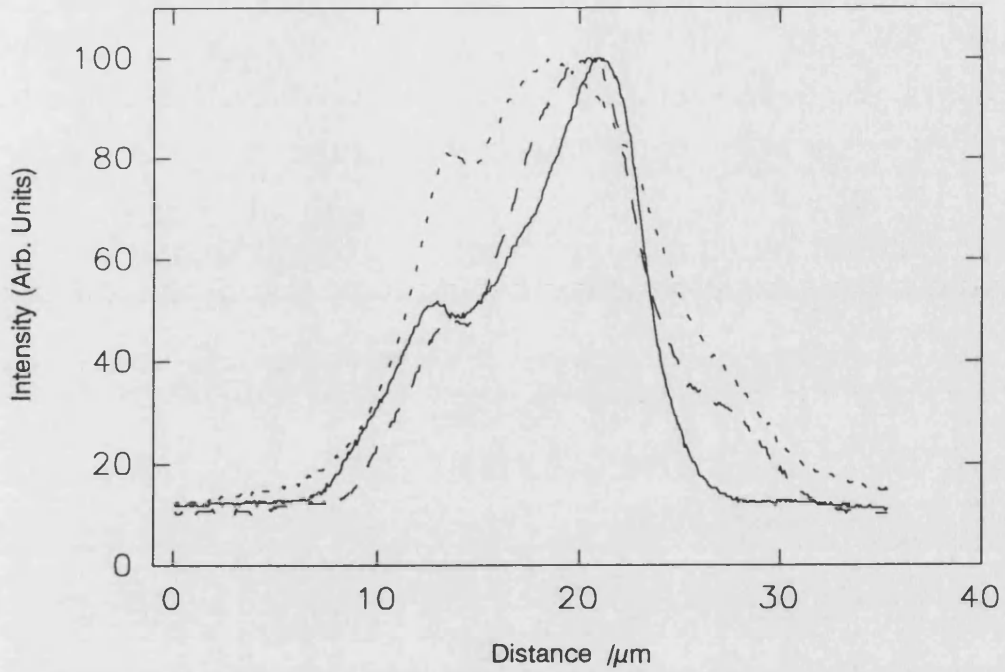

Figure 4.12.a. Near field intensity profiles at different currents from 10μm facet of UB853 before AR coating. 3-10μm width, 550μm total length parabolically tapered laser. Solid curve - Current = 120mA, Dashed curve - 60mA, Dotted curve - 20mA.

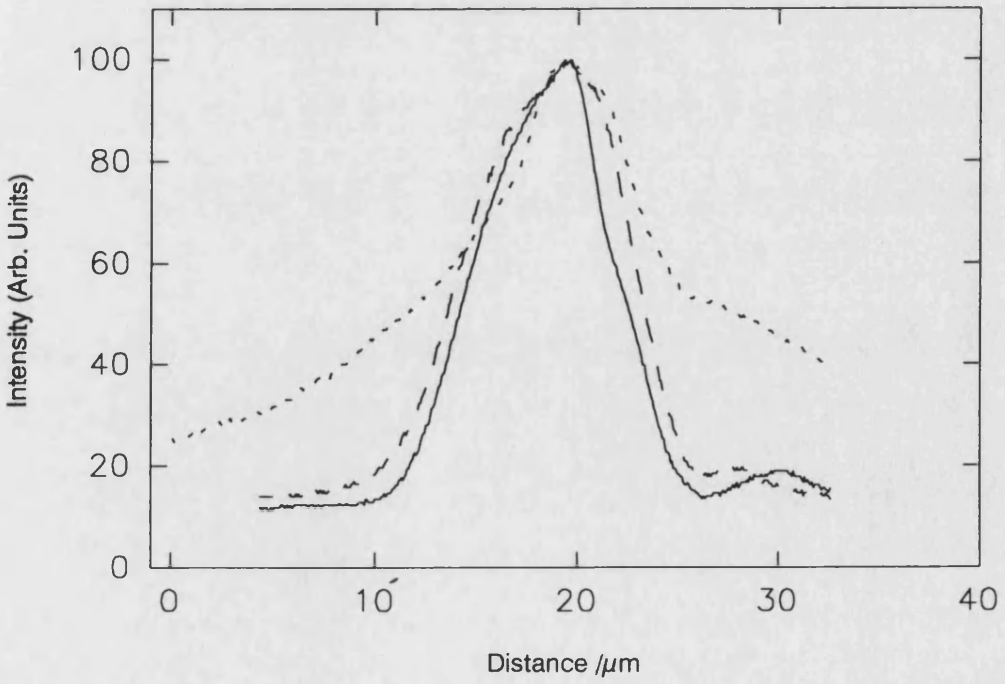

Figure 4.12.b. Near field intensity profiles at different currents from 3μm facet of UB853 before AR coating. 3-10μm width, 550μm total length parabolically tapered laser. Solid curve - Current = 120mA, Dashed curve - 60mA, Dotted curve - 20mA.

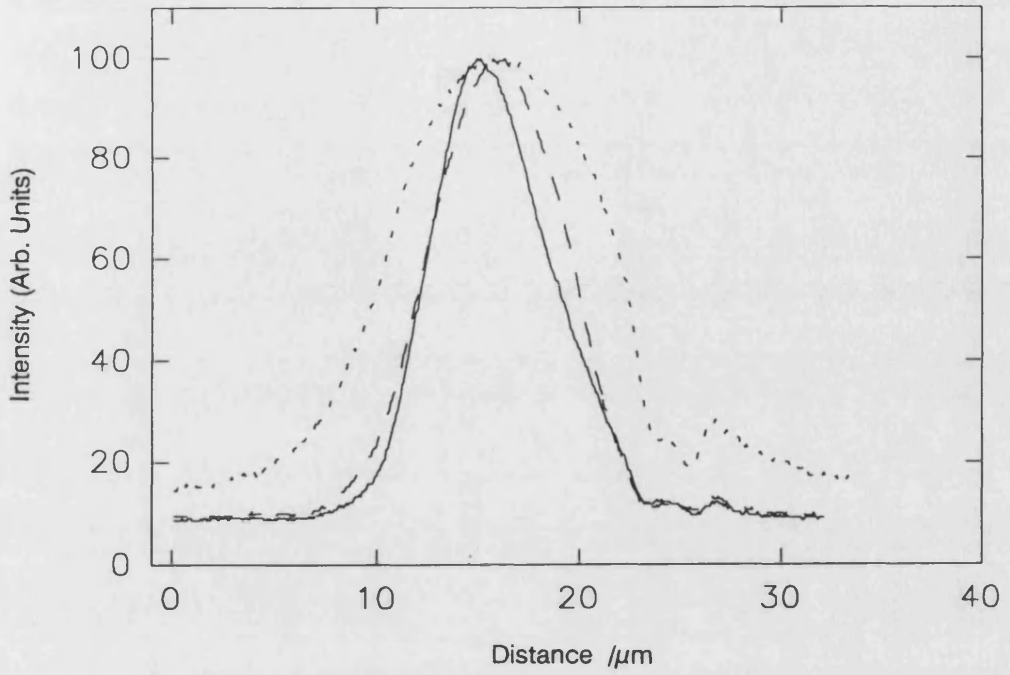

Figure 4.13.a. Near field intensity profiles at different currents from 10μm facet of UB855 before AR coating. 3-10μm width, 650μm total length, parabolically tapered laser. Solid curve - Current = 150mA, Dashed curve - 60mA, Dotted curve - 30mA.

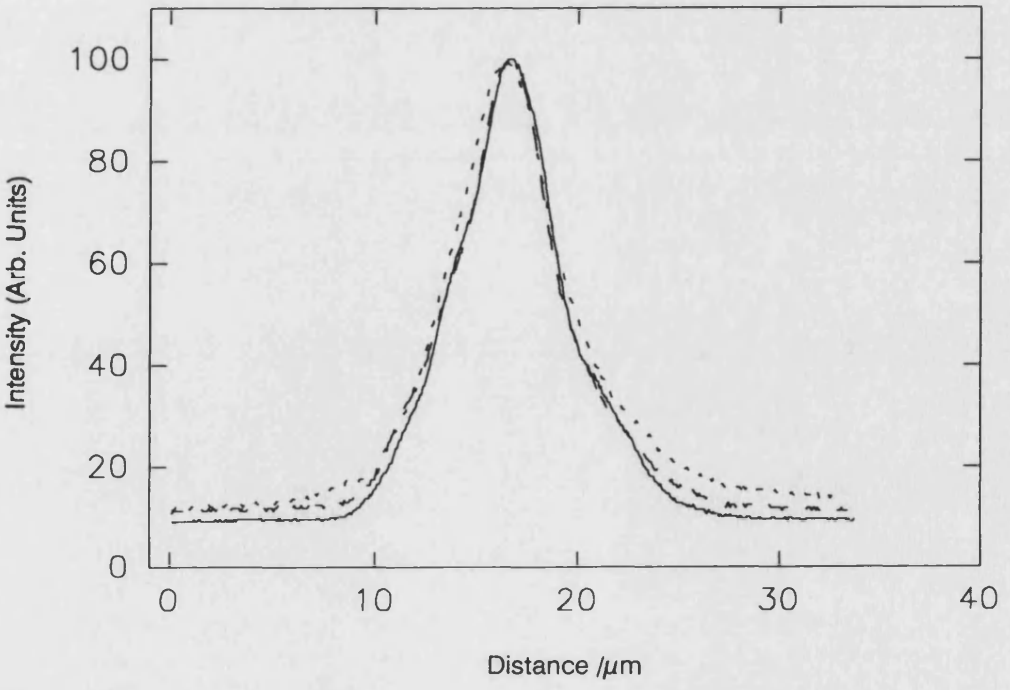

Figure 4.13.b. Near field intensity profiles at different currents from 3μm facet of UB855 before AR coating. 3-10μm width, 650μm total length, parabolically tapered laser. Solid curve - Current = 150mA, Dashed curve - 60mA, Dotted curve - 30mA.

Figures 4.14 and 4.15 show near field intensity profiles after AR coating of UB854 and UB855 respectively. At high currents a second peak was still seen at the back facet of laser UB854 although the front facet profile had changed, becoming a narrower single peak shifted to the right side of the facet with a shoulder on the opposite side. The intensity profiles measured from device UB855 had also changed. The profile at the front facet was narrower than previously and shifted slightly to one side. The back facet intensity profile gained shoulders to the sides of the main peak. Evidently, the higher carrier density required with reduced facet reflectivity increased the nonlinear effects on the refractive index and began to effect even this longest device.

Far field intensity measurements were also made for the wide facets of lasers UB854 and UB855 after AR coating. The profiles obtained are shown in figure 4.16. Considering firstly the profiles in figure 4.16.a measured from UB854 one can see a gradual shift in the angle of the peak emission as the current increases. This corresponds with the shift observed in the near field intensity profile at the facet. In addition, small side lobes were seen to one side of the main peak. The FWHM of the main peaks were all ~5°.

The results obtained from device UB855 were more complex. At 90mA a single peak was seen with FWHM ~4.5° (dotted curve in figure 4.16.b). When the current was increased to 150mA a change occurred. The laser output underwent beamsteering during the current pulse. The dashed curve in figure 4.16.b shows the intensity profile measured at 0.2μs after the beginning of the pulse. The solid curve in the figure shows the profile measured after 0.4μs of the current pulse had elapsed. A shift in the peak emission angle of >2° was seen accompanied by an increase in FWHM from ~4° to ~4.5°. The origin of this temporal steering is presumed to be temperature variation across the device altering the lateral waveguide.

Devices UB854 and UB855 were then tested with 0.5μs pulses to higher currents than previously. Curves of output power variation from the wide facets against current are shown in figure 4.17. Almost 90mW peak power was emitted by UB854 when it failed. Laser UB855 continued to function at currents greater than 250mW however the output power reached a maximum of 140mW at 220mA.

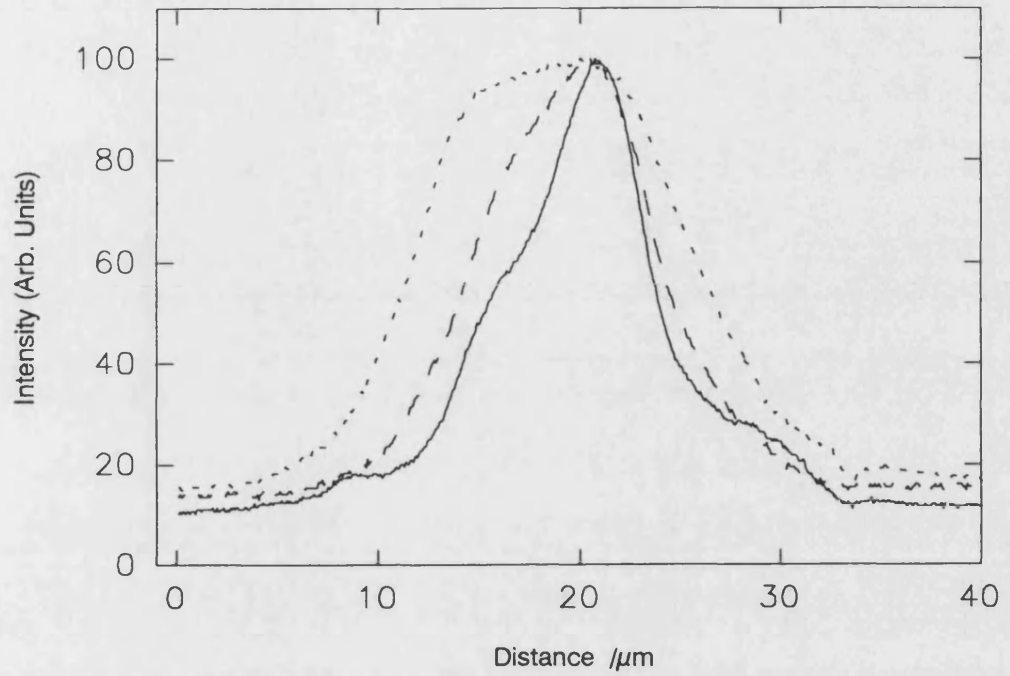

Figure 4.14.a. Near field intensity profiles at different currents from 10μm facet of UB854 after AR coating. 3-10μm width, 450μm total length, parabolically tapered laser. Solid curve - Current = 150mA, Dashed curve - 50mA, Dotted curve - 20mA.

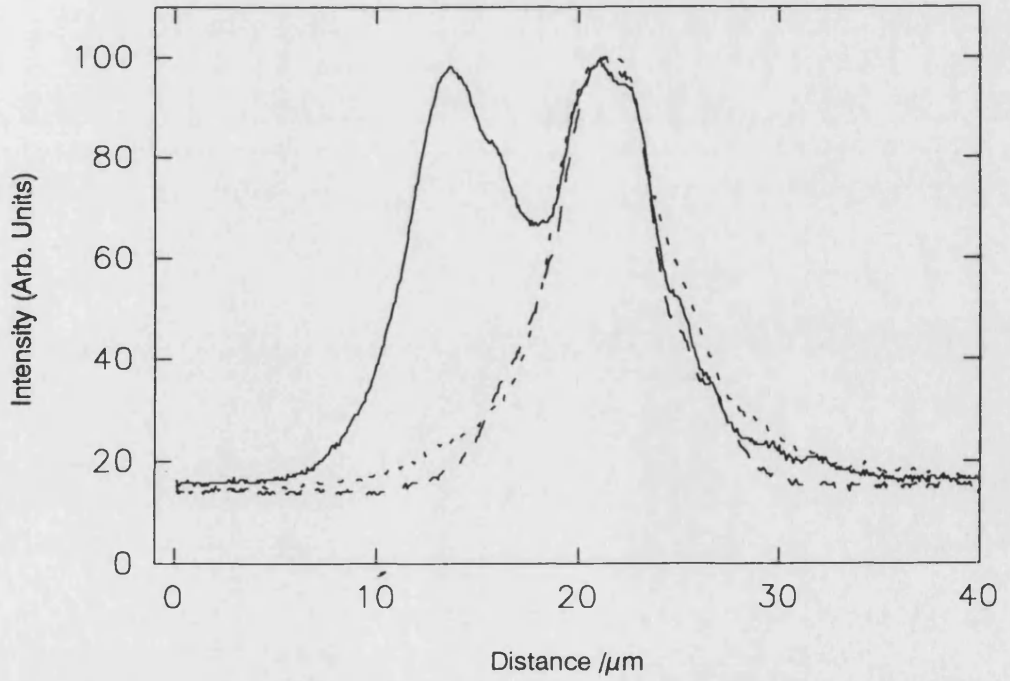

Figure 4.14.b. Near field intensity profiles at different currents from 3μm facet of UB854 after AR coating. 3-10μm width, 450μm total length, parabolically tapered laser. Solid curve - Current = 150mA, Dashed curve - 50mA, Dotted curve - 20mA.

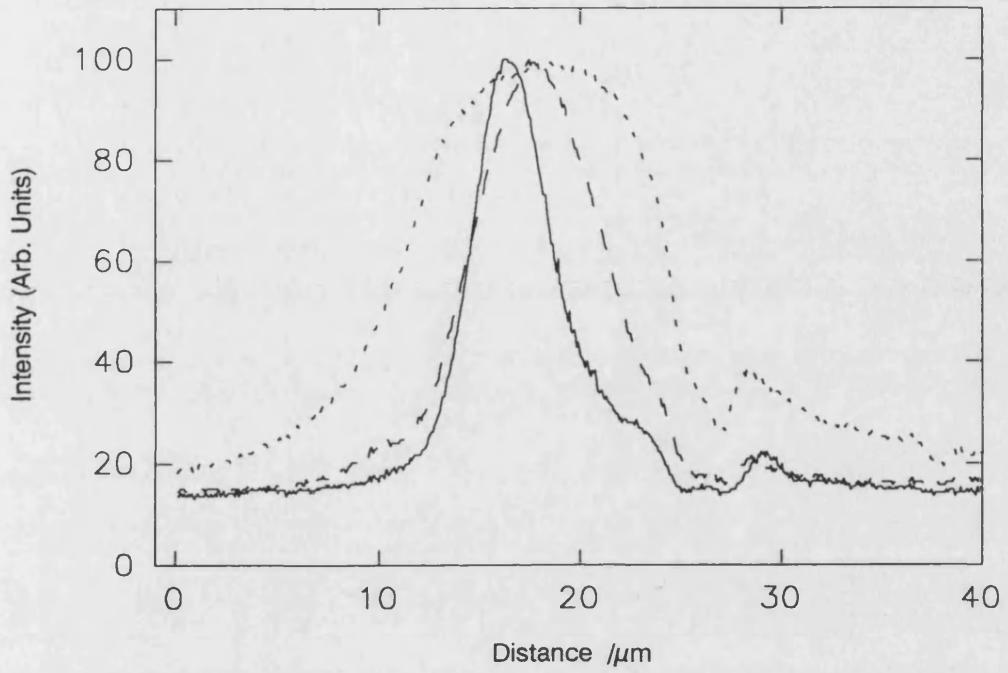

Figure 4.15.a. Near field intensity profiles at different currents from 10μm facet of UB855 after AR coating. 3-10μm width, 650μm total length, parabolically tapered laser. Solid curve - Current = 150mA, Dashed curve - 60mA, Dotted curve - 10mA.

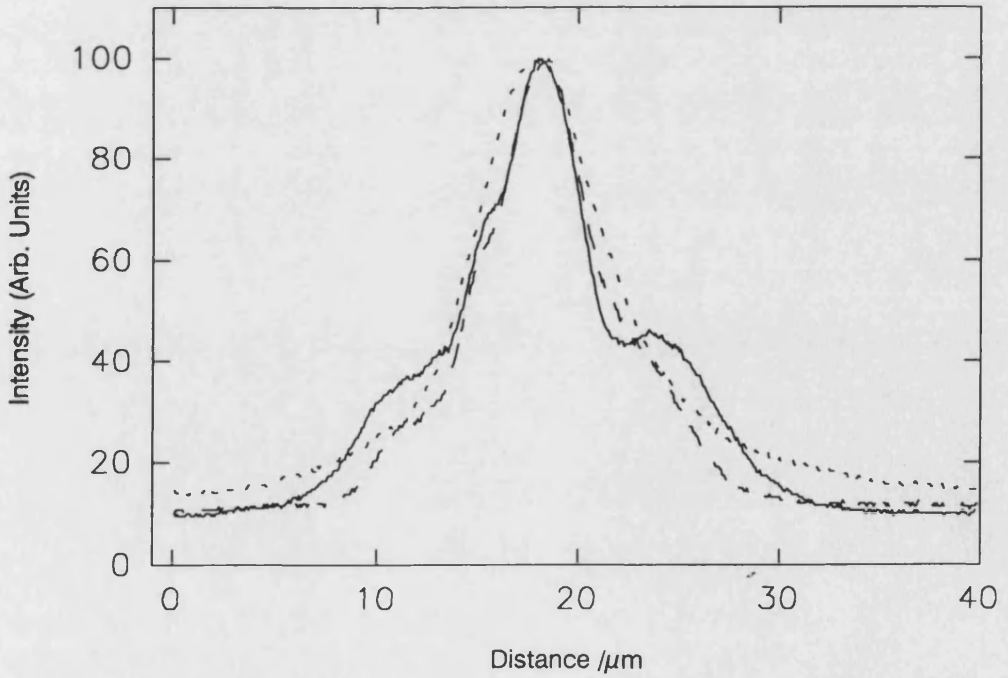

Figure 4.15.b. Near field intensity profiles at different currents from 3μm facet of UB855 after AR coating. 3-10μm width, 650μm total length, parabolically tapered laser. Solid curve - Current = 150mA, Dashed curve - 60mA, Dotted curve - 10mA.

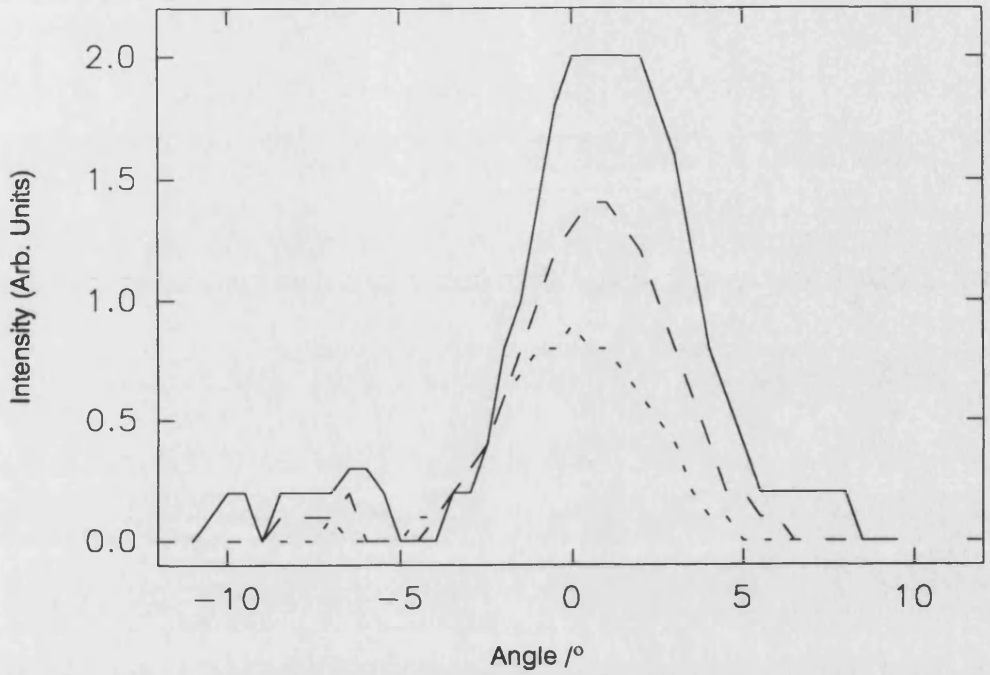

Figure 4.16.a. Far field intensity profiles at different currents from 10μm facet of UB854 after AR coating. 3-10μm width, 450μm total length, parabolically tapered laser. Solid curve - Current = 150mA, Dashed curve - 100mA, Dotted curve - 70mA.

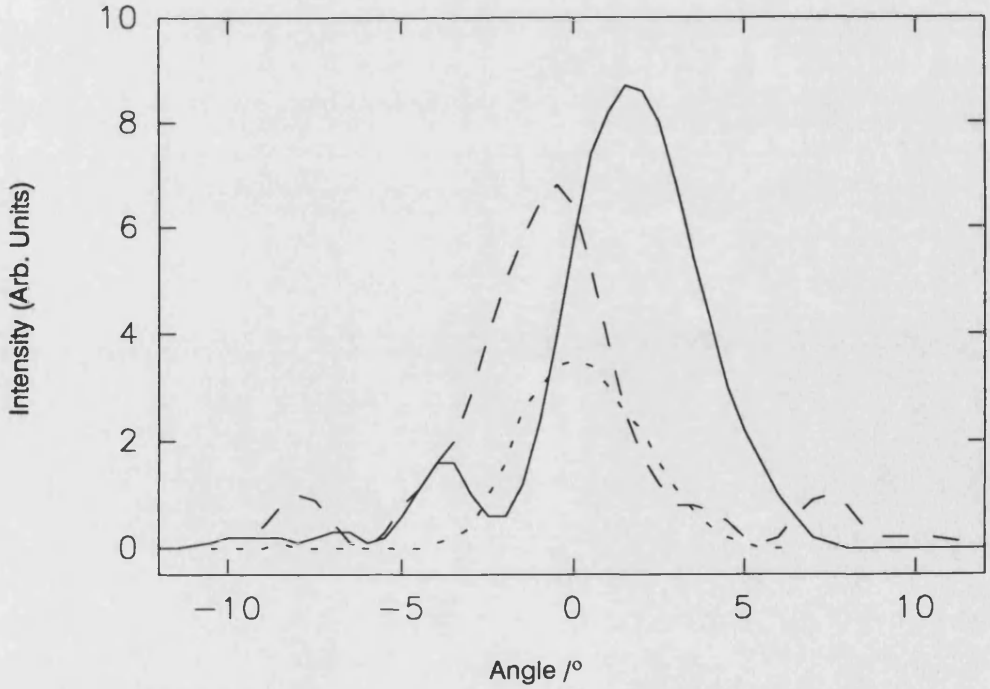

Figure 4.16.b. Far field intensity profiles at different currents from 10μm facet of UB855 after AR coating. 3-10μm width, 650μm total length, parabolically tapered laser. Solid curve - 150mA (0.4μs pulse width), Dashed curve - 150mA (0.2μs pulse width), Dotted curve - 90mA.

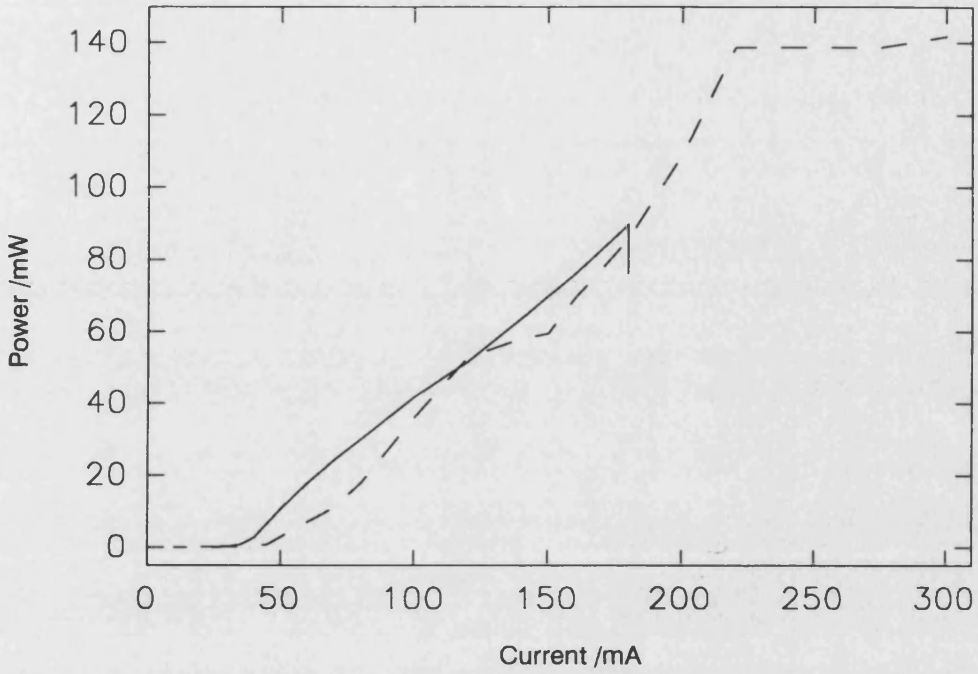

Figure 4.17. Output power vs. current curves after AR coating from 10μm facets of UB854 and UB855, 3-10μm width, parabolically tapered lasers. Measurements were taken using 0.5μs pulses with a duty cycle of 1000:1. Solid curve - UB854, Dashed curve - UB855.

4.4 Conclusions

Simulation results have shown that the slope efficiency of 1mm long parabolically tapered lasers can be more than doubled by reducing the wide facet reflectivity from 30% to 3%. Although there is a corresponding increase in threshold current density of ~50% the resultant device still has a higher overall efficiency at output powers above 40mW.

AR coated single taper lasers have been successfully realised resulting in devices with higher wide facet slope efficiencies. 140mW of peak power was emitted from the wide facet of the longest device measured here (UB855). However, estimates of the reflectivity values of the coated facets have shown that the results were variable. In addition, the combined slope efficiencies of the devices did not all increase due to AR coating indicating that a significant amount of power was being scattered or absorbed by the coatings.

The devices have been shown to be sensitive to refractive index changes caused by carrier density and temperature variations. Kinks in the light current curves and changes in the near field and far-field intensity profiles were all observed. It may be possible to reduce some of these effects by increasing the lateral effective index step of future devices and through the use of deflectors to the sides of the narrow region. It was observed that an increased length of narrow region resulted in more stable near field intensity profiles before the devices were AR coated. A further increase in length may also provide more stable devices in the future.

References

[1] G.H.B.Thompson, 'Physics of Semiconductor Laser Devices,' John Wiley & Sons Ltd., p.94, (1980)

[2] G.H.B.Thompson, 'Physics of Semiconductor Laser Devices,' John Wiley & Sons Ltd., p.96, (1980)

[3] J.Gowar, 'Optical Communication Systems (2nd Ed.)' Prentice Hall International (UK) Ltd., p. 398, (1993)

Chapter 5

New Devices

Simulation and experimental results for a number of parabolically tapered lasers have been presented in the previous chapters. Parabolic bow-tie lasers were shown to emit high powers (>100mW) with narrow lateral far field intensity profiles. Further experimental results from a variety of tapered lasers are presented in this chapter. A comparison of different taper shapes has been made and is presented section 5.1. Section 5.2 details the results from a number of bow-tie laser arrays. The measured efficiency increases made possible by single layer AR facet coatings to array devices are also presented. Section 5.3 presents the results of some collaborative work with the University of Michigan involving InGaAs active layer material. A variety of devices including narrow ridge lasers and large linearly tapered bow-tie lasers were fabricated and measured.

5.1 Shape Comparison - Parabolic, Linear and Exponential Bow-tie lasers

5.1.1 Introduction

It was mentioned in chapter 3 that only parabolic tapered lasers can be accurately analysed with the current model. However, the propagation characteristics of differently shaped passive tapered waveguides were analysed in chapter 2. From these results it was predicted that linearly and exponentially tapered lasers will be less efficient than parabolically tapered lasers because more power will be coupled into higher order lateral modes and then radiated from the sides of the tapers on reflection from the wide facet. It was also expected that parabolically tapered devices of certain dimensions should have slightly narrower far field profiles than similar linear and exponential devices. Exponential devices were expected to have the narrowest near field intensity distributions making them the least suitable for high power operation.

In order to test these predictions some 2mm long bow-tie lasers were fabricated with differently shaped tapers. For comparison a straight rib, broad area device was also fabricated at the same time. The details of the devices are contained in table 5.1. A diagram showing the different shapes is shown in figure 5.1.

Device #	UB823	UB836	UB827	UB824	UB862
Taper shape	Parabolic	Parabolic	Linear	Exponential	n/a - Straight
Total length	2mm	2mm	2mm	2mm	2mm
Centre length	10μm	10μm	10μm	10μm	n/a
Taper length	995μm	995μm	995μm	995μm	n/a
Centre width	3μm	3μm	3μm	3μm	(30μm)
Facet width	30μm	30μm	30μm	30μm	30μm
Contact area	39700 μm^2	39700 μm^2	32900 μm^2	23100 μm^2	60000 μm^2
Deflectors	No	No	No	No	No
Etch Depth	1.0μm	1.0μm	1.0μm	1.0μm	1.0μm
Material	QT829B	QT829B	QT829B	QT829B	QT829B

Table 5.1. Shape comparison device details

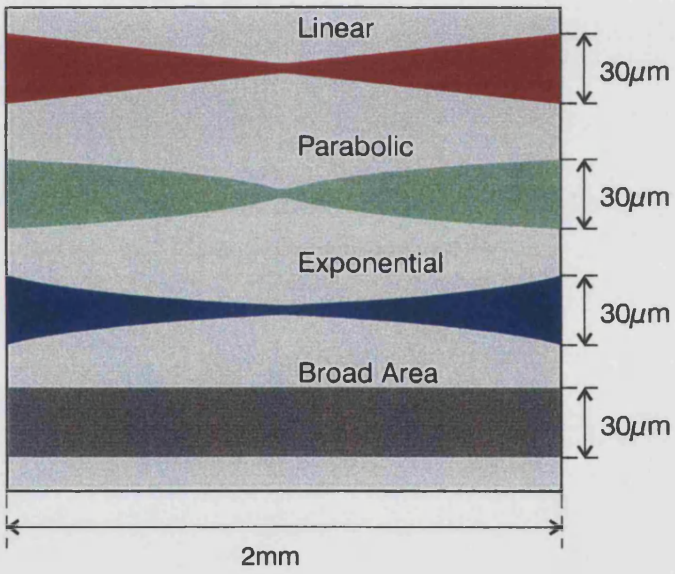

Figure 5.1. Diagram of device shapes used

5.1.2 Results

All of the measurements described were made with 3μs current pulses and a duty cycle of ~1:30. Figure 5.2 shows a plot of the light output power vs. current variation from the devices. One can clearly see that of the tapered devices the parabolic devices had the highest slope efficiencies. In fact the exponential device had a lower threshold current but this was due to the smaller active area of this device. The curves for the parabolic devices both cross the exponential curve before output powers of 50mW were reached.

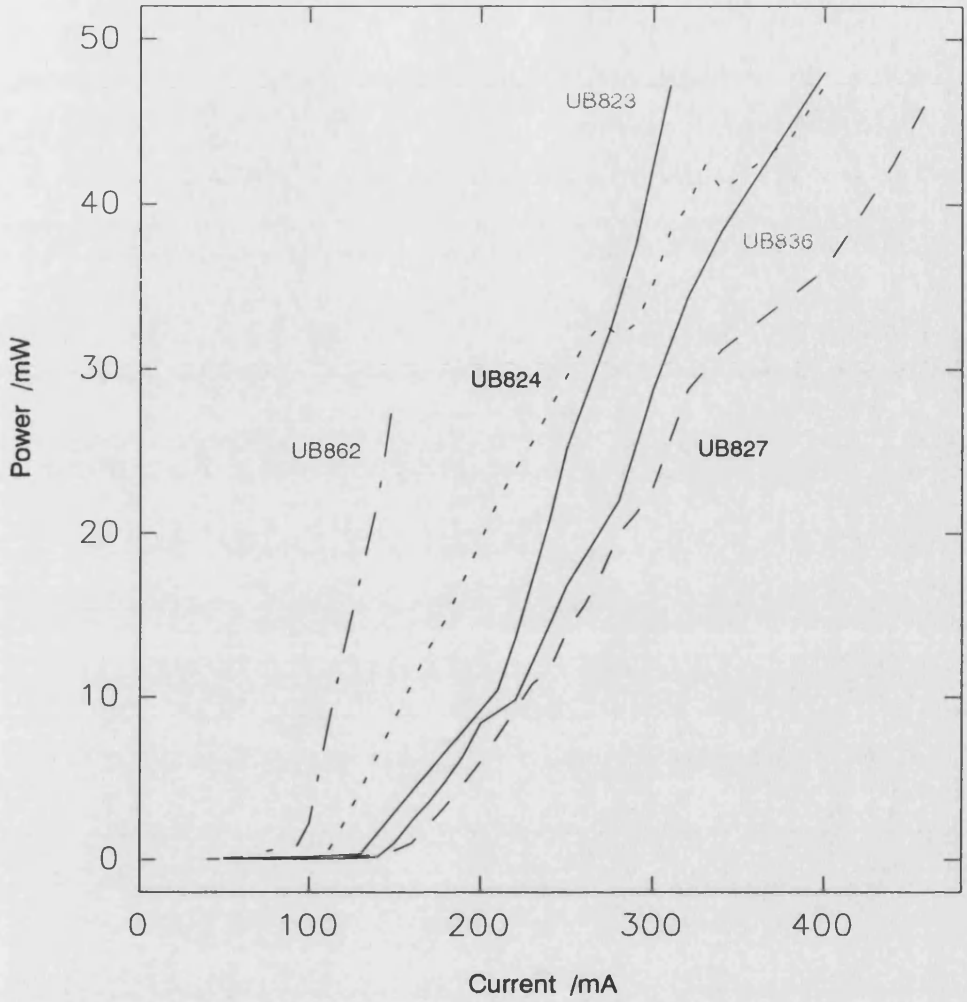

Figure 5.2. Output power vs. current curves from 2mm long, 30μm final width, bow-tie lasers with different taper shapes. Also shown is the curve for a 30μm wide, 2mm long, 'straight' rib waveguide broad area laser. The device details are given in table 5.1.

An interesting result that can be seen from this figure is that the straight, broad area device (UB862) had a lower threshold current and higher slope efficiency than any of the tapered devices. This is not what one might expect considering the larger active area of this device compared to the tapered devices. The threshold current density was therefore much lower for this device than the tapered devices.

There are two contributing factors to the increased current density in tapered devices. The first is that all the tapered lasers, including parabolic devices, are essentially unstable resonators. None of the tapered waveguides is strictly adiabatic and therefore some of the power escapes from the sides of the tapers introducing an extra 'loss' into the device. Secondly, and perhaps more importantly, the narrow regions of the tapered devices are much more significantly affected by current spreading and carrier diffusion.

As a result of this, the carrier density in the centre of a tapered device is much lower than in the centre of the straight device for a given current density. Therefore, to achieve similar round-trip gain a higher current density is required in the tapered devices than in the straight device.

Near field intensity profiles for devices UB836, UB827, UB824 and UB862 are shown in figures 5.3, 5.4, 5.5 and 5.6 respectively. Large amounts of asymmetry can be seen in the profiles from the tapered devices which was attributed to higher order lateral modes coupling across the narrow region of the devices. Only the fundamental bound mode was supported in the narrow region of these devices, however, if the region was short enough then power that was radiated as the higher order modes became cut-off may have coupled across this region and into higher order modes in the opposite tapered region resulting in the field profiles observed. There were two important differences between these new devices and those of chapter 3 where near-symmetric profiles were obtained from parabolically shaped bow-tie lasers. Firstly, cavity spoilers were omitted in the fabrication of the new devices and secondly, the new devices had shorter central regions of 10μm length rather than 50μm. Both of these factors will have contributed to the increased coupling of antisymmetric modes across the central region. The use of cavity spoilers in all future devices should remove this problem.

Examining the near field intensity profiles more closely and comparing the profiles from the differently shaped devices, one can see that the profiles from the exponential bow-tie laser (UB824) showed narrower peaks than the other devices which was in agreement with the profiles obtained from the model in chapter 2 for propagation through passive tapered waveguides. The profile from this device also changed significantly at the current values where kinks occurred in the light output against current curve.

The far field intensity profiles for the devices are shown in figures 5.7, 5.8, 5.9 and 5.10. The profile from the parabolic device (UB836) showed a clear twin peaked structure confirming that a significant fraction of the power was in antisymmetric modes within the device. This was in agreement with the multilobed near field intensity profile already described. UB827 and UB862 both had broader, multilobed far field profiles and hence had even poorer beam quality. The profiles from UB824 were the

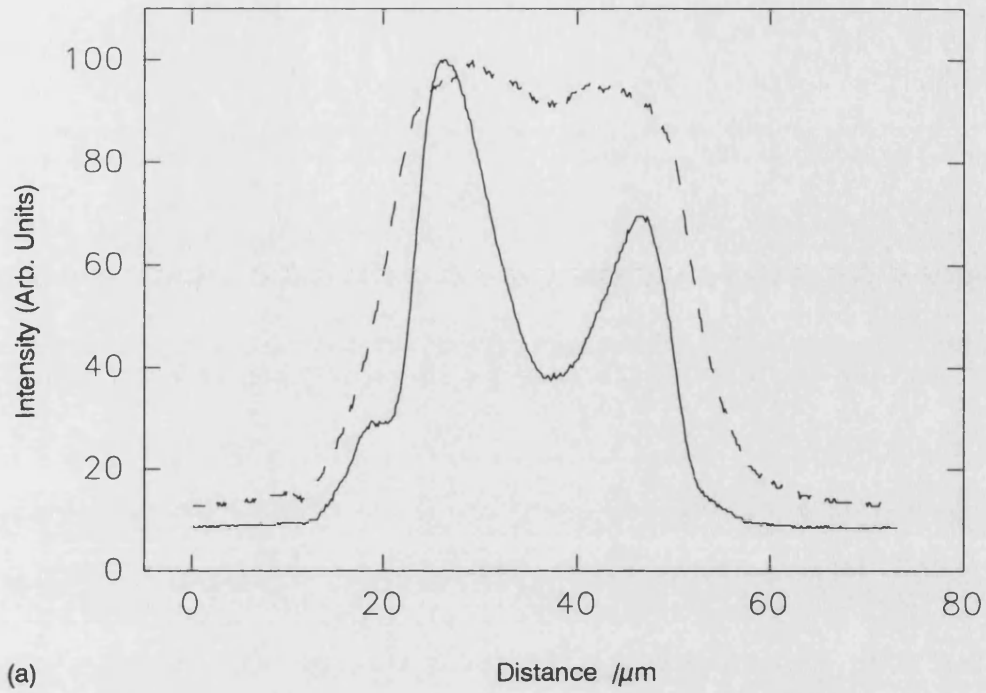

(a)

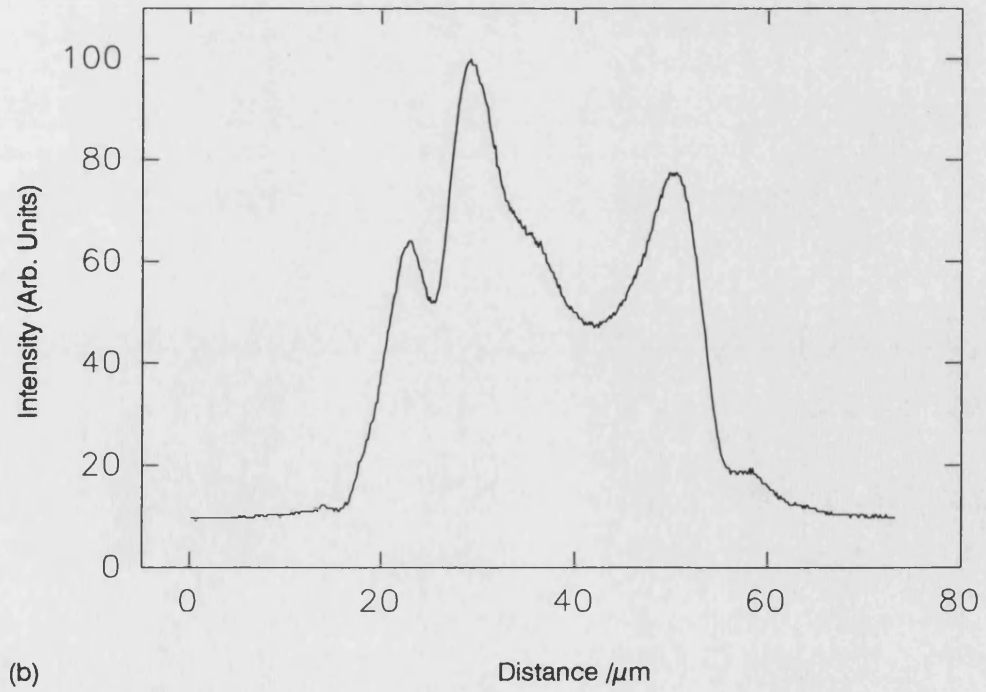

(b)

Figure 5.3. Measured near field intensity profiles at different currents from UB836. 30μm final width, 2mm long, parabolically tapered Bow-tie laser.
(a) Dashed curve - profile at 105mA. Solid curve - at 213mA. (b) Profile at 484mA.

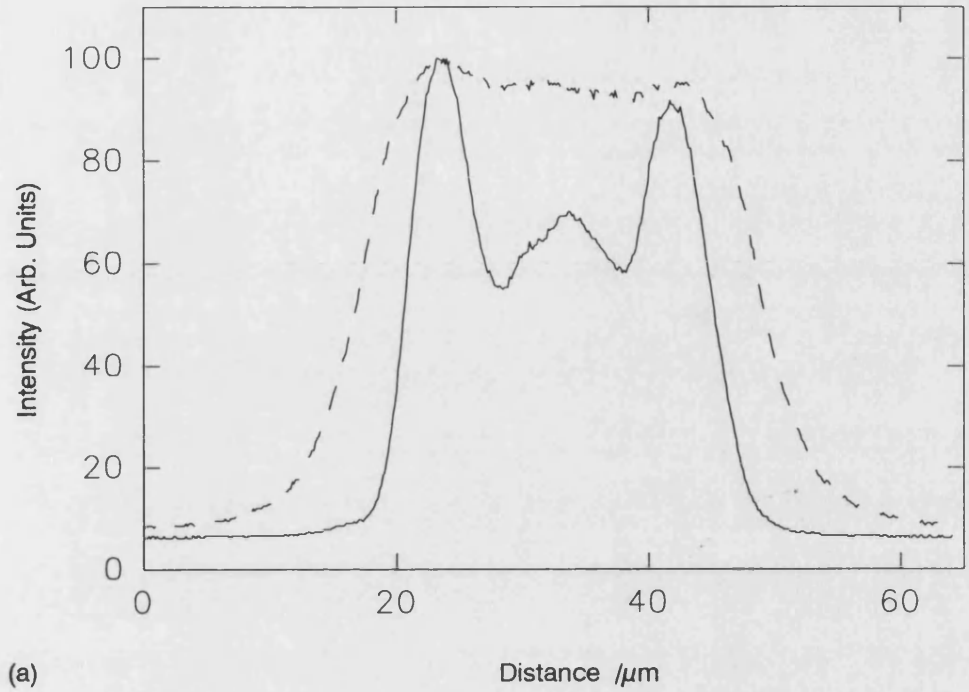

(a)

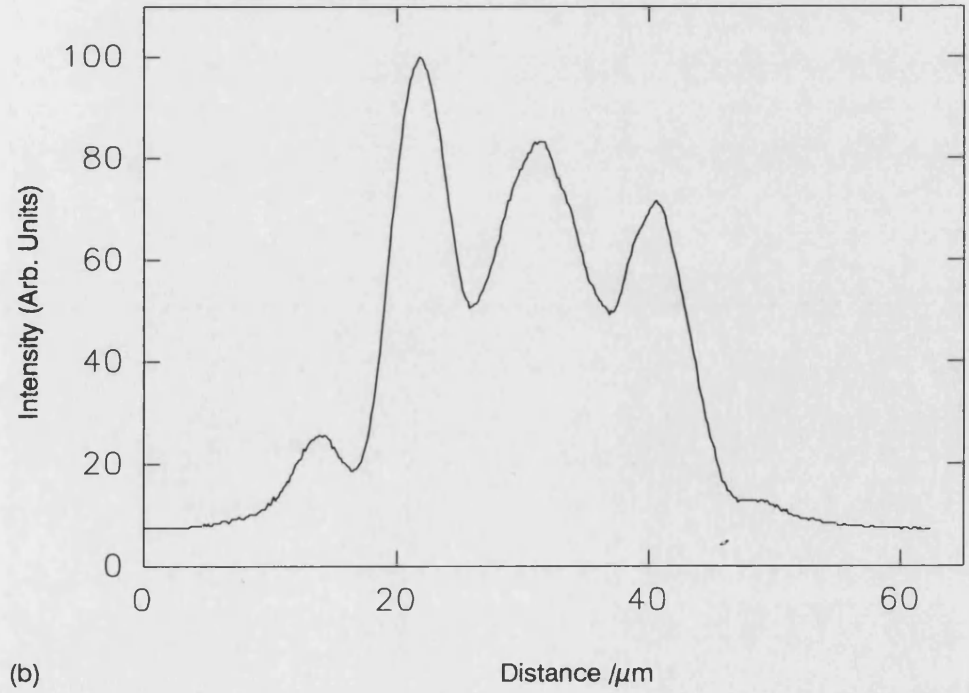

(b)

Figure 5.4. Measured near field intensity profiles at different currents from UB827. 30μm final width, 2mm long, linearly tapered Bow-tie laser.
(a) Dashed curve - profile at 87mA. Solid curve - at 211mA. (b) Profile at 467mA.

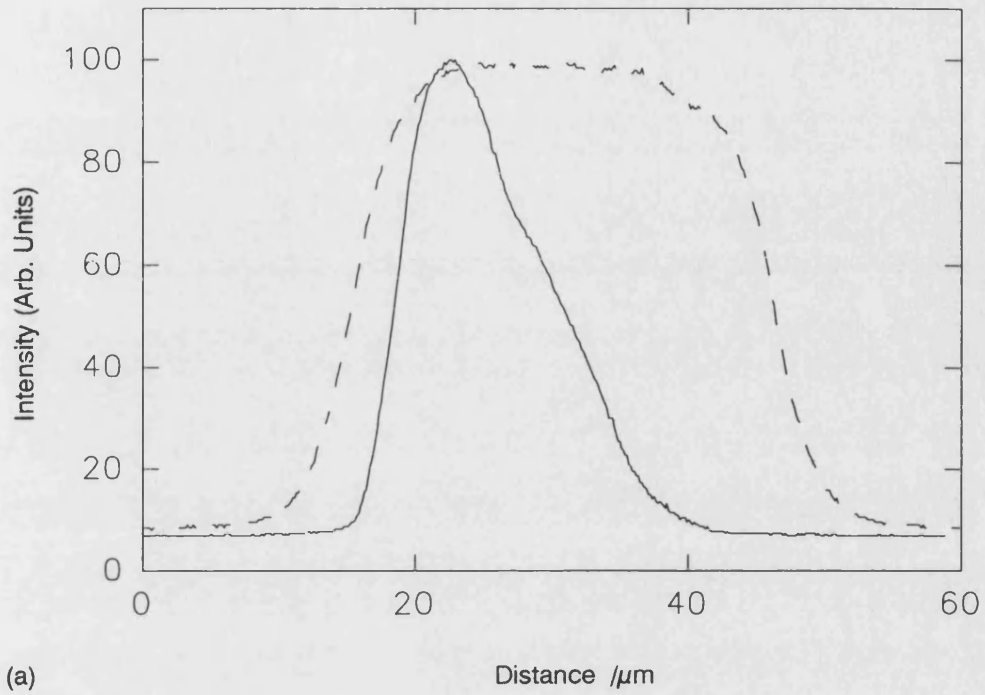

(a)

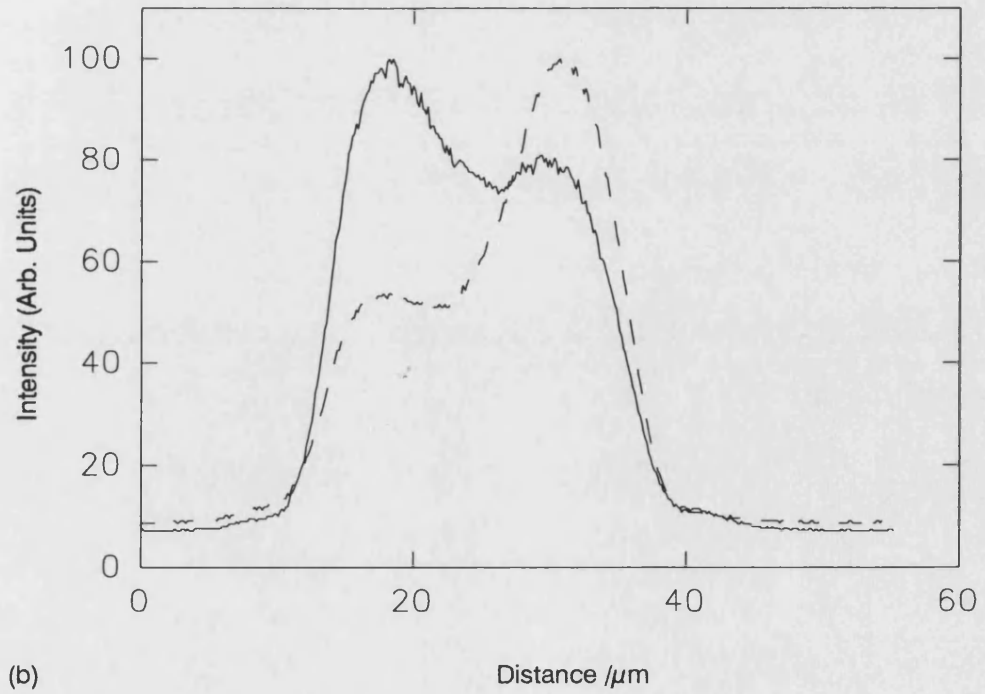

(b)

Figure 5.5. Measured near field intensity profiles at different currents from UB824. 30μm final width, 2mm long, exponentially tapered Bow-tie laser.
(a) Dashed curve - profile at 81mA. Solid curve - at 191mA.
(b) Dashed curve - profile at 294mA. Solid curve - at 450mA.

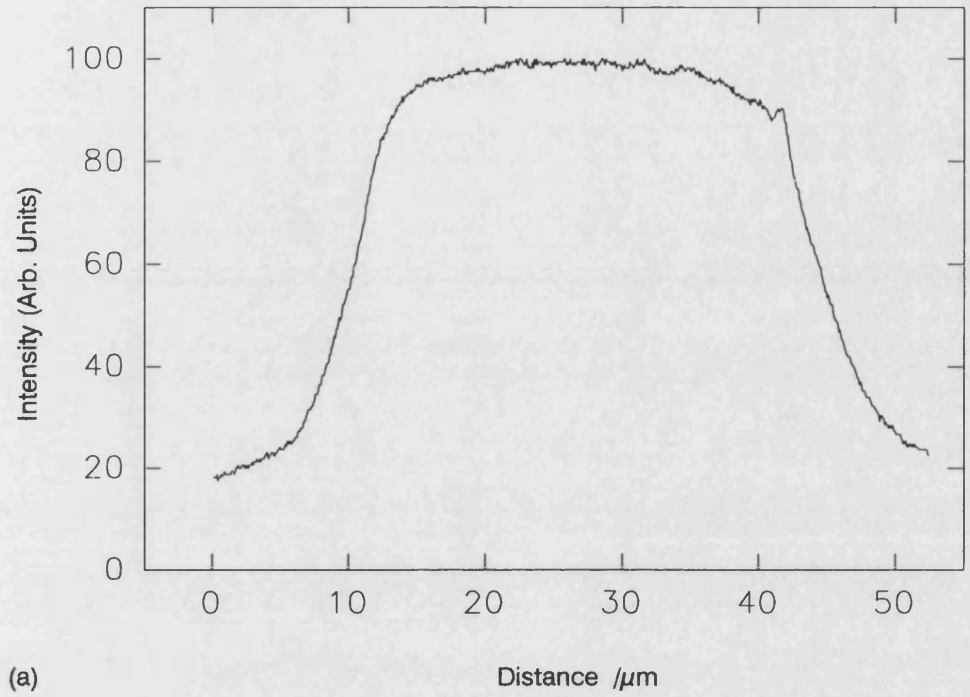

(a)

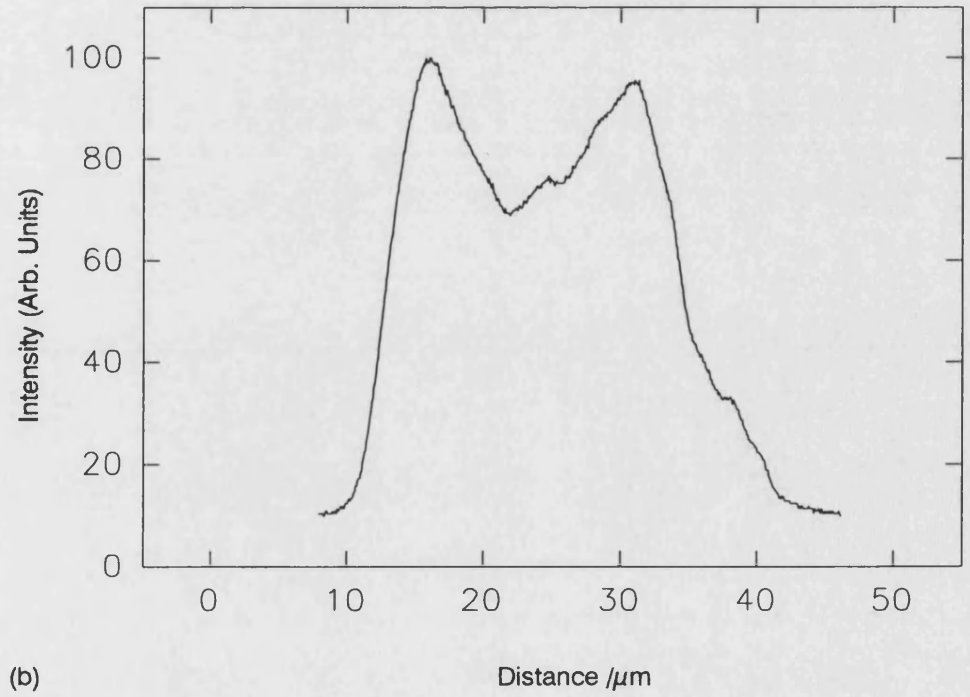

(b)

Figure 5.6. Measured near field intensity profiles at different currents from UB862. 30μm wide, 2mm long, 'straight' rib-waveguide laser. (a) Profile at 40mA. (b) Profile at 150mA.

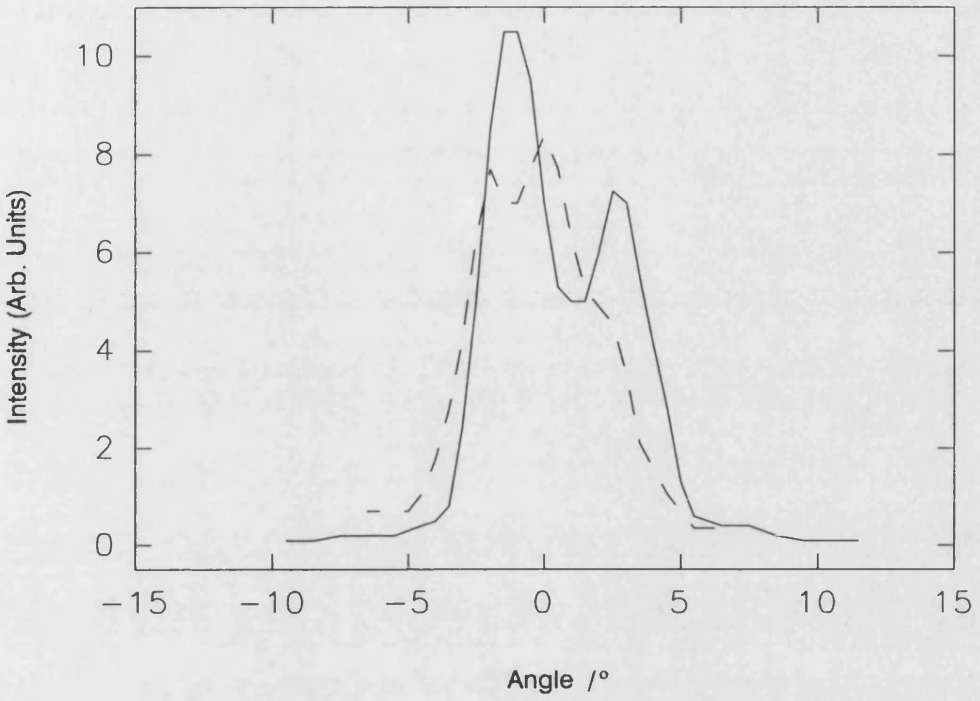

Figure 5.7. Measured far field intensity profiles at different currents from UB836.
30μm final width, 2mm long, parabolically tapered Bow-tie laser.
Dashed curve - profile at 200mA. Solid curve - at 500mA.

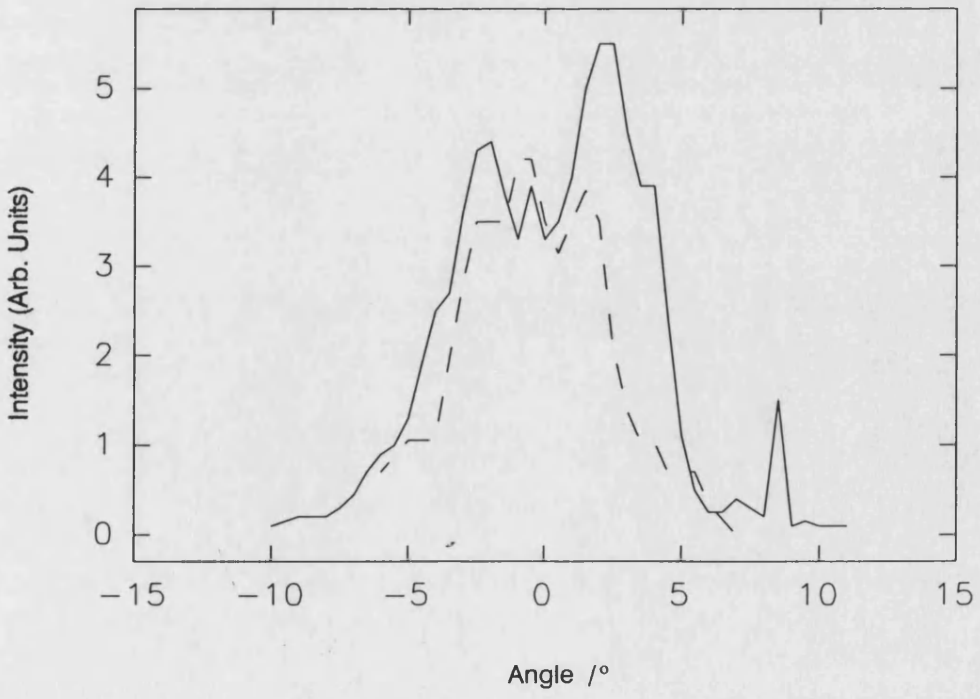

Figure 5.8. Measured far field intensity profiles at different currents from UB827.
30μm final width, 2mm long, linearly tapered Bow-tie laser.
Dashed curve - profile at 200mA. Solid curve - at 500mA.

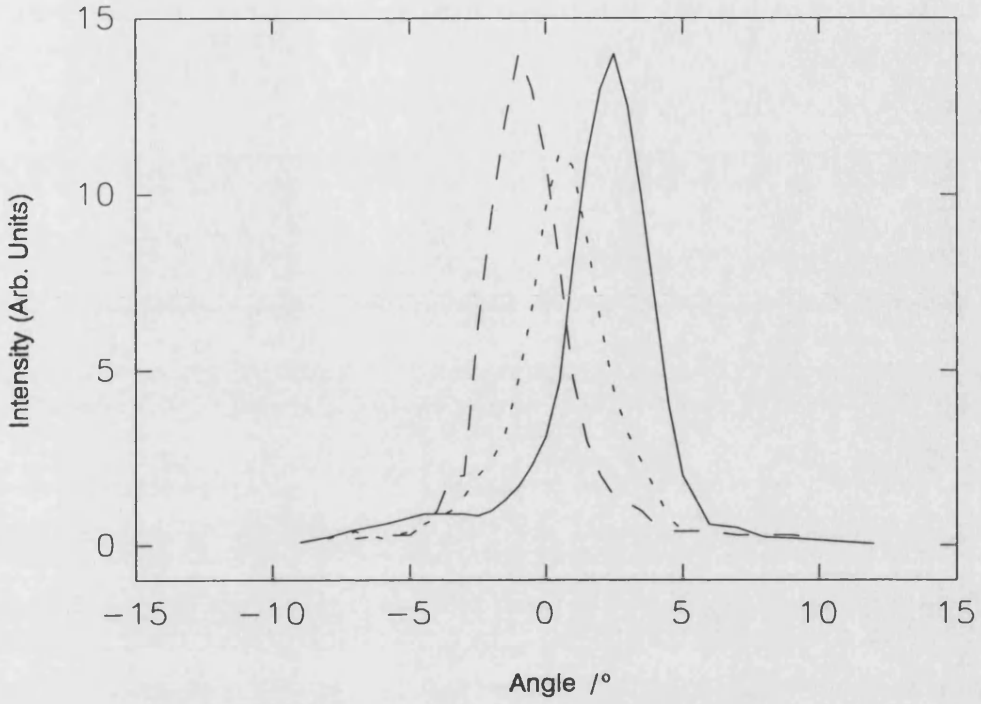

Figure 5.9. Measured far field intensity profiles at different currents from UB824.
30μm final width, 2mm long, exponentially tapered Bow-tie laser.
Dotted Curve - profile at 200mA. Dashed curve - profile at 300mA. Solid curve - at 500mA.

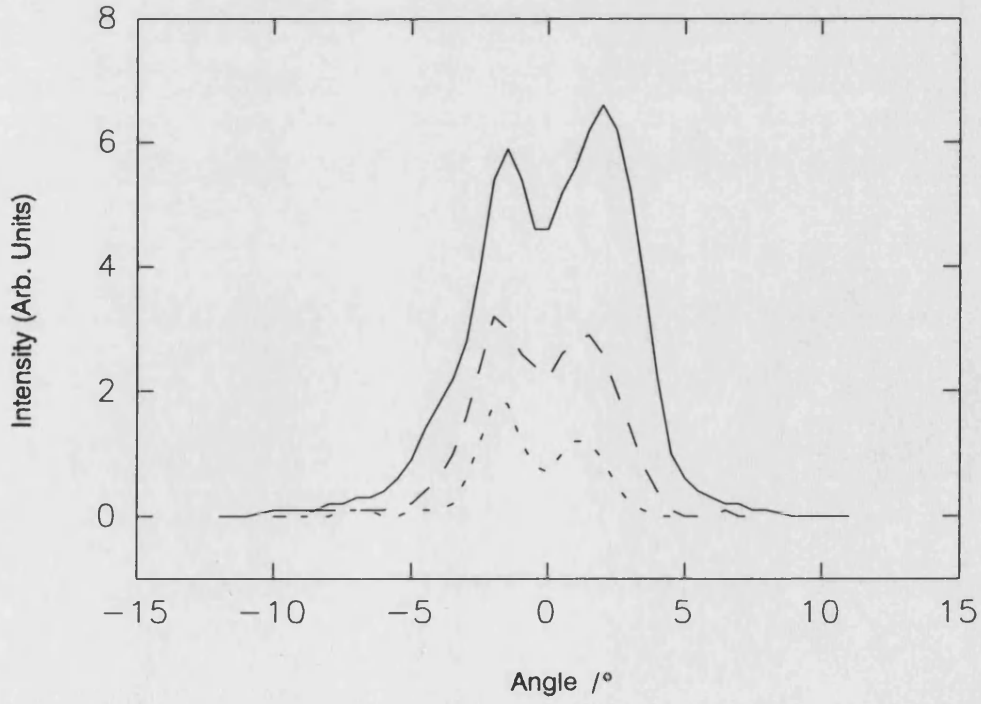

Figure 5.10. Measured far field intensity profiles at different currents from UB862.
30μm wide, 2mm long, 'straight' rib-waveguide laser.
Dashed curve - profile at 200mA. Solid curve - at 500mA.

narrowest of the different devices but show an angular shift of the peak value at each kink in output power with current where the near field intensity profiles also changed.

The output spectra of the tapered lasers all showed highly multimoded operation as expected from devices of this length. Figures 5.11, 5.12, 5.13 and show representative examples of the results that were obtained.

5.1.3 Conclusions

A number of differently shaped bow-tie lasers have been measured and the output characteristics compared with measurements from a broad area rib-waveguide laser. The light output vs current curves showed that the broad area laser had a lower threshold current and higher slope efficiency than any of the tapered devices making it the most efficient device. Of the bow-tie lasers the exponentially tapered device had the lowest threshold current but the parabolically tapered devices had the highest slope efficiency making them the most efficient at higher currents and therefore the most suitable bow-tie lasers for high power operation. Pronounced kinks were also observed in the curve from the exponentially tapered device.

The intensity profiles measured from the devices showed that significant fractions of the power occurred in higher order lateral modes within all of the devices. From the results described in chapter 3 it is expected that this problem can be removed from the tapered devices by adding cavity spoilers. However, this solution is not applicable to the broad area laser and therefore this device will always have poor beam quality. The output intensity profile from the exponentially tapered device has been shown to be subject to beam steering as the injected current increases. This was a further undesirable feature of this device.

In conclusion, linearly and exponentially tapered bow-tie lasers have been shown to be less efficient than parabolically tapered devices of the same external dimensions. Although poor beam quality was observed in all the devices, following the results presented in chapter 3, it is expected that the quality of the output from the parabolically tapered devices can be improved.

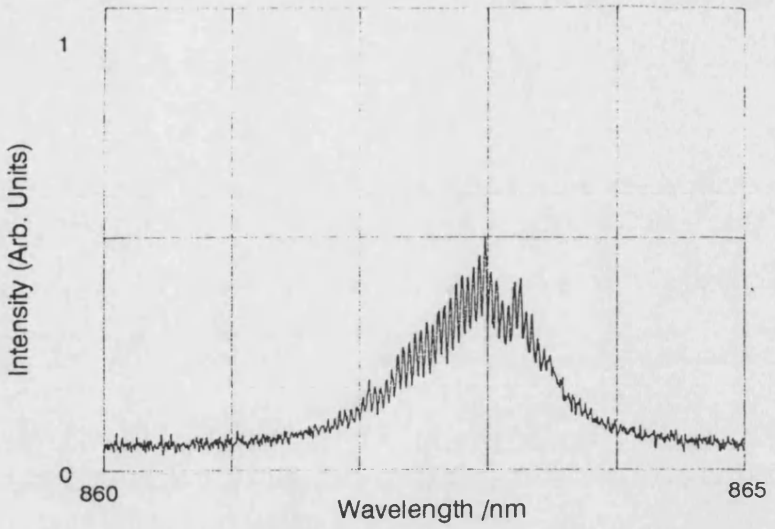

Figure 5.11. Emission spectrum at 200mA from UB836 parabolic Bow-tie laser.

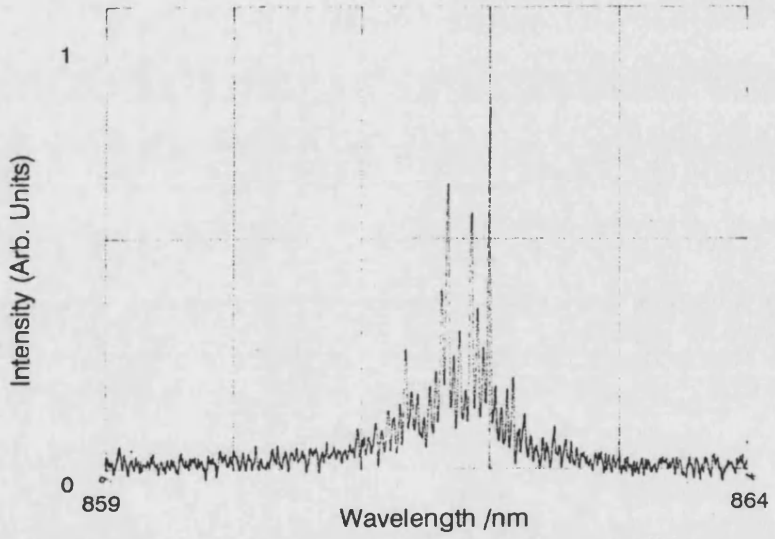

Figure 5.12. Emission spectrum at 200mA from UB827 linear Bow-tie laser.

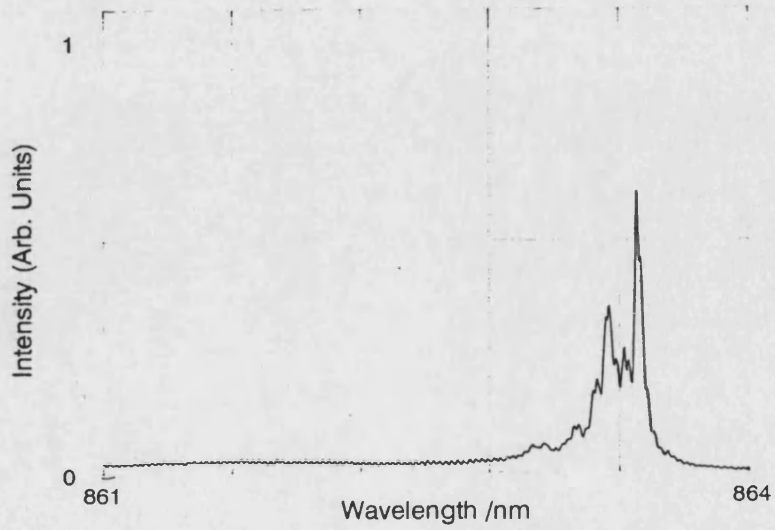

Figure 5.13. Emission spectrum at 200mA from UB824 exponential Bow-tie laser.

5.2 Bow-tie laser Arrays

5.2.1 Introduction

Arrays of tapered or bow-tie lasers have been reported previously for both CW [1] and pulsed operation [2]. Simply by increasing the active region width an uncoupled array of N elements offers the possibility of N times the power of a single element with a far field profile that can be as narrow as the single element case. Alternatively, if the elements can be coupled then the power from each element will be coherent and can be emitted into a much narrower far field intensity profile resulting in an N×N increase in intensity in the far field. 5-element arrays of parabolic and linear bow-tie lasers were fabricated where each element was based on a 2mm long, 30μm maximum width bow-tie laser. The lateral centre-to-centre separation of the elements was 29μm, slightly less than the element width, such that the rib waveguides merged a distance before the facets (see figure 5.14). For the parabolic devices this distance was approximately 60μm and for the linear devices it was 35μm.

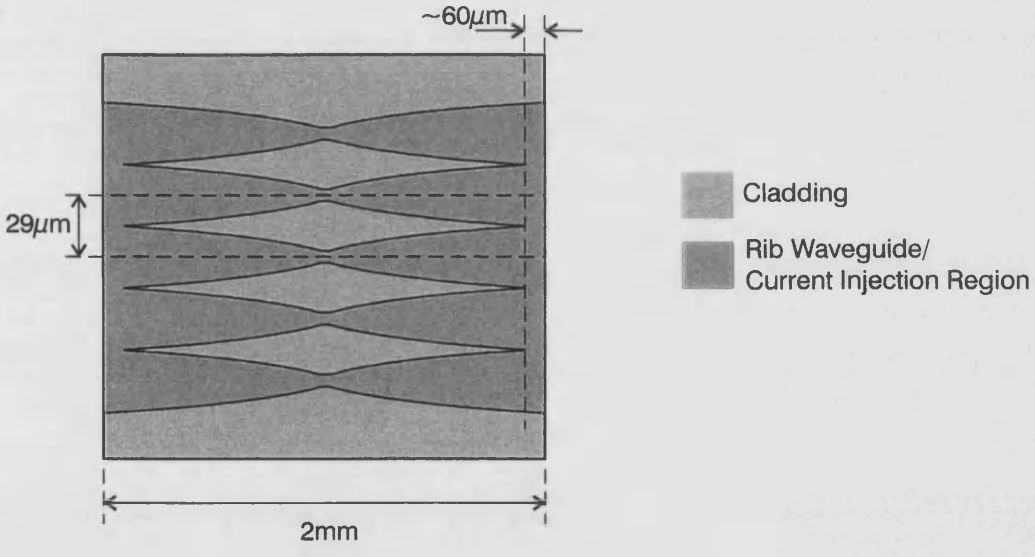

(a)

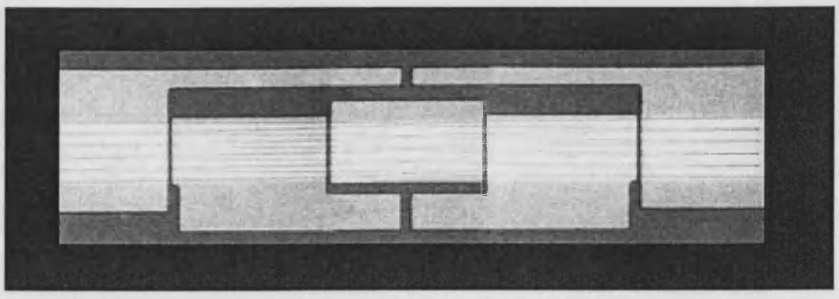

(b)

Figure 5.14. A bow-tie laser array. a. Schematic diagram. b. Photograph

5.2.2 Pulsed Results

Two pairs of devices were mounted p-side down on copper heatsinks. Each pair consisted of one parabolic and one linear bow-tie array. One of these pairs was tested with the facets as cleaved and the other had single-layer Zirconium Oxide/Titanium Oxide AR coatings applied to each facet.

Device	UB848	UB850	UB861P	UB861L
Taper shape	Parabolic	Linear	Parabolic	Linear
Total length	2mm	2mm	2mm	2mm
AR Coated	No	No	Yes	Yes

Table 5.2. Bow-tie array device details

The devices were tested with 1μs pulses at a duty cycle of approximately 1:100. Figures 5.15 and 5.16 show the light output against current curves for the uncoated and coated devices respectively. It can be seen that the uncoated parabolic device had a slightly lower threshold current than the uncoated linear device but the slope efficiences were similar for devices of different shapes with the same reflectivities. In fact, at high currents the linear devices emitted more power than the corresponding parabolic devices. Peak output powers of greater than 1.5W were achieved from all devices. However, the coated devices reached this power at around 4.5A whereas the uncoated devices took currents of greater 5.5A before this power was reached. 1.85W peak power was emitted from a single facet of the AR coated linearly tapered array at 5 Amps without failure. The slope efficiencies for the uncoated devices were both approximately 0.3W/A. For the coated devices the values were 0.44W/A and 0.4 W/A for UB861L and UB861P respectively. This represents an increase of more than 33%.

Figures 5.17 and 5.18 show the near field intensity profiles of the uncoated arrays UB848 and UB850 respectively. Five distinct peaks corresponding to the individual elements of the array were seen in the profiles measured at currents above the thresholds of the devices. The relative intensities of these peaks varied with current, and also, the peaks had multi-lobed fine structures which further varied.

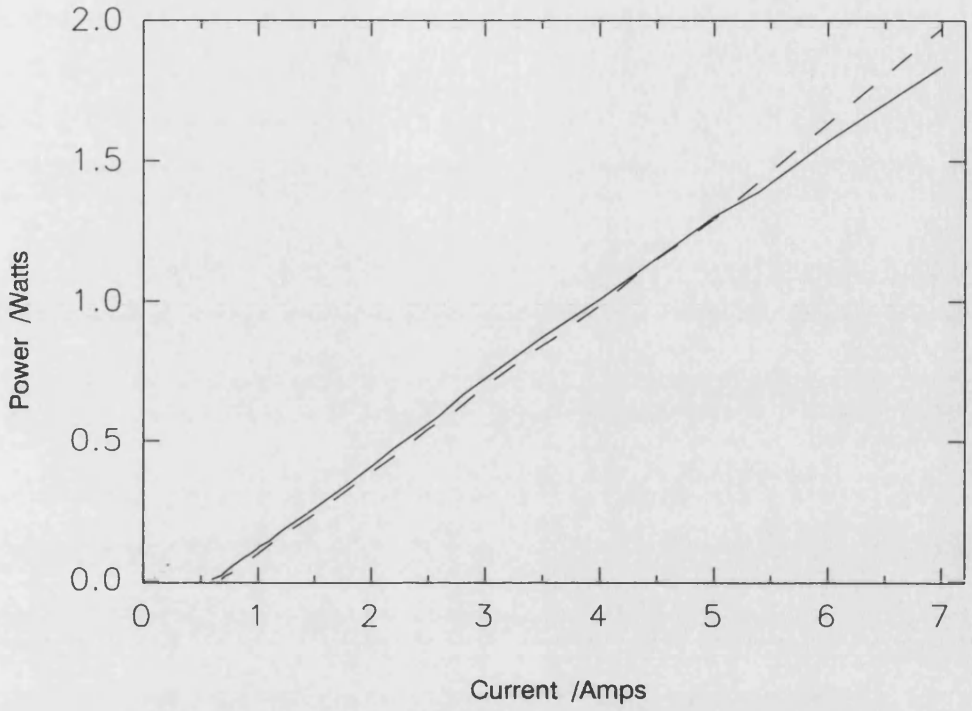

Figure 5.15. Measured output power vs. current curves from 2mm long, 5-element, bow-tie laser arrays with uncoated facets. 1μs current pulses, duty cycle 1:100. Solid curve - UB848 - parabolically tapered elements. Dashed curve - UB850 - linearly tapered elements.

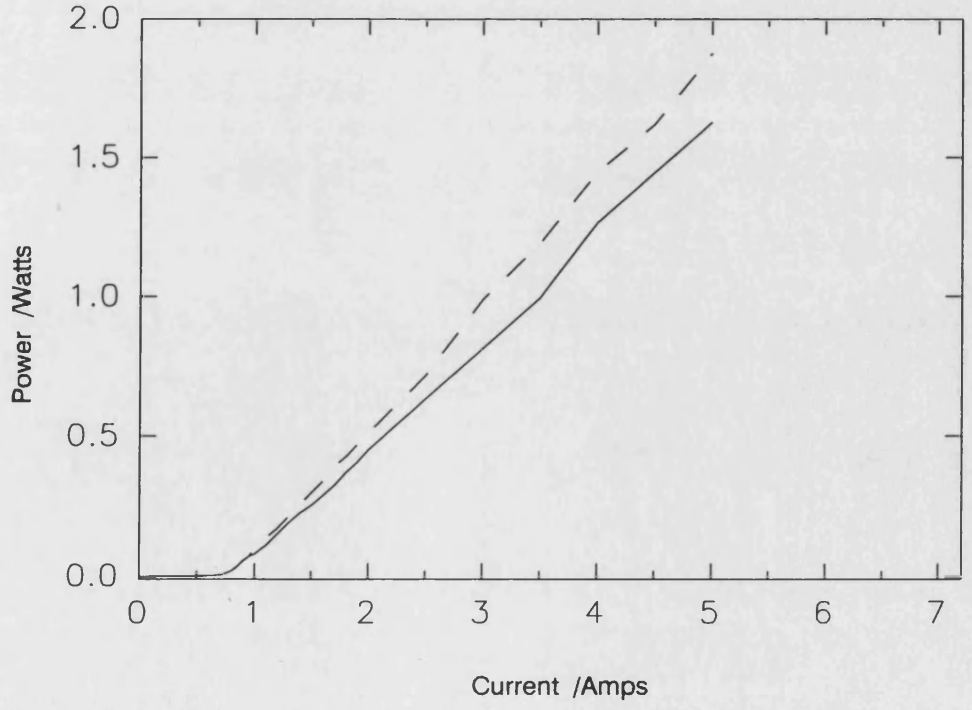

Figure 5.16. Measured output power vs. current curves from 2mm long, 5-element, bow-tie laser arrays with AR coated facets. 1μs current pulses, duty cycle 1:100. Solid curve - UB861P - parabolically tapered elements. Dashed curve - UB861L - linearly tapered elements.

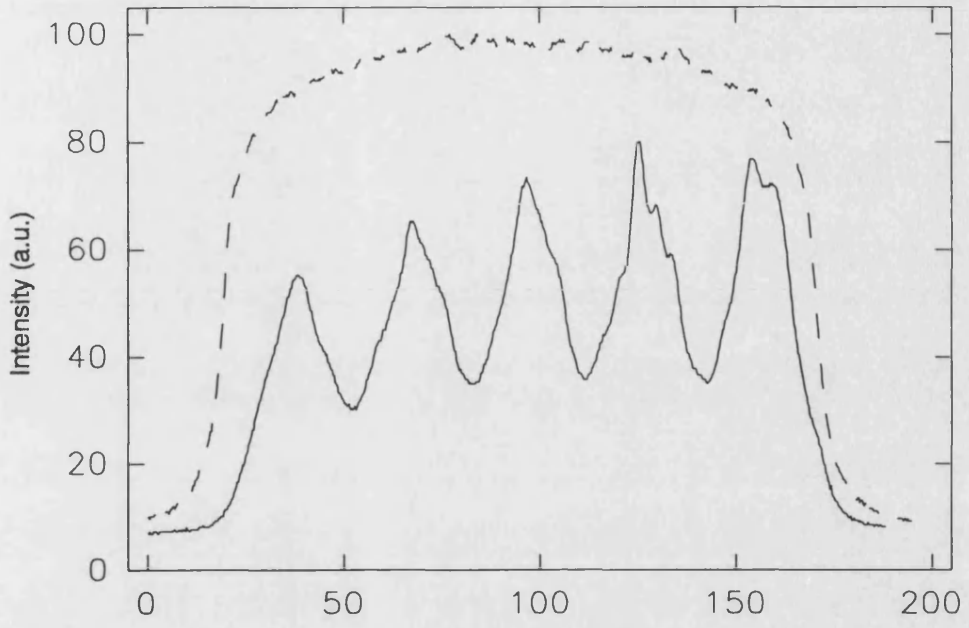

(a)

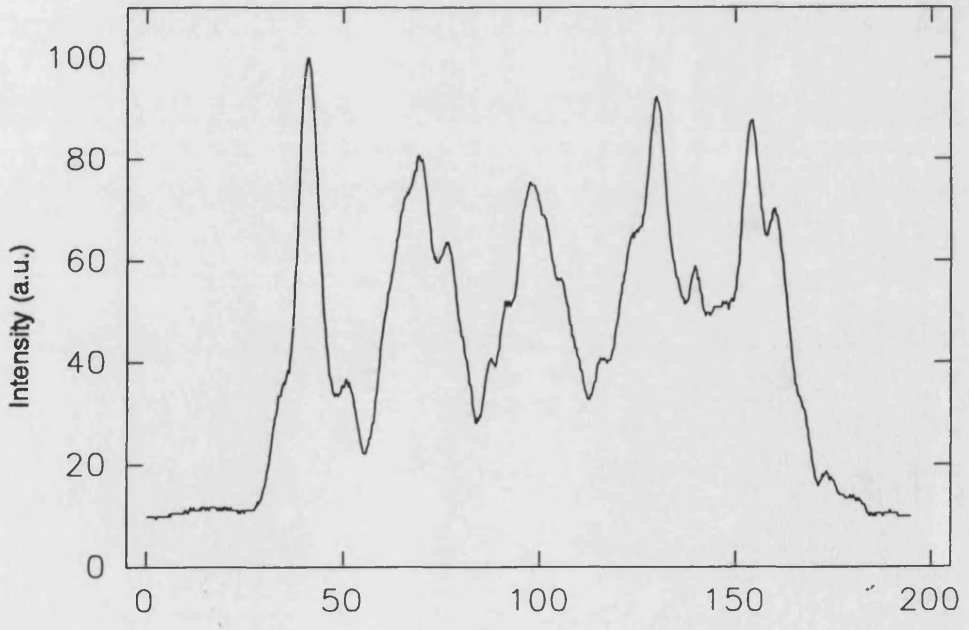

(b)

Figure 5.17. Near field intensity profiles from UB848 Parabolic Bow-tie laser array. The device was 2mm long with 5 elements and uncoated facets.
(a) Dashed curve - Profile at 100mA (below threshold). Solid curve - 560mA.
(b) Profile at 2 Amps.

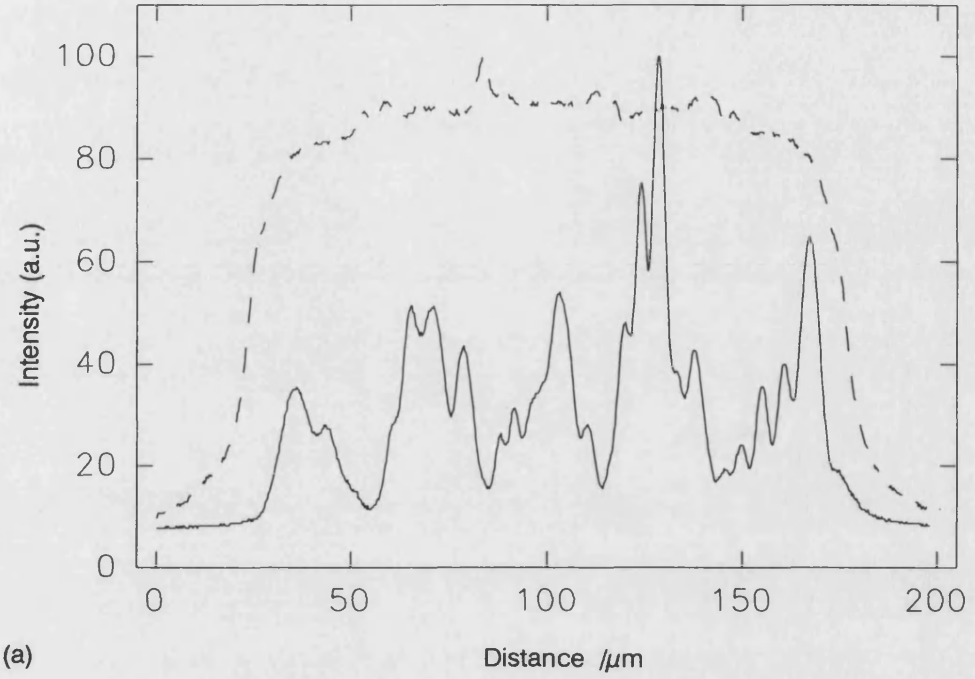

(a)

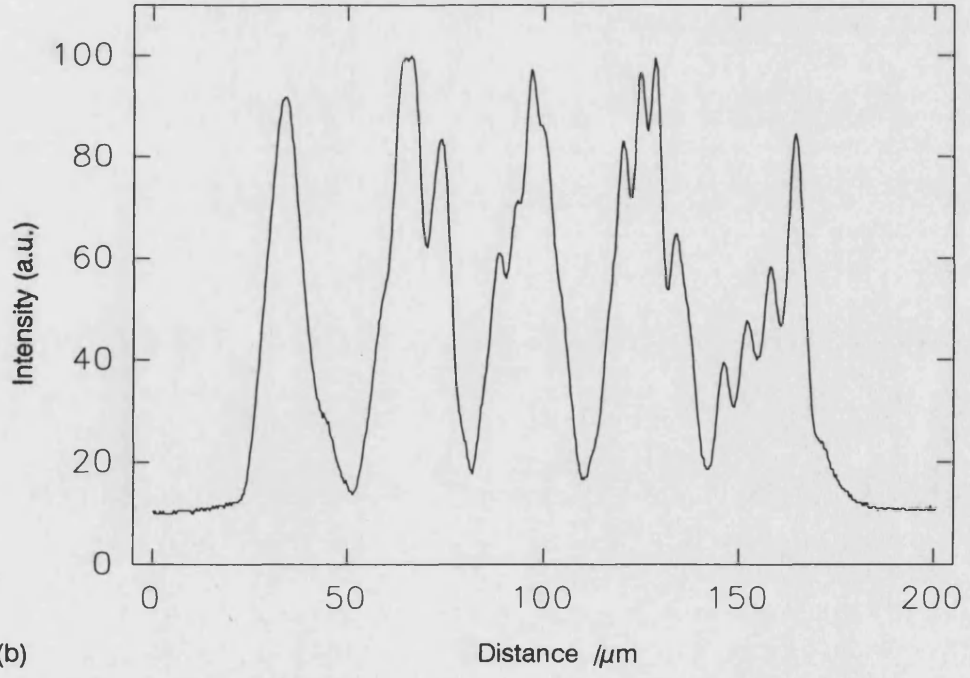

(b)

Figure 5.18. Near field intensity profiles from UB850 linear Bow-tie laser array.
The device was 2mm long with 5 elements and uncoated facets.
(a) Dashed curve - Profile at 200mA (below threshold). Solid curve - 680mA.
(b) Profile at 1 Amp.

The far field intensity profiles gave further information about the operation of the devices. Figures 5.19 and 5.20 show the profiles from the parabolically and linearly tapered laser arrays respectively. From figure 5.19 one can see that UB848 had a very narrow central peak with FWHM < 1°. This was narrower than the diffraction limited profile for a single element (~2°) and therefore implied that there was some coupling between the elements of the array. There were three broad peaks visible in the profile which were separated by ~6°. These peaks were a result of the ~8μm period modulation which was seen in the near field intensity profile (figure 5.17).

The far field intensity profile of device UB850 can be seen to be very broad with a large number of peaks showing that this device had very poor beam quality.

The spectral variation of the output of UB848 is shown in figure 5.21 for reference. The spectrum was very broad but does appear to show resolvable longitudinal modes. It was not possible to say if these were longitudinal modes of a coupled array or the modes of an individual element whose output was more efficiently coupled into the measuring apparatus. Therefore one can draw no further conclusions on the operation of the device from this result.

5.2.3 CW Results

A number of these devices were sent to MBI-Berlin for CW testing. A CW power of 600mW was achieved from a single facet of a parabolically tapered device. This is the highest CW power measured in this work. It should be noted that these devices had uncoated facets and therefore improvements in this figure should be easily realisable.

5.2.4 Conclusions

Bow-tie laser arrays have been measured and shown to emit high powers both CW (600mW) and under pulsed conditions (>1.8W peak). A 33% improvement in the slope efficiency of the devices was shown to be possible by applying single layer AR coatings to both facets. Some evidence of coupling has been seen in the far field intensity profile of a parabolically tapered bow-tie laser array. The central lobe of the profile had a FWHM of < 1° which was approximately 50% of the diffraction limit for a single element. However, significant lobes were measured at ± 5° and therefore the overall profile was no better than those described in chapter 3.

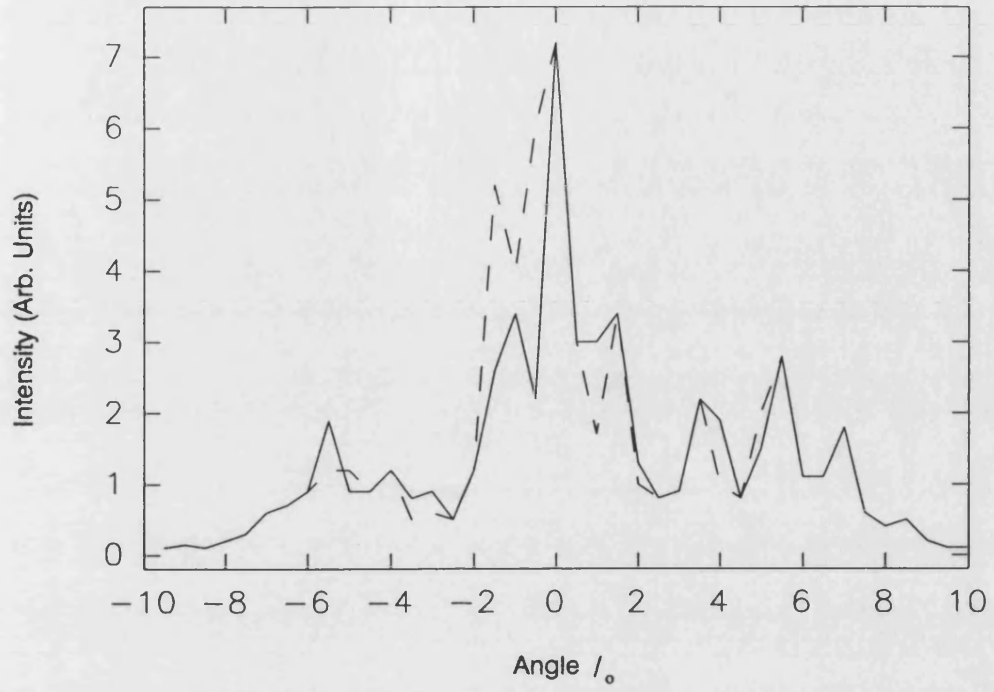

Figure 5.19. Measured far field intensity profiles at different currents from UB848. 2mm long, 5 element parabolic Bow-tie laser array. Dashed curve - profile at 700mA. Solid curve - at 800mA.

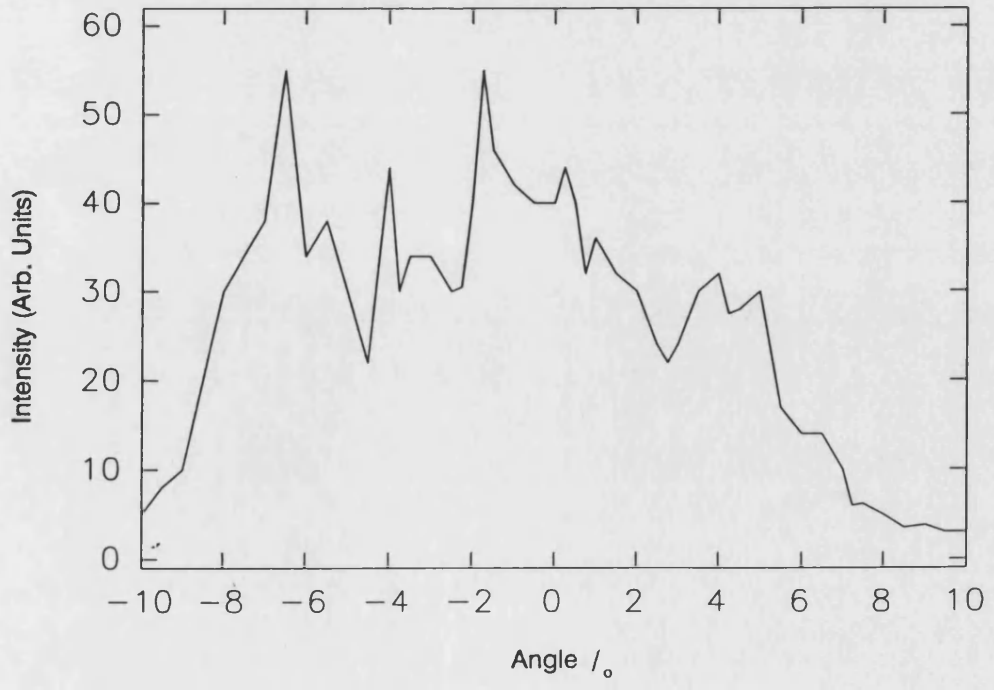

Figure 5.20. Measured far field intensity profile at 800mA from UB850. 2mm long, 5 element linear Bow-tie laser array.

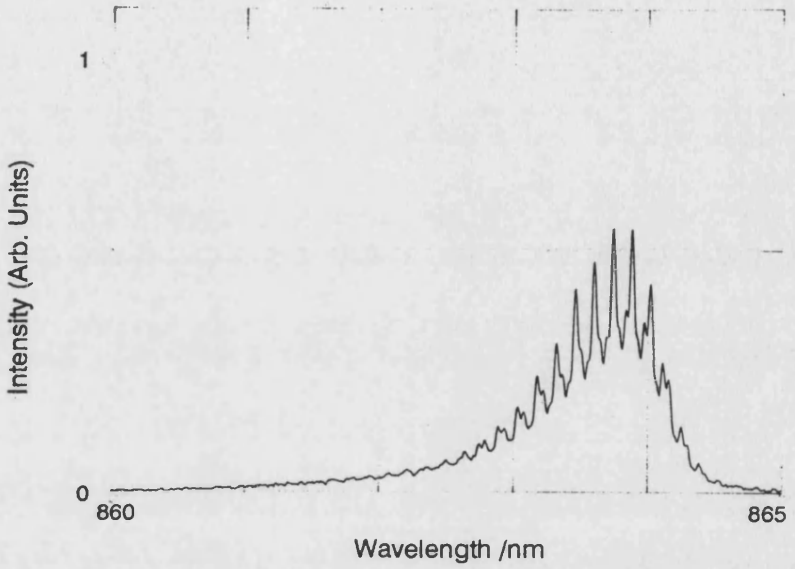

Figure 5.21.a. Emission spectrum at 800mA from UB848 parabolic Bow-tie laser array.

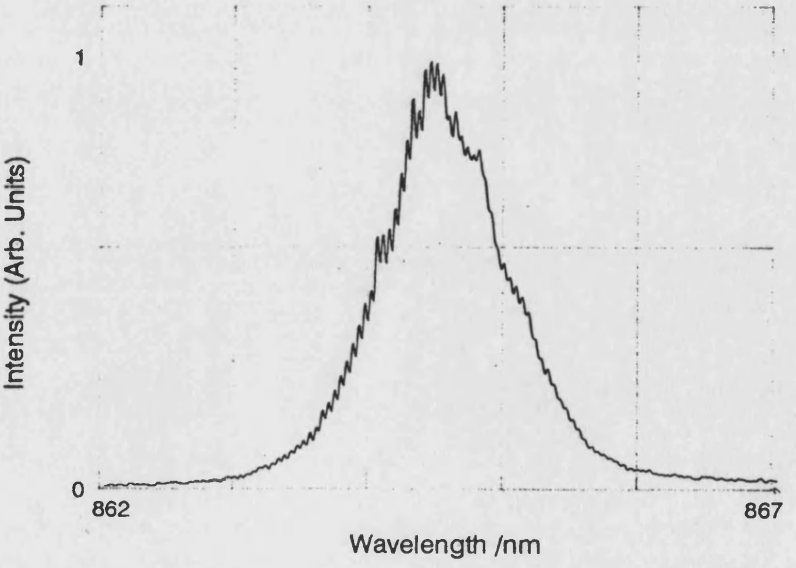

Figure 5.21.b. Emission spectrum at 800mA from UB850 linear Bow-tie laser array.

5.3 Collaboration with University of Michigan.

5.3.1 Introduction

A number of methods have been reported for producing different emission wavelengths from different areas of a single wafer of material. This is a useful achievement since it allows the production of two (or more) lasers operating at different wavelengths on the same chip. Another possibility is that one can have a region of the wafer that is non-absorbing, or 'passive', for the wavelength of light emitted from an adjacent region. This makes possible the integration onto a single chip of active and passive optical components. It was thought that 'passive' regions could also be useful in Bow-tie lasers since very high power densities can occur at the centre of a bow-tie laser which result in more significant effects from nonlinearities. If the centre is non-absorbing then it may not be necessary to pump this region and by removing the carriers the most important nonlinear effect is removed also. Alternatively, the region can remain pumped but since it is not absorbing at the lasing wavelength then the lateral carrier density profile will remain largely unaffected by the high optical power density and hence the key nonlinear effect is still removed.

A process has been developed for InGaAs QW active layer material at the University of Michigan in the USA that involves epitaxial growth on a patterned substrate [3]. Narrow regions (<15μm wide) of material that have an decrease ('blue-shift') in emission wavelength with respect to the rest of the wafer can be easily produced. The procedure requires only one growth step and no post growth processing which makes it very simple. Wavelength shifts are caused by variations in the Indium concentration of the quantum well over the area of the wafer. Trenches with vertical sidewalls are etched in the substrate before growth using reactive ion etching. These trenches act as migration centres for the Indium and Gallium ions during active layer growth and since Indium has a longer migration distance an increased concentration of Indium occurs at the sidewalls leaving the surrrounding area depleted and therefore shifted to a larger band gap. If a large enough band gap shift can be achieved then 'passive' regions may be formed.

The InGaAs QW material is of added value in this work since the emission wavelength is in the region of 980nm which is the most important optical pumping wavelength for Erbium Doped Fibre Amplifiers. For this reason there is a great deal of interest in high power InGaAs lasers.

5.3.2 The material

A pattern was drawn in order that a sample of material could be grown in Michigan with a variety of different lengths of wavelength-shifted region. These areas were defined by pairs of parallel trenches (figure 5.22). The width of each trench was 5μm and the separation between the trenches was 20μm centre to centre. Changing the separation between the trenches affects the total shift in wavelength achieved. However, in this case the dimension was fixed by colleagues in Michigan. The length of the pair of trenches defined the length of shifted region. A corresponding photolithographic mask was also designed and made so that a number of bow-tie and narrow ridge-waveguide lasers could be fabricated from the material.

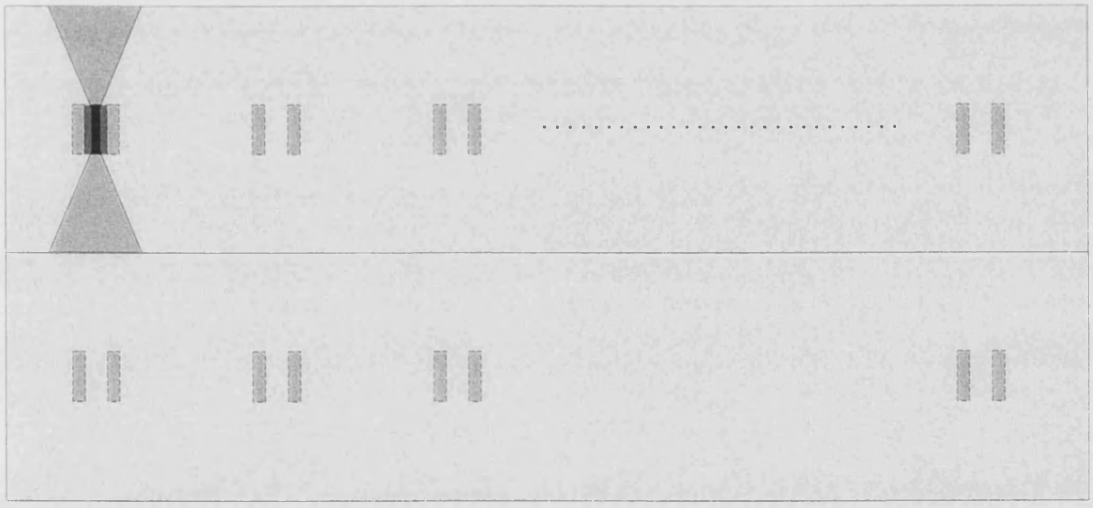

Figure 5.22. Schematic of pairs of trenches etched into substrate and also showing relative position of bow-tie laser.

The first sample of material proved to be unusable due to a leak in the growth chamber. A number of lasers were fabricated from it but none emitted any light. A new sample of material (V3359) was obtained and a single batch of lasers was fabricated from this. The layer structure of the material and the calculated effective indices for different etch depths are given in appendix 5.

5.3.3 Results from Narrow Rib Lasers

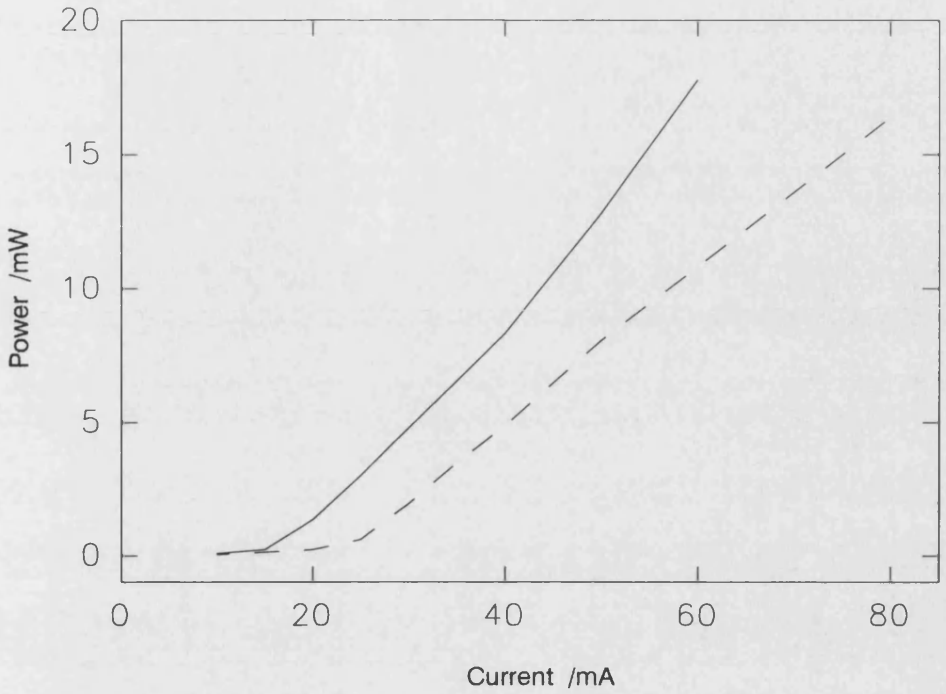

Figure 5.23. Measured output power vs. current curves from 300μm long, 3μm wide rib-waveguide lasers fabricated from Michigan InGaAs material. 0.1μs current pulses and a 1:1000 duty cycle were used. Solid curve - UB833 - homogenous material. Dashed curve - UB832 - 'wavelength-shifted' material.

The first devices to be measured were 3μm wide ridge waveguide lasers. UB833 was made from an unshifted part of the wafer. UB832 was made from a length of material that should all have been wavelength-shifted. The output power variation with current for the devices is shown in figure 5.23. One can see that the device made from the shifted material had a higher threshold and lower slope efficiency indicating that this region of the material had higher loss than the homogenous material. Figure 5.24. shows the emission spectra for UB833 at 30mA, approximately 2 times the threshold current. Figure 5.25. shows the emission spectra for UB832 at 40mA, which was approximately 2 times the threshold current for this device. The peaks were both at approximately 980nm due to the InGaAs quantum well. It can be seen that there was definitely no large difference in peak wavelength between the two devices. Therefore it was not expected that the bow-tie lasers made in the same batch had non-absorbing centre regions. However, only a small section of the wafer was used and it may still be possible that another area of wafer does contain regions with a large shift in emission wavelength. This has still to be investigated.

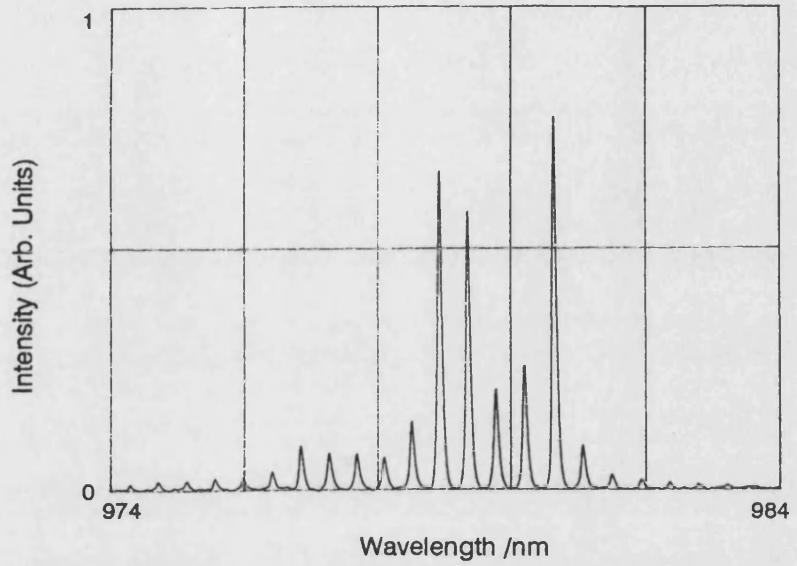

Figure 5.24. Emission spectrum at 30mA from UB833, 3×300μm rib waveguide laser fabricated from homogenous Michigan material.

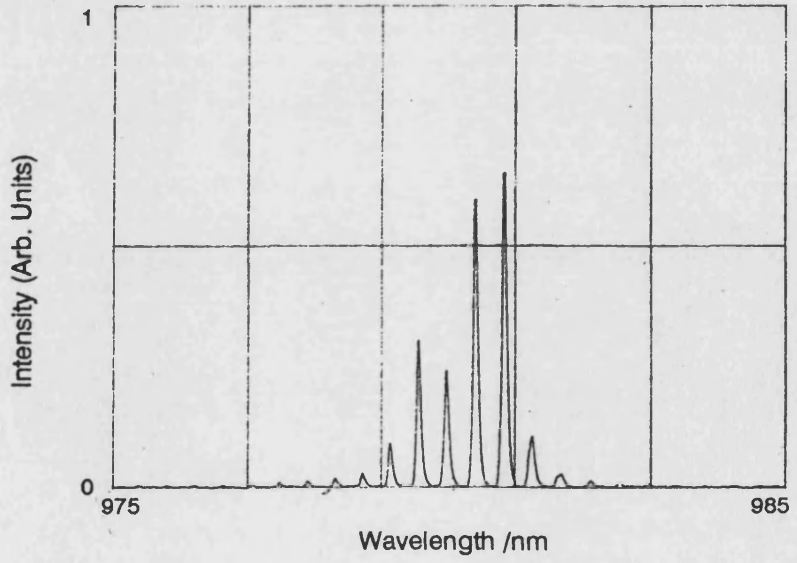

Figure 5.25. Emission spectrum at 40mA from UB832, 3×300μm rib waveguide laser fabricated from 'wavelength-shifted' Michigan material.

5.3.4 Results from Bow-tie Lasers

A number of bow-tie lasers were also made from the material. Although it was assumed that no significant wavelength shift was present in any of the devices the results were still of interest. The output characteristics from two pairs of these devices are presented now. The first pair, UB829Y and UB829B were 2mm long, linearly tapered bow-tie lasers with 100μm long, 3μm wide centre regions tapering to 140μm wide at the facets. The second pair, UB891B and UB891W were also 2mm long, linearly tapered bow-tie lasers but with 50μm long, 3μm wide centre regions and tapered to 90μm wide at the facets. The etch depth achieved was 0.85μm which should have given an index step of approximately 0.01. No cavity spoiling deflectors were etched into the devices. The difference between the two devices of each pair was that one was made with wavelength-shifted material at the centre (UB829B and UB891W). Therefore these lasers had 100μm long trenches in the substrate to the sides of the rib along the straight centre region and the beginnings of the tapered regions (figure 5.26). This region was still electrically pumped in these devices.

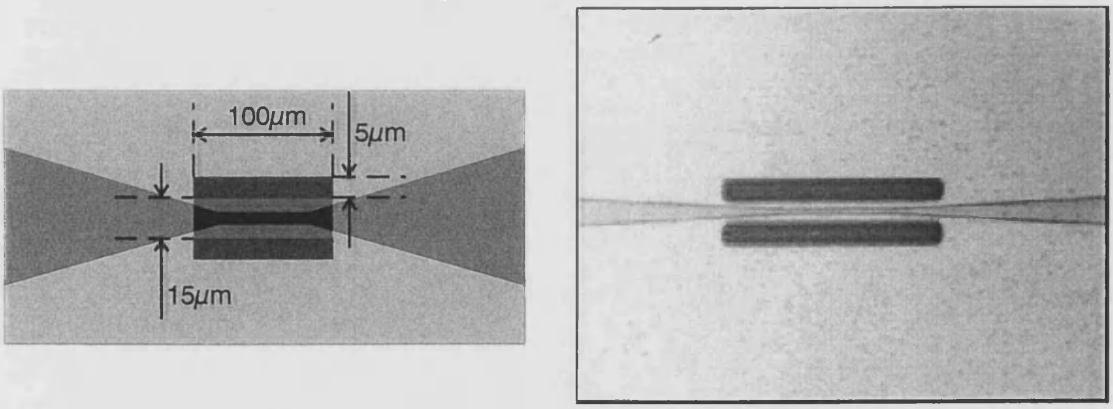

(a) (b)

Figure 5.26. Bow-tie laser fabricated with pair of trenches etched into substrate to the sides of the centre. (a) Schematic of device. (b) Photograph of the centre of an actual device.

Figures 5.27.a. and 5.27.b. show the output power against current variation for the two pairs of lasers measured at low currents (<500mA) using 3μs pulses at a duty cycle of about 1:30. The long pulse width was used because the output level from all of the lasers increased slowly until reaching a maximum after more than 1μs. The exact time taken to reach maximum output varied, reducing gradually as the current increased.

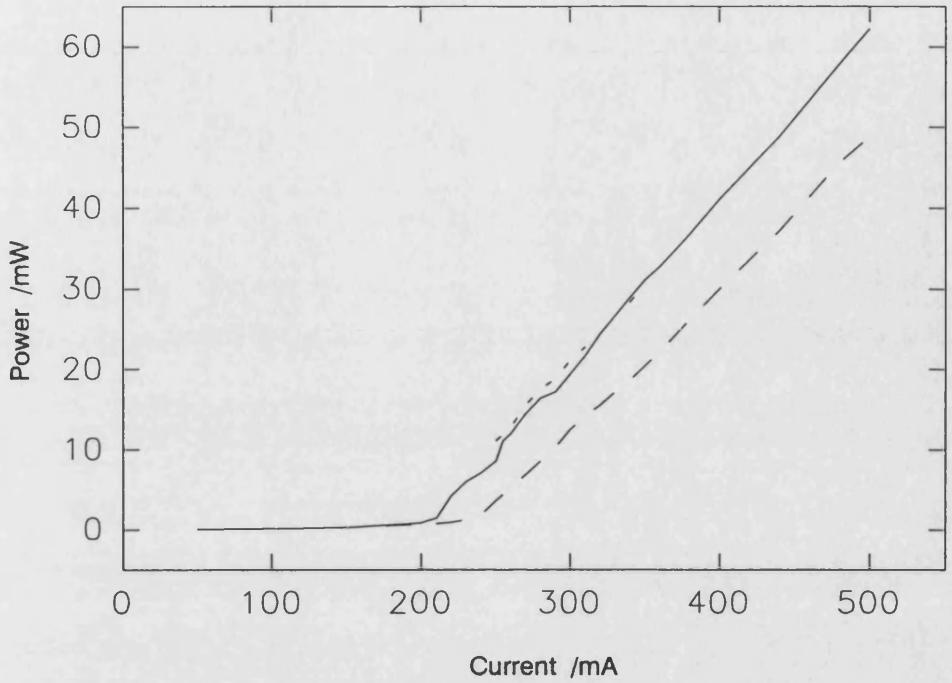

Figure 5.27.a. Measured output power vs. current curves from 2mm long Bow-tie lasers fabricated from Michigan InGaAs material. 3μs current pulses and a 1:300 duty cycle were used. Dashed curve - Output from UB829B - 'wavelength-shifted' material at centre of device. Solid curve - Dominant output level from UB829Y - homogenous material. Dotted curve - Secondary output level from UB829Y where temporal oscillations were observed.

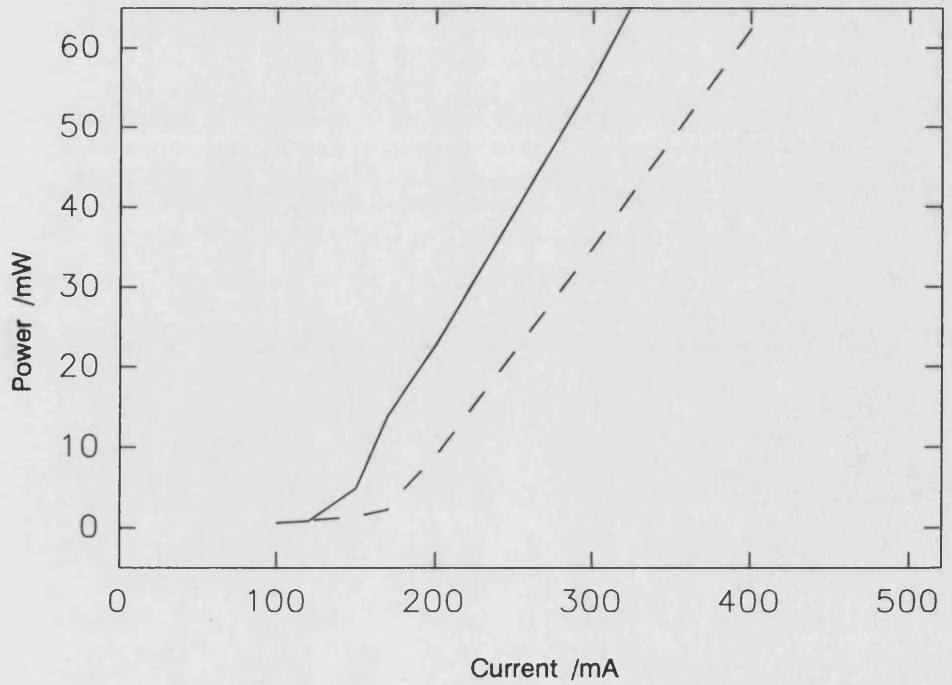

Figure 5.27.b. Measured output power vs. current curves from 2mm long Bow-tie lasers fabricated from Michigan InGaAs material. 3μs current pulses and a 1:300 duty cycle were used. Dashed curve - Output power from UB891W - 'wavelength-shifted' material at centre of device. Solid curve - Output power from UB891B - homogenous material.

The devices with the trenches beside the centre had higher threshold currents and slightly lower slope efficiencies than the corresponding devices without trenches. This was expected since the narrow rib devices (UB833 and UB832) showed that the shifted material had higher losses. However, the interesting feature of these measurements was in the time dependent nature of the light output. Considering first the wider pair of lasers, device UB829Y had a time dependent component to its output signal appearing to oscillate between two output levels for a range of currents. The period of this oscillation varied from ~1.5μs at 255mA to <100ns at 280mA. The secondary output level is shown as the dotted curve in figure 5.27.a. Device UB829B with trenches to the sides of the centre showed no evidence of similar temporal oscillations in its output. This would lead one to speculate that the oscillations were caused by some effect that occurred in the centre of the device and was prevented by the trenches in laser UB829B. However, the measurements from the second pair of lasers did not confirm this. Device UB891W, which had trenches to the sides of the centre, had an oscillating output over a range of currents with a period again of the order of ~100ns at 300mA.

From the relatively slow timescale it was concluded that this was a thermal effect. Following the work of Buda et al. [4] it was thought most likely that switching occurred as thermal variations altered the lateral index profile of the waveguide thereby changing the lateral mode. The gradual increase in output power during the first 1μs of the pulse confirmed the hypothesis that thermal effects on refractive index were important in determining the operating mode of the devices. However, from these measurements alone it was not possible to state in more detail the precise nature of the oscillations.

Further information was gained from near field intensity profile and beam waist measurements on the devices. Figure 5.28 shows the time averaged near field intensity profiles from UB829B and UB829Y. The device with trenches had a wider profile than the other device showing that the beam was diverging more inside this device. Also, the profile did not narrow significantly as the current increased unlike the second device. However, multiple narrow peaks did become more prominent in the profile at higher currents demonstrating that the beam quality was deteriorating either due to filamentation or the excitement of higher order modes.

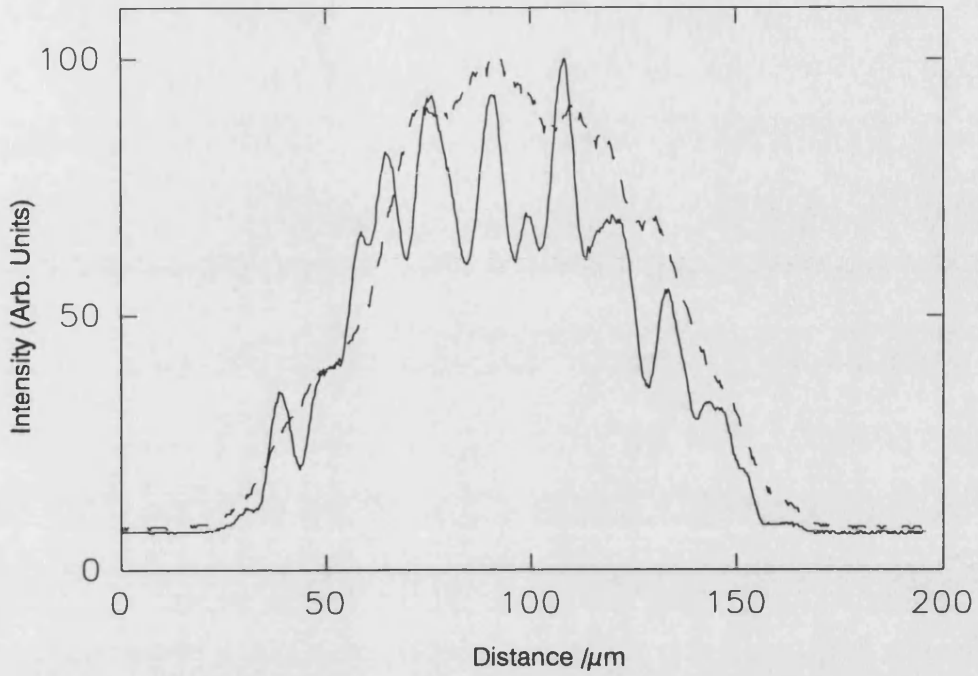

Figure 5.28.a. Near field intensity profiles at different currents from UB829B Linear Bow-tie laser. The device was 2mm long, tapering from 3-120μm in width and had 100μm long trenches to the side of the narrow centre region. Dashed curve - 230mA. Solid curve - 1A.

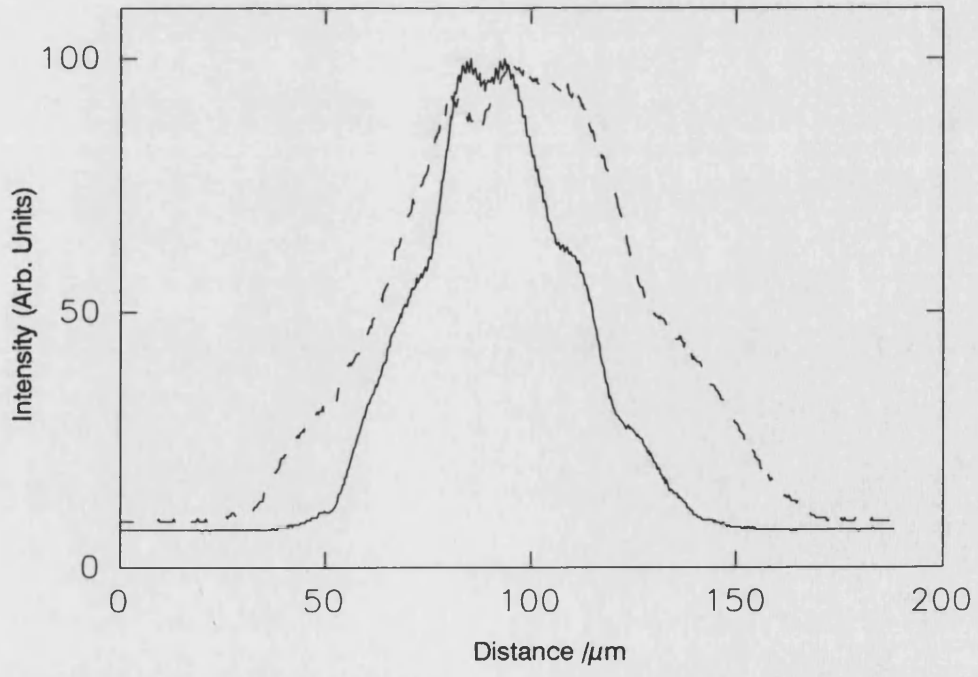

Figure 5.28.b. Near field intensity profiles at different currents from UB829Y Linear Bow-tie laser. The device was 2mm long, tapering from 3-120μm in width.
Dashed curve - 200mA . Solid curve - 640mA.

Figure 5.29 shows the measured intensity profiles at the beam waist for the two devices. A clear difference can again be seen. As desired from a large linearly tapered device the output from UB829B had a narrow beam waist of 4μm FWHM. However, device UB829Y was not operating in the same manner. This was almost certainly due to the lack of cavity spoiling elements in this device. The trenches in the substrate at the centre of device UB829B were evidently acting as spoilers in this device and were spatially filtering the field. Multiple side lobes were seen in the profile measured from UB829B which were a result of the multiple peaked nature of the near field intensity profile.

Similar behaviour was seen from the second pair of devices. Figure 5.30 shows the time averaged near field intensity profiles for these two devices at a number of currents. The FWHM of the near field intensity profile of the device with the trenches (UB891W) was >70μm. Again this was wider than the profile from the second device (<60μm). Also, multiple narrow (~20μm wide) peaks were seen to become more prominent in the profile from device UB891W as the current increased.

Figure 5.31 shows the time averaged intensity profiles at the beam waist for the pair of devices at several currents. Device UB891B had a large (FWHM>9μm) and poorly defined beam waist at currents above the threshold current. When making the above-threshold measurements on this device it was found that there was no clearly defined focal plane in which the output could be focussed to its narrowest width. Instead the width of the intensity profile varied slowly as the laser-lens distance was altered. The output from the device with trenches beside its centre (UB891W) had a narrow beam waist of <4μm FWHM at all currents. However, the different curves in figure 5.31.a show how the quality of this beam did deteriorate as the current was increased. The additional peaks which were seen to the sides of the main peak became more significant as the current was increased.

Far field intensity profiles of devices UB891W and UB891B were measured and are shown in figure 5.32. Figure 5.32.a shows the intensity distribution from UB891W at a number of current values. The profile had a relatively narrow central lobe with FWHM 3.5° at 1Amp. The intensity profiles from UB891B are shown in figure 5.32.b and had a FWHM of 4° at 1Amp. These were not the results that one might have desired although

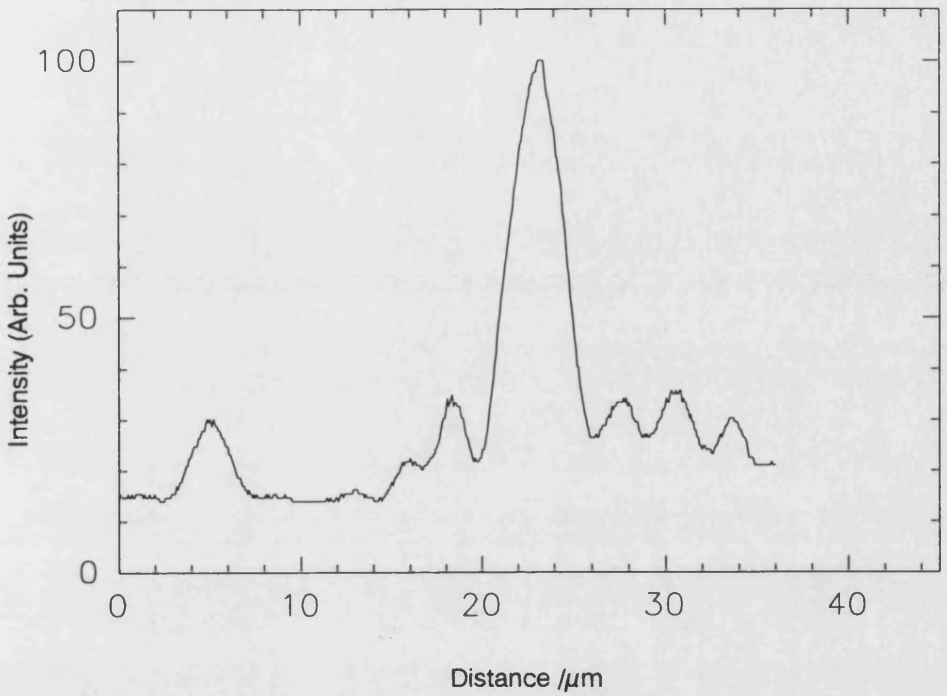

Figure 5.29.a. Measurement of the Beam waist of UB829B Linear Bow-tie laser. The device was 2mm long, tapering from 3-120μm in width and had 100μm long trenches to the side of the narrow centre region.

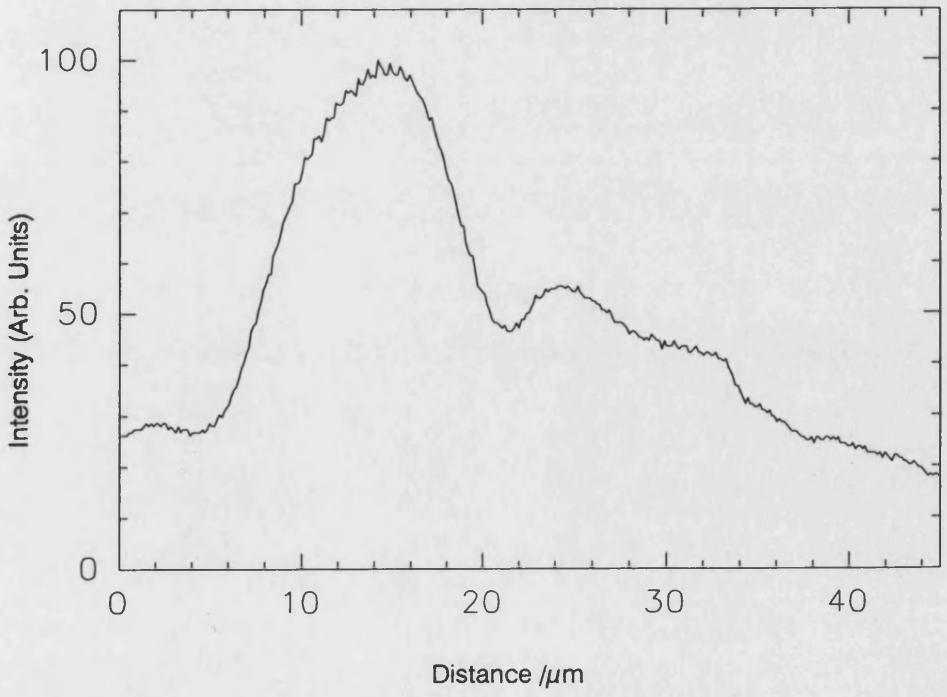

Figure 5.29.b. Measurement of beam waist of UB829Y Linear Bow-tie laser. The device was 2mm long, tapering from 3-120μm in width with no trenches to the sides of the centre.

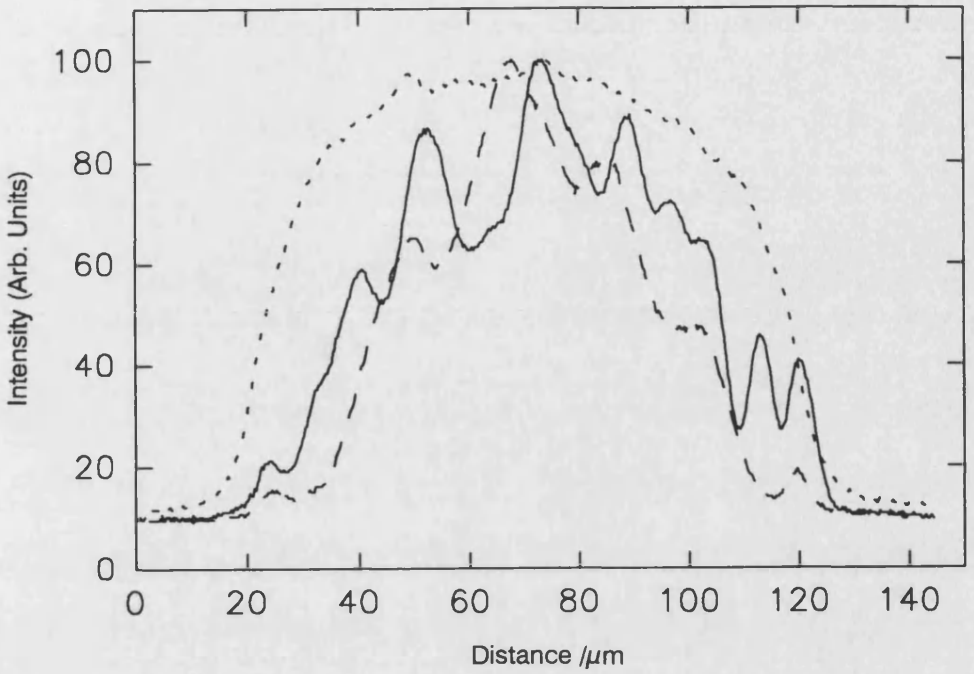

Figure 5.30.a. Near field intensity profiles at different currents from UB891W linear Bow-tie laser. The device was 2mm long, tapering from 3-90μm in width and had 100μm long trenches to the side of the narrow centre region. Dotted curve - 50mA. Dashed curve - 200mA. Solid curve - 1A.

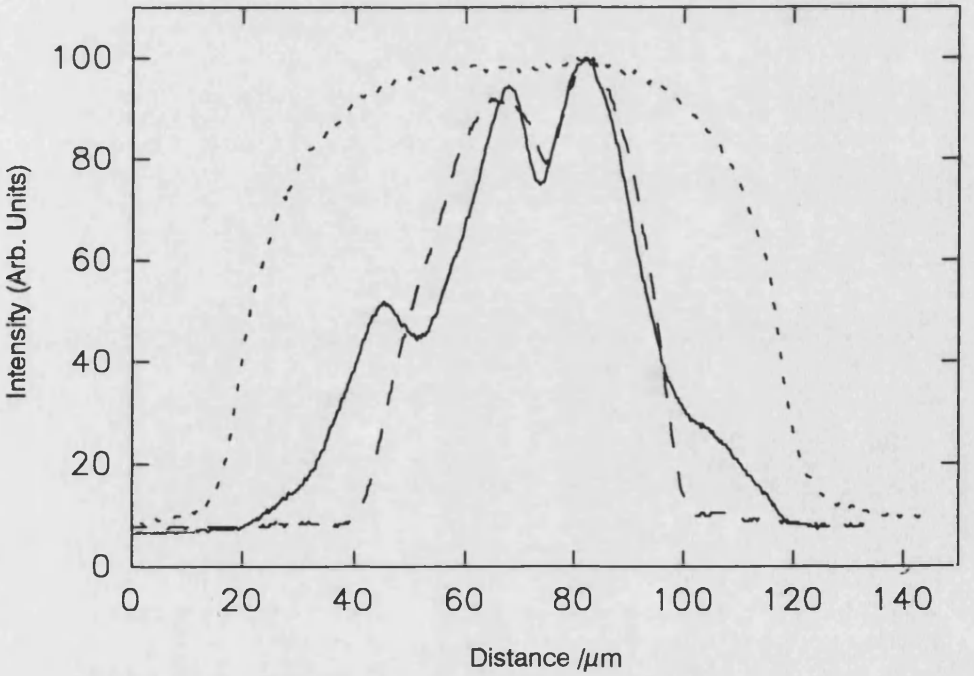

Figure 5.30.b. Near field intensity profiles at different currents from UB891B Linear Bow-tie laser. The device was 2mm long, tapering from 3-120μm in width. Dotted curve - 50mA. Dashed curve - 200mA . Solid curve - 1A.

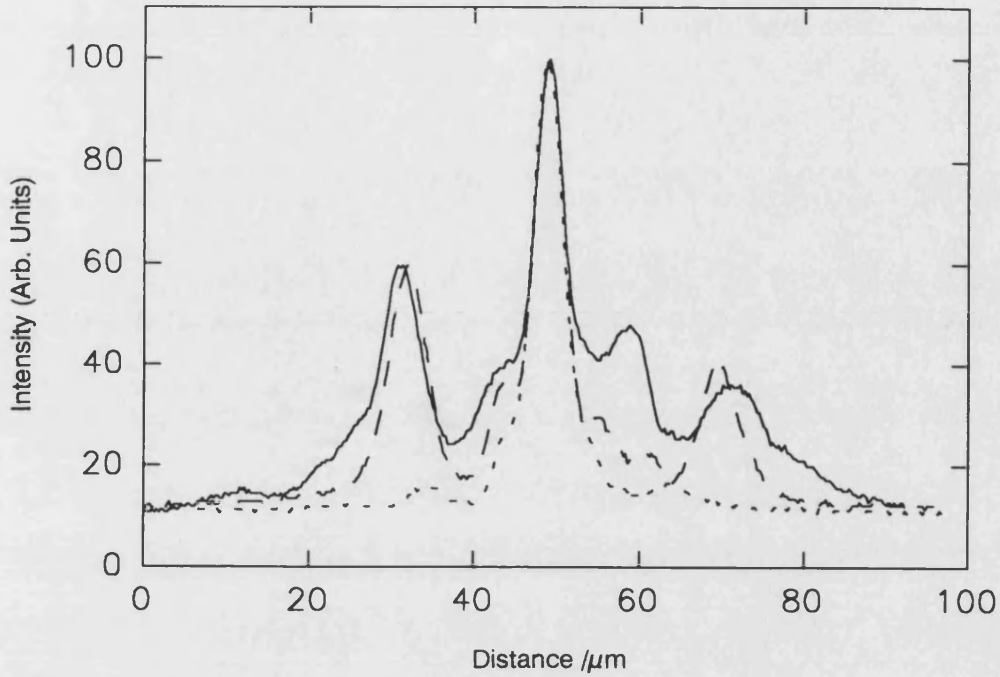

Figure 5.31.a. Intensity profile at the beam waist of UB891W linear Bow-tie laser. Dotted curve - 200mA. Dashed curve - 400mA. Solid curve - 1A.

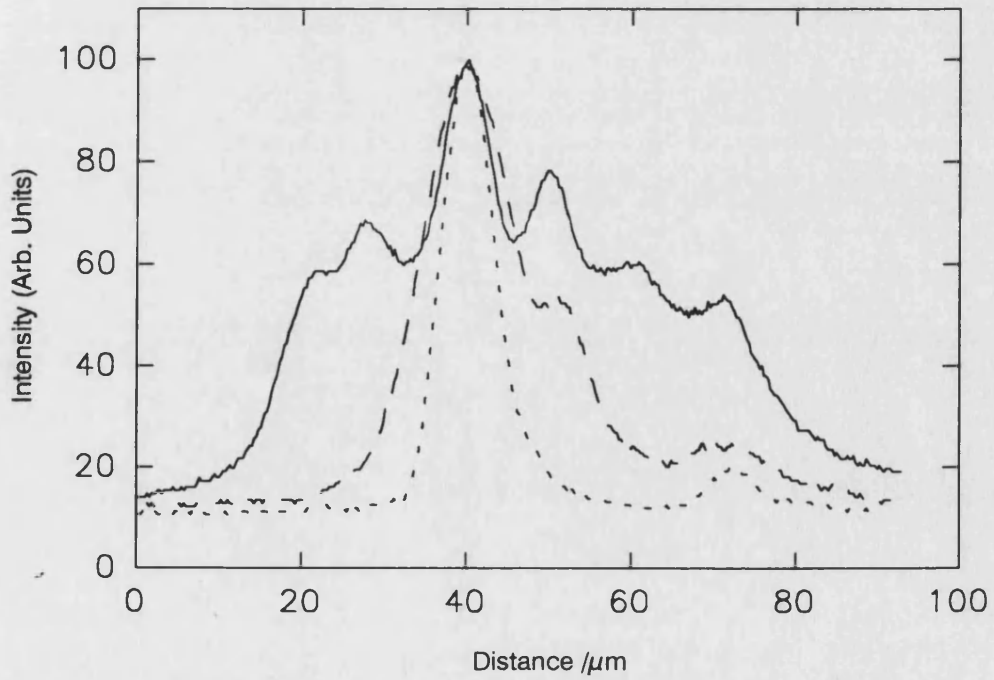

Figure 5.31.b. Intensity profiles at the beam waist of UB891B Linear Bow-tie laser. Dotted curve - 155mA. Dashed curve - 200mA . Solid curve - 1A.

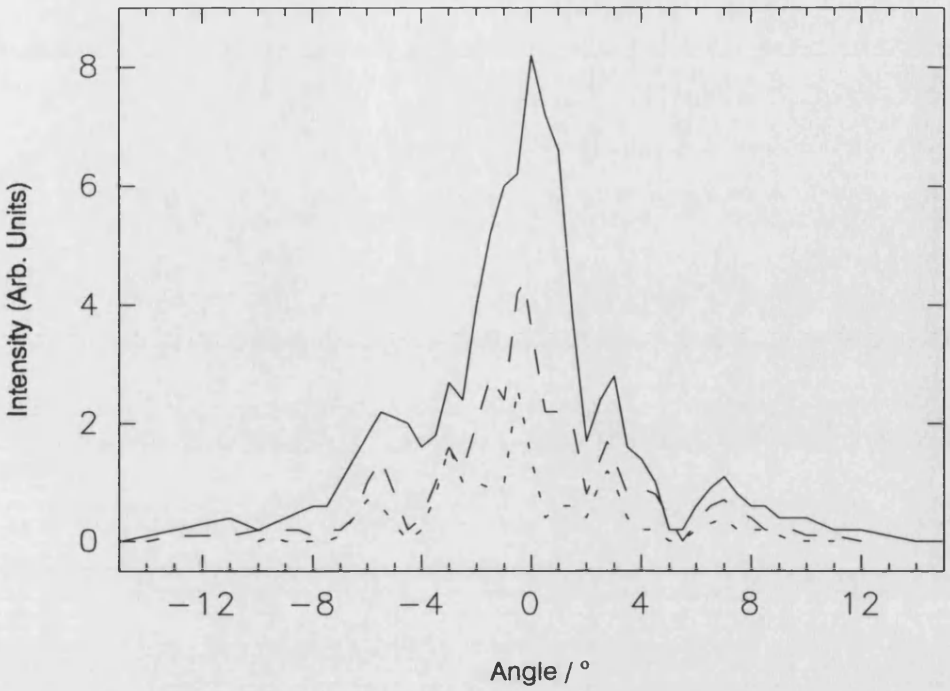

Figure 5.32.a. Far field intensity profiles at different currents from UB891W linear Bow-tie laser. Dotted curve - 400mA. Dashed curve - 600mA. Solid curve - 1A.

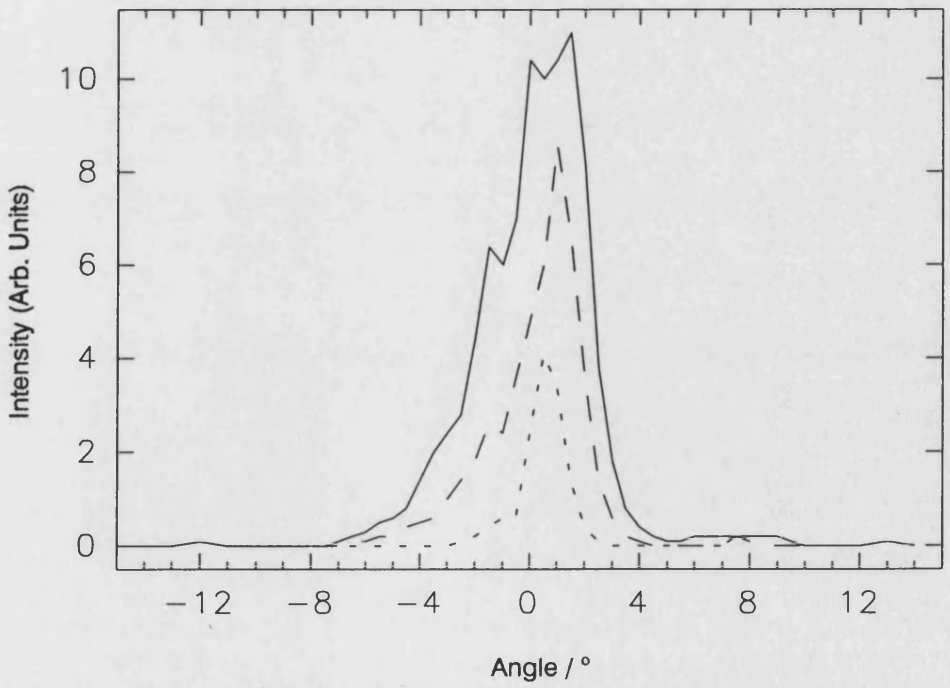

Figure 5.32.b. Far field intensity profiles at different currents from UB891B Linear Bow-tie laser. Dotted curve - 400mA. Dashed curve - 600mA . Solid curve - 1A.

they were consistent with the multiple peaked near field intensity profiles described above. Ideally, UB891W would be expected to have a much larger divergence angle than UB891B. The reduced FWHM was due to the multiple peaked nature of the lasing mode. Figure 5.32.a does clearly show significant side lobes demonstrating that a significant amount of power was emitted at angles up to +/- 6°. Measuring the widths of the profiles at ($1/e^2$) of the maximum intensity showed that the beam from device UB891W was more divergent (~11.5°) than the beam from device UB891B (~7°).

Finally, the output powers from devices UB891W and UB891B were measured at currents up to 2 Amps. Figure 5.33 shows the measured curves. At currents above 600 mA the devices have similar single-facet slope efficiencies of 0.35 W/A.

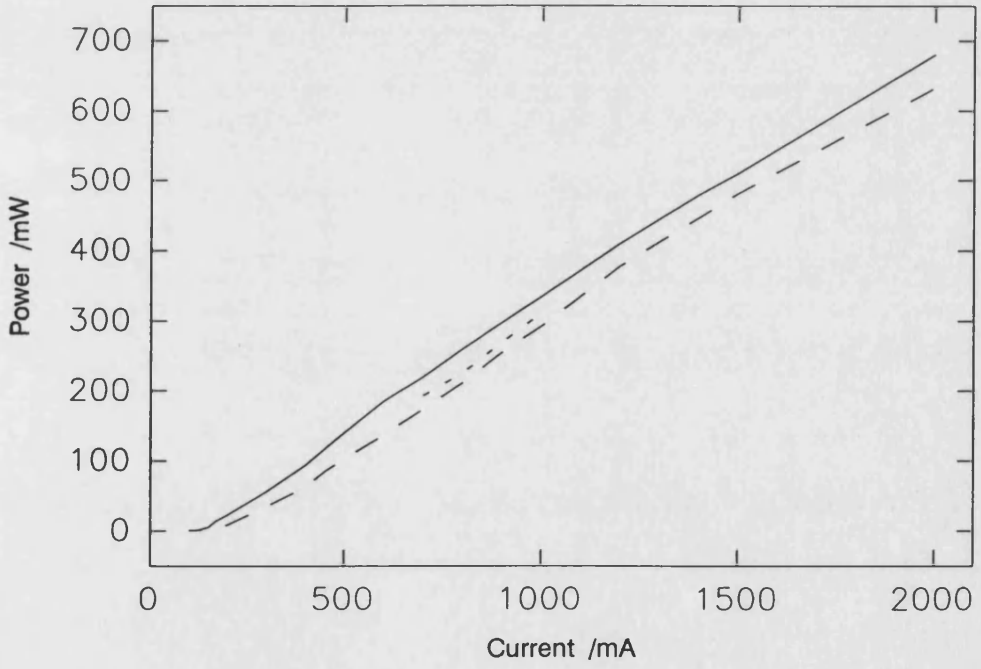

Figure 5.33. Measured output power vs. current curves from 2mm long Bow-tie lasers fabricated from Michigan InGaAs material. 3μs current pulses and a 1:300 duty cycle were used. Dashed curve - Dominant output level from UB891W - 'wavelength-shifted' material at centre of device. Dotted curve - Secondary output level from UB891W. Solid curve - Output power from UB891B - homogenous material.

5.3.5 Conclusions

Large linearly tapered bow-tie lasers have been realised in patterned substrate InGaAs QW material. Although a wavelength shift was not observed the etched trenches provided good spatial filtering of the field resulting in an output beam that could be focussed to a narrow beam waist. Excellent coupling efficiency to single mode fibre should be achievable with devices of this type. Furthermore, the devices were not optimised. Therefore, altering the dimensions and utilising facet coatings will allow a very high power, and high brightness, device to be realised.

Work still remains in order to establish the origin of the thermal effects that caused temporal instability in the output power at some currents. The reason this instability was more pronounced in some devices than others must also be investigated.

The cause of the deteriorating beam quality at high currents also requires further investigation. A spatially resolved measurement of the optical spectrum of the multiple peaks in the beam waist focal plane may reveal if the peaks were filaments or if the device was simply exciting higher order lateral modes.

5.4 Conclusions

Experimental results from a variety of devices have shown a number of interesting properties. Considering first the results from bow-tie lasers with different taper shapes it was seen that at low currents parabolic bow-tie lasers had a greater efficiency than exponentially or linearly tapered devices. The exponential device had a lower threshold current due to the smaller contact area, however, the slope efficiency was also lower. It was seen in chapter 2 that parabolically tapered waveguides retain more power in the local fundamental lateral mode along the length of the taper resulting in a near flat wavefront at the wide end. Upon reflection from the facet this field couples more efficiently into the centre of the device than the curved wavefront fields of the linearly and exponentially tapered devices. This led to the greater slope efficiency of the parabolic devices.

5 element bow-tie arrays with linearly and parabolically tapered sections have also been tested. 600mW CW was achieved from a 2mm long parabolically tapered array with no facet coatings. At low currents (<1A) these devices confirm the single-element measurements showing lower threshold currents for the parabolically tapered devices. However, when tested with 3μs pulses at higher currents, uncoated linearly and parabolically tapered devices show very similar output powers for a given current until the linearly tapered devices finally give higher output powers (~1.8W peak) shortly before failure at 7A. AR coated devices showed 33% higher slope efficiencies and 1.8W output power at 5A without failure when tested with 3μs pulses. A narrow far field profile (FWHM<1°) showed evidence of coupling between elements in a parabolically tapered bow-tie laser array. However, significant side lobes were also measured and much work will be needed in order to better understand and exploit this coupling.

Lasers fabricated from different areas of an InGaAs quantum well material sample grown on a patterned substrate have shown no variation in emission wavelength. However, large linearly tapered bow-tie lasers fabricated from the material have shown interesting properties. Trenches in the substrate have shown an excellent ability to spatially filter the optical field resulting in a diverging output beam that could be focussed to a narrow (4μm FWHM) beam waist.

Multiple quasi-stable output states could be seen for some devices at particular currents. The laser output power appeared to oscillate between these states on a time scale of 50ns-1.5μs but with no characteristic switching frequency. Tapered devices tested previously have also exhibited some time dependence in the light output at similar currents ($>2 \cdot I_{TH}$) [5]. From the relatively slow timescale one can conclude that this is a thermal effect. Following the work of Buda et al. [4] it is thought most likely that the switching occurs as thermal variations alter the lateral index profile of the waveguide thereby changing the lateral mode.

References

[1] J.J.Lewandowski, M.C.Farries, D.J.Robbins, P.J.Williams, B.K.Nayar, 'High power tapered laser arrays at 980nm,' SIOE conference, Cardiff, 1997.

[2] D.Kitchen, F.R.Laughton, R.V.Penty, I.H.White, 'Q-switched Bow-tie laser arrays', SIOE conference, Cardiff, 1997.

[3] J.Phillips, K.Kamath, J.Singh, P.Bhattacharya, 'Adatom migration effects during molecular beam epitaxial growth of InGaAs/GaAs quantum well on patterned substrates with vertical sidewalls: Blue shift in luminescence spectra,' Applied Physics Letters, Vol. 68, p1120-1122, 1996.

[4] M.Buda, W.C.van der Vleuten, Gh.Iordache, G.A.Acket, T.G.van de Roer, C.M.van Es, E.Smalbrugge, 'Lateral thermal waveguiding in low confinement, edge emitting laser diodes for very high power operation', SIOE conference, Cardiff 1998.

[5] I.Middlemast, J.Sarma, R.Mueller, A.Klehr, M.Voss, K.A.Shore, 'Observation of spatial switching in bow-tie lasers,' SIOE conference, Cardiff, 1996.

Chapter 6

Longitudinal Mode Discrimination in Lasers with Coarse Gratings

6.1 Introduction - Single Longitudinal Mode Lasers

Distributed feedback (DFB) and distributed Bragg reflector (DBR) lasers are used extensively in applications where stable, single wavelength sources are vital. Both devices make use of low order Bragg gratings to achieve highly wavelength dependent feedback such that lasing only occurs for one particular wavelength. However, these devices require relatively complex fabrication procedures to produce the fine grating and high quality AR facet coatings needed. It has previously been shown that perturbations within a standard Fabry-Perot cavity laser [1,2] can cause the device to oscillate in particular longitudinal modes in preference to other modes.

The results published by Corbett et al. [2] are of particular interest. In this work slots were etched across the rib of standard rib waveguide lasers in order to change the effective refractive index of the transverse mode at these points. Importantly, these slots were not etched through the active layer. The change in refractive index between the slot and the adjacent regions caused small reflections to the field and resulted in sub-cavities within the main cavity that was formed by the facets. The authors showed that longitudinal modes that were resonant within the sub-cavities lased before other modes. Hence, by positioning the slots at precise points along the cavity, corresponding to L/2 and L/4 where L was the cavity length, the authors were able to produce lasers that emitted only in every fourth longitudinal mode. No mathematical explanation was given for the operation of the lasers.

A transmission line model has been used previously to examine the operation of cavities with coarse gratings [3]. Grating periods of around 10-20μm were considered in that work. This model was adapted in order to model structures with perturbations positioned at arbitrary points along the cavity length and more complex cavities including those with gratings over all or part of the length. A brief description of this model is given in the next section. Simulation results from the model for a variety of structures are given in section 6.3.

6.2 Transmission Line Model

Appendix 3 details the analogy between propagating optical fields and transmission lines and shows how this can be used to investigate the transmission properties of laser cavities. A typical cavity is shown in figure 6.1. It is assumed that, in general, there is gain in the different sections of dielectric and therefore the dielectric constant is complex. However, the gain has been assumed constant within each section and independent of wavelength.

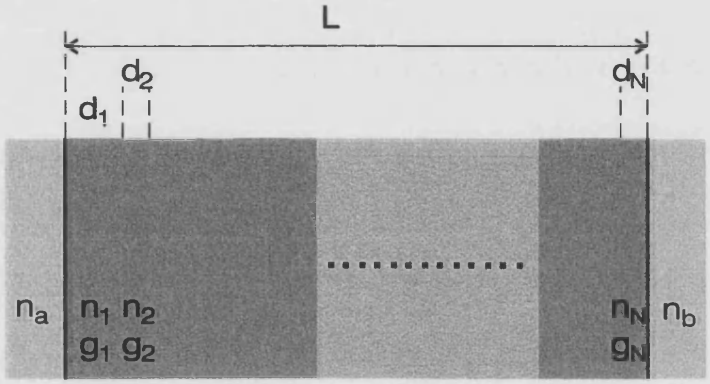

Figure 6.1. Schematic of a typical multi-section laser cavity.

Equation A3.3 in appendix 3 gives the threshold condition for the structure. Rearranging this equation gives:

$$\frac{\left(\frac{AZ_B + B}{CZ_B + D}\right)}{Z_A} = -1 \qquad \{A3.3\}$$

The left hand side of the equation represents the normalised loop impedance of the structure where the coefficients A, B, C, and D are dependent on the cavity. Plotting this impedance against wavelength shows the longitudinal mode structure of the cavity (see figure 6.2). Lasing threshold is reached when this impedance is purely real and has a magnitude of 1. If the impedance has a magnitude greater than 1 and is purely real then this corresponds to a potential longitudinal mode that is below threshold. Conversely, if the magnitude is less than 1 then the mode is above threshold at this gain value. Therefore one can use this quantity to judge the relative lasing potential of different longitudinal modes.

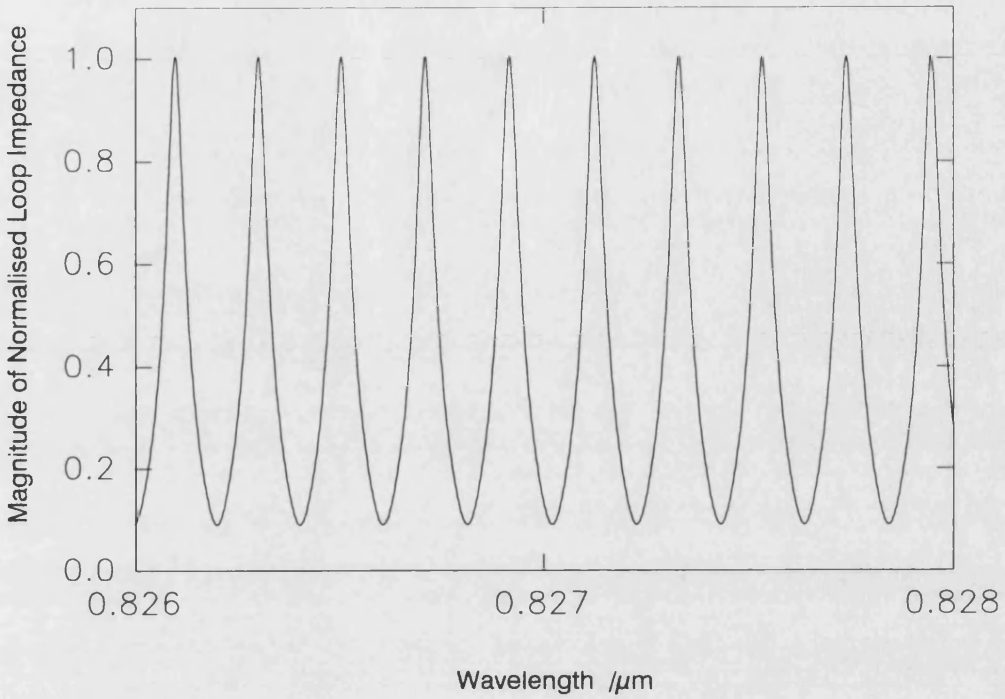

Figure 6.2. Plot of the normalised loop impedance magnitude variation with wavelength for a Fabry-Perot cavity. Each of the ten peaks corresponds to a longitudinal mode.

6.3 Simulation Results

A variety of cavities were analysed in order to establish the effects of gratings and arbitrary perturbations on device performance. Figure 6.3.a. shows the variation of loop impedance with wavelength for a standard Fabry-Perot cavity at threshold gain. In this case the cavity was 500μm long with an unperturbed effective refractive index of 3.4. Each peak occurs at a point where the impedance is purely real and corresponds to a longitudinal mode. It can be seen that in this simplest cavity all of the peaks are of equal height and therefore all of the longitudinal modes would reach threshold at the same gain value.

Figure 6.3.b. shows the variation of loop impedance with wavelength if 5μm wide low index perturbations are placed at every 1/4 of the cavity length. An effective index step of 0.01 was used in the calculation. Figures 6.3.c and d show the effects of perturbations at every 1/8 and 1/16 respectively. The index steps were again 0.01. It can be seen that the separation between enhanced longitudinal modes (those most likely to lase), represented by the lower peaks, is dependent on the grating period. With a grating period of 1/8 of the cavity length every eighth mode is enhanced.

Figure 6.4. shows again the variation of loop impedance with wavelength when perturbations are placed at every 1/16 of the cavity length. Figure 6.4.a repeats the case for 5μm wide perturbations with an effective index step of 0.01. Figure 6.4.b shows the variation for 3μm wide perturbations at every 1/16 with an index step of 0.01. Comparing this plot with figure 6.4.a shows the effect of the perturbation width on the enhancement envelope. Use of narrower perturbations increases the wavelength range over which there is a large (or small) enhancement between near longitudinal modes. Figure 6.4.c shows the variation for 5μm perturbations for an index step of 0.005. A real index step of 0.0 with a gain step of 100% was used in the calculations for figure 6.4.d. Comparing these two plots with figure 6.4.a. one can see that the enhancement of the modes increases with increasing index step and that a 'gain grating' provides much less enhancement than an index grating can.

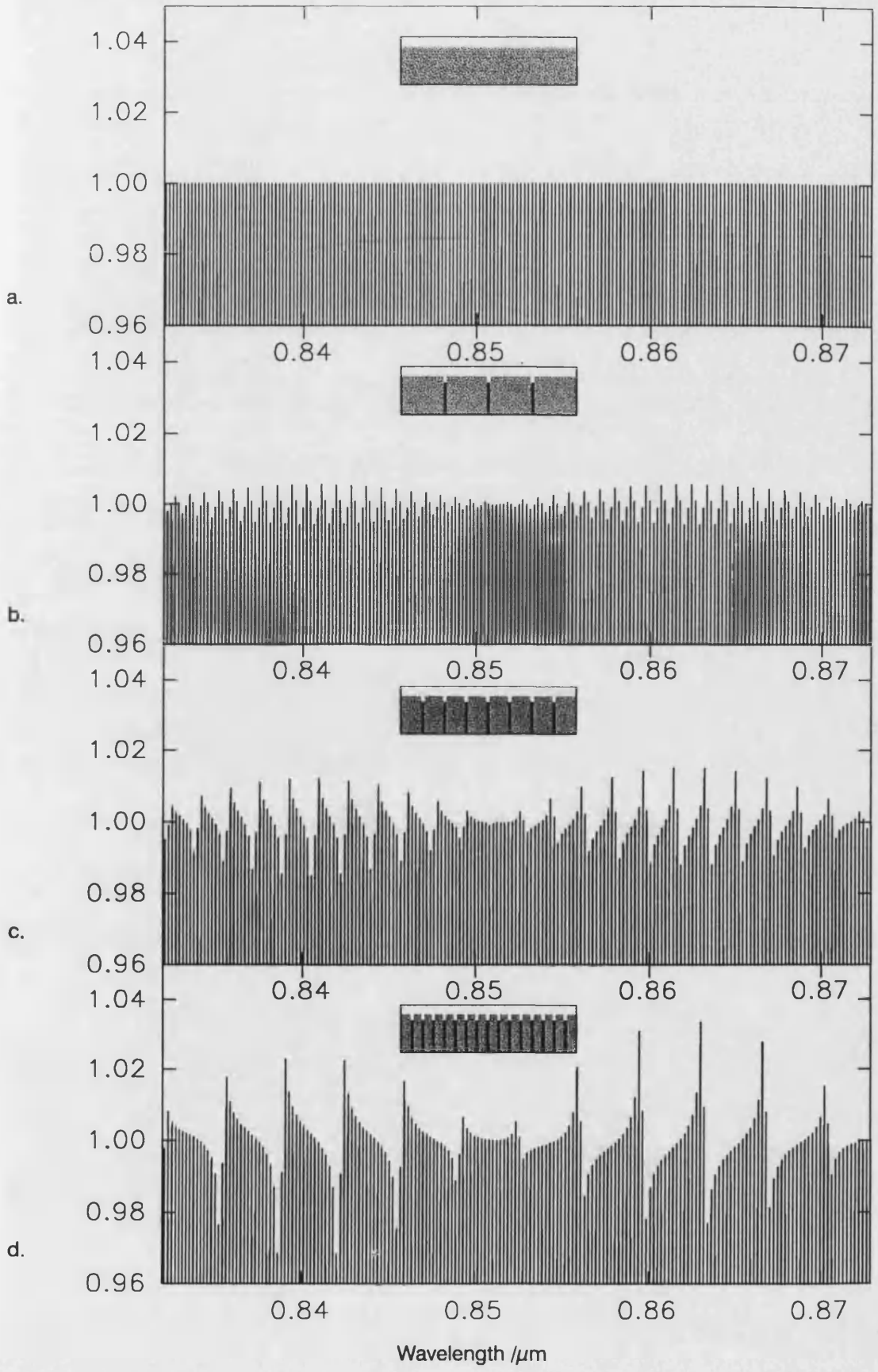

Figure 6.3. Plots of loop impedance magnitude against wavelength for different cavities.

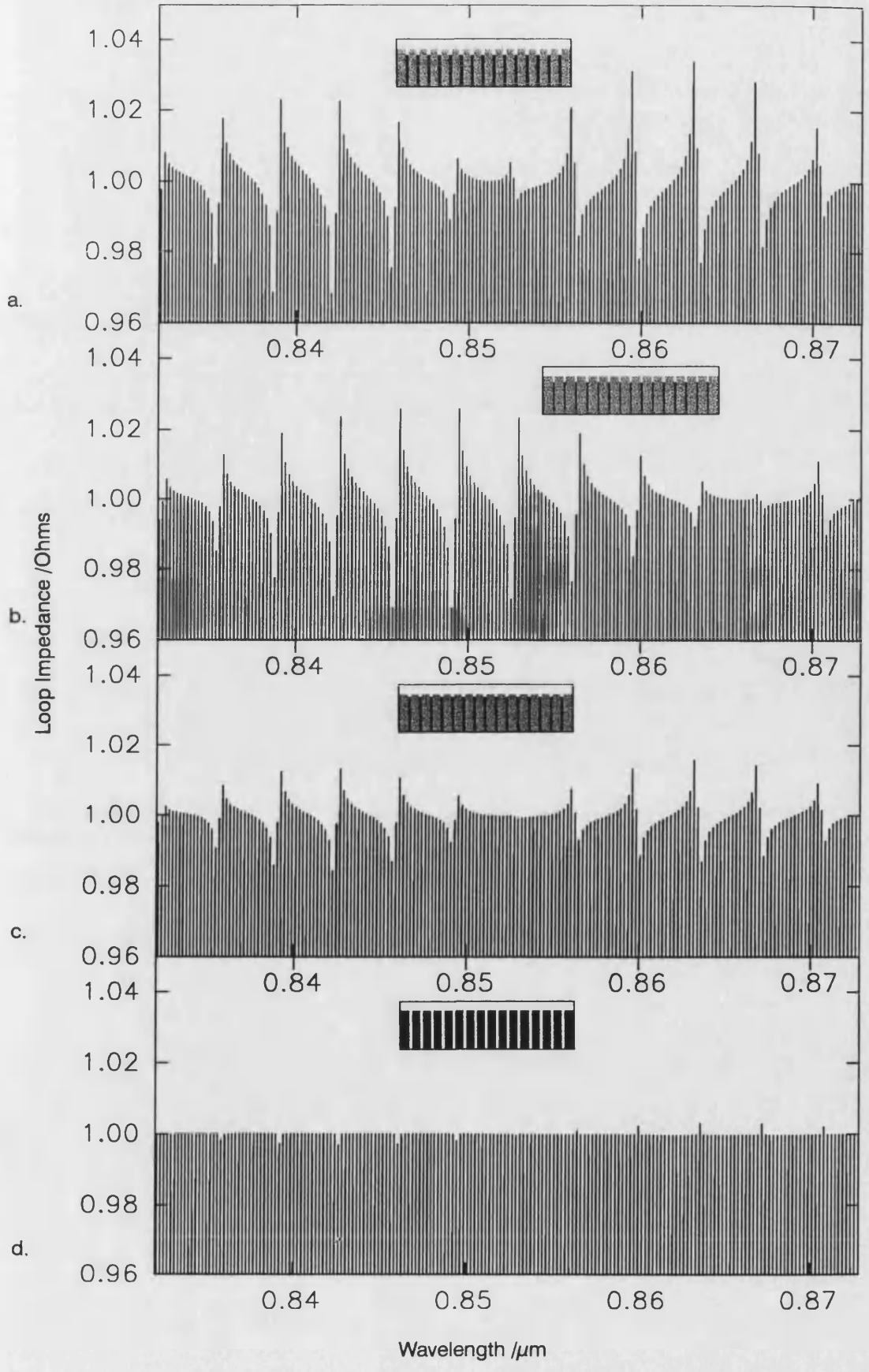

Figure 6.4. Plots of loop impedance magnitude against wavelength for different cavities.

In figure 6.5 the difference between having a grating over the length of the cavity and having unequally spaced perturbations is examined. Figure 6.5.a shows the mode spectrum for a cavity with 5μm perturbations positioned at L/8, L/4 and L/2, where L is the cavity length. There are no perturbations at 3/8, 5/8, 3/4 and 7/8 of the cavity length. If this plot is compared with figure 6.3.c one can see that employing a grating, i.e. a perturbation at every 1/8 of the cavity, significantly increases the discrimination between the lowest threshold mode and its nearest neighbours. Figure 6.5.b is for a cavity with 5μm perturbations at L/16, L/8, L/4 and L/2. The cavity that produced the profile in figure 6.5.c has perturbations at 15L/16, 7L/8, and 3L/4 as well as L/16, L/8, L/4 and L/2. Comparing these two figures shows that the amount of discrimination is approximately doubled by having perturbations 15L/16, 7L/8, and 3L/4 as well as L/16, L/8, L/4 and L/2. Figure 6.5.d shows the discrimination that occurs when only one perturbation is present at L/16.

Figure 6.6 shows the results of an investigation into the tolerance of the concept to the misalignment of a cleaved facet. Figure 6.6.a repeats the mode spectrum of a cavity with real index perturbations at every 1/16 of the cavity length. Figure 6.6.b shows the mode spectrum if the second facet was cleaved 1μm out of place to produce a longer than designed device. The perturbations are identically spaced to the case of figure 6.6.a however the final section is now 1μm longer. Figure 6.6.c shows the spectrum if the cavity were cleaved 2μm too long. The spectrum for a cavity that is 1μm too short is given in figure 6.6.d.

The effect of starting the grating in different parts of its cycle is investigated in figure 6.7. Two gratings were examined. Figures 6.7.a and c are the mode spectra for cavities with gratings having a period equal to 1/8 of the cavity length. For the spectrum in fig. 6.7.a the first low index region occurred at 1/8 of the cavity length. For the spectrum in fig. 6.7.c the first low index region occurred at 1/16 of the total cavity length. Similarly, figures 6.7.b and d. are for cavities with gratings having a period of 1/16th of the cavity length. For the first plot the first low index region occurred at 1/16 of the length while for the second plot the region occurred at 1/32 of the cavity length.

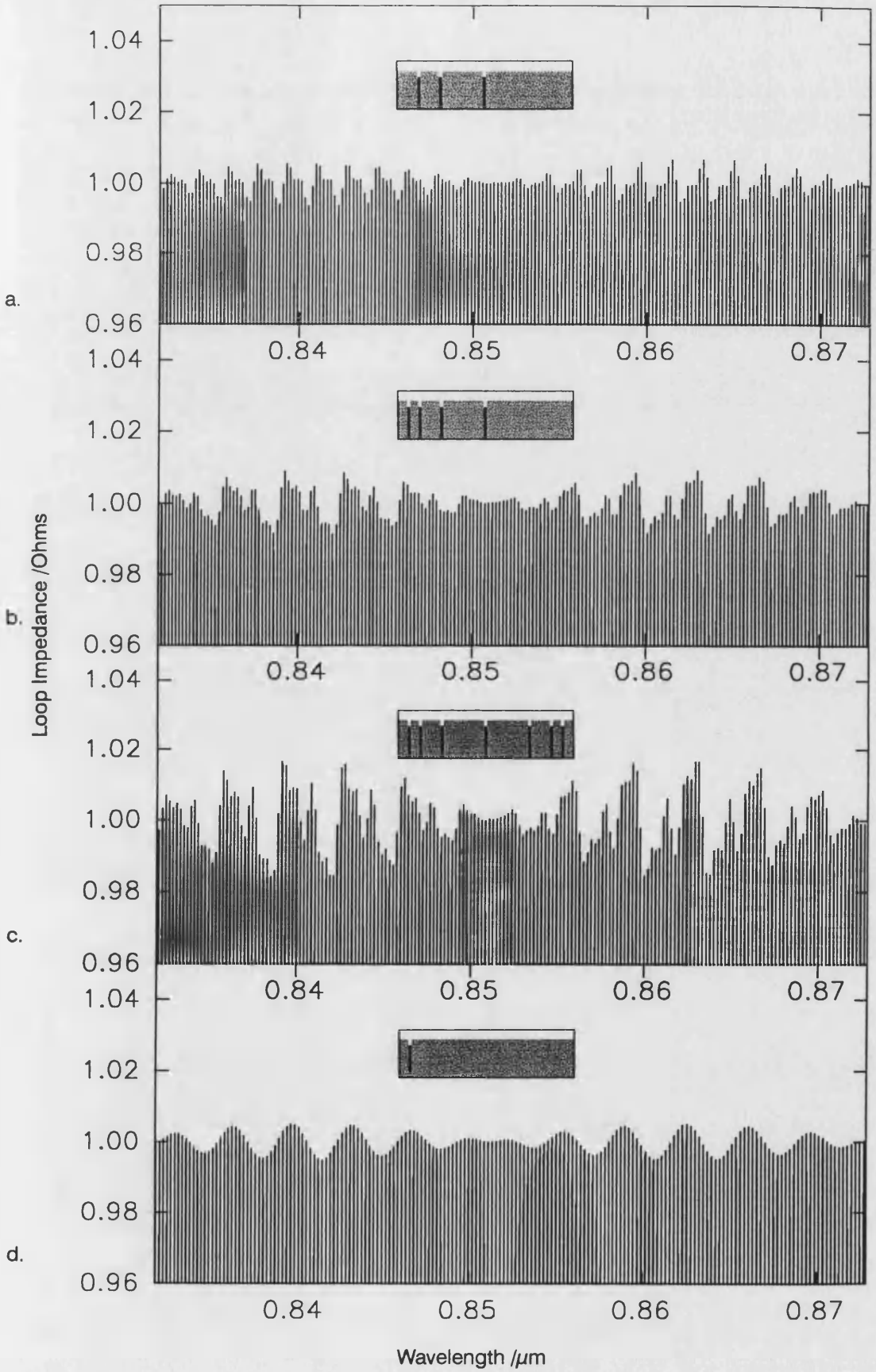

Figure 6.5. Plots of loop impedance magnitude against wavelength for different cavities.

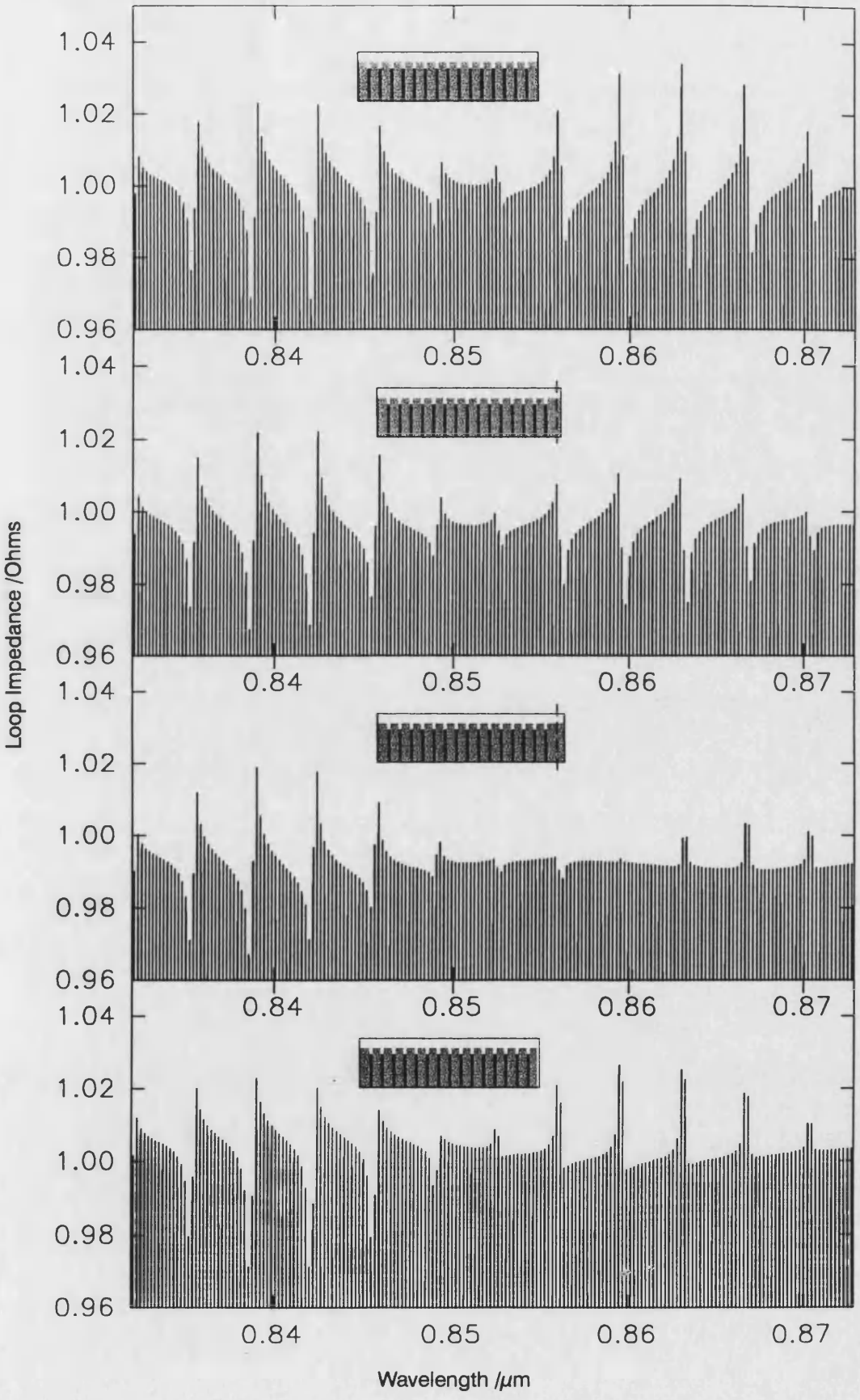

Figure 6.6. Plots of loop impedance magnitude against wavelength for different cavities.

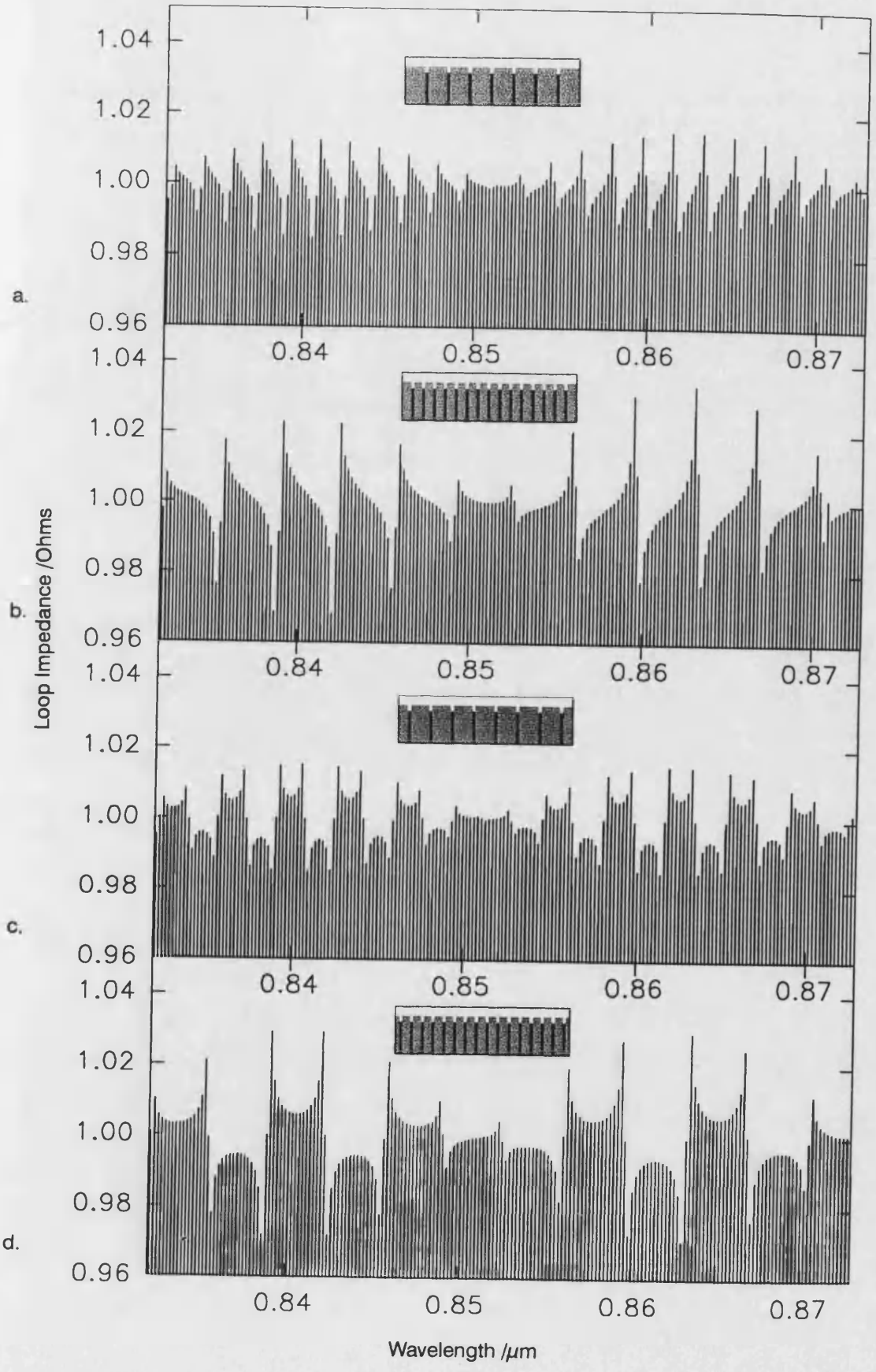

Figure 6.7. Plots of loop impedance magnitude against wavelength for different cavities.

6.4 Conclusions

The transmission line model has shown that the longitudinal mode spectrum of a Fabry-Perot laser can be modified with perturbing slots placed at various positions within the cavity. It can be clearly seen that a grating over the length of the device should result in improved discrimination when compared with a number of differently spaced perturbations. In particular, a large improvement in the discrimination between adjacent modes is found. It can also be seen that real refractive index gratings produce much more significant effects than gain gratings.

The concept is reasonably tolerant to error in the position of a cleaved facet. Good discrimination can still be achievable with a facet at 2μm from its designed position. The mode discrimination is also essentially unaffected by having the first perturbation of a grating at Λ or $\Lambda/2$, where Λ is the spatial period of the grating.

However, the model has given only a qualitative indication of the mode discrimination possible. Experimental results are needed in order to quantitatively establish the grating characteristics required to produce a desired amount of side-mode suppression.

References

[1] D.A. Kozlowski, J.S. Young, J.M.C. England, R.G.S. Plumb, 'Singlemode 1.3μm Fabry-Perot lasers by mode suppression,' Electronics Letters, Vol. 31, p.648-650, 1995.

[2] B. Corbett, D. McDonald, 'Single longitudinal mode ridge waveguide 1.3μm Fabry-Perot lasers by modal perturbation,' Electronics Letters, Vol. 31, p.2181-2182, 1995.

[3] F. Nazzarri, 'Coarse gratings for integrated optical semiconductor devices,' MEng Thesis, University of Bath, 1997.

Chapter 7

Conclusions and further work

7.1. Conclusions

A compact model for tapered waveguides and lasers has been developed and used to arrive at designs for high power tapered lasers. A systematic procedure was followed. A number of passive tapered waveguides were analysed to examine the effects of different taper parameters on the propagation characteristics of the devices. Comparisons were made with the output obtained from propagating diffracting fields in a 2D homogenous medium. In particular, different taper shapes were analysed and the parabolic shape shown to keep most of the power in the local lateral fundamental mode of the waveguide provided the overall expansion is limited. Consequently, parabolically tapered waveguides gave the narrowest far field profiles.

Extension of the model to active devices allowed the analysis of parabolically tapered lasers. Exponentially and linearly tapered lasers could not be analysed without further improvements to the model to include the continuum modes in order to account for the power radiated from the rib waveguide in these devices. Since a compact, efficient model rather than a general model was sought for the present work this additional extension was not made. The model was used to analyse several parabolically tapered lasers of different sizes in order to choose appropriate dimensions for devices to be fabricated.

Devices have been fabricated to correspond with those simulated. Comparisons with the simulation results show excellent agreement between model and experiment for several devices of different sizes. Pulsed measurements showed in excess of 300mW peak powers were possible from a single facet of a 30μm wide parabolic bow-tie laser. CW power of 200mW from a single facet has been achieved from a similar device.

Low current measurements on bow-tie lasers with different taper shapes have shown that parabolically tapered devices have higher slope efficiencies than linearly and exponentially tapered devices. This confirms the findings of the model that more power is coupled into higher order modes in linearly and exponentially tapered devices and that this power is radiated from the sides of the device lowering the efficiency.

The importance of cavity spoilers has been demonstrated by comparing the later results with the results obtained from the first batch of parabolically tapered lasers. The first lasers had cavity spoilers and showed excellent agreement with the model having narrow single-lobed far field profiles. The later lasers had no spoilers and the parabolically shaped device had a double peaked far-field profile providing evidence of higher order lateral modes. It is believed that such higher order modes would have been blocked by cavity spoilers.

The model has also been used to examine the effects on device performance of changes to the wide facet reflectivity and variations in current density along the length of the device. This work has shown that reducing the reflectivity results in much increased slope efficiencies and lower power densities in the narrow region for a given output power. The model predicted that only small improvements in threshold current will result from varying the current density along the length of the device.

Experimental measurements have been made showing a reduction in narrow facet output power density for a constant wide facet output power from some single-taper lasers in order to confirm the theoretical predictions. Increased slope efficiencies have also been measured although these results showed that the quality of the facet coatings was variable.

Bow-tie laser arrays have been realised producing 600mW CW power from a single facet and almost 2W peak power in 3μs pulses. Under pulsed conditions an improvement of 33% in the slope efficiency of bow-tie laser arrays due to anti-reflection (AR) coating of both facets has been measured.

Large linearly tapered bow-tie lasers have been realised in InGaAs/GaAs material. It has been shown that operation of a linearly tapered bow-tie laser is possible with a large astigmatism and that high power output from such a device can be focussed to a small beam waist (<4μm FWHM). Temporally stable operation has been observed from one device although the other devices all showed some kind of oscillations in output power over a range of currents. The reasons for this are as yet unclear but believed to be thermal in origin due to the timescale of the oscillations.

In addition to the above work on tapered devices some analysis has been performed on Fabry-Perot laser cavities that contain small perturbations to the refractive index. The

usefulness of different perturbations in producing discrimination between longitudinal modes has been examined using a model based on the analogy between transmission lines and optical propagation through dielectric layers. The results have shown how it is possible to preferentially excite certain longitudinal modes compared to others through the use of coarse effective index gratings with spatial periods of the order of 50μm.

7.2. Future Work

The work contained in this thesis has shown that tapered lasers can produce high powers with good beam quality. Parabolically tapered bow-tie lasers with narrow far field profiles and linear bow-tie lasers with narrow beam waists have both been demonstrated. However, much work still remains. Future work on tapered devices can be divided into two broad categories. The first of these is the analysis and optimisation of existing designs. Secondly, there are further novel features that can be incorporated into tapered devices.

7.2.1. Analysis of current designs

A more comprehensive experimental study of AR coatings applied to tapered lasers is needed. Examination of the deposition process and different coating substances may help to produce more consistent results. CW measurements of AR coated devices should be compared to results from similar uncoated devices.

No work has yet been carried out on optimising the material structure for high power operation. Adopting a 'broadened waveguide' or 'large optical cavity' structure [1] to increase the width of the vertical mode profile and decrease the power density should lead to increased maximum output powers from all types of tapered devices. Aluminium-free materials should also increase the maximum power density before failure. In addition, since evidence of gain guided operation was seen in some devices then methods of increasing the lateral index step of devices could be examined. This could include fabricating buried heterostructure devices, for example, although this is not possible in Bath.

Temperature measurements are of importance for several reasons. Local temperature variations due to defects or poor contacts cause differences in refractive index which alter the waveguide and affect the operation of a device. Such variations are thought to

be responsible for the oscillations seen in the output from the large linearly tapered 980nm devices of chapter 5. Temperature measurements are also of interest in studies of the degradation and failure of devices. For example, absorption of laser light at the facets by interface states results in local heating and can eventually lead to catastrophic optical damage where the facet essentially melts.

Measuring the spontaneous emission spectrum of the device, including above threshold, allows one to evaluate the temperature within the active layer. Several schemes have been employed to measure the spontaneous emission while filtering the laser light. The most generally applicable scheme for broad area lasers is to fabricate a laser with a narrow window in the p-side contact (see figure 7.1.a) through which spontaneous emission will be transmitted. This window should be etched through the highly doped capping layer of the material to reduce signal attenuation but be narrow enough that the free carriers spread across beneath it and the carrier profile at the active layer is then unaffected by the window's presence. A scanning near field optical microscope (SNOM) can then be used to detect this light and obtain the longitudinal temperature profile. The disadvantage with this method is that it is only applicable to broad area lasers (widths greater than approximately 15μm) and requires the laser to be mounted substrate side down to the heatsink which is not the standard procedure for good thermal contact and may therefore affect the temperature of the device. The advantage is that the method is not material-specific.

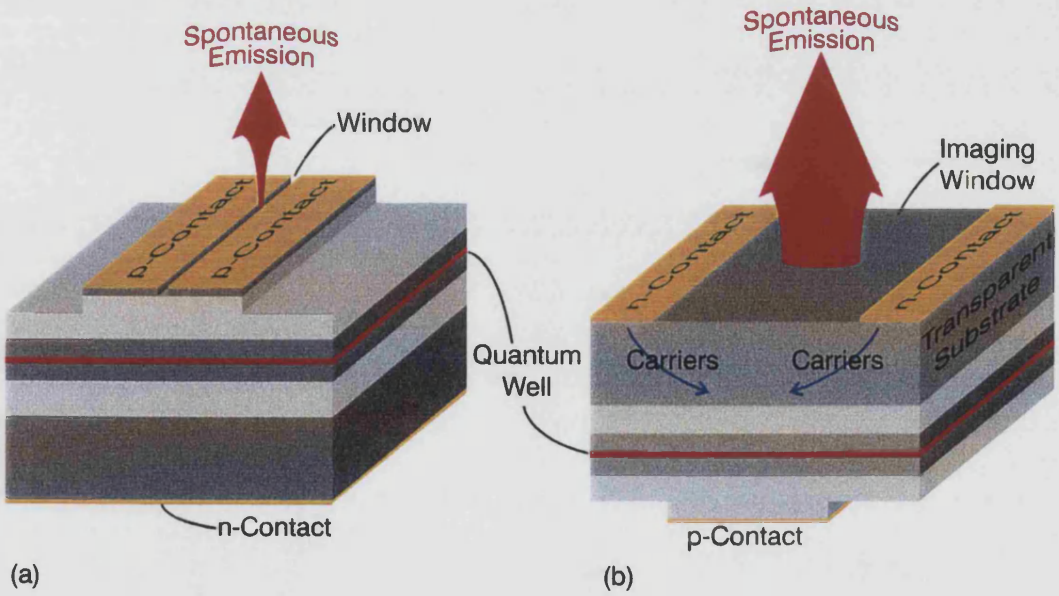

Figure 7.1. Alternative window arrangements for spontaneous emission measurements
(a) Schematic of a broad area laser with a narrow longitudinal window in the p-contact
(b) Schematic of a transparent substrate laser with an imaging window in the n-contact.

Alternatively, when using materials where the substrate is transparent to the emitted light, such as the 980nm Michigan material, it is possible to fabricate a device with a broad window in the n-side contact (see figure 7.1.b). The spontaneous emission from the active layer can then be imaged and a 2-dimensional profile of the temperature variation can be obtained [2]. Due to the thick nature of the substrate (>100μm) the carriers are able to spread across beneath the window. Further, the laser is mounted in the standard p-side down configuration for good thermal contact to the heatsink and device operation is therefore unaffected. However, since the method relies on the substrate being transparent it is only useful with a limited number of materials.

In this work CW and quasi-CW operation only of devices were considered. It was shown theoretically that longitudinal current variation in segmented devices gives little or no advantage in CW operation. However, if high speed modulation of the laser output is desired then a segmented contact may prove useful. An investigation could be made into the modulation speeds obtainable when the current in only one device segment is modulated and the other regions of the device are continuously energised. Results could be compared with the case where the current through the whole device is modulated.

Some evidence was seen of coupling between elements of bow-tie laser arrays. This should be further investigated. Laterally resolved spectral measurements of the output from these devices may yield some further information on the operation of these devices. Also, the effect of increased element separation on the output could be measured.

7.2.2. Novel designs

The use of etched, curved facets in tapered lasers remains to be investigated. Figure 7.2 shows a photograph of a curved facet device. Near-concentrically placed curved facets have been used previously [3] to form a stable resonator cavity with interesting results. Relatively small device dimensions were used with the length at 600μm and maximum width of 40μm. As one might expect the device operated as a stable resonator only over a limited current range. At high currents nonlinear carrier effects on refractive index became more important causing the device to operate as an unstable resonator. As the current was further increased the effective beam waist appeared to move steadily away

from the facet. Hence, it was not thought possible to produce a tapered device that will operate as a stable resonator over a large current range using curved facets. It might be of more interest then to use curved facets in an unstable resonator to collimate or focus the output beam. Curved facet devices with various radii of curvature should be investigated and compared with planar facet devices in order to establish if improvements in efficiency or beam quality can be obtained.

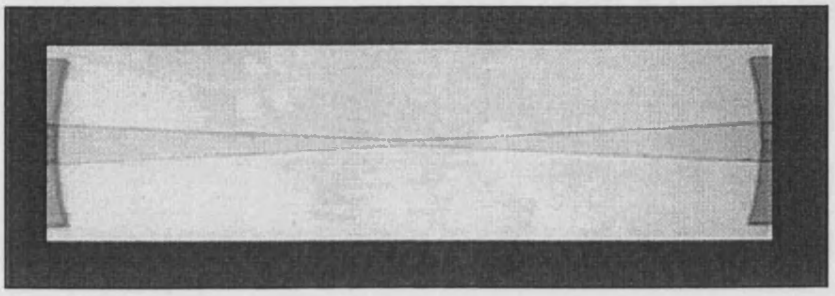

Figure 7.2. Photograph of a bow-tie laser with etched, curved facets.

It was shown in chapter 6 that a coarse effective index grating with a spatial period of 20-50μm should produce some discrimination between longitudinal modes of a laser and may result in a single mode device. Experimental measurements on narrow rib waveguide devices should be made in the future in order to quantify the grating characteristics, such as period and index step, that are needed to achieve a single mode device. The principle may then be applicable to tapered devices in order to produce high powers in a quasi-single longitudinal mode. Figure 7.3 shows a photograph of a segmented tapered device.

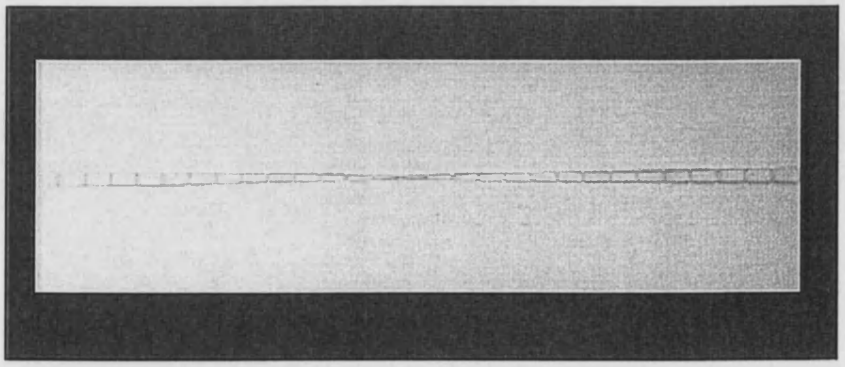

Figure 7.3. Photograph of a bow-tie laser with a segmented rib.

References

[1] see for example D. Garbuzov, 'Broadened waveguide design for separate confinement quantum well lasers,' in the proceedings of IEEE-LEOS '96 conference, Boston, USA, Vol. 1, p344-345, 1996.

[2] P. O'Brien, J. O'Callaghan, J. McInerney, 'Internal temperature distribution measurements in high power semiconductor lasers,' Electronics Letters, Vol. 34, p.1399-1401, 1998

[3] S.A. Biellak, Y. Sun, S.S. Wong, A.E. Siegman, 'Lateral mode behavior of reactive-ion-etched stable-resonator semiconductor lasers,' Journal of Applied Physics, Vol. 78, p.4294-4296, 1995.

Appendix 1.

Modes of the Slab Waveguide

In this appendix the bound modes of a symmetric slab waveguide will be derived from Maxwell's equations. Although not a complete set without the continuum modes these modes form the basis functions used to describe the optical field in the model used in this thesis.

Maxwell's Equations:

Bold type represents vector quantities. Maxwell's equations for electromagnetic waves are:

$$\nabla\times\mathbf{E}(x,y,z,t)=-\frac{\partial}{\partial t}\mathbf{B}(x,y,z,t) \qquad \{A1.1\}$$

$$\nabla\times\mathbf{H}(x,y,z,t)=\mathbf{J}(x,y,z,t)+\frac{\partial}{\partial t}\mathbf{D}(x,y,z,t) \qquad \{A1.2\}$$

$$\nabla\cdot\mathbf{D}(x,y,z,t)=\rho(x,y,z,t) \qquad \{A1.3\}$$

$$\nabla\cdot\mathbf{B}(x,y,z,t)=0 \qquad \{A1.3\}$$

where **E** and **H** are the electric and magnetic field vectors respectively and **J** and ρ are the current and charge sources. **D** and **B** are the electric and magnetic displacement vectors and are given by:

$$\mathbf{D}(x,y,z,t)=\varepsilon_0\varepsilon\mathbf{E}(x,y,z,t)+\mathbf{p}(x,y,z,t) \qquad \{A1.5\}$$

$$\mathbf{B}(x,y,z,t)=\mu[\mathbf{H}(x,y,z,t)+\mathbf{m}(x,y,z,t)]$$

where **p** and **m** are the electric and magnetic polarisation vectors of the material, $\varepsilon_0\varepsilon$ is the permittivity of the material and μ is the magnetic permeability. No magnetic material is considered here, hence $\mu = \mu_o$, the free space value. The permittivity has been represented as the free space value, ε_0, multiplied by the material dependent relative permittivity, ε. It will also be assumed that there is no net charge in the cases to be considered here, $\rho = 0$. **p** and **m** are considered static in time such that their differentials contribute nothing to equations {1.2} and {1.1} respectively.

Further, it will be assumed that all functions are time harmonic. Therefore, for some general function, F:

$$F(x,y,z,t) = f(x,y,z)\,\mathrm{Re}[e^{j\omega t}] \qquad \{A1.6\}$$

Hence, in equations {1.1} and {1.2}, $\partial/\partial t$ can be replaced with $j\omega$. The time dependency exponential term will, in general, be omitted but is always implied. Current density is given by $\mathbf{J} = \sigma\mathbf{E}$, where σ is the conductivity. Including these conditions then combining equations {1.1} and {1.4} gives equation {1.7} and equations {1.2} and {1.3} give {1.8}. For generality, the conductivity is represented as a complex term in the dielectric constant in equation {1.8} however this term will frequently be omitted in the analysis of passive waveguides.

$$\nabla\times\mathbf{E}(x,y,z) = -j\omega\mu\mathbf{H}(x,y,z) \qquad \{A1.7\}$$

$$\nabla\times\mathbf{H}(x,y,z) = j\omega\varepsilon'\mathbf{E}(x,y,z) \qquad \text{where } \varepsilon' = \varepsilon_0\varepsilon - j\frac{\sigma}{\omega} \qquad \{A1.8\}$$

These equations can be rearranged in order to eliminate $\mathbf{H}$ giving the wave equation:

$$\nabla^2\mathbf{E}(x,y,z) + \omega^2\mu\varepsilon'\mathbf{E}(x,y,z) = 0 \qquad \{A1.9\}$$

Thus far no assumptions have been made about the geometric structure to be considered. The slab waveguide structure, as shown in figure A1.1, will now be introduced. It is assumed to be infinite in the y and z directions and lossless, hence the permittivity is purely real. The field shall be independent of the y-direction, hence $\partial/\partial y = 0$. Two sets of equation are now obtained by expanding {1.7}and {1.8}:

$$\frac{\partial E_y}{\partial z} = j\omega\mu H_x \qquad \frac{\partial E_y}{\partial x} = -j\omega\mu H_z \qquad \frac{\partial H_x}{\partial z} - \frac{\partial H_z}{\partial x} = j\omega\varepsilon E_y \qquad \{A1.10\}$$

$$\frac{\partial H_y}{\partial z} = -j\omega\varepsilon E_x \qquad \frac{\partial H_y}{\partial x} = j\omega\varepsilon E_z \qquad \frac{\partial E_z}{\partial x} - \frac{\partial E_x}{\partial z} = j\omega\mu H_y \qquad \{A1.11\}$$

where each field component is a function of x and z. The first set correspond to the transverse electric field, $(TE)_x$ situation and the second set to the transverse magnetic field situation, $(TM)_x$.

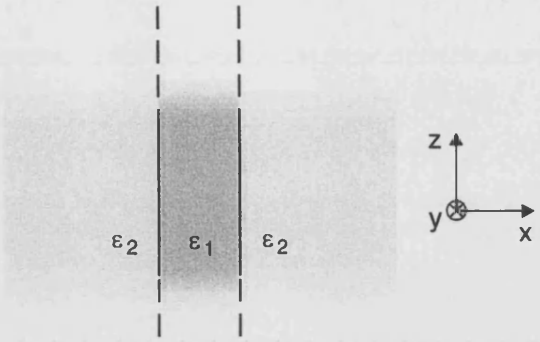

Figure A1.1. A symmetric slab waveguide structure.

Considering propagation in the z-direction, it will be assumed that fields have a z-dependence of the form: $\mathbf{F}(x,y,z) = \mathbf{F}(x,y)\cdot e^{-j\beta z}$

Equation {A1.9} now becomes:

$$\frac{\partial^2 \mathbf{E}}{\partial x^2} + (k_0^2\varepsilon - \beta^2)\mathbf{E} = 0 \qquad \text{where } k_0^2 = \omega^2\mu_0\varepsilon_0 = \frac{2\pi}{\lambda_0} \qquad \{A1.12\}$$

where λ_0 is the free space wavelength.

For $\varepsilon_1 > \varepsilon_2$ in figure A1.1, equation {A1.12} has a group of discrete solutions which are the bound modes of the waveguide. There is also a continuum of radiation modes. Only the bound modes for the $(TE)_x$ case will be derived here as the $(TM)_x$ case follows a similar procedure.

For the $(TE)_x$ case, $\mathbf{E}(x,z) = E_y(x,z)\cdot\hat{y}$ where $\hat{y}$ is a unit vector in the y-direction. The wave equation can now be written:

$$\frac{d^2E_y}{dx^2} + (k_0^2\varepsilon_1 - \beta^2)E_y = 0 \qquad \text{for } |x| \le b \qquad \{A1.13a\}$$

$$\frac{d^2E_y}{dx^2} + (k_0^2\varepsilon_2 - \beta^2)E_y = 0 \qquad \text{for } |x| \ge b \qquad \{A1.13b\}$$

Discrete solutions occur where $k_0^2\varepsilon_2 < \beta^2 < k_0^2\varepsilon_1$.

Solutions to equation {A1.13} take the form:

$$E_y = A\cos(k_1 x) + B\sin(k_1 x) \qquad \text{for } |x| \le b \qquad \{A1.14a\}$$

$$E_y = C\exp(k_2|x|) + D\exp(-k_2|x|) \qquad \text{for } |x| \ge b \qquad \{A1.14b\}$$

where $k_1^2 = k_0^2\varepsilon_1 - \beta^2$ {A1.15a}

and $k_2^2 = \beta^2 - k_0^2\varepsilon_2$ {A1.15b}

Imposing the boundary condition that the field must decay as $|x| \to \infty$ then it can be seen that $C \equiv 0$.

For the symmetric slab waveguide considered here these solutions can be subdivided into symmetric (B=0) and antisymmetric (A=0) modes. Considering first the symmetric solutions then matching the field and derivative at the guide and cladding interface gives:

$$E_y(b) = A \cdot \cos(k_1 \cdot b) = D \cdot \exp(-k_2 \cdot b) \qquad \{A1.16\}$$

$$\frac{dE_y(b)}{dx} = -k_1 \cdot A \cdot \sin(k_1 \cdot b) = -k_2 \cdot D \cdot \exp(-k_2 \cdot b) \qquad \{A1.17\}$$

Dividing equation {A1.17} by {A1.16} and multiplying through by b gives:

$$u \cdot \tan(u) = v \qquad \text{where } u = k_1 b \text{ and } v = k_2 b \qquad \{A1.18\}$$

Adding equation {A1.15a} and {A1.15b} yields:

$$k_1^2 + k_2^2 = k_0^2(\varepsilon_1 - \varepsilon_2) \qquad \{A1.19\}$$

Multiplying through by b and substituting gives:

$$u^2 + v^2 = w^2 \qquad \text{where } w^2 = k_0^2 \cdot b \cdot (\varepsilon_1 - \varepsilon_2) \qquad \{A1.20\}$$

Equations {A1.18} and {A1.20} can be solved numerically for u, and hence k_1, k_2 and β.

A similar derivation can be performed for the anti-symmetric solutions leading to:

$$u \cdot \cot(u) = -v \qquad \{A1.21\}$$

which is also solved numerically with equation {A1.20}.

The procedure for $(TM)_x$ modes is similar and will not be presented here.

Appendix 2.

Transmission Characteristics of a Fabry-Perot Cavity

Consider the cavity shown in figure A2.1.

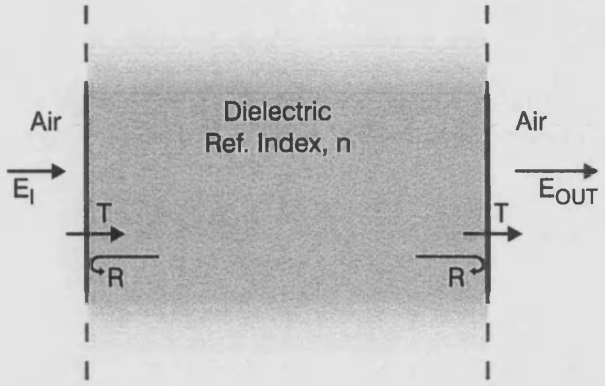

Figure A2.1. A Fabry-Perot cavity.

The electric field at the output from the cavity can be expressed as a series. The first term represents the fraction of the field that is transmitted through the cavity and immediately exits with no reflections. The second term gives the field that propagates additionally over one round trip before escaping the cavity. The third term then represents the field that propagates over two round trips and so on. Hence, the output, E_{OUT}, is given by:

$$E_{OUT} = E_I \cdot T \cdot \exp(gL - jk_0 nL) + E_I \cdot T \cdot R \cdot \exp(3gL - j3k_0 nL) +$$

$$E_I \cdot T \cdot R^2 \cdot \exp(5gL - j5k_0 nL) + \ldots \qquad \{A2.1\}$$

where, T is the fraction of the field intensity transmitted at each interface, R is the fraction of the field intensity reflected at each interface, and k_0 is the wavenumber of the light. Using the substitution G=exp(2gL), equation {A2.1}can be re-expressed as:

$$E_{OUT} = E_I \cdot T \cdot G^{1/2} \cdot \exp(-jk_0 nL) \cdot \left[1 + R \cdot G \cdot \exp(-j2k_0 nL) + \right.$$

$$\left. R^2 \cdot G^2 \cdot \exp(4gL - j4k_0 nL) + \ldots\right] \qquad \{A2.2\}$$

The right hand side of equation {A2.2} is a geometric progression. Provided that $[R \cdot G \cdot \exp(-j2k_0 nL)] < 1$ (the multiplying factor is less than 1) then the following expression can be used to simplify equation {A2.2}:

$$\sum_{i=0}^{\infty} R^i \cdot G^i \cdot \exp(-j2ik_0 nL) = \frac{1}{1 - R \cdot G \cdot \exp(-j2k_0 nL)} \qquad \{A2.3\}$$

The field at the output from the etalon then becomes:

$$E_{OUT} = \frac{E_{IN} \cdot T \cdot G^{1/2} \cdot \exp(-jk_0 nL)}{1 - R \cdot G \cdot \exp(-j2k_0 nL)} \qquad \{A2.4\}$$

The output intensity is then:

$$I_{OUT} = E_{OUT} \cdot E_{OUT}^* = \frac{E_{IN}^2 \cdot T^2 \cdot G}{1 + R^2 \cdot G^2 - R \cdot G \cdot \exp(-j2k_0 nL) - R \cdot G \cdot \exp(+j2k_0 nL)} \qquad \{A2.5\}$$

Using the substitution, $C = \frac{4RG}{(1-RG)^2}$, equation {A2.5} can be rewritten

$$I_{OUT} = E_{OUT} \cdot E_{OUT}^* = \frac{E_{IN}^2 \cdot T^2 \cdot G}{(1-RG)^2} \cdot \frac{1}{1 + C \cdot \sin^2(k_0 nL)} \qquad \{A2.6\}$$

This expression has a maximum value

$$I_{MAX} = \frac{E_{IN}^2 \cdot T^2 \cdot G}{(1-RG)^2} \qquad \text{when } k_0 nL = m\pi \qquad \{A2.7a\}$$

and a minimum value

$$I_{MIN} = \frac{E_{IN}^2 \cdot T^2 \cdot G}{(1+RG)^2} \qquad \text{when } k_0 nL = \frac{(2m+1)\pi}{2} \qquad \{A2.7b\}$$

where m is an integer.

Appendix 3.

Transmission Line Analogy

In the previous appendices the bound modes of a 3 layer slab waveguide and the propagation characteristics of a Fabry-Perot cavity were derived. These were both very simple cases with analytic solutions. Throughout the work in this thesis it has been necessary to analyse more complicated structures where the procedures used earlier are not applicable or become very cumbersome. For example, the method of appendix 1 is not adequate to find the effective index of the vertical mode in the materials used in this work since they have more than 3 layers and are not symmetric structures.

The analogy between the voltage and current in a two conductor transmission line and the electric and magnetic vectors of propagating optical fields is used to analyse more complex structures. Each layer of refractive index, ε, and thickness, d, can be represented by an equivalent transmission line matrix:

$$\begin{pmatrix} V_i \\ I_i \end{pmatrix} = \begin{pmatrix} \cos\theta & jZ_i \sin\theta \\ j\sin\theta / Z_i & \cos\theta \end{pmatrix} \begin{pmatrix} V_{i+1} \\ I_{i+1} \end{pmatrix} \qquad \{A3.1\}$$

where $\theta_i = \theta_i(\varepsilon,d,\lambda)$ and $Z_i = Z_i(\varepsilon)$.

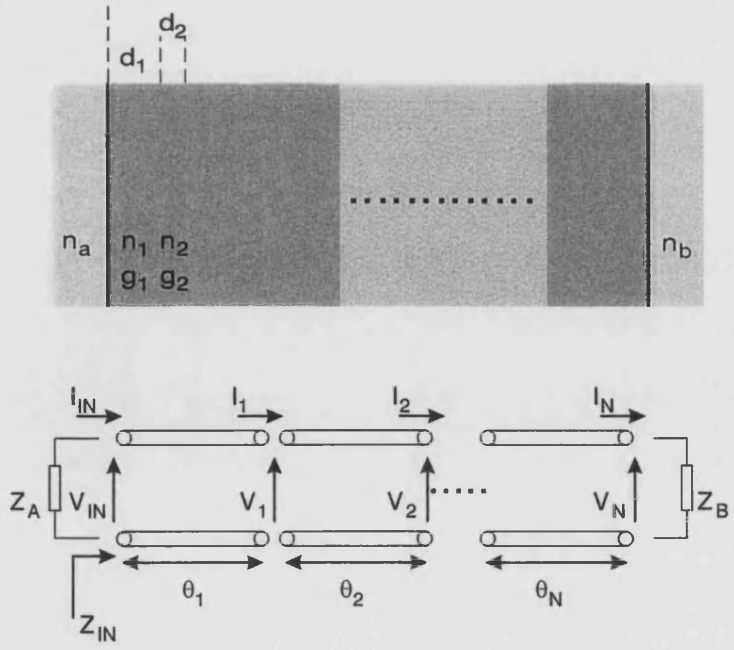

Figure A3.1. A complex planar dielectric structure and equivalent transmission line.

By multiplying together the matrices from all the individual layers the whole structure can be represented by a single matrix:

$$\begin{pmatrix} V_1 \\ I_1 \end{pmatrix} = \begin{pmatrix} A & B \\ C & D \end{pmatrix} \begin{pmatrix} V_2 \\ I_2 \end{pmatrix} \qquad \{A3.2\}$$

The infinite layers outside of the structure are represented by terminal impedances as shown in figure A3.1. The resonant condition is found by making the impedance in both directions equal at any point in the structure. Hence, for figure A3.1, $Z_A = Z_{IN}$. Applying this to equation {A3.2} with a terminal impedance of Z_B gives the eigenvalue equation:

$$Z_A = \left(\frac{AZ_B + B}{CZ_B + D} \right) \qquad \{A3.3\}$$

Bound modes of multilayer waveguides.

When using the transmission line analogy to find the bound modes of a multilayer waveguide the electrical length, θ_i, of the ith layer is given by:

$$\theta = d\sqrt{k_0^2 \varepsilon_i - \beta^2} \qquad \{A3.4\}$$

and the impedance, Z_i, is given by:

$$Z_i = \frac{1}{\sqrt{\varepsilon_i - \varepsilon_{eff}}} \quad \text{for TE modes} \qquad \{A3.5a\}$$

and $$Z_i = \frac{\sqrt{\varepsilon_i - \varepsilon_{eff}}}{\varepsilon_i} \quad \text{for TM modes} \qquad \{A3.5b\}$$

where $\beta^2 = k_0^2 \varepsilon_{eff}$ gives the relationship with the modal propagation constant. Equation A3.3 is then solved numerically to find ε_{eff}. Once ε_{eff} is found it is used in the layer matrices to find the value of the voltage (field) across the dielectric layers.

Longitudinal modes of complex cavities.

In this case the electrical length, θ_i, of the ith layer is given by:

$$\theta = d\sqrt{k_0^2 \varepsilon_i} \qquad \{A3.6\}$$

and the impedance by:

$$Z_i = \frac{1}{\sqrt{\varepsilon_i}} \qquad \{A3.7\}$$

Appendix 4.

First Order Perturbation Theory

Consider Schrödinger's equation:

$$\hat{H}\psi_n = E_n\psi_n \qquad \{A4.1\}$$

If one has solutions to the equation, $\psi_n^{(0)}$ and $E_n^{(0)}$, then one can write

$$\hat{H}_0\psi_n^{(0)} = E_n^{(0)}\psi_n^{(0)} \qquad \{A4.2\}$$

where all quantities are known.

Now consider a small perturbation, $\hat{H}'$, to $\hat{H}_0$ such that

$$\hat{H} = \hat{H}_0 + \hat{H}' \qquad \{A4.3\}$$

One can look for solutions to the perturbed eigenequation in the form of series. Hence,

$$\psi_n = \psi_n^{(0)} + \psi_n^{(1)} + \psi_n^{(2)} + \ldots \qquad \{A4.4\}$$

and $$E_n = E_n^{(0)} + E_n^{(1)} + E_n^{(2)} + \ldots \qquad \{A4.5\}$$

The derivation for the first order correction terms can be found in any quantum mechanics book [1] and will not be repeated here. The eigenfunction and eigenvalue become, respectively:

$$\psi_n = \psi_n^{(0)} + \sum_{i \neq n} \frac{H'_{in}}{E_n^{(0)} - E_i^{(0)}} \cdot \psi_n^{(0)} \qquad \{A4.6\}$$

$$E_n = E_n^{(0)} + H'_{nn} \qquad \{A4.7\}$$

where $$H'_{ij} = \int_{-\infty}^{\infty} \psi_i^{(0)} \cdot \hat{H}' \cdot \psi_j^{(0)*} dx \qquad \{A4.8\}$$

One can apply this perturbation theory to the electromagnetic wave equation of a waveguide {A1.12}in order to evaluate correction terms to the propagation constants of the modes.

Equation {A1.12} rearranges as:

$$\left[\frac{\partial^2}{\partial x^2} + k_0^2 \varepsilon_C(x)\right] F_m(x) = \beta_m^2 F_m(x) \qquad \{A4.9\}$$

which is equation {A4.1} with the substitutions:

$$\hat{H}_0 = \left[\frac{\partial^2}{\partial x^2} + k_0^2 \varepsilon_C(x)\right] \qquad \{A4.10\}$$

$$\psi_n^{(0)} = F_m(x) \qquad \{A4.11\}$$

$$E_n^{(0)} = \beta_m^2 \qquad \{A4.12\}$$

Applying a perturbation of the form:

$$\hat{H}' = k_0^2 \Delta\varepsilon_C(x) \qquad \{A4.13\}$$

Equation {A4.7} becomes:

$$(\beta_m + \Delta\beta_m)^2 = \beta_m^2 + H'_{mm} \qquad \{A4.14\}$$

which rearranges to:

$$\beta_m^2 + 2 \cdot \beta_m \cdot \Delta\beta_m + \Delta\beta_m^2 = \beta_m^2 + H'_{mm} \qquad \{A4.15\}$$

Since $\Delta\beta_m \ll \beta_m$ one can make the assumption $\Delta\beta_m^2 \approx 0$ and ignore this term. Equation {A4.15} then rearranges to give

$$\Delta\beta_m = \frac{H'_{mm}}{2 \cdot \beta_m} \qquad \{A4.16\}$$

an expression for the first order correction term, $\Delta\beta_m$, to the propagation constant, β_m, where

$$H'_{mm} = \int_{-\infty}^{\infty} F_m^2 \cdot k_0^2 \Delta\varepsilon_C(x)\, dx \qquad \{A4.17\}$$

Appendix 5.

Material Parameters

A5.1 Materials Used

Two different materials have been used in this work. The wafer structures of these materials are given below. Plots of effective index and vertical mode confinement factor against etch depth are also given.

A5.1.1 QT829B (University of Sheffield)

Layer	Thickness (μm)	Composition	Doping Density (cm^{-3})	Doping Type	Dopant
Contact	0.30	GaAs	9.0×10^{18}	p++	Zn
Cladding	0.60	$Al_{0.60}Ga_{0.40}As$	2.2×10^{18}	p+	C
Cladding	0.20	$Al_{0.60}Ga_{0.40}As$	5.0×10^{17}	p-	--
Guide	0.15	$Al_{0.28}Ga_{0.72}As$	undoped	i	--
Active	103/100 Å	GaAs/ $Al_{0.28}Ga_{0.72}As$	DQW	i	--
Guide	0.15	$Al_{0.28}Ga_{0.72}As$	undoped	i	--
Cladding	1.60	$Al_{0.60}Ga_{0.40}As$	1.5×10^{18}	n-	Si
Buffer	0.1	GaAs	1.0×10^{18}	n	Si
Substrate	---	GaAs	---	n+	--

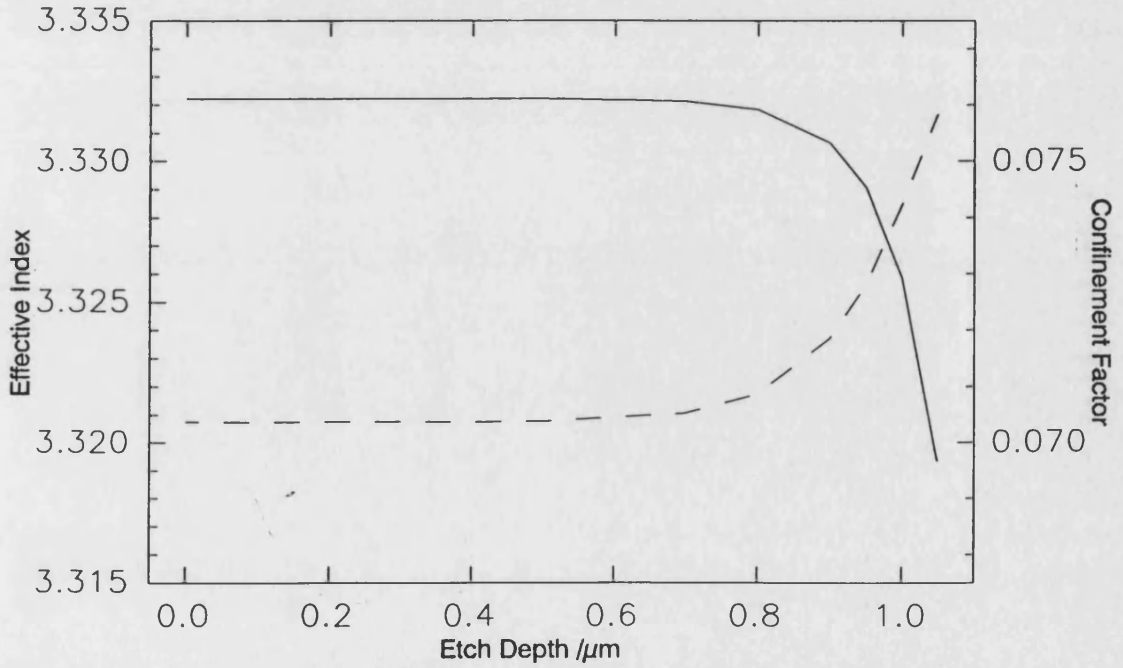

Figure A5.1. Plots of effective index (Solid curve) and confinement factor (dashed curve) against etch depth for material QT829B.

A5.1.2 V3359 (University of Michigan)

Layer	Thickness (μm)	Composition	Doping Density (cm^{-3})	Doping Type
Contact	0.1	GaAs	1×10^{19}	p++
Graded	0.1	$Al_xGa_{(1-x)}As$	$>5 \times 10^{17}$	p
Cladding	0.8	$Al_{0.6}Ga_{0.4}As$	$=5 \times 10^{17}$	p
Graded	0.1	$Al_xGa_{(1-x)}As$	$<5 \times 10^{17}$	p
Barrier	50Å	GaAs	undoped	i
QW	50Å	$In_{0.25}Ga_{0.75}As$	undoped	i
Barrier	50Å	GaAs	undoped	i
Graded	0.1	$Al_xGa_{(1-x)}As$	$<5 \times 10^{17}$	n
Cladding	0.8	$Al_{0.60}Ga_{0.40}As$	$=5 \times 10^{17}$	n
Graded	0.1	$Al_xGa_{(1-x)}As$	$>5 \times 10^{17}$	n
Buffer	0.1	GaAs	$=5 \times 10^{18}$	n+
Substrate	---	GaAs	---	n+

'x' for the graded layers is varied between 0.2 and 0.4. Substrate was patterned.

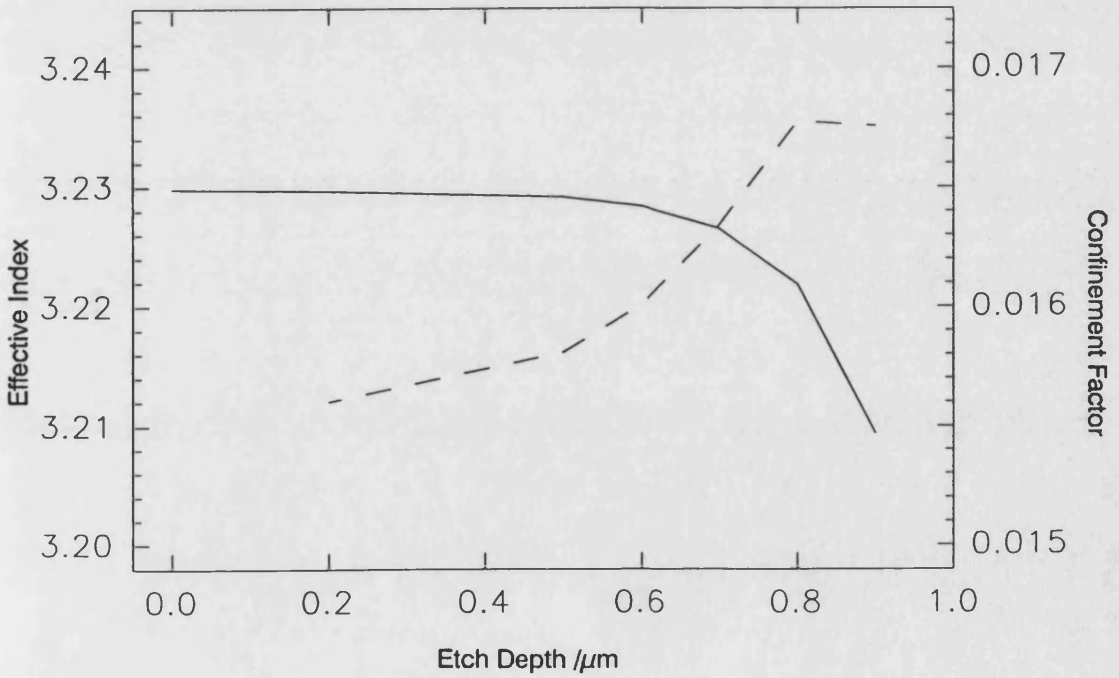

Figure A5.2. Plots of effective index (Solid curve) and confinement factor (dashed curve) against etch depth for material V3359.

A5.2 Measurement of Material Characteristics

A series of broad area lasers were fabricated with each batch of lasers. These were used to measure some of the material properties. The procedures for these measurements are given below.

Absorption loss coefficient

Measurement of the material absorption loss followed a standard procedure as described by Casey and Panish [] or Thompson []. The differential quantum efficiencies, η_D, of a number of similar broad area lasers of different lengths were measured.

The differential quantum efficiency is given by:

$$\eta_D = \frac{\eta_{ST}}{1 + 2\alpha L / \ln(1/R_1 R_2)} \qquad \{A5.1\}$$

where η_{ST} is the internal quantum efficiency, α is the absorption coefficient, L is the laser cavity length, and R_1, R_2 are the facet reflectivities. Plotting $1/\eta_D$ against cavity length for the measured devices yielded a straight line where the intercept with the vertical axis gave $1/\eta_{ST}$. A value for α was then obtained by using the value obtained for η_{ST} in equation A5.1.

Diffusion Constant

An experimental measurement of the lateral carrier density distribution, N(x), was compared with a calculated profile in order to evaluate the diffusion constant, D. The value of D was varied in the calculation until the curves matched.

The 1D diffusion equation {A5.2} was solved for N(x) to obtain the calculated profile.

$$D \cdot \frac{d^2N(x)}{dx^2} - B_R[N(x) + n_0] \cdot N(x) - \gamma_A \cdot N^3(x) - g(x) \cdot P(x) + \frac{J(x)}{q \cdot d} = 0 \qquad \{A5.2\}$$

where 'D' is the diffusion coefficient, 'N(x)' is the carrier density, 'B_R' is the bimolecular recombination constant, 'n_0' is the active layer doping density, 'γ_A' is the Auger recombination constant, 'P(x)' is the photon density, 'J(x)' is the current density, 'q' is the electronic charge, 'd' is the active layer thickness and 'g(x)' is the local gain.

The experimental profile was obtained by measuring the short wavelength spontaneous emission intensity at the facet at a current well below threshold. Low current density was used for this measurement so that there was negligible stimulated emission. The stimulated emission term [g(x).P(x)] in equation A5.2 could then be ignored in the calculation. Also, Auger recombination was ignored for the materials used in this work.

Appendix 6.

Experimental setup for different measurements

A6.1 LI + Polarisation

This is probably the simplest measurement performed in this work. At low output powers the laser is simply positioned closely to a reverse-biased large area photodiode. The current through the laser is monitored using a 'search-coil' current probe connected to an oscilloscope. The output signal from the photodiode is terminated in 50Ω at the oscilloscope and can be related to the optical power assuming that the responsivity is known for the wavelength being measured.

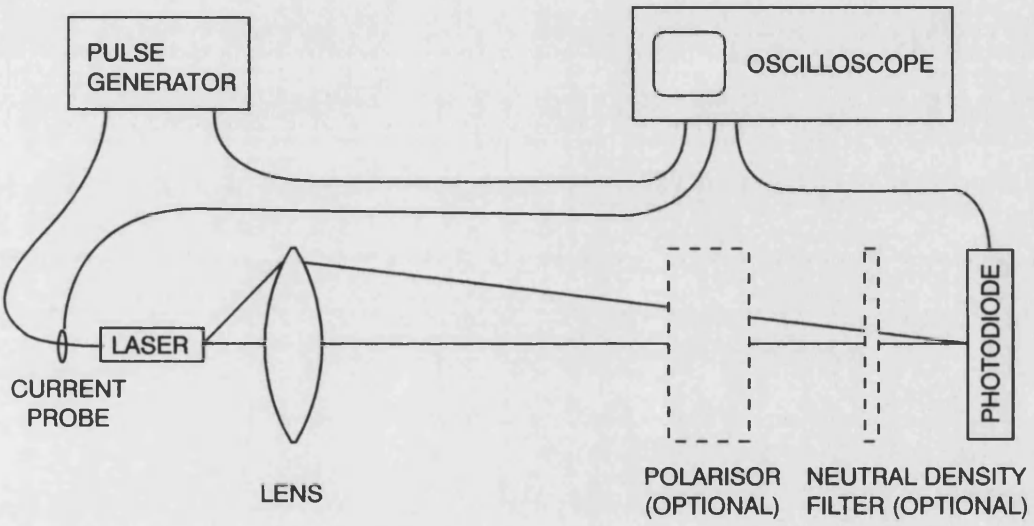

Figure A6.1. Diagram of apparatus used to measure output power and polarisation of a laser.

At higher output powers the photodiode will saturate. In order to measure power levels beyond this it is necessary to attenuate the optical signal by a known fraction. This is achieved by introducing a Neutral Density Filter between the laser and the photodiode. This type of filter is used because it attenuates the optical signal evenly over the whole wavelength range of interest. Since it is not physically possible to place the filter between the laser and photodiode when very closely spaced then an alternative optical system is needed. Figure A6.1 shows the apparatus used. The diverging laser light is collected by a lens and focussed back down to a spot at the detector. Space is then available between the lens and detector for a Neutral density filter to be introduced. The overall attenuation of the lens/filter system must be measured for each laser in order to correctly evaluate the laser power output.

Ideally, two lenses should be employed such that the beam passing through the filter is collimated. However, if the distance between lens and photodiode is sufficiently large then the beam will be nearly collimated and this is then unnecessary.

It is also possible to introduce other optical components into the system such as a polarisor. The same apparatus can then be used to measure the polarisation of the laser output.

A6.2 Near Field

The apparatus employed to measure the near field intensities of the lasers in this work is shown in figure A6.2. Again, the system is fairly simple. A single lens is used to form an image of the laser facet at the camera. The intensity variation in one dimension is then recorded by the computer.

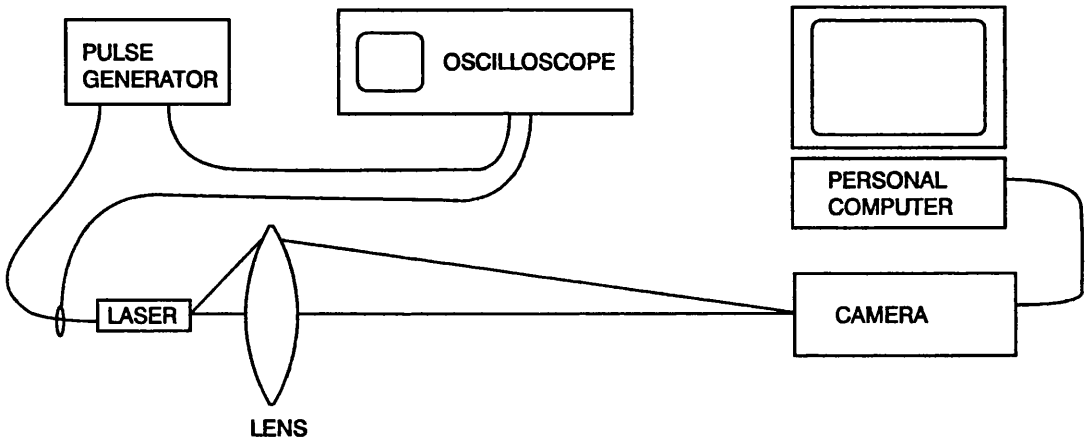

Figure A6.2. Diagram of apparatus used to measure the near field intensity profile of a laser.

When the intensity level becomes too high the camera saturates and hence it is necessary again introduce a neutral density filter after the lens in order to attenuate the optical signal when making measurements at high powers.

A6.3 Far Field

The apparatus employed to measure the far field intensities of the lasers in this work is shown in figure A6.3. The laser is mounted on a rotating stage such that the facet is on the axis of rotation. A photodiode is placed some distance away from the device with an aperture positioned close to it. As the laser is rotated the power incident on the photodiode is measured.

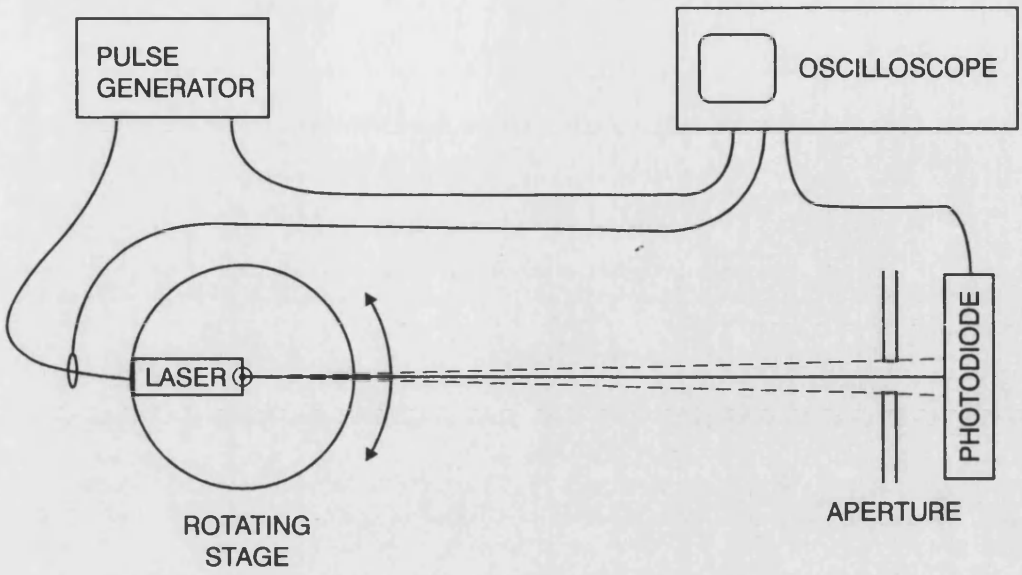

Figure A6.3. Diagram of apparatus used to measure the far field intensity profile of a laser.

The angular resolution of the measurement is set either by the smallest division on the rotating stage or by the width of the aperture and its distance from the laser facet. The smallest division on the rotating stage used in this work was 0.5°. Typically, a 0.5mm wide slit was used as the aperture at a distance of ~70mm which subtends an angle of <0.5° and therefore the resolution was set by the rotating stage at 0.5°. This led to less smooth curves than if the resolution were set by the aperture but gave the highest resolution achievable with the equipment available.

A6.4 Spectra

Figure A6.4 shows the apparatus used to measure the optical spectrum of a device. The light output is focussed onto the input aperture of the monochromator. The transmitted beam is then reflected by a curved mirror onto a planar reflection grating. This grating is angled such that the first order diffraction peak is incident on a further curved mirror and reflected onto the output aperture. Any optical power transmitted through this aperture is then collected and measured on a photodiode. Since different wavelengths are diffracted by different amounts then only a small range of wavelengths will be transmitted by the output aperture for a given grating angle. Scanning the grating through a range of angles then allows a measurement of intensity variation with wavelength to be made.

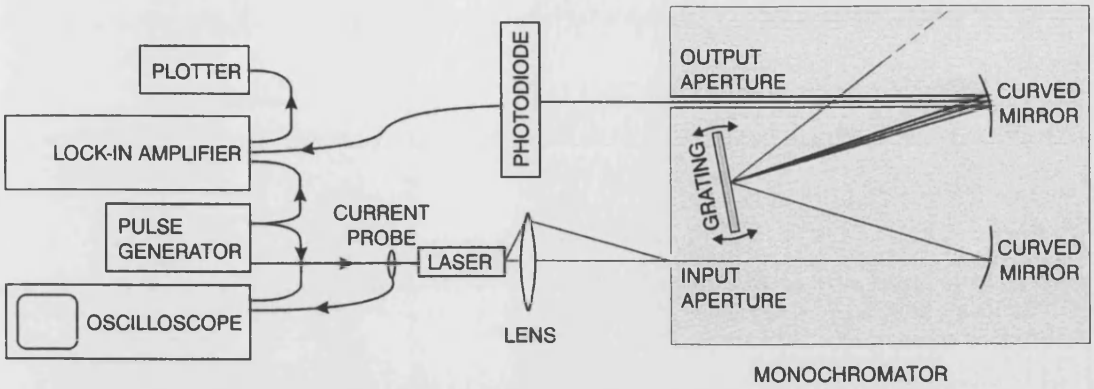

Figure A6.4. Diagram of apparatus used to measure the output spectrum of a laser.

Only very small signals were seen at the output aperture and therefore it was necessary to use a photodiode with integral amplifier and electronic signal recovery equipment in order to measure this output. The signal from the photodiode was fed into a lock-in amplifier which was synchronised with the pulse generator powering the laser. The output signal from the lock-in amplifier was then sent to an X-Y plotter and plotted against time while the monochromator scanned the grating through a range of angle giving a plot of output power against wavelength for the device.

The resolution of the monochromator is controlled by the width of the input and output aperture slits. The maximum resolution is ~0.1nm with the slits closed to less than 50nm. However, as the slits are narrowed the output is reduced until the signal becomes too noisy and therefore a compromise between resolution and signal strength can be required for some low power devices.

Appendix 7.

Calibration of Measuring Equipment

A7.1 Vidicon Camera Linearity

Near field intensity profiles were measured using an Infra-red vidicon camera. This camera had a nonlinear response to light intensity which had to be measured and corrected for.

Near field intensity profiles were measured using an infra-red vidicon camera. However, the camera tube had a nonlinear response to light intensity which it was necessary to account for. In addition, the change in dark current with temperature varied the dynamic range of the camera and burn-in affected the saturation level. Electronics were included in the camera to reduce the nonlinearity but the temperature and burn-in effects could not be compensated for and it was therefore necessary to measure the response of the camera during each set of measurements and then correct the measured intensity profiles.

The light intensity incident on the camera was varied by altering the laser pulse repetition frequency while keeping the current constant. Due to the slow time response of the camera (~3 secs) the light from successive pulses was integrated and the effective incident intensity was therefore proportional to the laser pulse frequency. A curve was then fitted to the camera output and laser pulse rate data and this curve was used to correct the measured near field intensity profiles.

A7.2 Photodiode Responsivity

Materials emitting at different wavelengths have been used in this work. The responsivity of the photodiodes used to measure output power varied with wavelength. Although, the value at a wavelength of 860nm was well known, since this is near the peak responsivity, when making the measurements at 980nm in chapter 5 the responsivity had also to be measured. This was done by simply comparing the output from the photodiode with a calibrated power meter.

A7.3 Lens Resolution

The resolution of the apparatus used to measure near field intensity profiles was limited by the lens used. The resolution, Z, of a lens is given by:

$$Z = \frac{0.61\lambda}{\mathrm{NA}}$$

where NA is the numerical aperture. The highest magnification lens used in this work had a numerical aperture of 0.65 giving a resolution of 0.80μm at a wavelength of 850nm or 0.92μm at 980nm. This would not have greatly affected the profiles measured since devices greater than 10μm wide were being considered.

Appendix 8.

Conference publications from this work

[1] N.S.Brooks, J.Sarma & I.Middlemast, 'A compact model of tapered geometry semiconductor optical devices', Semiconductor Integrated Optoelectronics '96 conference (SIOE '96), Cardiff, March 1996.

[2] N.S.Brooks, J.Sarma & I.Middlemast, 'A new design for tapered-geometry high power semiconductor optical sources', Proceedings of LEOS 96, IEEE-LEOS Annual Meeting, Boston, USA, Vol.2, p. 207-208, November 1996.

[3] N.S.Brooks, J.Sarma & I.Middlemast, 'An alternative shape for tapered geometry semiconductor optical sources', Proceedings of the International Conference on Fibre Optics and Photonics '96, Madras (Chennai), India, Vol.1, p.133-138, December 1996.

[4] N.S.Brooks, J.Sarma & I.Middlemast, 'Optical characterisation of parabolic tapered lasers', SIOE '97, Cardiff, March 1997.

[5] F.Causa, N.S.Brooks & J.Sarma, 'Hermite-Gauss functions for modelling parabolic tapered lasers: Comparison with mode matching method and with experiments', SIOE 97, Cardiff, March 1997.

[6] N.S.Brooks, F.Nazzarri & J.Sarma, 'Longitudinal mode discrimination using cavity perturbations - a transmission line analysis', SIOE '98, Cardiff, April 1998.

[7] N.S.Brooks & J.Sarma, 'Bow-tie semiconductor lasers - An experimental comparison of different taper shapes', *to be presented* at the Photonics-98 International Conference on Fibre Optics and Photonics, Delhi, India, December 1998.